



Thèse

Présentée à

L'Université de Lille

(École Doctorale des Sciences de la Matière, du Rayonnement et de l'Environnement)

par

**Jennifer Sarely GÓMEZ BADILLO**

En vue d'obtenir le grade de

**Docteur**

Filière: Molécules et Matière Condensée

Discipline: Chimie des Matériaux

---

Développement de méthodes RMN-(DNP) à hauts champs pour la  
détection des noyaux quadripolaires sur des surfaces

(Development of high-field (DNP)-NMR methods to detect  
quadrupolar nuclei on surfaces)

---

Thèse soutenue publiquement le 5 Novembre 2021

Composition du Jury:

Directeurs de thèse:

Olivier Lafon, Professeur, Université de Lille, UCCS, directeur de thèse

Frédérique Pourpoint, Maître de Conférences, École Centrale de Lille, co-directrice de thèse

Rapporteurs:

Ulla Gro Nielsen, Professeur, University of Southern Denmark, Department of Physics, Chemistry and Pharmacy

Thomas Vosegaard, Professeur, Aarhus University, Interdisciplinary Nanoscience Center (iNANO)

Examineur:

Mattias Edén, Professeur, Stockholm University, Department of Materials and Environmental Chemistry

Président du Jury:

Laurent Delevoye, Directeur de Recherche, Université de Lille, UCCS, CNRS



Dedicated to my parents Nancy and Jaime who  
with all their effort, wisdom and love,  
made me the person I am today

Dedicado a mis padres Nancy y Jaime, quienes  
con su esfuerzo, sabiduria y amor,  
me han hecho la persona que soy hoy



# Abstract

Surfaces are fundamental in the performance of modern materials. Surface properties play an important role in many fields as diverse as nanoscience, electrochemistry, electronics, energy conversion and storage as well as medicine. Therefore, fundamental understanding of surface processes and the characterization of their chemical properties are of central importance in developing new materials to meet nowadays challenges. However, the structural characterization of surface species at the atomic level is frequently challenging because they often lack long-range positional order and their fractions, among all sites, typically are quite low. Solid-state NMR spectroscopy provides unique information on the local atomic-level structure. Nevertheless, the lack of sensitivity of NMR poses a major limitation to surface characterization especially when the investigated materials contain quadrupolar nuclei.

Half-integer quadrupolar nuclei, such as  $^{11}\text{B}$ ,  $^{17}\text{O}$  and  $^{27}\text{Al}$ , represent about two thirds of stable NMR-active nuclei and are present in several organic, inorganic and biological solids. However, the NMR observation of these nuclei in solid surfaces remains often more challenging because of the larger size of the density matrix for quadrupolar nuclei as well as the large quadrupolar interaction, which broadens their resonances and complicates the spin dynamics. The NMR signal of the surface can be selectively detected by a coherent transfer of the  $^1\text{H}$  polarization to the surface nuclei. In the case of half-integer quadrupolar nuclei, the cross-polarization under magic-angle spinning (CPMAS) technique lacks robustness and it is preferable to use methods for which no spin-lock is applied to the quadrupolar nucleus. Two types of sequences, without any spin-lock, can be used in this case: through-space refocused INEPT (*D*-RINEPT) and PRESTO.

In this work, we introduced new robust symmetry-based heteronuclear dipolar recouplings built from composite inversion pulses, which can be combined with *D*-RINEPT and PRESTO schemes to transfer the polarization of protons to quadrupolar nuclei at MAS frequencies higher than 20 kHz. These transfers can be combined with DNP to enhance the NMR signals of quadrupolar isotopes, notably near the surface of

the materials. Furthermore, they can be used to acquire heteronuclear correlation spectra of protons and quadrupolar nuclei at fast MAS (62.5 kHz).

For the observation of homonuclear proximities between quadrupolar nuclei, we have compared the performances of symmetry-based homonuclear dipolar recoupling schemes for nuclei with spin value  $I = 3/2$ , such as  $^{11}\text{B}$ , and  $5/2$ , such as  $^{27}\text{Al}$ . For both isotopes, the double-quantum (DQ) - single-quantum (SQ) sequences are recommended, which yields good efficiency for both the cross- and auto-correlation peaks. For  $^{11}\text{B}$  isotope, the chemical shift differences are small or moderate, and therefore, bracketed recoupling schemes are recommended. For  $^{27}\text{Al}$  nuclei, the chemical shift differences are larger and un-bracketed recoupling schemes are recommended.

We also investigated the surface of boron nitride and oxide supported on dendritic fibrous nanosilica, which are catalyst for the oxidative dehydrogenation of propane. Through a combination of 1D and 2D multinuclear ( $^1\text{H}$ ,  $^{29}\text{Si}$  and  $^{11}\text{B}$ ) solid-state NMR experiments, it was demonstrated that BN phase undergoes a transformation to  $\text{B}_2\text{O}_3$  (oxidation) during the reaction, which led to a larger fraction of hydrogen-bonded BOH groups at the surface of oxidized DFNS/BN with respect to as-prepared DFNS/ $\text{B}_2\text{O}_3$ . This structural difference could explain the higher selectivity towards propene of oxidized DFNS/BN.

# Résumé

Les surfaces sont des régions-clefs des matériaux. Les propriétés de surface jouent un rôle important pour de nombreuses applications, telles que les nanosciences, l'électrochimie, l'électronique, la conversion et le stockage d'énergie, ou encore la médecine. Par conséquent, la compréhension des processus de surface et la caractérisation de leurs propriétés chimiques sont d'une grande importance dans le développement de nouveaux matériaux. Cependant, la caractérisation structurale des espèces de surface au niveau atomique est souvent difficile en raison de leur absence d'ordre à longue distance et de leur faible abondance par rapport aux autres sites. La spectroscopie RMN à l'état solide fournit des informations uniques sur la structure atomique locale. Cependant, la faible sensibilité intrinsèque de la RMN représente une limitation importante pour la caractérisation de la surface, surtout lorsque les matériaux étudiés contiennent des noyaux quadripolaires.

Les noyaux quadripolaires de spin demi-entier, tels que  $^{11}\text{B}$ ,  $^{17}\text{O}$  et  $^{27}\text{Al}$ , constituent environ les deux tiers des noyaux stables magnétiquement actifs et sont présents dans de nombreux solides organiques, inorganiques et biologiques. Cependant, l'observation par RMN de ces noyaux sur des surfaces solides reste souvent difficile en raison de la taille importante de la matrice de densité ainsi que de l'interaction quadripolaire, qui élargit les raies et complique la dynamique de spin. Le signal RMN de surface peut être détecté sélectivement par transfert cohérent de la polarisation des protons vers les noyaux de surface. Dans le cas des noyaux quadripolaires demi-entiers, la technique de polarisation croisée en rotation à l'angle magique (*cross-polarization under magic-angle spinning*, CPMAS, en anglais) manque de robustesse et il est préférable d'utiliser des méthodes n'utilisant pas de verrouillage de l'aimantation (*spin lock* en anglais) des noyaux quadripolaires. Deux types de séquences de ce type ont été proposées: la séquence *D*-RINEPT et la séquence PRESTO.

Dans ce travail, nous avons introduit de nouveaux recouplages dipolaires hétéronucléaires robustes basés sur la symétrie construits à partir d'impulsions d'inversion composites, qui peuvent être incorporées dans les séquences *D*-RINEPT et

PRESTO pour transférer la polarisation des protons aux noyaux quadripolaires à des fréquences MAS supérieures à 20 kHz. Ces transferts peuvent être combinés avec la polarisation dynamique nucléaire (*dynamic nuclear polarization*, DNP, en anglais) pour augmenter les signaux RMN des noyaux quadripolaires, en particulier près de la surface des matériaux. De plus, ils peuvent être utilisés pour enregistrer des spectres de corrélation hétéronucléaire de protons et de noyaux quadripolaires à des fréquences MAS élevées (62,5 kHz).

Pour l'observation des proximités homonucléaires entre noyaux quadripolaires, nous avons comparé les performances de recouplages dipolaires homonucléaires basés sur la symétrie pour les noyaux de spin  $I = 3/2$  (tels que  $^{11}\text{B}$ ) et  $5/2$  (tels que  $^{27}\text{Al}$ ). Pour les deux isotopes, les séquences de corrélation double-quantum (DQ) simple-quantum (SQ) sont recommandées car elles conduisent à une bonne efficacité, à la fois pour les pics de corrélation et d'auto-corrélation, fournissant l'ensemble des proximités spatiales, même pour les résonances ayant des fréquences de résonance proches ou identiques.

Nous avons également étudié au cours de cette thèse la structure à l'échelle atomique de nitrure et d'oxyde de bore supportés sur des nanoparticules de silice fibreuses dendritiques, qui sont des catalyseurs pour la déshydrogénation oxydative du propane. Grâce des expériences de RMN à l'état solide multinucléaires 1D et 2D ( $^1\text{H}$ ,  $^{29}\text{Si}$  et  $^{11}\text{B}$ ), il a été montré que la phase BN se transforme en  $\text{B}_2\text{O}_3$  (oxydation) au cours de la réaction, conduisant à une plus grande fraction de groupement BOH impliqués dans des liaisons hydrogène à la surface des matériaux du DFNS/BN oxydé que des nanoparticules DFNS/ $\text{B}_2\text{O}_3$ . Cette différence structurelle pourrait expliquer la plus grande sélectivité envers le propène du DFNS/BN oxydé.



# Acknowledgements

Undertaking this PhD has been a life-changing experience for me. I have been blessed to do my PhD studies at the University of Lille, and to have this exceptional experience in France. I have grown both professionally and personally in these three years, and it would not have been possible without the support and guidance that I have received from many people.

First, I would like to thank the members of the jury who kindly agreed to evaluate my doctoral work. Thomas Vosegaard, professor at Aarhus University, Ulla Gro Nielsen, professor at University of Southern Denmark, Mathias Edén, professor at Stockholm University and Laurent Delevoye, directeur de recherche at the University of Lille.

I would like to express my greatest gratitude to my supervisor Olivier Lafon, for his guidance, support and encouragement throughout the development of my thesis and daily life. Words cannot express how grateful I am to have worked alongside him. His constant feedback, time and dedication, inspired me to give my best every day. Also, I would like to give my sincere thanks to Professor Jean-Paul Amoureux, the great-grandfather of NMR as he calls himself, for welcoming me when I arrived in France, for teaching me all about quadrupolar nuclei and methodology, for his advice and guidance. It has been a pleasure for me to work with him. I would also like to thank Frédérique Pourpoint, for co-supervising my thesis, for her time and advice.

I also would like to acknowledge the funding received towards my PhD from the project funded by the European Soft Matter Infrastructure EUSMI (H2020 INFRAIA 2016). Thanks also to Laurent Delevoye, director of the RMN2I team, for his support, understanding and motivation, and for helping me improve my level of French in the corridor talks. I would like to express my deep gratitude to Julien Trébosc, for his patience, advice, dedication and commitment to all NMR experiments and simulations, who makes all the pulse sequences and experiments work after a coffee.

I am also very grateful to Bertrand Doumert and Bertrand Revel, for their support, patience and explanations when doing NMR experiments. Thanks also to Manju Reddy, for the scientific talks and coffee.

This thesis would not have been possible without our collaborators from India, Japan and France. I would like to thank Professor Vivek Polshettiwar, from the Tata Institute in India, for his collaboration with the DFNS/BN project. From Japan, thanks to Yu Tsutsumi, from Bruker Japan for his collaboration with the *D*-RINEPT simulations, and Nghia T. Duong from RIKEN Institute for his help with the *D*-HOMCOR project. Special thanks to Hiroki Nagashima from the AIST Institute in Japan for his collaboration with the *D*-RINEPT projects and the DNP experiments.

In Lille, thanks to Martine Trentesaux for the characterization by RAMAN and XPS, Pascal Blanchard for his guidance and help with the sample preparation, and a very special thanks to Professor Edmond Payen for his invaluable advice and collaboration with the MoO<sub>3</sub>/TiO<sub>2</sub> samples, and who recently passed away. Thanks also to Philippe Devaux for the porosimetry measurements, and Pascal Roussel for the XRD measurements. Special thanks to Myriam Wastiaux who was always so helpful in the lab.

I am profoundly grateful to Andrew Rankin, for sharing his knowledge with me when I started my PhD, for his help, support, and encouragement during this time. I would like also to thank Piotr Paluch for his help with SIMPSON simulations.

I would like to deeply thank my friends and colleagues from the RM2I team. Thanks to Guillaume and Racha, for the invaluable experiences lived together, for their help, support and friendship. Thanks also to Parth, Florian, Diane, Jess and Lama, for the time shared and all the great things I have learned from each of them.

This experience would not have been the same without the constant support of my friends. Thanks to my friend Yady, who takes care of me and encourages me every day from Australia. It is a blessing to have her friendship and unconditional support. Also, thanks to my friend Elizabeth in Colombia, who is a warrior, who gives me strength and supports me no matter what. Her tenacity, her passion for her work and

her immense heart inspire me every day. Also, a huge thank you to my friend Jeniffer, who always encourages me to follow my dreams. I would also like to thank my friend Anny in Mexico for her friendship and support.

In Lille I have been fortunate to meet loving people who have welcomed and supported me. I would like to thank Dioni and Gloria, for welcoming me into their home, for their friendship and trust. Thanks also to Claudia, who was a blessing when I arrived in Lille, and who has been a great friend and support throughout this time. And I also want to thank the ‘Latin mafia’, Eleonora, Elisa, Marica and Diksha, for their friendship and the warmth they extended to me; for all the food, the yoga, the trips and all the moments we shared together. And thanks to Diana and her baby Valeria, for being a great friend and for preparing the most delicious sushi.

And finally, the biggest thanks go to my beloved family, who have supported me unconditionally and encouraged me to follow my dreams, even if it means that we are separated. They are my strength and motivation to keep going and become the best version of me. I have no way of thanking God for having them. I want to thank my parents for all the effort, love, dedication and hard work to educate us despite all the circumstances of our environment. My mother Nancy is my inspiration and role model. I would not be the woman I am without her. My father Jaime, who with his strength and knowledge have motivated me to be strong and focused. My sisters, Wendy, Maira and Gaby, for taking care of me, motivating me and loving me despite the distance. Also, my deepest thanks to my Marcus, who has been my unconditional support throughout this time and without whom I could not have done it; for all his love, comprehension, patience, positivism, encouragement, for motivating me to follow my dreams and not give up. I could not have found a better partner than him. Thanks also to my other family in Denmark, Annekatrin, Eva and Christoph, for all their love and support.



# Table of Contents

Abstract .....	i
Acknowledgements .....	v
Table of Contents .....	ix
List of Figures .....	xiii
List of Tables.....	xxiii
<b>General introduction.....</b>	<b>1</b>
<b>Chapter 1: Observation of quadrupolar nuclei near surfaces using solid-state NMR.....</b>	<b>7</b>
1.1 IMPORTANCE OF SURFACES .....	7
1.1.1 Applications to materials science .....	7
1.1.2 Techniques to characterize surfaces .....	8
1.1.3 NMR of surfaces .....	10
1.1.4 Importance of quadrupolar nuclei near surfaces .....	15
1.2 QUADRUPOLAR INTERACTION .....	17
1.3 EFFECTS OF RF FIELD FOR QUADRUPOLAR NUCLEI.....	20
1.4 HIGH-RESOLUTION NMR SPECTRA OF QUADRUPOLAR NUCLEI ....	22
1.4.1 MQMAS.....	23
1.4.2 STMAS.....	28
1.5 METHODS TO ENHANCE THE SENSITIVITY FOR QUADRUPOLAR NUCLEI .....	29
1.5.1 High-fields.....	29
1.5.2 Population transfer .....	30
1.5.3 QCPMG.....	31
1.5.4 Dynamic Nuclear Polarization (DNP).....	33
1.6 OUTLINE OF THE THESIS .....	41
References .....	42
<b>Chapter 2: Improved NMR transfer of magnetization from <sup>1</sup>H to half-integer quadrupolar nuclei at 20 and 62.5 kHz MAS.....</b>	<b>61</b>
2.1 STATEMENT OF CONTRIBUTION .....	61
2.2 INTRODUCTION .....	61
2.3 THEORETICAL BACKGROUND .....	65
2.3.1 Symmetry-based dipolar recouplings.....	65
2.3.2 Scaling factor $\kappa$ .....	67
2.3.3 Adiabatic pulses .....	68
2.3.4 PRESTO-III sequence .....	69
2.3.5 Recoupling schemes for PRESTO .....	71
2.3.6 <i>D</i> -RINEPT sequence .....	75
2.3.7 Recoupling schemes for <i>D</i> -RINEPT .....	76

2.4	$^1\text{H} \rightarrow ^{27}\text{Al}$ PRESTO AND <i>D</i> -RINEPT NMR EXPERIMENTS .....	79
2.4.1	Samples and experimental conditions .....	79
2.4.2	Performances of PRESTO and <i>D</i> -RINEPT at $\nu_R = 20$ kHz .....	80
2.4.3	Performances of PRESTO and <i>D</i> -RINEPT at $\nu_R = 62.5$ kHz .....	89
2.5	2D $^1\text{H} \rightarrow ^{27}\text{Al}$ HETCOR EXPERIMENTS .....	95
2.6	MEASUREMENT OF THE DECAY OF THE TRANSVERSE $^1\text{H}$ MAGNETIZATION DURING RECOUPLING .....	97
2.7	CONCLUSIONS .....	98
	References .....	99
<b>Chapter 3: Comparison of double and single quantum dipolar NMR correlations of quadrupolar nuclei .....</b>		<b>107</b>
3.1	STATEMENT OF CONTRIBUTION .....	107
3.2	INTRODUCTION .....	107
3.3	PULSE SEQUENCES .....	109
3.4	SYMMETRY-BASED MATHEMATICAL DESCRIPTION .....	111
3.4.1	SQ-SQ .....	111
3.4.2	DQ-SQ .....	114
3.5	MATERIALS AND METHODS .....	115
3.5.1	Samples .....	115
3.5.2	Synthesis of lithium diborate .....	115
3.5.3	Phase identification .....	116
3.5.4	NMR experiments .....	118
3.5.4.1	Experiments at 9.4 T .....	118
3.5.4.2	Experiments at 18.8 T .....	119
3.6	RESULTS AND DISCUSSION .....	120
3.6.1	$^{11}\text{B}$ - $^{11}\text{B}$ <i>D</i> -HOMCOR experiments on $\text{Li}_2\text{B}_4\text{O}_7$ .....	120
3.6.1.1	SQ-SQ .....	122
3.6.1.2	DQ-SQ .....	127
3.6.1.3	SQ-SQ vs DQ-SQ .....	130
3.6.2	$^{27}\text{Al}$ - $^{27}\text{Al}$ experiments on $\text{AlPO}_4$ -14 .....	131
3.6.2.1	SQ-SQ .....	132
3.6.2.2	DQ-SQ .....	134
3.6.2.3	SQ-SQ vs DQ-SQ .....	137
3.7	CONCLUSIONS .....	138
	References .....	139
<b>Chapter 4: Boron nitride and oxide coated dendritic fibrous nanosilica for oxidative dehydrogenation: Insights into the catalytic sites from solid-state NMR .....</b>		<b>145</b>
4.1	STATEMENT OF CONTRIBUTION .....	145
4.2	INTRODUCTION .....	145
4.3	STATE OF THE ART .....	147
4.3.1	Catalysts for ODH of light alkanes .....	147
4.3.2	Catalytic activity of DFNS/BN and DFNS/ $\text{B}_2\text{O}_3$ .....	149

4.4	SOLID-STATE NMR EXPERIMENTS .....	152
4.4.1	Samples .....	152
4.4.2	Experiments at 9.4 T .....	152
4.4.3	Experiments at 18.8 T .....	153
4.5	RESULTS AND DISCUSSION.....	155
4.5.1	Probing $^1\text{H}$ and $^{11}\text{B}$ environments and their proximities.....	155
4.5.2	Probing $^{29}\text{Si}$ environments and $^{29}\text{Si}$ - $^{11}\text{B}$ proximities.....	160
4.5.3	Insights into the boron species .....	163
4.6	CONCLUSIONS .....	171
	References .....	171
	<b>General conclusions .....</b>	<b>179</b>
	<b>Perspectives.....</b>	<b>183</b>
	DNP-ENHANCED MQMAS EXPERIMENTS USING <i>D</i> -RINEPT TRANSFER	183
	DNP-ENHANCED SOLID-STATE NMR OF QUADRUPOLAR NUCLEI IN MoO <sub>3</sub> /TiO <sub>2</sub> NANOPARTICLES .....	187
	<b>Curriculum vitae .....</b>	<b>195</b>
	<b>Appendices .....</b>	<b>197</b>





# List of Figures

<b>Figure 1.</b> Schematic representation of the surface analysis methods presented in Table 1. ....	10
<b>Figure 2.</b> Summary of the most important interactions in solid-state NMR and the available information. ....	11
<b>Figure 3.</b> Schematic representation of the nuclear quadrupolar interaction which arises from the coupling between the electric quadrupolar moment $eQ$ and the electric field gradient (EFG) $\nabla E$ . (left). The EFG is mathematically described by a 3x3 matrix and is defined by its three tensor components $V_{XX}$ , $V_{YY}$ and $V_{ZZ}$ , with $V_{ZZ} \geq V_{YY} \geq V_{XX}$ by convention (middle). The orientations of the PAS for the EFG tensor with respect to the external magnetic field, $B_0$ (right). ....	18
<b>Figure 4.</b> Schematic energy level diagram for a spin $I = 3/2$ nucleus showing the effect of the Zeeman, first-order and second-order quadrupolar interactions. The first-order quadrupolar interaction splits the NMR spectrum into $2I - 1$ lines with resonance frequencies affected by the quadrupolar splitting parameter $\omega_Q$ , while the central transition CT remains unaffected at the Larmor frequency $\omega_0$ . The second-order quadrupolar interaction affects all the lines. ....	19
<b>Figure 5.</b> Schematic frequency domain representation of rf irradiation of quadrupolar nuclei with spin $I = 3/2$ . ....	21
<b>Figure 6.</b> Pulse sequences and coherence pathways for (a) the z-filter and (b) the split- $t_1$ shifted-echo 3QMAS experiments (the coherence pathway is given for the z-filter approach on a spin $I = 3/2$ , depicted at the top, with echo and antiecho pathway signals represented by solid and dashed lines, respectively) and (c) DQF-STMAS z-filter experiment. ....	24
<b>Figure 7.</b> Different types of schemes that can be used for the excitation and conversion for the MQMAS experiment: hard pulses (HP), rotation-induced adiabatic coherence transfer (RIACT), soft-pulses added mixing (SPAM), double frequency sweeps (DFS), fast-amplitude modulation pulse trains (FAM-N), long pulses (LP) and cosine long pulses (Cos-LP). ....	27
<b>Figure 8.</b> Pulse sequences of (a) Quadrupolar echo, (b) QCPMG and (c) WURST-QCPMG. ....	32
<b>Figure 9.</b> High-field DNP-NMR system with gyrotron microwave source (gyrotron tube indicated in purple), microwave transmission line (yellow) and low-temperature NMR probe (light blue). ....	35
<b>Figure 10.</b> Schematic representation of indirect and direct DNP experiments. After microwave irradiation, polarization from electrons can be transferred directly to nuclei of the investigated materials ( <i>direct</i> DNP) or indirectly, by transferring the polarization first to $^1\text{H}$ and then to the detected nuclei by CP or other methods ( <i>indirect</i> DNP). ....	37

<b>Figure 11.</b> Structures of some of the organic radicals used as PA for high-field MAS DNP. ....	40
<b>Figure 12.</b> Schematic representation of two $RN_n^v$ schemes employed in this work: R22 <sub>2</sub> <sup>7</sup> built from rectangular 180 <sub>0</sub> pulses and R16 <sub>7</sub> <sup>6</sup> built from composite 270 <sub>0</sub> 90 <sub>180</sub> pulses. ....	67
<b>Figure 13.</b> <sup>1</sup> H → <sup>27</sup> Al (a,c) PRESTO- $RN_n^v$ and (b,c) <i>D</i> -RINEPT-CWc- $RN_n^v$ pulse sequences. Those applied to <sup>1</sup> H and <sup>27</sup> Al channels are shown in (a,b) and (c), respectively. The narrow and broad black bars represent $\pi/2$ and $\pi$ -pulses, respectively. The acquisition of the FIDs (indicated with the vertical dashed line) starts after (a) the end of the $RN_n^v$ block in the case of PRESTO or (b) on top of the echo shifted with $\tau_R/2$ with respect to the end of the last recoupling block in the case of RINEPT. ....	70
<b>Figure 14.</b> Type of pulses employed in $RN_n^v$ sequences for PRESTO-III. ....	72
<b>Figure 15.</b> Schematic representation of the selection of $RN_n^v$ schemes for PRESTO based on the symmetry numbers $N$ , $n$ and $v$ , the RF requirement and the $\phi$ angle. The selected $RN_n^v$ schemes are presented in Tables 3-5. ....	72
<b>Figure 16.</b> Type of pulses employed in $RN_n^v$ sequences for <i>D</i> -RINEPT-CWc. ....	76
<b>Figure 17.</b> Schematic representation of the selection of $RN_n^v$ schemes for <i>D</i> -RINEPT-CWc based on the symmetry numbers $N$ , $n$ and $v$ , and the $\phi$ angle. The selected $RN_n^v$ schemes are presented in Table 6. ....	77
<b>Figure 18.</b> Spin echo sequence used to measure the decay of the transverse <sup>1</sup> H magnetization. ....	80
<b>Figure 19.</b> <sup>27</sup> Al 1D spectra of $\gamma$ -alumina at 18.8 T with $\nu_R = 20$ (a) and 62.5 (b) kHz acquired using <sup>1</sup> H → <sup>27</sup> Al transfers with RINEPT-CWc sequence and SR4 <sub>1</sub> <sup>2</sup> (tt), SR4 <sub>1</sub> <sup>2</sup> (270 <sub>0</sub> 90 <sub>180</sub> ) and R12 <sub>3</sub> <sup>5</sup> (270 <sub>0</sub> 90 <sub>180</sub> ) recoupling, or PRESTO scheme and (a) R22 <sub>2</sub> <sup>7</sup> (180 <sub>0</sub> ) or R18 <sub>2</sub> <sup>5</sup> (180 <sub>0</sub> ), or (b) R16 <sub>7</sub> <sup>6</sup> (270 <sub>0</sub> 90 <sub>180</sub> ) and R14 <sub>6</sub> <sup>5</sup> (270 <sub>0</sub> 90 <sub>180</sub> ) recoupling. The $\tau$ delays and $\nu_1/\nu_{1,\max}$ RF-fields were fixed to their optimum values given in Tables 7 and 9. ....	82
<b>Figure 20.</b> <sup>27</sup> AlO <sub>6</sub> on-resonance signal of $\gamma$ -alumina at $\nu_R = 20$ kHz as function of $\nu_1$ or $\nu_{1,\max}$ for PRESTO-R22 <sub>2</sub> <sup>7</sup> (180 <sub>0</sub> ) and -R18 <sub>2</sub> <sup>5</sup> (180 <sub>0</sub> ) as well as RINEPT-CWc-SR4 <sub>1</sub> <sup>2</sup> (tt), -SR4 <sub>1</sub> <sup>2</sup> (270 <sub>0</sub> 90 <sub>180</sub> ) and -R12 <sub>3</sub> <sup>5</sup> (270 <sub>0</sub> 90 <sub>180</sub> ). For each curve, $\tau$ was fixed to its optimum value given in Table 7. ....	84
<b>Figure 21.</b> <sup>27</sup> AlO <sub>6</sub> signal of $\gamma$ -alumina at $\nu_R = 20$ kHz as function of offset for PRESTO-R22 <sub>2</sub> <sup>7</sup> (180 <sub>0</sub> ) and -R18 <sub>2</sub> <sup>5</sup> (180 <sub>0</sub> ) as well as RINEPT-CWc-SR4 <sub>1</sub> <sup>2</sup> (tt), -SR4 <sub>1</sub> <sup>2</sup> (270 <sub>0</sub> 90 <sub>180</sub> ) and -R12 <sub>3</sub> <sup>5</sup> (270 <sub>0</sub> 90 <sub>180</sub> ). For each curve, $\tau$ and $\nu_1$ or $\nu_{1,\max}$ were fixed to their optimum values given in Table 7. ....	84
<b>Figure 22.</b> <sup>27</sup> Al 1D spectra of AlPO <sub>4</sub> -14 at 18.8 T with $\nu_R = 20$ (a) and 62.5 (b) kHz acquired using <sup>1</sup> H → <sup>27</sup> Al transfers with RINEPT-CWc sequence and SR4 <sub>1</sub> <sup>2</sup> (tt), SR4 <sub>1</sub> <sup>2</sup> (270 <sub>0</sub> 90 <sub>180</sub> ) and R12 <sub>3</sub> <sup>5</sup> (270 <sub>0</sub> 90 <sub>180</sub> ) recoupling, or PRESTO sequence and (a) R22 <sub>2</sub> <sup>7</sup> (180 <sub>0</sub> ) and R18 <sub>2</sub> <sup>5</sup> (180 <sub>0</sub> ), or (b) R16 <sub>7</sub> <sup>6</sup> (270 <sub>0</sub> 90 <sub>180</sub> ) and R14 <sub>6</sub> <sup>5</sup> (270 <sub>0</sub> 90 <sub>180</sub> ) recoupling. The $\tau$ delays and	

$\nu_1/\nu_{1,\max}$ RF-fields were fixed to their optimal values given in Tables 8 and 10. The resonance at <i>ca.</i> 11 ppm in (a) is due to an impurity. ....	86
<b>Figure 23.</b> $^1\text{H}$ MAS spectrum of $\text{AlPO}_4\text{-14}$ acquired at $B_0 = 18.8$ T and $\nu_R = 20$ kHz by averaging 16 transients separated by a recycle interval of 1 s, using the DEPTH pulse sequence for probe background suppression, with $\nu_1 \approx 208$ kHz. <sup>72</sup> .....	87
<b>Figure 24.</b> $^{27}\text{AlO}_4$ signal of $\text{AlPO}_4\text{-14}$ at $\nu_R = 20$ kHz as function of $\nu_1$ or $\nu_{1,\max}$ of the recoupling for PRESTO-R22 <sub>2</sub> <sup>7</sup> (180 <sub>0</sub> ) and -R18 <sub>2</sub> <sup>5</sup> (180 <sub>0</sub> ) as well as RINEPT-CWc-SR4 <sub>1</sub> <sup>2</sup> (tt), -SR4 <sub>1</sub> <sup>2</sup> (270 <sub>0</sub> 90 <sub>180</sub> ) and -R12 <sub>3</sub> <sup>5</sup> (270 <sub>0</sub> 90 <sub>180</sub> ). For each curve, $\tau$ was fixed to its optimum value given in Table 8. ....	88
<b>Figure 25.</b> $^{27}\text{AlO}_4$ signal of $\text{AlPO}_4\text{-14}$ at $\nu_R = 20$ kHz as function of offset of the recoupling for PRESTO-R22 <sub>2</sub> <sup>7</sup> (180 <sub>0</sub> ) and -R18 <sub>2</sub> <sup>5</sup> (180 <sub>0</sub> ) as well as RINEPT-CWc-SR4 <sub>1</sub> <sup>2</sup> (tt), -SR4 <sub>1</sub> <sup>2</sup> (270 <sub>0</sub> 90 <sub>180</sub> ) and -R12 <sub>3</sub> <sup>5</sup> (270 <sub>0</sub> 90 <sub>180</sub> ). For each curve, $\tau$ and $\nu_1$ or $\nu_{1,\max}$ were fixed to their optimum values given in Table 8. ....	88
<b>Figure 26.</b> $^{27}\text{AlO}_6$ on-resonance signal of $\gamma$ -alumina at $\nu_R = 62.5$ kHz as function of $\nu_1$ or $\nu_{1,\max}$ for PRESTO-R16 <sub>7</sub> <sup>6</sup> (270 <sub>0</sub> 90 <sub>180</sub> ) and -R14 <sub>6</sub> <sup>5</sup> (270 <sub>0</sub> 90 <sub>180</sub> ) as well as RINEPT-CWc-SR4 <sub>1</sub> <sup>2</sup> (tt), -SR4 <sub>1</sub> <sup>2</sup> (270 <sub>0</sub> 90 <sub>180</sub> ) and -R12 <sub>3</sub> <sup>5</sup> (270 <sub>0</sub> 90 <sub>180</sub> ). For each curve, $\tau$ was fixed to its optimum value given in Table 9. ....	90
<b>Figure 27.</b> $^{27}\text{AlO}_6$ signal of $\gamma$ -alumina at $\nu_R = 62.5$ kHz as function of offset for PRESTO-R16 <sub>7</sub> <sup>6</sup> (270 <sub>0</sub> 90 <sub>180</sub> ) and -R14 <sub>6</sub> <sup>5</sup> (270 <sub>0</sub> 90 <sub>180</sub> ) as well as RINEPT-CWc-SR4 <sub>1</sub> <sup>2</sup> (tt), -SR4 <sub>1</sub> <sup>2</sup> (270 <sub>0</sub> 90 <sub>180</sub> ) and -R12 <sub>3</sub> <sup>5</sup> (270 <sub>0</sub> 90 <sub>180</sub> ). For each curve, $\tau$ and $\nu_1$ or $\nu_{1,\max}$ were fixed to their optimum values given in Table 9. ....	90
<b>Figure 28.</b> $^{27}\text{AlO}_4$ signal of $\text{AlPO}_4\text{-14}$ at $\nu_R = 62.5$ kHz as function of $\nu_1$ or $\nu_{1,\max}$ of the recoupling for PRESTO-R16 <sub>7</sub> <sup>6</sup> (270 <sub>0</sub> 90 <sub>180</sub> ) and -R14 <sub>6</sub> <sup>5</sup> (270 <sub>0</sub> 90 <sub>180</sub> ) as well as RINEPT-CWc-SR4 <sub>1</sub> <sup>2</sup> (tt), -SR4 <sub>1</sub> <sup>2</sup> (270 <sub>0</sub> 90 <sub>180</sub> ) and -R12 <sub>3</sub> <sup>5</sup> (270 <sub>0</sub> 90 <sub>180</sub> ). For each curve, $\tau$ was fixed to its optimum value given in Table 10. ....	93
<b>Figure 29.</b> $^{27}\text{AlO}_4$ signal of $\text{AlPO}_4\text{-14}$ at $\nu_R = 62.5$ kHz as function of offset of the recoupling for PRESTO-R16 <sub>7</sub> <sup>6</sup> (270 <sub>0</sub> 90 <sub>180</sub> ) and -R14 <sub>6</sub> <sup>5</sup> (270 <sub>0</sub> 90 <sub>180</sub> ) as well as RINEPT-CWc-SR4 <sub>1</sub> <sup>2</sup> (tt), -SR4 <sub>1</sub> <sup>2</sup> (270 <sub>0</sub> 90 <sub>180</sub> ) and -R12 <sub>3</sub> <sup>5</sup> (270 <sub>0</sub> 90 <sub>180</sub> ). For each curve, $\tau$ and $\nu_1$ or $\nu_{1,\max}$ were fixed to their optimum values given in Table 10. ....	93
<b>Figure 30.</b> $^1\text{H}$ - $^{27}\text{Al}$ D-HETCOR 2D spectrum of $\text{AlPO}_4\text{-14}$ , along with its skyline projections, at $B_0 = 18.8$ T and $\nu_R = 62.5$ kHz acquired in only 72 min with only <i>ca.</i> 2.5 $\mu\text{L}$ of active volume with NUS 25% using RINEPT-CWc-SR4 <sub>1</sub> <sup>2</sup> (270 <sub>0</sub> 90 <sub>180</sub> ) transfer. ....	95
<b>Figure 31.</b> Skyline projections along a) F2 and b) F1 of $^1\text{H}$ - $^{27}\text{Al}$ HETCOR 2D spectra of $\text{AlPO}_4\text{-14}$ recorded with RINEPT-CWc-SR4 <sub>1</sub> <sup>2</sup> (270 <sub>0</sub> 90 <sub>180</sub> ), SR4 <sub>1</sub> <sup>2</sup> (tt), SR4 <sub>1</sub> <sup>2</sup> (180 <sub>0</sub> 90 <sub>180</sub> ) and PRESTO-R16 <sub>7</sub> <sup>6</sup> (270 <sub>0</sub> 90 <sub>180</sub> ) transfers. All 2D spectra were acquired using NUS 25% in 72 min. ....	96

- Figure 32.** Pulse sequences used for (a) SQ-SQ and (b) DQ-SQ HOMCOR experiments of half-integer spin quadrupolar nuclei. All pulses are CT-selective with  $\nu_1 = \nu_R(2I + 1)$ . The black squares are  $\pi/2$ -pulses, whereas the blue one in (b) is a  $\pi$ -pulse. In (b) a  $[RN_n^\nu]$  bracketed recoupling is shown with five  $\pi/2$ -pulses, whereas an un-bracketed version should only require the last reading  $\pi/2$ -pulse. The  $RN_n^\nu$  recoupling parts are represented with grey zones. .... 110
- Figure 33.** Minimum cycle times with (a)  $SR2_{2,2}^1$ , (b)  $SR2_{4,4}^1$ , (c)  $SR2_{8,8}^1$ , (d)  $SR4_{4,4}^1$ , and (e)  $BR2_{2,2}^1$ . In (a-c,e), white and grey colors mean phases of  $90^\circ$  and  $270^\circ$  respectively, and in (d) yellow and green colors mean phases of  $45^\circ$  and  $315^\circ$  respectively. In each case, the number is the flip-angle for the CT-selective pulse. .... 112
- Figure 34.** Comparison of powder XRD patterns of crystallized lithium diborate  $Li_2O \cdot 2B_2O_3$  and the glass sample initially prepared. Vertical lines represent the positions of diffraction lines of  $B_4Li_2O_7$ . .... 117
- Figure 35.** Crystalline structure of  $Li_2B_4O_7$  based on the cif file. The diborate unit is indicated with the atoms of boron tri- and four-coordinated, B3 and B4, respectively. .... 117
- Figure 36.** Comparison and difference between the powder XRD pattern of crystallized lithium diborate  $Li_2O \cdot 2B_2O_3$  and reference XRD patterns of  $\alpha$ - $LiBO_2$  and  $B_4Li_2O_7$ . .... 118
- Figure 37.** Lineshape deconvolution obtained from the  $^{11}B$  1D spectrum of the  $Li_2B_4O_7$  crystallized sample recorded at 18.8 T and  $\nu_R = 20$  kHz. Fitting was carried out using int2QUAD model in DMFit.<sup>45</sup> The relative amounts of  $Li_2B_4O_7$  and  $\alpha$ - $LiBO_2$  phases are 90 and 10 %. .... 121
- Figure 38.** (a) 2D  $^{11}B$  z-filtered MQMAS spectrum of  $Li_2B_4O_7$  recorded at  $B_0 = 9.4$  T and  $\nu_R = 16$  kHz. Panel (b) is an expansion of panel (a). The oblique lines are the Chemical-Shift axes. .... 122
- Figure 39.** Series of 2D  $^{11}B$  SQ-SQ *D*-HOMCOR spectra of  $Li_2B_4O_7$  acquired at  $B_0 = 18.8$  T with a MAS frequency of 20 kHz and a non-uniform sampling (NUS) retaining 50% of the  $t_1$  points, with the carrier frequency optimized (Fig. 40) at  $\nu_{offset} = 3$  kHz (11.7 ppm), shown with an arrow between the  $B^{III}$  and  $B^{IV}$  resonances. The spectra acquired with recoupling schemes,  $(SR2_{2,2}^1)_4$ ,  $(SR2_{4,4}^1)_4$  and  $(SR2_{8,8}^1)_4$ , are shown in the first, second and third column, respectively. The negative cross-peaks are shown in green. The length of  $\tau_{mix} = 3.2, 6.4$  or  $9.6$  ms, is indicated in red on each panel. The top projections are those related to  $\tau_{mix} = 3.2$  ms. The 2D spectra result from averaging 48 transients using a relaxation delay  $\tau_{RD} = 1$  s for each of 120  $t_1$ -increments, leading to an experimental time  $T_{exp} = 48$ -55 min. .... 124
- Figure 40.** 2D  $^{11}B$  SQ-SQ *D*-HOMCOR spectra of  $Li_2B_4O_7$  acquired at  $B_0 = 18.8$  T with a MAS frequency of 20 kHz and a non-uniform sampling (NUS) retaining 50% of the  $t_1$  points with  $\nu_{offset} = 0, 3, 6$  kHz, as indicated in black and with arrows. The spectra acquired with recoupling schemes  $(SR2_{2,2}^1)_4$ ,  $(SR2_{4,4}^1)_4$  and  $(SR2_{8,8}^1)_4$  are shown in the first, second or third column, respectively. The negative signals are shown in green. The

length of  $\tau_{mix} = 1.6, 3.2$  or  $6.4$  ms is indicated in red on each sub-figure. The top projections are those related to the spectra on the 1<sup>st</sup> line. The other experimental parameters are the same as in Fig. 39. .... 125

**Figure 41.** Slices of the 2D spectra corresponding to the  $B^{34}$  ( $B^{III}$ - $B^{IV}$ ) cross-peak of  $Li_2B_4O_7$  observed with the  $^{11}B$  SQ-SQ *D*-HOMCOR sequence and  $(SR2_{2}^1)_4$ ,  $(SR2_{4}^1)_4$  and  $(SR2_{8}^1)_4$  recoupling schemes, shown in the first, second or third column, respectively. (a,c,e)  $v_{offset} = 3$  kHz and  $\tau_{mix} = 1.6, 3.2, 6.4$  and  $9.6$  ms; (b,d,f)  $v_{offset} = 0, 1.5, 3, 4.5, 6$  kHz and  $\tau_{mix} =$ (b)  $3.2$ , (d)  $1.6$  and (f)  $6.4$  ms. These slices are extracted from the 2D spectra shown in Figs. 39 and 40. .... 126

**Figure 42.** 1D slices of the  $^{11}B$  SQ-SQ *D*-HOMCOR spectra shown in Fig. 8 of  $Li_2B_4O_7$  with  $(SR2_{2}^1)_4$ ,  $(SR2_{4}^1)_4$  and  $(SR2_{8}^1)_4$  schemes, with  $v_{offset} = 3$  kHz (11.7 ppm) and  $\tau_{mix} = 3.2$  ms. These slices show that the  $B^{34}$  ( $B^{III}$ - $B^{IV}$ ) and  $B^{43}$  ( $B^{IV}$ - $B^{III}$ ) cross-peaks are hardly observable with  $(SR2_{4}^1)_4$ , and especially  $(SR2_{8}^1)_4$ . .... 127

**Figure 43.** Experimental 1D  $^{11}B$  DQ-filtered signal of  $Li_2B_4O_7$  observed with a 1D ( $t_1 = 0$ ) version of the  $[SR2_{2}^1]$ ,  $[BR2_{2}^1]$  and  $BR2_{2}^1$ , sequences versus (a)  $v_1$  ranging from 1 to 8 kHz and (b)  $v_{offset}$  ranging from +10 to -10 kHz. The spectra obtained with  $SR2_{2}^1$  scheme are not shown because it is much less efficient than these three schemes (see Fig. 44). The optimum values are indicated with \*. .... 128

**Figure 44.** Comparison of the (a)  $F_2$  or (b)  $F_1$  projections of 2D DQ-SQ 2D spectra of  $Li_2B_4O_7$  acquired at  $B_0 = 18.8$  T with a MAS frequency of 20 kHz with NUS retaining 33% of the  $t_1$  points and recorded with  $[SR2_{2}^1]$ ,  $[BR2_{2}^1]$ ,  $SR2_{2}^1$  and  $BR2_{2}^1$  sequences. The 2D spectra result from averaging 64 transients using a relaxation delay  $\tau_{RD} = 1$  s for each of 120  $t_1$ -increments, leading to an experimental time  $T_{exp} = 45$ -50 min. We employed optimal rf field strength equal to  $v_1 = 3.7$  and  $4.1$  kHz for  $BR2_{2}^1 / SR2_{2}^1$  and  $[BR2_{2}^1] / [SR2_{2}^1]$ , respectively. .... 129

**Figure 45.** Comparison of  $F_2$  slices containing (a)  $B^4$  or (b)  $B^3$  diagonal peaks of 2D  $^{11}B$  the SQ-SQ and DQ-SQ *D*-HOMCOR spectra of  $Li_2B_4O_7$  using  $(SR2_{2}^1)_4$  recoupling for SQ-SQ scheme and  $[BR2_{2}^1]$ ,  $[SR2_{2}^1]$  and  $BR2_{2}^1$  recoupling for DQ-SQ sequence at  $B_0 = 18.8$  T with a MAS frequency of 20 kHz. An expansion of the cross-peaks is also shown. All 2D spectra were acquired using uniform sampling. The 2D DQ-SQ and SQ-SQ spectra result from averaging 64 and 48 transients, respectively, using a relaxation delay  $\tau_{RD} = 1$  s for each of 120  $t_1$ -increments, leading to an experimental time  $T_{exp} = 2$ h30 min and 1h50 min, respectively. The signal was normalized with respect to the number of transients. We employed optimal rf field strength equal to  $v_1 = 3.7$  kHz for  $BR2_{2}^1$ ,  $4.1$  kHz for  $[BR2_{2}^1]$  and  $[SR2_{2}^1]$  and  $v_1 = 3.9$  kHz for  $SR2_{2}^1$ . .... 130

**Figure 46.** 2D  $^{27}Al$  SQ-SQ *D*-HOMCOR spectrum of  $AlPO_4-14$  using  $(SR2_{2}^1)_4$  recoupling at  $B_0 = 18.8$  T with a MAS frequency of 20 kHz acquired with NUS retaining 33% of the  $t_1$  points. Cross- and diagonal peaks are indicated with orange and blue ovals, respectively. The extra framework impurity at  $-2$  kHz is indicated with a star. We used  $\tau_{mix} =$

3.2 ms,  $\nu_1 = 2.4$  kHz and  $\nu_{\text{offset}} = 4$  kHz (19.2 ppm) for the recoupling. The 2D SQ-SQ spectrum results from averaging 48 transients using a relaxation delay  $\tau_{\text{RD}} = 1$  s for each of 330  $t_1$ -increments, leading to an experimental time  $T_{\text{exp}} = 1$  h 40 min. .... 133

**Figure 47.** Comparison of the cross-peak intensities of the SQ-SQ spectra of  $\text{AlPO}_4\text{-14}$  at  $B_0 = 18.8$  T with a MAS frequency of 20 kHz acquired with NUS retaining 33% of the  $t_1$  point, obtained from 1D slices taken from the 2D spectra recorded with  $(\text{SR}2_{2}^1)_4$  ( $\tau_{\text{mix}} = 4.8$  ms,  $\nu_{\text{offset}} = 2.82$  kHz (13.5 ppm)) and  $(\text{SR}2_{4}^1)_4$  ( $\tau_{\text{mix}} = 3.2$  ms,  $\nu_{\text{offset}} = 4$  kHz (19.2 ppm)) recoupling schemes. The auto-peaks, which bring no information, have been truncated at 5 % of their maximum values. We employed rf field strength equal to  $\nu_1 = 2.4$  kHz. The other experimental parameters are identical to those of Fig. 46. .... 134

**Figure 48.** 2D  $^{27}\text{Al}$  DQ-SQ  $D$ -HOMCOR spectrum of  $\text{AlPO}_4\text{-14}$  using  $\text{BR}2_{2}^1$  recoupling acquired with NUS retaining 33% of the  $t_1$  points at  $B_0 = 18.8$  T with a MAS frequency of 20 kHz. Cross- and auto-peaks are indicated with orange and blue circles, respectively. The 2D SQ-SQ spectrum results from averaging 64 transients using a relaxation delay  $\tau_{\text{RD}} = 1$  s for each of 330  $t_1$ -increments, leading to an experimental time  $T_{\text{exp}} = 2$ h. The recoupling used the following parameters:  $\nu_1 = 2.9$  kHz,  $\nu_{\text{offset}} = 4$  kHz (19.2 ppm) and  $\tau_{\text{mix}} = 0.8$  ms. .... 135

**Figure 49.**  $F_2$  slices of three 2D  $^{27}\text{Al}$  DQ-SQ  $D$ -HOMCOR spectra of  $\text{AlPO}_4\text{-14}$  acquired using  $\text{BR}2_{2}^1$  recoupling and NUS retaining 33% of the  $t_1$  points at  $B_0 = 18.8$  T with a MAS frequency of 20 kHz for  $\nu_{\text{offset}} = 3, 4$  or 5 kHz. The other experimental parameters are identical to those of Fig. 48. .... 136

**Figure 50.** Robustness with respect to (a) rf-field and (b) offset of 1D  $^{27}\text{Al}$  DQ-filtered  $D$ -HOMCOR spectra of  $\text{AlPO}_4\text{-14}$ , recorded with  $\text{BR}2_{2}^1$  (blue,  $\tau_{\text{mix}} = 0.8$  ms) or  $[\text{BR}2_{2}^1]$  (red,  $\tau_{\text{mix}} = 0.4$  ms) recoupling at  $B_0 = 18.8$  T with a MAS frequency of 20 kHz. The 1D NMR spectra result from averaging 64 transients with  $\tau_{\text{RD}} = 1$  s. In panel (a),  $\nu_{\text{offset}} = 4$  kHz, whereas in panel (b),  $\nu_1 = 2.9$  and 3 kHz for  $\text{BR}2_{2}^1$  and  $[\text{BR}2_{2}^1]$ , respectively. .... 136

**Figure 51.** Comparison of three  $F_2$  slices of 2D  $^{27}\text{Al}$  DQ-SQ and SQ-SQ  $D$ -HOMCOR spectra of  $\text{AlPO}_4\text{-14}$  acquired using  $\text{BR}2_{2}^1$  and  $(\text{SR}2_{2}^1)_4$  recoupling with  $\tau_{\text{mix}} = 0.8$  and 3.2 ms, respectively, and NUS retaining 33% of the  $t_1$  points at  $B_0 = 18.8$  T with a MAS frequency of 20 kHz. The offset of the recoupling schemes was equal to  $\nu_{\text{offset}} = 4$  kHz (19.2 ppm). The acquisition parameters of DQ-SQ and SQ-SQ experiments are identical to those of Figs. 46 and 48, respectively. The signal of the SQ-SQ spectrum has been multiplied by 1.33 to compensate for the difference in the number of transients. The auto-correlation peaks of SQ-SQ spectrum bring no information, and hence, these signals are truncated to the percentage of their maximal intensity indicated on each panel. .... 138

**Figure 52.** Schematic representation of the ODH of propane to propene. .... 147

<b>Figure 53.</b> Fibrous morphology of DFNS/BN revealed by (a) SEM and (b) TEM. The BN loading and textural properties of this material is described below.....	148
<b>Figure 54.</b> Fibrous morphology of DFNS/B <sub>2</sub> O <sub>3</sub> revealed by (a) SEM and (b) TEM. The BN loading and textural properties of this material is described below. ....	148
<b>Figure 55.</b> (a, c) Conversion and selectivity for propane dehydrogenation at 490 °C and (b, d) productivity for the same reaction and temperature using (a, b) DFNS/BN and (c, d) DFNS/B <sub>2</sub> O <sub>3</sub> . ....	150
<b>Figure 56.</b> Comparison of DFNS/BN and DFNS/B <sub>2</sub> O <sub>3</sub> with a selection of previously reported unsupported and supported catalysts for propane dehydrogenation. <sup>6,14</sup> .....	151
<b>Figure 57.</b> 1D (a, b, c) <sup>1</sup> H DEPTH and (d, e, f) <sup>11</sup> B quantitative (short tip angle) MAS NMR spectra of (a, d) as-prepared DFNS/BN, (b, e) DFNS/BN after catalysis and (c, f) as-prepared DFNS/B <sub>2</sub> O <sub>3</sub> . Experiments were recorded at <i>B</i> <sub>0</sub> = 18.8 T with <i>v</i> <sub>R</sub> = 20 kHz. ....	156
<b>Figure 58.</b> <sup>11</sup> B quantitative ( <i>i.e.</i> , short tip angle) 1D NMR spectra of pure BN, as-prepared DFNS/BN and DFNS/B <sub>2</sub> O <sub>3</sub> . Experiments were recorded at <i>B</i> <sub>0</sub> = 18.8 T with <i>v</i> <sub>R</sub> = 20 kHz. ....	157
<b>Figure 59.</b> 2D <sup>11</sup> B- <sup>1</sup> H} <i>D</i> -HMQC (a) as-prepared DFNS/BN (b) DFNS/BN after catalysis and (c) as-prepared DFNS/B <sub>2</sub> O <sub>3</sub> along with their skyline projections in both dimensions. The spectra were acquired at <i>B</i> <sub>0</sub> = 18.8 T and <i>v</i> <sub>R</sub> = 20 kHz.....	158
<b>Figure 60.</b> Comparison of 1D <sup>11</sup> B quantitative (short tip angle) spectrum and the summation projection in the <i>F</i> <sub>2</sub> dimension of the <sup>11</sup> B- <sup>1</sup> H} <i>D</i> -HMQC spectrum of as-prepared DFNS/BN. The spectra were normalized to the intensity at 12 ppm.....	159
<b>Figure 61.</b> <sup>1</sup> H→ <sup>29</sup> Si CP MAS NMR spectra of (a) as-prepared DFNS/BN, (b) DFNS/BN after catalysis and (c) as-prepared DFNS/B <sub>2</sub> O <sub>3</sub> . Experiments were recorded at <i>B</i> <sub>0</sub> = 9.4 T with <i>v</i> <sub>R</sub> = 10 kHz.....	160
<b>Figure 62.</b> Deconvolutions of the lineshapes obtained from <sup>1</sup> H→ <sup>29</sup> Si CP MAS experiments on (a) as-prepared DFNS/BN, (b) DFNS/BN after catalysis and (c) as-prepared DFNS/B <sub>2</sub> O <sub>3</sub> . Fitting was carried out using the Gaussian/Lorentzian model in DMFit. <sup>63</sup> In (c), the small peak at <i>ca.</i> -20 ppm in the <sup>1</sup> H→ <sup>29</sup> Si CP MAS spectrum of as-prepared DFNS/B <sub>2</sub> O <sub>3</sub> is probably due to residual organic species, so was not included in the fitting process.....	161
<b>Figure 63.</b> 2D <sup>11</sup> B- <sup>29</sup> Si} <i>D</i> -HMQC NMR spectra of (a) as-prepared DFNS/BN and (b) as-prepared DFNS/B <sub>2</sub> O <sub>3</sub> along with their skyline projections in both dimensions. The spectra were recorded at <i>B</i> <sub>0</sub> = 18.8 T and <i>v</i> <sub>R</sub> = 14.286 kHz.....	163
<b>Figure 64.</b> 2D <sup>11</sup> B MQMAS spectra of (a) as-prepared DFNS/BN, (b) DFNS/BN after catalysis and (c) as-prepared DFNS/B <sub>2</sub> O <sub>3</sub> . The projections in <i>F</i> <sub>1</sub> indirect dimension of MQMAS spectra along with their deconvolution	

are shown in Figs. 65 and 66. The MQMAS spectra were acquired at $B_0 = 18.8$ T and $\nu_R = 20$ kHz.....	164
<b>Figure 65.</b> (a-c) Deconvolutions of the lineshapes obtained from total projections of the $F_1$ dimension of the $^{11}\text{B}$ MQMAS spectrum of as-prepared DFNS/BN. Fitting was carried out using the Gaussian/Lorentzian model in DMFit. <sup>63</sup> .....	166
<b>Figure 66.</b> Deconvolutions of the lineshapes obtained from total projections of the $F_1$ dimension of the $^{11}\text{B}$ MQMAS spectrum of (a) DFNS/BN after catalysis and (b) as-prepared DFNS/ $\text{B}_2\text{O}_3$ . Fitting was carried out using the Gaussian/Lorentzian model in DMFit. <sup>17</sup> The $\text{BO}_4$ peak is folded, and thus, not shown.....	167
<b>Figure 67.</b> $^1\text{H} \rightarrow S$ $D$ -RINEPT-MQMAS-QCPMG. (a) Pulse sequence, with the red selective $\pi$ -pulse, just after the 2 <sup>nd</sup> FAM- $N$ pulse, omitted in the case of $S = 3/2$ . (b,c) Coherence transfer pathways for quadrupolar spin in the case of $S \geq 5/2$ (b) or $S = 3/2$ (c). $R = 7/9, 19/12, 101/45, 91/36$ for $S = 3/2, 5/2, 7/2, 9/2$ , respectively.....	184
<b>Figure 68.</b> 2D $^{11}\text{B}$ high-resolution MQMAS spectra of DFNS/BN acquired at $\nu_R = 10$ kHz and 9.4 T with direct excitation (split- $t_1$ MQMAS pulse sequence - in black) and $D$ -RINEPT-MQMAS-QCPMG sequence with recoupling time $\tau_{\text{dip}} = 1440$ $\mu\text{s}$ (in blue) and 320 $\mu\text{s}$ (in red). .....	185
<b>Figure 69.</b> Isotropic projection of the 2D $^{11}\text{B}$ high-resolution MQMAS spectra of DFNS/BN presented in Fig. 68.....	186
<b>Figure 70.</b> DNP-enhanced $^1\text{H} \rightarrow ^{13}\text{C}$ CPMAS spectra at $B_0 = 9.4$ T and 105 K with $\nu_R = 10$ kHz of $\text{MoO}_3/\text{TiO}_2(\text{P25})$ impregnated with TEKPol solution in TCE. <sup>5</sup> .....	187
<b>Figure 71.</b> DNP-enhanced $^1\text{H} \rightarrow ^{17}\text{O}$ RINEPT-SR2 $\frac{1}{2}(\text{tt})$ -QCPMG spectra of isotopically unmodified $\text{MoO}_3/\text{TiO}_2$ impregnated with 110 mM TEKPol solution in TCE with $\tau =$ (a) 1.9 and (b) 0.1 ms at $B_0 = 9.4$ T and $\nu_R = 10$ kHz. The spectra are the FT of the sum of QCPMG echoes. <sup>5</sup> .....	188
<b>Figure 72.</b> $^{47,49}\text{Ti}$ QCPMG NMR spectra of isotopically unmodified $\text{MoO}_3/\text{TiO}_2$ impregnated with 110 mM TEKPol solution in TCE at $B_0 = 9.4$ T with $\nu_R = 10$ kHz enhanced by (a) indirect DNP using $^1\text{H} \rightarrow ^{47,49}\text{Ti}$ RINEPT-SR2 $\frac{1}{2}(\text{tt})$ transfer with $\tau = 2.9$ ms and (b) DFS scheme. The spectra are the FT of the sum of QCPMG echoes. <sup>5</sup> .....	189
<b>Figure 73.</b> Raman spectrum of $\text{MoO}_3/\text{TiO}_2(\text{P25})$ . The signals corresponding to the $\text{MoO}_3$ particles are observed at $\sim 815$ and $992$ $\text{cm}^{-1}$ , while the signal from the polyoxomolybdates phase appears at $\sim 980$ $\text{cm}^{-1}$ .....	191
<b>Figure 74.</b> Raman spectrum of $\text{MoO}_3/\text{TiO}_2(\text{rutile})$ with 2, 7 and 10 % wt content of $\text{MoO}_3$ .....	191
<b>Figure 75.</b> Mo 3d XPS spectrum of $\text{MoO}_3/\text{TiO}_2(\text{P25})$ indicating the presence of Mo(V) and Mo(VI) species.....	192



**Figure 76.** DNP-enhanced  $^{17}\text{O}$  DFS-QCPMG NMR spectrum of  $\text{MoO}_3/\text{TiO}_2(\text{P25})$  impregnated with 110 mM TEKPol solution in TCE acquired at  $B_0 = 18.8$  T and  $\nu_R = 10$  kHz..... 194



# List of Tables

<b>Table 1.</b> General characteristics of common surface analysis methods .....	9
<b>Table 2.</b> Summary of the nuclear magnetic properties of some nuclei commonly found in solid surfaces. <sup>64,65</sup> .....	12
<b>Table 3.</b> Selected $RN_n^V = 2$ SQ hetero-nuclear dipolar recoupling for $\nu_R = 20$ kHz.....	73
<b>Table 4.</b> Selected $RN_n^V = 2$ SQ hetero-nuclear dipolar recoupling with $45^\circ \leq \phi \leq 135^\circ$ for $\nu_R = 62.5$ kHz.....	74
<b>Table 5.</b> Selected $RN_n^V = 2$ SQ hetero-nuclear dipolar recoupling built from single $\pi$ pulses with $20^\circ \leq \phi \leq 160^\circ$ and $\kappa \geq 0.15$ for $\nu_R = 62.5$ kHz. ....	74
<b>Table 6.</b> Selected $RN_n^V = 2$ two-spin order hetero-nuclear dipolar recoupling.....	78
<b>Table 7.</b> Comparison of the performances of $^1\text{H} \rightarrow ^{27}\text{Al}$ RINEPT-CWc and PRESTO transfers using various recouplings for $\text{AlO}_6$ signal of $\gamma$ -alumina at $\nu_R = 20$ kHz.....	83
<b>Table 8.</b> Comparison of the performances of $^1\text{H} \rightarrow ^{27}\text{Al}$ RINEPT-CWc and PRESTO transfers with $\text{AlPO}_4\text{-14}$ at $\nu_R = 20$ kHz. ....	85
<b>Table 9.</b> Comparison of the performances of $^1\text{H} \rightarrow ^{27}\text{Al}$ RINEPT-CWc and PRESTO transfers using various recouplings for the $\text{AlO}_6$ signal of $\gamma$ -alumina at $\nu_R = 62.5$ kHz.....	91
<b>Table 10.</b> Comparison of the performances of $^1\text{H} \rightarrow ^{27}\text{Al}$ RINEPT-CWc and PRESTO transfers using various recouplings for $\text{AlPO}_4\text{-14}$ at $\nu_R = 62.5$ kHz.....	92
<b>Table 11.</b> Distances between the different H atoms and their closest Al neighbours in the structure of isopropylamine templated $\text{AlPO}_4\text{-14}$ determined from X-ray diffraction. <sup>73</sup> The H and Al atoms are numbered according to the cif file. ....	94
<b>Table 12.</b> $^1\text{H}$ $T_2'$ values of $\text{AlPO}_4\text{-14}$ without recoupling or with SR412 recoupling built from (180 <sub>0</sub> ), (270 <sub>0</sub> 90 <sub>180</sub> ) or tt inversion element. The estimated error bars are equal to 7 %.....	97
<b>Table 13.</b> Data obtained from the deconvolution of the $^{11}\text{B}$ 1D spectrum of the $\text{Li}_2\text{B}_4\text{O}_7$ (using the int2QUAD model in DMFit. <sup>45</sup> ) presented in Fig. 37. ....	121
<b>Table 14.</b> Aluminum species present in $\text{AlPO}_4\text{-14}$ reported by Sasaki <i>et al.</i> <sup>46</sup> .....	132
<b>Table 15.</b> Comparison of conventional catalysts with DFNS/BN and DFNS/ $\text{B}_2\text{O}_3$ for propane dehydrogenation. <sup>6,14</sup> .....	151
<b>Table 16.</b> Data obtained from the deconvolutions of the $^1\text{H} \rightarrow ^{29}\text{Si}$ CP MAS NMR spectra (using the Gaussian/Lorentzian model in DMFit <sup>63</sup> ). Parameters include: peak assignment; <sup>27,64-69,71,72,75,76</sup> chemical shift, $\delta$ ; full width at half maximum, FWHM; absolute integrated area (%). ....	162

<b>Table 17.</b> Possible boron species present in DFNS supported catalysts obtained from fitting the $F_1$ dimensions of MQMAS spectra of DFNS/BN before and after catalysis, and DFNS/B <sub>2</sub> O <sub>3</sub> before catalysis. <sup>10,14–16,46,51–62,77</sup> It should be noted that the $\delta_1$ values presented here result from a linear combination of $\delta_2$ and $\delta_{1(\text{non-sheared})}$ . They do not directly correspond to $\delta_{\text{iso}}$ (the isotropic chemical shift). <sup>35,78</sup> .....	168
<b>Table 18.</b> Main plausible local environments in as prepared DFNS/BN, DFNS/BN after catalysis and as-prepared DFNS/B <sub>2</sub> O <sub>3</sub> based on solid-state NMR data.....	169
<b>Table 19.</b> Synthesized MoO <sub>3</sub> /TiO <sub>2</sub> (rutile) catalysts with various content of MoO <sub>3</sub> .....	190
<b>Table 20.</b> Specific area BET and pore volume for the various TiO <sub>2</sub> supports. ....	190
<b>Table 21.</b> Proportion of Mo(V) species found in MoO <sub>3</sub> /TiO <sub>2</sub> catalysts before and after impregnation with TEKPol solutions. ....	193

# General introduction

---

Surfaces are a key region of materials. Their physical and chemical properties define the way materials interact with the environment and determine their reactivity. Understanding the role of surfaces is of increasing relevance in many fields as diverse as heterogeneous catalysis, corrosion inhibition, nanoscience, electronics, energy conversion and storage, as well as health and medicine.<sup>1-4</sup> With the emerging new technologies, there is a need for understanding of fundamental processes and controlling the assembly of atoms and molecules of highly complex surfaces. However, the structural characterization of solid surfaces is frequently challenging because of the significantly small proportions of atoms at the very surface, and the difficulty of detecting them and distinguishing them from those located in the bulk region of the material. Solid-state NMR spectroscopy has emerged as a powerful characterization tool for solid surfaces. It provides unique information on the local atomic-level of surface sites, thus probing short-range ordering and dynamics. Nevertheless, its lack of sensitivity poses a major limitation to surface characterization, especially when the investigated materials contain quadrupolar nuclei.

Quadrupolar nuclei with a half-integer spin value ( $I = 3/2, 5/2, 7/2$  and  $9/2$ ) represent two-thirds of the NMR active isotopes.<sup>5,6</sup> Nuclei, such as  $^{11}\text{B}$ ,  $^{17}\text{O}$  and  $^{27}\text{Al}$ , are present in organic, inorganic and biological solids. Nevertheless, the NMR observation of these nuclei near surfaces remains often more challenging than those of spin-1/2 nuclei. This difficulty comes notably from the large anisotropic quadrupolar interaction, which broadens the resonance, decreases their intensity and complexifies the spin dynamics. Moreover, some of the relevant quadrupolar isotopes have low gyromagnetic ratios ( $\gamma$ ), or low natural abundance, which represent additional challenges for the NMR detection.

Dynamic Nuclear Polarization (DNP), which consists in the microwave-driven transfer of polarization from unpaired electrons to surrounding nuclei, has enabled the selective enhancement of NMR signals of surface species, notably for spin-1/2 nuclei. This approach has been called dynamic nuclear polarization surface-enhanced

spectroscopy (DNP-SENS) and generally relies on indirect DNP *via* protons, since  $^1\text{H}$ - $^1\text{H}$  spin diffusion efficiently transports the polarization within the sample. The DNP-enhanced  $^1\text{H}$  polarisation is usually transferred to the detected nuclei using cross-polarization under magic-angle spinning (CPMAS) sequence.<sup>7</sup> In the case of inorganic particles, for which the bulk region contains no or a limited amount of protons, this CPMAS transfer allows the selection of the surface nuclei. Nevertheless, in the case of half-integer quadrupolar nuclei, the CPMAS technique lacks robustness and it is preferable to use methods for which no spin-lock is applied to the quadrupolar nucleus.<sup>8</sup> Two types of sequences, without any spin-lock, can be used in this case: through-space refocused INEPT (*D*-RINEPT) and PRESTO, which use symmetry-based heteronuclear dipolar recouplings solely applied to the  $^1\text{H}$  channel. More recently a new variant of the *D*-RINEPT scheme was introduced, which uses adiabatic recoupling and continuous wave irradiation in order to improve the decoupling of  $^1\text{H}$ - $^1\text{H}$  interactions. These transfers were combined with DNP to detect the NMR signals of quadrupolar isotopes with low natural abundance ( $^{17}\text{O}$ ) and low gyromagnetic ratio ( $^{47,49}\text{Ti}$ ,  $^{67}\text{Zn}$ ,  $^{95}\text{Mo}$ ), notably near the surface of  $\text{MoO}_3/\text{TiO}_2$  and Al-doped ZnO nanoparticles.

This thesis aims at developing methods for detecting quadrupolar nuclei near surfaces, based on symmetry-based recoupling schemes, for reintroducing hetero- and homo-nuclear dipolar couplings. These new heteronuclear dipolar recoupling techniques will be combined with PRESTO and *D*-RINEPT techniques to transfer DNP-enhanced  $^1\text{H}$  polarization to half-integer quadrupolar isotopes. We will also compare different approaches to probe proximities between identical quadrupolar nuclei. Therefore, this dissertation makes an important contribution to the observation of quadrupolar nuclei in materials, notably near surfaces. The overall structure of the study takes the form of four chapters organized in the following way.

Chapter 1 lays out the importance of surfaces and presents the theoretical background of NMR of quadrupolar nuclei and methods used for this study.

Chapter 2 introduces new recoupling schemes based on single and composite  $\pi$  pulses for PRESTO and *D*-RINEPT sequences. Their performances were evaluated for  $^1\text{H} \rightarrow ^{27}\text{Al}$  magnetization transfers at moderate (20 kHz) and high (62.5 kHz) MAS

frequencies, using samples of  $\gamma$ -Al<sub>2</sub>O<sub>3</sub> and AlPO<sub>4</sub>-14, which exhibit small and moderate <sup>1</sup>H-<sup>1</sup>H dipolar interactions, respectively. These techniques are expected to be useful for transferring the DNP-enhanced magnetization of <sup>1</sup>H to quadrupolar nuclei in indirect MAS DNP experiments at  $\nu_R \geq 20$  kHz, notably used at high magnetic fields.

Chapter 3 concerns the comparison of different homonuclear dipolar recoupling schemes for single-quantum (SQ)-SQ and double-quantum (DQ)-SQ through-space homonuclear correlation (*D*-HOMCOR) sequences. Their performances were evaluated for <sup>11</sup>B-<sup>11</sup>B and <sup>27</sup>Al-<sup>27</sup>Al *D*-HOMCOR at  $\nu_R = 20$  kHz using samples of Li<sub>2</sub>B<sub>4</sub>O<sub>7</sub> and AlPO<sub>4</sub>-14, respectively. The most efficient recoupling schemes for the two HOMCOR variant were identified. Furthermore, we compared the efficiencies of these HOMCOR variants using these recoupling schemes.

Chapter 4 presents new insights into the surface of boron nitride and oxide supported on dendritic fibrous nanosilica, through a combination of 1D and 2D multinuclear (<sup>1</sup>H, <sup>29</sup>Si and <sup>11</sup>B) solid-state NMR experiments. Notably, methods such as *D*-HMQC and MQMAS, have been applied to probe the local environment of quadrupolar nuclei on the surface of these materials. These methods have shown the anchoring of boron nitride and oxide phases on the silica surface.

---

<sup>1</sup> Somorjai, G. A.; Li, Y. Impact of Surface Chemistry. *Proceedings of the National Academy of Sciences* **2011**, *108* (3), 917–924. <https://doi.org/10.1073/pnas.1006669107>.

<sup>2</sup> Yates, J. T.; Campbell, C. T. Surface chemistry: Key to Control and Advance Myriad Technologies. *Proceedings of the National Academy of Sciences* **2011**, *108* (3), 911–916. <https://doi.org/10.1073/pnas.1006671107>.

<sup>3</sup> Marchetti, A.; Chen, J.; Pang, Z.; Li, S.; Ling, D.; Deng, F.; Kong, X. Understanding Surface and Interfacial Chemistry in Functional Nanomaterials via Solid-State NMR. *Adv. Mater.* **2017**, *29* (14), 1605895. <https://doi.org/10.1002/adma.201605895>.

<sup>4</sup> Biener, J.; Wittstock, A.; Baumann, T.; Weissmüller, J.; Bäumer, M.; Hamza, A. Surface Chemistry in Nanoscale Materials. *Materials* **2009**, *2* (4), 2404–2428. <https://doi.org/10.3390/ma2042404>.

<sup>5</sup> Ashbrook, S. E.; Duer, M. J. Structural Information from Quadrupolar Nuclei in Solid State NMR. *Concepts in Magnetic Resonance Part A* **2006**, *28A* (3), 183–248. <https://doi.org/10.1002/cmr.a.20053>.

<sup>6</sup> Ashbrook, S. E.; Sneddon, S. New Methods and Applications in Solid-State NMR Spectroscopy of Quadrupolar Nuclei. *J. Am. Chem. Soc.* **2014**, *136* (44), 15440–15456. <https://doi.org/10.1021/ja504734p>.

<sup>7</sup> Lesage, A.; Lelli, M.; Gajan, D.; Caporini, M. A.; Vitzthum, V.; Miéville, P.; Alauzun, J.; Roussey, A.; Thieuleux, C.; Mehdi, A.; Bodenhausen, G.; Coperet, C.; Emsley, L. Surface Enhanced NMR Spectroscopy by Dynamic Nuclear Polarization. *J. Am. Chem. Soc.* **2010**, *132* (44), 15459–15461. <https://doi.org/10.1021/ja104771z>.

<sup>8</sup> Amoureux, J.-P.; Pruski, M. Theoretical and Experimental Assessment of Single- and Multiple-Quantum Cross-Polarization in Solid State NMR. *Molecular Physics* **2002**, *100* (10), 1595–1613. <https://doi.org/10.1080/00268970210125755>.





---

# CHAPTER 1

---



# Chapter 1: Observation of quadrupolar nuclei near surfaces using solid-state NMR

---

## 1.1 IMPORTANCE OF SURFACES

### 1.1.1 Applications to materials science

Surfaces and interfaces play a significant role in defining the boundary region of a material and controlling the interactions with its environment.<sup>1</sup> Both the nature and strength of these interactions are defined by interfacial properties.<sup>2</sup> Many critical processes, such as corrosion, adhesion, adsorption, friction and catalysis, take place at the boundaries of a material<sup>3,4</sup> and can affect the chemical composition and/or atomic and electronic structure of the surfaces.<sup>1</sup> Understanding the role of surfaces and interfaces is relevant to fields as diverse as catalysis, surface physics, corrosion, nanoscience, tribology, electronics, geochemistry, electrochemistry, energy conversion and storage, chemical and petroleum processing, as well as health and medicine.<sup>1,5-9</sup> Furthermore, modern surface science has become increasingly important in the field of nanomaterials,<sup>7,10</sup> where surfaces are critical in determining the properties, stability and functionalities of materials such as quantum dots,<sup>11,12</sup> battery materials,<sup>13</sup> nanoparticles,<sup>14-16</sup> nanocrystals<sup>17</sup> and nanowires.<sup>18</sup>

Generally, the chemical composition of the surfaces differs from that of the bulk. Surface atoms have fewer neighbours and therefore cannot satisfy their bonding requirements, resulting in higher chemical reactivity.<sup>5,19-21</sup> This property makes surface chemistry unique, and a favoured medium for many chemical and biological reactions to occur.<sup>1</sup> With the advent of new technologies and applications, there is a need for improved understanding and controlling the assembly of atoms and molecules at well-defined surfaces in complex environments.<sup>5,7</sup> Therefore, fundamental and applied studies of surface and interface processes and characterization of the electronic, magnetic and chemical properties are of central importance in developing new materials to meet today's challenges.

### 1.1.2 Techniques to characterize surfaces

One of many grand challenges of surface chemistry is the difficulty of experimentally determining surface structure. This stems from the significantly small proportion of atoms at the very surface, and the difficulty of detecting them and distinguishing them from those located in the bulk region of the material.<sup>1,22</sup> In recent years, many surface science techniques have been developed and adapted to study interfacial phenomena at the molecular level.<sup>1</sup>

Adsorption-desorption methods<sup>5</sup> and microscopies, can provide information about the topology of the surface and its surface area. The microscopies encompass scanning probe microscopies, such as atomic force microscopy (AFM) and scanning tunnelling microscopy (STM),<sup>5,22,23</sup> and electron microscopies, such as transmission electron microscope (TEM) and the scanning electron microscope (SEM).<sup>24,25</sup>

Information on the chemical composition and atomic-level structures of the surfaces can be obtained using surface-sensitive spectroscopies, including X-ray photoelectron and Auger electron spectroscopies, as well as secondary ion mass spectrometry (SIMS). Furthermore, compared to techniques mentioned in the previous paragraph, they can be employed in practical working environments (operando or in-situ).<sup>14,26,27</sup> They are based on stimulating the surface of the sample with incoming (incident) particles (photons, electrons and ions) and monitoring the signals produced by the ejected particles (photons, electrons and ions) that are only emitted by the surface, as a result of said stimulation.<sup>6,28-30</sup> The analysis can reveal key information about the elemental composition as well as the atomic-level structure of the surface of the studied material.<sup>6,14</sup> The main characteristics and type of information that can be extracted from most commonly used surface methods are summarized in Table 1.

**Table 1.** General characteristics of common surface analysis methods

<b>Technique</b>	<b>Probe/Detected</b>	<b>Lateral resolution</b>	<b>Information depth</b>	<b>Depth resolution</b>	<b>Type of information</b>
<b>X-ray photoelectron spectroscopy (XPS)</b>	Photons/Electrons	~ 2-10 $\mu\text{m}$	2-10 nm	~ 2 nm	Surface elemental and chemical composition. Depth profiling
<b>Auger electron spectroscopy (AES)</b>	Electrons/Electrons	~ 10 nm	2 nm	~ 2 nm	Elemental composition of whole material or individual large particles. Depth profiling
<b>Surface enhanced Raman spectroscopy (SERS)</b>	Photons/Photons	~ 2 $\mu\text{m}$	>10 nm	Single molecule	Detection of fingerprint signals of molecules and for the investigation of surface reactions intermediates
<b>Low-energy ion scattering (LEIS)</b>	Ions/Ions	~ 5 $\mu\text{m}$	~10 nm	~0.2 nm	Elemental composition at the outer atomic layer of a sample
<b>Time-of-flight secondary ion mass spectrometry (ToF-SIMS)</b>	Ions/Ions	~60 nm	1 nm	<1 nm	Surface elemental composition and isotope distributions

In X-ray photoelectron spectroscopy (XPS), also known as electron spectroscopy for chemical analysis (ESCA), photons are used as a probe and electrons are detected.<sup>31,32</sup> Conversely in Auger Electron Spectroscopy (AES), electrons are used both a probe and a detected particle, whereas in Raman spectroscopy, the probe and the detected particles are photons. Recent advances in Raman spectroscopy led to surface enhanced Raman spectroscopy (SERS), a powerful detection technique with

high sensitivity.<sup>33–35</sup> In ion scattering spectroscopy (ISS), also known as low-energy ion scattering (LEIS), and time-of-flight secondary ion mass spectroscopy (ToF-SIMS), ions are used as a probe and the detected particles.<sup>36,37</sup> These different surface characterization methods are summarized in Figure 1.

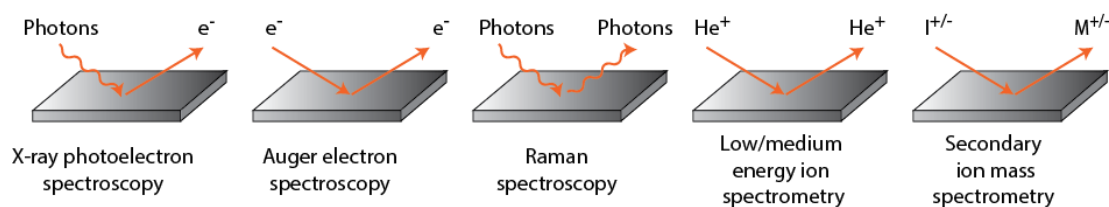


**Figure 1.** Schematic representation of the surface analysis methods presented in Table 1.

Each technique has a specific sampling profile and its own unique capabilities. Most of these methods have a nanometric resolution in at least one dimension and require that the analysis be performed in an ultra-high vacuum apparatus.<sup>1,6</sup> Generally, no single technique provides enough information to solve a complex real-world problem. However, different surface analysis techniques can provide complementary and comprehensive information.<sup>8</sup> The methods presented here are under continuous development. Advances in technology and instrumentation, such as more efficient vacuum systems made possible characterization of the structure and reactivity of a wide range of surfaces.

### 1.1.3 NMR of surfaces

Recently, solid-state NMR spectroscopy has emerged as a powerful characterization tool for solid surfaces.<sup>38</sup> It allows determining the atomic-level structure of surface species, thus probing short-range ordering and dynamics.<sup>7,39</sup> This makes solid-state NMR an ideal tool for establishing structure-property relationships and the development of advanced materials including catalysts,<sup>39–42</sup> thin-films,<sup>43–45</sup> and nanoparticles<sup>46–49</sup>.

Compared to diffraction techniques, which detect long-range ordering and require some structural regularity,<sup>38,50</sup> solid-state NMR is sensitive to local interactions and

geometries<sup>51</sup> of real-world materials on the micro- and nano-scale and thus, is well-suited for disordered or non-crystalline surfaces.<sup>7,52,53</sup>

However, the low concentration of the surface sites and the inherent low sensitivity of NMR poses limit to a broader application of this technique.<sup>51,54,55</sup> Recent advances in polarization techniques that selectively enhance surface NMR signals<sup>56</sup> and selective labelling,<sup>57,58</sup> have potentiated its application and opened new insights in surface chemistry.

Isotropic chemical shifts are the most employed information obtained from solid-state NMR.<sup>51</sup> They allow structural assignments of various surface chemical species of the nucleus under study, as the chemical shifts are directly related to the chemical environment that arises from the interaction of the probed nucleus and its electronic cloud.<sup>38,59</sup> Figure 2 summarizes the internal interactions in solid-state NMR and the structural information that can be obtained from the NMR spectra.

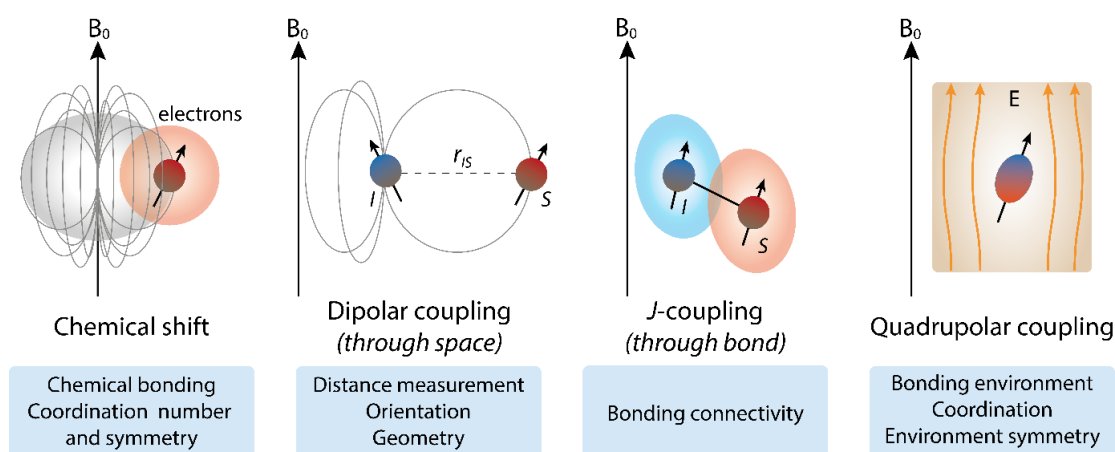


**Figure 2.** Summary of the most important interactions in solid-state NMR and the available information.

However, unlike in solution-state NMR, the effect of anisotropic interactions, such as dipolar coupling and chemical shift anisotropy (CSA), can broaden the NMR signals and prevents the measurement of the isotropic chemical shifts.<sup>60</sup> By spinning the sample at the magic angle ( $54.74^\circ$ ) with respect to the direction of the magnetic field, it is possible to average these anisotropic interactions, and to measure reliably the isotropic chemical shifts,  $\delta_{\text{iso}}$ .<sup>61,62</sup>

One-dimensional (1D) solid-state magic angle spinning NMR (MAS NMR) experiments have been used to reveal detailed structural information on the surface of a wide-range of materials.<sup>7,38,63</sup>  $^1\text{H}$ ,  $^{13}\text{C}$ ,  $^{29}\text{Si}$  and  $^{31}\text{P}$  nuclei are the most commonly detected spin-1/2 isotopes to solve questions regarding local structures and chemical processes on surfaces.<sup>39,52</sup> Details of these nuclei and other common NMR-active nuclei found on solid surfaces and their nuclear magnetic properties are listed in Table 2.

**Table 2.** Summary of the nuclear magnetic properties of some nuclei commonly found in solid surfaces.<sup>64,65</sup>

Nucleus	Spin	NA (%) <sup>a</sup>	$\nu^0$ at 18.8 T (MHz) <sup>b</sup>	$Q$ (fm <sup>2</sup> ) <sup>c</sup>
$^1\text{H}$	1/2	99.99	800.00	-
$^2\text{H}$	1	0.01	122.81	0.286
$^{13}\text{C}$	1/2	1.07	201.16	-
$^6\text{Li}$	1	7.59	117.75	-0.0801
$^7\text{Li}$	3/2	92.41	310.96	-4.010
$^{11}\text{B}$	3/2	80.4	256.71	4.059
$^{14}\text{N}$	1	99.63	57.81	2.044
$^{15}\text{N}$	1/2	0.37	81.09	-
$^{17}\text{O}$	5/2	0.04	108.45	-2.558
$^{17}\text{F}$	1/2	100.00	752.75	-
$^{23}\text{Na}$	3/2	100.00	211.61	10.400
$^{25}\text{Mg}$	5/2	10.00	48.97	19.940
$^{27}\text{Al}$	5/2	100.00	208.46	14.660
$^{29}\text{Si}$	1/2	4.68	158.94	-
$^{31}\text{P}$	1/2	100.00	323.85	-
$^{35}\text{Cl}$	3/2	75.76	78.39	-8.165
$^{39}\text{K}$	3/2	93.26	37.33	5.850
$^{47}\text{Ti}$	5/2	7.44	45.11	30.200
$^{49}\text{Ti}$	7/2	5.41	45.12	24.700
$^{67}\text{Zn}$	5/2	4.10	50.05	15.000
$^{95}\text{Mo}$	5/2	15.70	52.14	-2.200

<sup>a</sup>Natural abundance.

<sup>b</sup>Larmor frequency at 18.8 T.

<sup>c</sup> $Q$  is the nuclear quadrupolar moment,  $eQ$ , divided by the elementary charge  $e = 1.602 \times 10^{-19}$  C.



The development of MAS and cross-polarization (CP)<sup>66,67</sup> has enabled the acquisition of 1D spectra under high-resolution. The CPMAS technique, which transfers the polarization of protons to another isotope through dipolar couplings, allows the detection of insensitive nuclei like <sup>13</sup>C and <sup>15</sup>N.<sup>67</sup> Under Hartman-Hann conditions,<sup>68</sup> the CPMAS sequence is commonly employed to obtain selectively NMR spectra of surface nuclei, such as <sup>29</sup>Si or <sup>31</sup>P, in materials, such as oxides, in which protons are only located on the surface.<sup>69</sup> A wide range of surface species has been characterized using CPMAS spectroscopy.<sup>70-72</sup> For example, 1D <sup>1</sup>H-<sup>29</sup>Si CPMAS and <sup>1</sup>H-<sup>31</sup>P CPMAS experiments have been applied to probe the surface of silicon-nanocrystals,<sup>54</sup> Si-nanopowders<sup>73</sup> and functionalized silica nanoparticles,<sup>74</sup> providing key information to resolve the chemical structure of the surface.

In addition to 1D experiments, multidimensional experiments are often needed to elucidate structural information and confirm assignments made from one-dimensional experiments. One of the most commonly employed 2D methods is heteronuclear correlation spectroscopy (HETCOR) using CP transfer (CP-HETCOR).<sup>75</sup> For instance, CP-HETCOR NMR is used to determine the proximity between protons and heteronuclei (e.g. <sup>13</sup>C, <sup>29</sup>Si, <sup>31</sup>P) by establishing correlations between neighbouring atoms.<sup>76</sup> Advances in proton homo-nuclear decoupling schemes<sup>54</sup> have enabled the detection of high-resolution 2D-HETCOR experiments. For instance, <sup>1</sup>H-<sup>29</sup>Si HETCOR NMR spectroscopy allowed selectively filtering the NMR signal of <sup>1</sup>H close to <sup>29</sup>Si surface sites in hybrid organic-inorganic interfaces in surfactant templated silicas that have been prepared under acidic and basic conditions, showing the clear difference in the number of Si-OH groups between the acidic and basic systems. The acidic sample exhibits a silanol rich surface with a longer distance between the Si surface sites and the polar head groups, whereas the basic sample exhibits a small amount of Si-OH groups and a short distance between the Si-O- surface groups and the surfactant polar head group.<sup>77</sup>

Remarkable gains in sensitivity have been achieved by recording HETCOR experiments through the detection of <sup>1</sup>H rather than moderate to low- $\gamma$  nuclei such as <sup>13</sup>C, as <sup>1</sup>H has a larger gyromagnetic ratio ( $\gamma$ ) and natural abundance of 99.985%. This indirect detection of heteronuclei can be achieved using double CP transfer. The gain in sensitivity provided by indirect detection allows the acquisition of through-space

2D HETCOR spectra of species bound to a surface at natural abundance with a reduced acquisition time.<sup>78</sup> As an illustration, 2D  $^1\text{H}$ - $^{13}\text{C}$  HETCOR NMR and  $^1\text{H}$ - $^{15}\text{N}$  HETCOR NMR spectra of allyl groups covalently bound to the surfaces of mesoporous silica nanoparticles reveal the spatial proximity between allyl groups and the silica surface.<sup>79</sup> More recently, Swanson and collaborators demonstrated the application of  $^1\text{H}$ - $^{13}\text{C}$  HETCOR NMR and  $^1\text{H}$ - $^{15}\text{N}$  HETCOR spectra in combination with CPMAS experiments to probe the different interactions with water molecules at the silica surface in histidine bound to fumed silica nanoparticles (His-FSN). This work illustrates the power of high-resolution MAS NMR techniques to solve the structure of interfaces in hybrid materials at an atomic level.<sup>80</sup>

Besides heteronuclear correlations, detailed information of surface species can be extracted through homonuclear correlation experiments. Through-space double quantum (DQ)–single quantum (SQ) correlation NMR is a powerful method to probe the proximities between nearby nuclei. It relies on dipolar interactions between nuclei in spatial proximity. Therefore, the correlations observed in 2D DQ-SQ NMR spectra arise from nuclei that are dipolar coupled to another nucleus of the same isotope in equivalent or different environments.<sup>81,82</sup> 2D  $^1\text{H}$ - $^1\text{H}$  DQ-SQ MAS NMR spectra have been successfully applied to distinguish protonated species on surfaces. Sorte *et al.* have used DQ-SQ correlation spectroscopy in combination with DFT calculations to further characterize the multiple proton environments in MgO-based minerals.<sup>83</sup> These 2D-NMR experiments make possible to characterize different proton species bonded at the surface with improved resolution, as well as to probe the spatial arrangement of the different proton environments. Likewise, Vancompernelle *et al.* recorded 2D  $^1\text{H}$ - $^1\text{H}$  DQ-SQ MAS NMR spectra to get insights into the molecular-level structure of bis-silylamido aluminium grafted on silica surface, revealing correlations arising from the different proton environments in this material.<sup>84</sup> 2D  $^{29}\text{Si}$ - $^{29}\text{Si}$  DQ-SQ MAS NMR also have been used to probe through-space proximities between all silicon species in the surface of functionalized mesoporous silica nanoparticles.<sup>85,86</sup> The acquisition of a train of echoes using Carr-Purcell Meiboom-Gill (CPMG) sequence<sup>87</sup> can further enhance the NMR signal of these  $^{29}\text{Si}$  DQ-SQ experiments.

### 1.1.4 Importance of quadrupolar nuclei near surfaces

Many inorganic materials contain quadrupolar nuclei with spin  $I \geq 1$ , which represent about 75% of NMR-active isotopes.<sup>88</sup> Nuclei, such as  $^{27}\text{Al}$  ( $I = 5/2$ ),  $^{17}\text{O}$  ( $I = 5/2$ ),  $^6\text{Li}$  ( $I = 1$ ),  $^7\text{Li}$  ( $I = 3/2$ ),  $^{11}\text{B}$  ( $I = 3/2$ ),  $^{14}\text{N}$  ( $I = 1$ ),  $^{23}\text{Na}$  ( $I = 3/2$ ),  $^{25}\text{Mg}$  ( $I = 5/2$ ),  $^{35}\text{Cl}$  ( $I = 3/2$ ), and  $^{39}\text{K}$  ( $I = 3/2$ ), are present in catalysts, inorganic oxides, polymers, clays, glasses, energy materials, pharmaceutical and biomaterials.<sup>65,89–91</sup>

Compared to spin-1/2 nuclei, an additional difficulty for the detection of quadrupolar nuclei near surfaces is that their NMR signals are broadened by the quadrupolar interaction, which results from the interaction between the electric quadrupolar moment of the quadrupolar nuclei and the electric field gradient. This interaction is generally stronger than the dipolar and CSA interactions and gives rise to broadening often over several megahertz, which cannot be removed by MAS.<sup>88,92</sup> Second, some of the commonly studied nuclei have low gyromagnetic ratios ( $\gamma$ ), or high quadrupole moments and or low natural abundances, which represent additional challenges for the NMR detection.<sup>93,94</sup> Furthermore, the lower coordination number of surface atoms results in higher electric field gradient and hence, larger quadrupolar interaction.

However, structural information can be obtained by evaluating the quadrupolar interaction, which depends on the quadrupolar coupling constant ( $C_Q$ ) and the asymmetry parameter of the electric field gradient ( $\eta_Q$ ).<sup>88</sup> Both parameters are sensitive to the coordination environment, and combined with isotropic chemical shifts  $\delta_{\text{iso}}$ , they can help determining the local structure of surface sites.<sup>60</sup>

The NMR spectra of half-integer spin quadrupolar nuclei (e.g.  $^{27}\text{Al}$ ,  $^{11}\text{B}$ ,  $^{17}\text{O}$ ) are often dominated by the central transition (CT) between energy levels  $m_I = +1/2$  and  $-1/2$  since this transition is not broadened by the first-order quadrupolar interaction but only by the second-order quadrupolar interaction.<sup>95</sup> Nevertheless, this second-order quadrupolar interaction is not completely averaged out by MAS.<sup>61</sup> Conversely, high magnetic fields reduce the broadening due to the second-order quadrupolar interaction and thus, improve the resolution of the NMR spectra of quadrupolar nuclei.<sup>96,97</sup>

Furthermore, multiple-quantum MAS (MQMAS) experiment is a 2D NMR method, which allows the acquisition of high-resolution NMR spectra of quadrupolar nuclei by removing broadening due to second-order quadrupolar interaction.<sup>98</sup> This technique correlates different transitions within the spin system and yields an isotropic spectrum from the projection onto the indirect dimension. Other approaches have been proposed to record high-resolution spectra of quadrupolar nuclei. Some of these techniques involve sample rotation around two different angles: simultaneously for double rotation (DOR), and sequentially for dynamic-angle spinning (DAS).<sup>99</sup> The MQMAS, DOR and DAS experiments will be presented in more details in Section 1.4.

An example of quadrupolar nucleus detected near surface is  $^{27}\text{Al}$ , which is present in alumina, a widely used catalyst support.<sup>100</sup> Its 100% natural abundance and its moderate gyromagnetic ratio,  $\gamma(^{27}\text{Al})/\gamma(^1\text{H}) \approx 0.26$ , facilitate the detection of this isotope near surface. Valuable information on local structure and chemistry of aluminium in its various environments can be obtained from NMR parameters, such as isotropic chemical shifts as well as  $C_Q$  and  $\eta_Q$  quadrupolar parameters.<sup>88</sup> In particular, the coordination of the aluminium can be deduced from its isotropic chemical shift.

For example, Xu *et al.* used  $^{27}\text{Al}$  MAS and MQMAS NMR experiments combined with high magnetic fields to study a series of transition aluminium oxides where the  $\gamma$ -,  $\delta$ -, or  $\theta$ - $\text{Al}_2\text{O}_3$  dominates.<sup>101</sup> Specifically, MQMAS was used to resolve and obtain the quadrupolar parameters of the different aluminium sites, thus, allowing to distinguish the aluminium environments of each of the  $\gamma$ -,  $\delta$ - and  $\theta$ -phases. It was found that  $\delta$ - $\text{Al}_2\text{O}_3$  contains three distinct octahedral sites and two aluminium tetrahedral sites. These results allowed to determine also that the  $\gamma$ - $\text{Al}_2\text{O}_3$  consists of local structures similar to those found in  $\theta$ - $\text{Al}_2\text{O}_3$  as well as  $\delta$ - $\text{Al}_2\text{O}_3$  phases but with less ordering, which before could not be observed at low field-NMR. More recently, Kaushik *et al.* reported the use of 1D and 2D NMR experiments (including  $^{27}\text{Al}$  MAS,  $^{27}\text{Al}\{^1\text{H}\}$  and  $^{29}\text{Si}\{^{27}\text{Al}\}$  *D*-HMQC and  $^{27}\text{Al}$  DQ/SQ) to get detailed insight into the structure of the surface species on alumina oxide/silica thin-films prepared by atomic layer deposition (ALD).<sup>102</sup> The results showed that in films with  $\sim 3$  wt% of Al, a sub-monolayer is formed and possibly contains aluminium species ( $^{[n]}\text{Al}$  where  $n = 4, 5$  or

6) which have been substituted by Si in the second coordination sphere such as  $^{[4]}\text{Al}_{(3\text{Si})}$ ,  $^{[4]}\text{Al}_{(4\text{Si})}$  and  $^{[5]}\text{Al}_{(2\text{Si})}$  on the silica surface, with most of these sites attached to OH groups, whereas films with ~9 or 15 wt% of Al exhibit characteristics of an amorphous alumina phase with a high concentration of  $^{[5]}\text{Al}$  species and OH groups. In addition, the results gave further evidence that the most likely species at the interface between silica and alumina are  $^{[4]}\text{Al}_{(2\text{Si})}$ ,  $^{[4]}\text{Al}_{(3\text{Si})}$  and  $^{[5]}\text{Al}_{(2\text{Si})}$ .

Another isotope of interest for the characterization of surfaces is  $^{17}\text{O}$  since it is present at the surface of numerous oxide-based materials. Solid-state NMR spectroscopy of oxygen-17 can provide detailed chemical and structural information of the various oxygen atoms in oxide-based solids.<sup>103,104</sup> Nevertheless,  $^{17}\text{O}$  NMR is inherently insensitive due to the extremely low natural abundance of  $^{17}\text{O}$  nuclei (0.037%) and usually requires isotropic enrichment.<sup>58</sup> Merle *et al.* performed  $^{17}\text{O}$  MAS, MQMAS, and *D*-HMQC NMR experiments to probe the  $^{17}\text{O}$  local environment on  $^{17}\text{O}$ -surface labelled silica and M-SiO<sub>2</sub> (M= W, Ta, Zr).<sup>105</sup> MQMAS allowed to extract the quadrupolar parameters of the Si-OH, Si-O-Si, and Si-O-M surface sites for all the materials, while *D*-HMQC helped to probe the proximities between  $^{17}\text{O}$  and  $^1\text{H}$  sites and gain further information on the spatial configuration of the surface species. These results show that  $^{17}\text{O}$  NMR can provide unprecedented information on the interactions between the metallic complexes and their support in supported catalysts.  $^{17}\text{O}$  NMR spectroscopy has been also applied to study CeO<sub>2</sub> nanoparticles.<sup>49,106,107</sup> They made use of hyperpolarization techniques, in particular dynamic nuclear polarisation (DNP), to selectively enhance the NMR signals of the surface species on isotopically-labelled samples. This technique so-called DNP-SENS<sup>108</sup> will be discussed in more detail in section 1.5.4.

## 1.2 QUADRUPOLAR INTERACTION

Quadrupolar nuclei, as mentioned above, have spin  $I$  larger than 1/2. These nuclei have a non-spherical distribution of charge in the nucleus that gives rise to an electric quadrupolar moment ( $eQ$ ), independent of its environment.<sup>92,98</sup> The quadrupolar interaction then, results when the quadrupolar moment interacts with the surrounding electric field gradient (EFG). The EFG is generated by the electronic charge

distribution and is defined by three components,  $V_{XX}$ ,  $V_{YY}$  and  $V_{ZZ}$ , in its principal axis system (PAS) (Figure 3).<sup>109</sup> The quadrupolar interaction is anisotropic i.e., depends upon orientation and is usually described in terms of two parameters: the quadrupolar coupling constant,  $C_Q = eQV_{ZZ}/h$  (with  $h = 6.626 \times 10^{-34}$  J.Hz<sup>-1</sup> being the Planck constant and  $C_Q$  in units of hertz) which quantifies its magnitude, and the asymmetry parameter,  $\eta_Q = (V_{XX} - V_{YY})/V_{ZZ}$ , which describes the shape of the interaction and takes values between  $0 \leq \eta_Q \leq 1$ .<sup>110,111</sup>

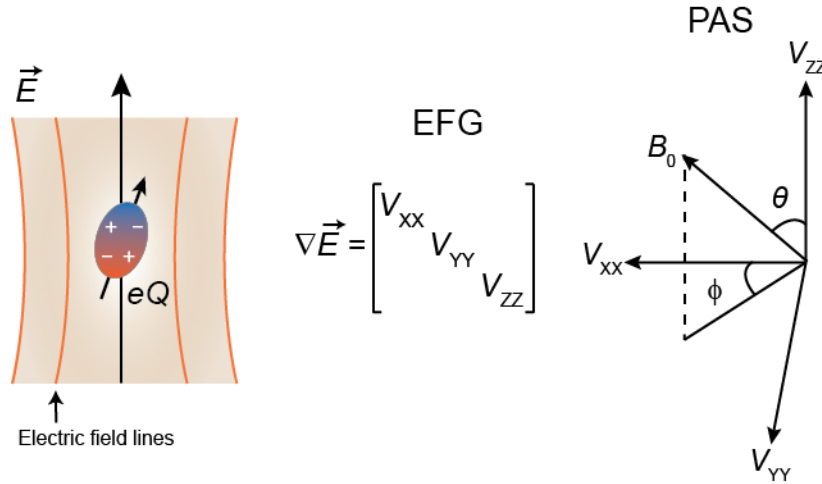


**Figure 3.** Schematic representation of the nuclear quadrupolar interaction which arises from the coupling between the electric quadrupolar moment  $eQ$  and the electric field gradient (EFG)  $\nabla E$ . (left). The EFG is mathematically described by a 3x3 matrix and is defined by its three tensor components  $V_{XX}$ ,  $V_{YY}$  and  $V_{ZZ}$ , with  $|V_{ZZ}| \geq |V_{YY}| \geq |V_{XX}|$  by convention (middle). The orientations of the PAS for the EFG tensor with respect to the external magnetic field,  $B_0$  (right).

The  $C_Q$  values are typically in the order of a few megahertz to tens of megahertz for quadrupolar spins in sites of non-cubic symmetry.<sup>88</sup> However, in most practical cases the quadrupolar interaction is much smaller than the Zeeman interaction, and thus, its effect can be considered as a perturbation to the Zeeman energy levels.<sup>92,110</sup> The quadrupolar interaction can be divided into two contributions: the first-order,  $H_Q^{(1)}$ , and second-order,  $H_Q^{(2)}$ .<sup>109,112</sup> Figure 4 shows the Zeeman energy levels for nuclei with  $I = 3/2$  and the perturbation caused by the quadrupolar interaction when considering  $H_Q^{(1)}$  and  $H_Q^{(2)}$ .

The first-order quadrupolar interaction generates small shifts of the energy levels and splits the NMR signal into  $2I$  allowed transitions between the  $2I + 1$  Zeeman levels.<sup>65,92,109</sup> For half-integer quadrupolar nuclei, they are referred as the central transition (CT) occurring between energy levels  $m_I = +1/2$  and  $-1/2$ , and the satellite transitions (STs) between energy levels  $m_I$  and  $m_I+1$ . The resonance frequency of STs depends on both first- and second-order quadrupolar interactions. As the strength of the first-order quadrupolar interaction generally exceeds the MAS frequency, this interaction cannot be completely removed by MAS and the STs exhibits several spinning sidebands.<sup>111</sup> Conversely, the central transition (CT) is unaffected by the quadrupolar interaction to the first-order<sup>113</sup> and hence, is in many cases the only transition observed experimentally.<sup>92</sup>

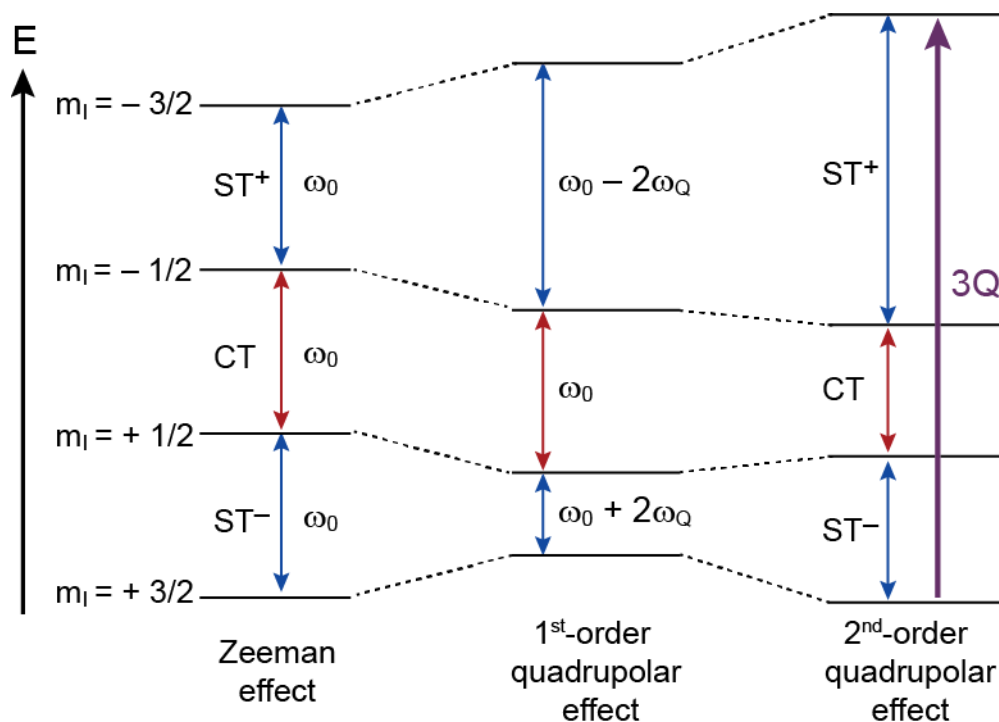


**Figure 4.** Schematic energy level diagram for a spin  $I = 3/2$  nucleus showing the effect of the Zeeman, first-order and second-order quadrupolar interactions. The first-order quadrupolar interaction splits the NMR spectrum into  $2I - 1$  lines with resonance frequencies affected by the quadrupolar splitting parameter  $\omega_Q$ , while the central transition CT remains unaffected at the Larmor frequency  $\omega_0$ . The second-order quadrupolar interaction affects all the lines.

The effect of  $H_Q^{(2)}$  is to shift further all the lines, including the CT,<sup>109</sup> as observed in Figure 4. This interaction has a more complex angular dependence than the first-order quadrupolar interaction, therefore the  $H_Q^{(2)}$  effect on the NMR spectrum is only partially averaged by MAS.<sup>111</sup> Nevertheless, the second-order quadrupolar broadening is proportional to  $C_Q^2/B_0$  and hence the use of high magnetic fields improves the spectral resolution.<sup>110</sup>

### 1.3 EFFECTS OF RF FIELD FOR QUADRUPOLEAR NUCLEI

Radiofrequency (rf) field irradiation allows the manipulation of the magnetization and coherences in NMR.<sup>114</sup> In contrast to their spin  $I = 1/2$  counterparts, the rf interaction with quadrupolar nuclei in a high magnetic field is much more complicated, and renders NMR experiments of these nuclei challenging.<sup>114–116</sup> The response of the spins to the rf irradiation depends on the relative magnitudes of three parameters: (i) the rf amplitude ( $\omega_1$ ) of the pulse, (ii) the first-order quadrupolar splitting ( $\omega_Q$ ), and (iii) the irradiation offset ( $\Delta\omega_0$ ), which is the difference between the resonance frequency and the carrier frequency of the rf pulse.<sup>115,117,118</sup> Usually, the first-order quadrupolar interaction is much larger than the achievable nutation frequencies (i.e. rotation of the magnetization under the influence of the rf field), and therefore cannot be neglected during the excitation of the spin system.<sup>110,118</sup>

The rf pulses on quadrupolar nuclei can be classified as selective or non-selective,<sup>119</sup> as illustrated in Figure 5 for a spin  $I = 3/2$ . Consequently, the behaviour of quadrupolar spins under rf irradiation, can be summarized in three regimes.<sup>117</sup>

In the limiting case where the rf pulse amplitude is greater than the strength of the first-order quadrupolar interaction,  $\omega_1 \gg \omega_Q$ , this corresponds to a non-selective or hard pulse irradiation where all NMR transitions (central and satellite transitions) are excited simultaneously (Case A).<sup>118</sup> Under this regime, the nutation frequency of the CT is given by  $\omega_{nut} = \omega_1$ .<sup>117,118</sup> These non-selective RF pulses are used primarily for the acquisition of one-dimensional (1D) NMR spectra. In addition, for acquiring quantitative 1D NMR spectra, the quadrupolar nuclei are excited by a single non-selective pulse that produces small flip angle rotations of the CT magnetization.<sup>110</sup>



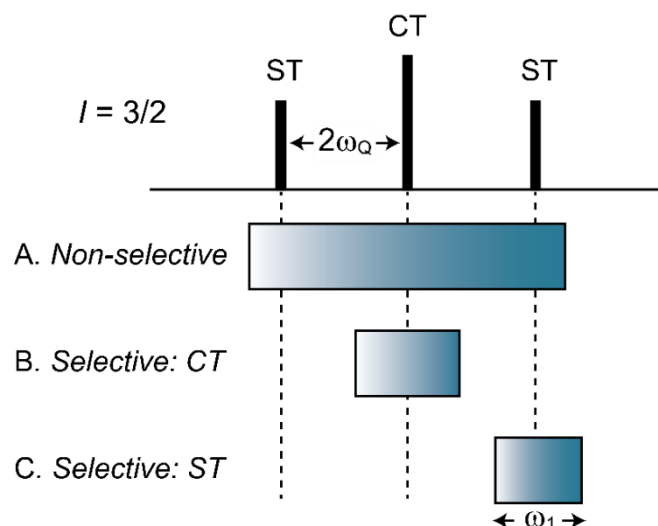


**Figure 5.** Schematic frequency domain representation of rf irradiation of quadrupolar nuclei with spin  $I = 3/2$ .

In the case where  $\omega_Q \gg \omega_1$ , this leads to the selective excitation of the central transition CT (Case B).<sup>117,118</sup> Then, the effective nutation frequency of the CT magnetization,  $\omega_{nut}^{eff}$ , occurs at  $\omega_{nut}^{eff} = \left(I + \frac{1}{2}\right) \omega_{rf}$ , where  $\omega_{rf}$  is the rf nutation frequency for an isotropic liquid or a solid with  $C_Q = 0$ .<sup>110,119,120</sup> Most NMR studies<sup>121</sup> of half-integer quadrupolar nuclei involve selective excitation of the CT transition.<sup>119</sup> These CT-selective pulses are mainly used to tilt the magnetization related to the CT away from the  $B_0$  axis by an arbitrary angle.<sup>110</sup> For example,  $90^\circ$  and  $180^\circ$  CT-selective pulses are employed in numerous pulse sequences that are described in section 1.4. Furthermore, selective pulses can be used to excite the satellite transitions STs (Case C) by using a nutation frequency  $\omega_{nut} = \omega_1\sqrt{3}$ . However this particular case only involves single crystal samples, since selective excitation of STs cannot be achieved simultaneously for all crystallites in a powder sample.<sup>115</sup>

In between these two regimes, there is a fourth regime, where  $\omega_Q \approx \omega_1$ . The spin dynamics of quadrupolar spins become complex and the degree of excitation highly depends on the strength of the quadrupolar interaction.<sup>110,117</sup> Nevertheless, the magnetization can be also converted into multiple quantum coherences.<sup>117,122</sup> In particular, triple quantum coherences can be excited with a hard pulse, thus allowing experiments as MQMAS.<sup>121</sup> This experiment is explained in more detail in section 1.4.1.

## 1.4 HIGH-RESOLUTION NMR SPECTRA OF QUADRUPOLEAR NUCLEI

The power of solid-state NMR to probe the structure of materials relies strongly on the availability of recording high-resolution spectra.<sup>123</sup> As mentioned earlier, the second-order quadrupolar interaction poses a limit to obtaining high resolution spectra of quadrupolar spins, since it cannot be completely removed by MAS due to its complex angular dependence.<sup>119</sup> There are several sophisticated methods to remove the broadening caused by this interaction.<sup>120</sup> One experimental approach to overcome this is to find an angle  $\theta$  such that  $P_2(\cos \theta) = P_4(\cos \theta) = 0$  (where  $P_2$  and  $P_4$  denote the second- and fourth-order Legendre polynomials) is satisfied.<sup>117</sup> Two techniques, DOR (Double Rotation)<sup>124</sup> and DAS (Dynamic Angle Spinning)<sup>125</sup>, were initially developed to remove the second-order broadening of the CT. They involved space averaging of the second-order quadrupolar interaction through mechanical rotation of the sample holder.<sup>117</sup>

In DOR, the sample is placed within an inner rotor, which is spun inside an outer rotor, and the assembly is spun simultaneously around two different axes ( $30.56^\circ$  and  $54.74^\circ$ ) relative to  $B_0$ .<sup>126</sup> The DOR technique enables the elimination of the first- and second-order terms of the quadrupolar interaction in a 1D experiment.<sup>127</sup> On the other hand, DAS is a 2D experiment that works by rapidly switching the rotor between two axes.<sup>128,129</sup> Therefore, it requires specialized instrumentation for the rapid switching and stabilization of the rotor during the experiment.<sup>130,131</sup> Since this is a 2D experiment, experimental times are typically longer than those for DOR.<sup>116,131</sup> Even if the development of DOR and DAS allowed an elegant solution to the high resolution problem, their use is limited nowadays since they both require dedicated NMR probes.<sup>110</sup>

The advent of 2D experiments such as MQMAS<sup>121,132</sup> and later satellite transition MAS (STMAS)<sup>133,134</sup>, have revolutionized the observation of half-integer quadrupolar nuclei.<sup>116</sup> They use conventional MAS hardware and provide high-resolution NMR spectra by cancelling out the broadening due to both first- and second order quadrupolar interactions.<sup>110,117</sup>

### 1.4.1 MQMAS

The MQMAS approach introduced by Frydman and Harwood,<sup>121</sup> is the most popular method for studying quadrupolar nuclei.<sup>92,117,135</sup> Unlike the DAS and DOR techniques, the MQMAS experiment requires rotation of the sample around a single angle (i.e. at the magic-angle, which also eliminates dipole and CSA interactions) and therefore, can be performed using a conventional MAS probe.<sup>92,111</sup> The elimination of the quadrupolar second-order interaction is achieved in a two-dimensional experiment by correlating multiple quantum coherences, typically triple-quantum coherences (between energy levels  $m_I = +3/2 \leftrightarrow m_I = -3/2$ , indicated as 3Q in Figure 4), with the CT coherence.<sup>92,98,136</sup>

The simplest MQMAS experiment involves two-pulses and served as foundation for the subsequent developments in MQMAS.<sup>98,129</sup> The first RF pulse excites all possible (non-observable) multi-quantum (MQ) coherences during the  $t_1$  evolution. The second RF pulse converts these MQ coherences into observable -1Q-CT coherence during  $t_2$ .<sup>98,135</sup> The 2D spectra provides an isotropic high-resolution spectrum along the indirect dimension (F1), correlated with its corresponding MAS spectrum in the detection dimension (F2).<sup>117,118</sup> This is achieved by selecting only coherences between energy levels with opposite magnetic quantum numbers  $p/2$  and  $-p/2$  with  $p = 2m$  with  $m = -I, -I + 1, \dots, I$ , that corresponds to  $p$ Q transitions which are not affected by the first-order quadrupolar broadening (only second-order broadening is present for these transitions with opposite magnetic quantum numbers).<sup>98,117</sup> For spins  $I > 3/2$ , higher order coherences can be excited, thus,  $p$  can take values as 3, 5, etc, corresponding to 3Q and 5Q coherence pathways, respectively.<sup>129</sup> Nevertheless, 3QMAS experiment remains as the most used to the date owing to its higher sensitivity.<sup>116</sup>

Most of the MQMAS spectra are presented after a shearing transformation, which is implemented to produce an isotropic spectrum in the indirect dimension that is free from the second-order quadrupolar broadening. The projection of the spectrum onto the F1 dimension reveals one narrow NMR peak for each individual crystallographic site. Therefore, the 3QMAS experiment allows the determination of the number of crystallographic sites, and their NMR parameters as the isotropic chemical shifts and

the quadrupolar parameters, which are not possible to obtain with the conventional 1D MAS spectra, in which signals of different sites often overlap.<sup>118</sup>

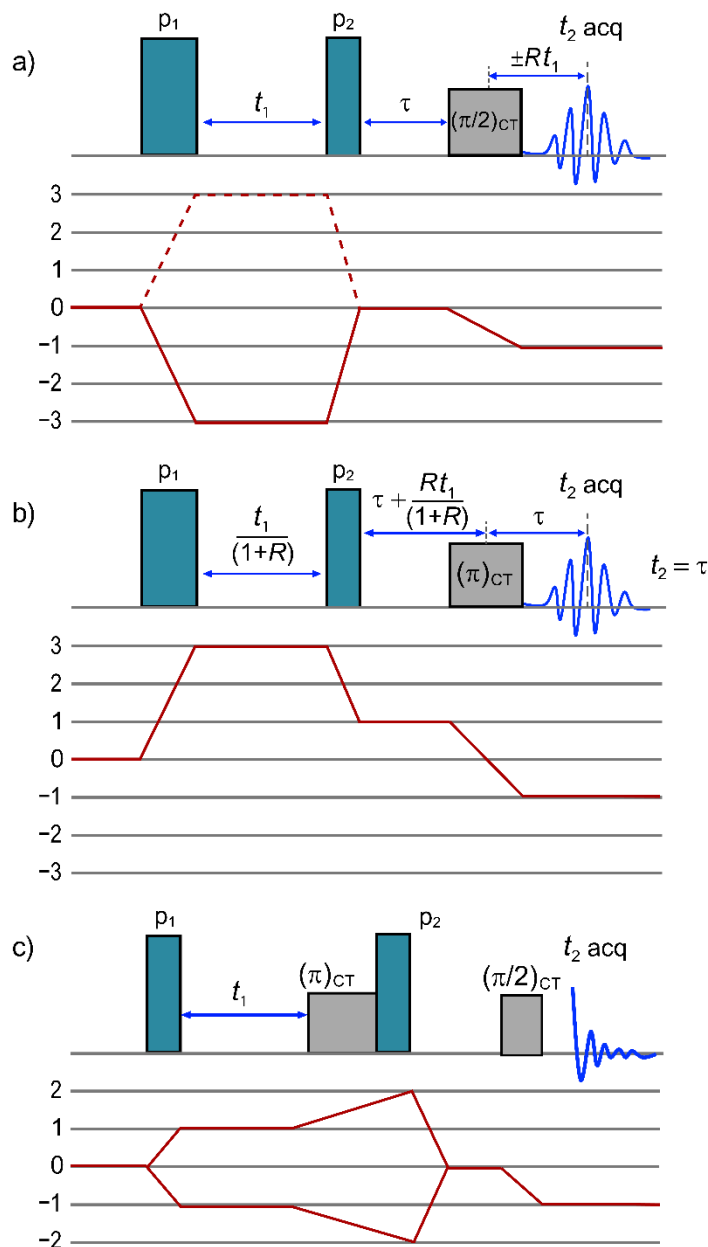


**Figure 6.** Pulse sequences and coherence pathways for (a) the z-filter and (b) the split- $t_1$  shifted-echo 3QMAS experiments (the coherence pathway is given for the z-filter approach on a spin  $I = 3/2$ , depicted at the top, with echo and antiecho pathway signals represented by solid and dashed lines, respectively) and (c) DQF-STMAS z-filter experiment.

The most commonly used MQMAS sequences are composed of three-pulses: z-filter and split- $t_1$ . The pulse sequence and coherence pathways of these two schemes are shown in Figure 6. The z-filter approach proposed by Amoureux *et al*<sup>137</sup> is robust and easy to optimize. It involves two hard pulses (excitation and conversion) followed by a short z-filter delay to store the magnetization along the z-axis as 0Q, after which the magnetization is transferred into observable 1Q coherences by a soft  $\pi/2$  (selective) pulse that only excites the CT. The purpose of the last pulse is to symmetrize the echo and antiecho coherence pathways (Figure 6a). As it acquires both signals with the same intensity, the z-filter method produces a 2D pure-absorption lineshape.<sup>98</sup> Experimentally, the rf field strength of the hard-pulses must be set to the highest power level that is compatible with the rf power specification of the probehead. Usually, a z-filter delay of 10-20  $\mu\text{s}$  and an rf-field  $\nu_1 = 10\text{-}20$  kHz for the last soft-pulse, are employed.<sup>117</sup>

The split- $t_1$  approach was introduced as an alternative to the z-filter method.<sup>138</sup> In this method,  $t_1$  is split into MQ and SQ evolution periods for time fractions of  $t_1/(1 + R)$  and  $Rt_1/(1 + R)$ , respectively (Figure 6b), where  $R$  is a factor that takes values for 3Q excitation of  $+7/9$  and  $12/19$  for  $I = 3/2$  and  $5/2$ , respectively.<sup>121</sup> This factor avoids the need for the shearing transformation after the acquisition. As a result, the second order anisotropic broadening is refocused at the end of the  $t_1$  period, and the echo will appear at the same  $t_2$  time for all  $t_1$  periods.<sup>117</sup> The split- $t_1$  experiment gives a higher signal-to-noise ratio (S/N) than the z-filter approach. Its sensitivity is usually  $\sqrt{2}$  higher than the z-filter experiment because a full echo is acquired.<sup>110</sup> This experiment does not require a shearing transformation.

One of the most relevant benefits of MQMAS, is that it provides a direct separation of the contributions from the chemical shift and quadrupolar coupling. After shearing transformation (for the z-filter MQMAS) and scaling of the MQMAS spectrum; information about the isotropic chemical and quadrupolar-induced shifts (CS and QIS) are obtained by analyzing the 2D spectrum. Indeed, the analysis and interpretation of the MQMAS spectra is facilitated by introducing three axes: CS, QIS and anisotropic (A) axes. In the obtained spectrum, the resonances with zero quadrupolar coupling are sharp and appear along the CS axis. On the other hand, resonances with significant

quadrupole coupling experience a shift of the centre of gravity away from the CS axis in the direction of the QIS axis, due to the quadrupole second-order shift. The A axis, defined by the orientation of anisotropic ridges in the MQMAS spectrum, appears parallel to the direct F2 axis. The slopes of the CS and QIS axes are determined based on the general convention for scaling the isotropic dimension after shearing.<sup>139</sup> The slopes of CS and QIS axes proposed by Amoureux *et al.*<sup>98</sup> are 1 and  $-10/17$ , respectively.

Although the MQMAS is a widely used and robust method, its intrinsically poor sensitivity is a limiting factor for many practical applications. This is due to the inefficient excitation of MQ coherences and the subsequent conversion of these MQ coherences to SQ, since MQ transitions are prohibited for the quantum mechanics rules.<sup>123,140</sup> In addition, the efficiency of MQMAS is highly dependent on the  $C_Q$  value of the crystallographic sites and the rf field. Several methods have been proposed to improve the generation and/or conversion of MQ coherences.<sup>135,141</sup> In particular, the conversion process remained as the central target.<sup>140</sup> Figure 7 summarizes some of the excitation/conversion schemes that can be used for this purpose.

The conversion of triple-to single-quantum coherences can be carried out by using different type of pulses such as hard pulses (HP),<sup>121</sup> double frequency sweeps (DFS),<sup>142,143</sup> hyperbolic secant pulses (HS),<sup>144</sup> rotor assisted population transfer (RAPT)<sup>145,146</sup> and soft-pulses added mixing (SPAM).<sup>141,147</sup> HP and rotation-induced adiabatic coherence transfer (RIACT) for  $I = 3/2$  have been employed for the excitation of MQ coherences.<sup>148</sup> More recently, fast-amplitude modulation pulse trains (FAM-N) scheme developed by Colaux *et al.*, has been proposed for the efficient 1Q-CT  $\leftrightarrow$  3Q transfers.<sup>136</sup>

Very recently, two new types of excitation/conversion pulses have been introduced by Hung and Gan, to transfer the coherences and excite all crystallites simultaneously.<sup>149</sup> They are based on two identical long-pulses with inverse changes of coherence order and require moderate rf-field power. The version with two-long square pulses applied for MQMAS has been named as LP-MQMAS, whereas its improved version (called Cos-LP-MQMAS) uses a cosine double irradiation pulse that

last  $1T_R$  to cancel all anisotropic dephasings that may occur during the  $1Q-CT \leftrightarrow 3Q$  transfers. However, this last method is mainly efficient for  $I = 3/2$ . A representation of these types of pulses can be also observed in Figure 7.

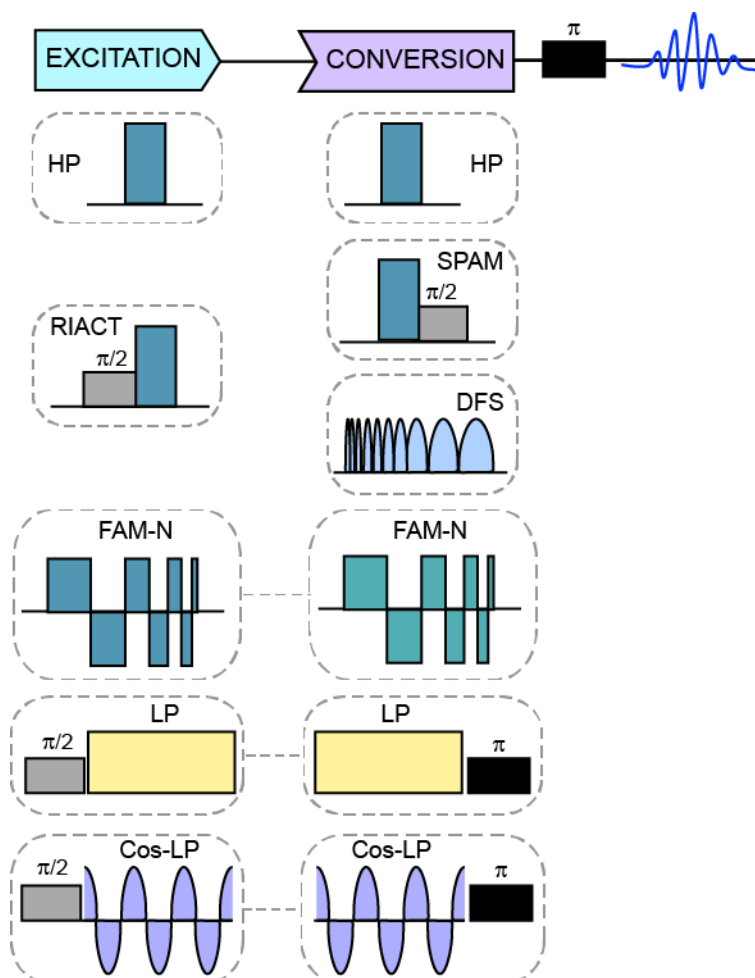


**Figure 7.** Different types of schemes that can be used for the excitation and conversion for the MQMAS experiment: hard pulses (HP), rotation-induced adiabatic coherence transfer (RIACT), soft-pulses added mixing (SPAM), double frequency sweeps (DFS), fast-amplitude modulation pulse trains (FAM-N), long pulses (LP) and cosine long pulses (Cos-LP).

Further methodological developments involving MQMAS include its combination with polarization transfer between the quadrupolar isotope and neighbouring spins  $I = 1/2$ .<sup>110</sup> It is possible to combine CP with MQMAS for either spectral editing of the MQMAS spectra or to acquire heteronuclear correlation 2D spectra endowed with high resolution. The MQMAS scheme can be inserted before or after the CP transfer.<sup>98</sup> However, polarization transfers with CP are difficult to optimize due to the complex

spin dynamics of quadrupolar nuclei during spin lock. The heteronuclear correlation with MQ-HETCOR provides high-resolution in the indirect F1 dimension and has been utilized in many applications.<sup>98,150</sup> For example, 3Q-HETCOR experiment with SPAM conversion was used to correlate  $^{27}\text{Al}$ - $^{31}\text{P}$  nuclei on  $\text{AlPO}_4\text{-14}$ , showing its utility in the structural study of these microporous materials.<sup>151</sup> Alternatively the CP transfer can be replaced by REDOR scheme for spectral editing as well as dipolar-mediated refocused INEPT to acquire high-resolution HETCOR 2D spectra.<sup>98,152</sup> In particular, REDOR-MQMAS allows for measurement of the dipolar interactions and internuclear distances between pairs of spin-1/2 and quadrupolar nuclei with high-resolution for the latter isotope.<sup>153</sup>

### 1.4.2 STMAS

The STMAS experiment is an alternative method to MQMAS to obtain high resolution spectra of half integer quadrupolar nuclei.<sup>133</sup> This 2D technique correlates the 1Q-ST and 1Q-CT coherences, which increases the sensitivity significantly. This correlation generates isotropic spectra, in a similar way than MQMAS, but with higher efficiency since the coherence transfer occurs between 1Q coherences.<sup>134</sup> However, the STs are affected by the first- and second-order quadrupolar interactions, making the experiment difficult to carry out. To overcome this, STMAS experiment requires extremely precise magic angle adjustment (with better than  $\pm 0.002^\circ$  accuracy), stable rotation rate and that the applied pulses are timed accurately. These experimental settings have greatly increased the difficulty of its implementation and thus, limited its use.<sup>134</sup>

The most frequently used sequences of the STMAS experiment are composed of three pulses: two hard pulses (the first one for the creation of inner STs and the second for transferring the coherences to the CT) and one soft pulse. The correlation of the dephasing occurring on the STs in  $t_1$  and the CT during  $t_2$ , is achieved because the refocusing of the second-order quadrupole frequencies are equal for two symmetrical STs, therefore, producing isotropic peaks.<sup>110,154</sup> The appearance of the resulting STMAS spectrum is very similar to that of a MQMAS spectrum.<sup>155</sup> However, due to the difficult experimental setting mentioned above, this method does not belong to the routine NMR experiments.



Another difficulty of the STMAS approach is the presence of large diagonal peaks in the 2D spectra, which arise from unwanted autocorrelation signals of the CT evolution during  $t_1$  and  $t_2$  periods, and in a minor extent from the STs, which cannot be cancelled out by phase cycling.<sup>156,157</sup> The DQF-STMAS z-filter experiment introduced by Kwak and Gan addresses this problem.<sup>158</sup> In this pulse sequence (Figure 6c), a CT selective  $\pi$  pulse is introduced at the end of  $t_1$  delay and right before the 1Q conversion in order to produce and select the 2Q coherences. This DQF allows filtering out the unwanted CT-CT and ST-CT transitions are filtered out with a suitable phase cycling scheme. This double-quantum excitation is performed with almost no sensitivity loss.<sup>157</sup> Furthermore, many of the techniques designed to improve the sensitivity of MQMAS can also be employed for STMAS. For example, SPAM has been successfully applied with DQF-STMAS by Sasaki *et al.*<sup>147</sup> More recently, with the advent of LP, a new type of STMAS has been introduced (LP-STMAS), which, like LP-MQMAS, requires less rf-field to be implemented.<sup>159</sup>

## 1.5 METHODS TO ENHANCE THE SENSITIVITY FOR QUADRUPOLEAR NUCLEI

### 1.5.1 High-fields

High magnetic fields are valuable for solid-state NMR of quadrupolar nuclei. They improve the spectral resolution by reducing the second-order quadrupolar broadening ( $\propto B_0^{-1}$ ), that remains under MAS.<sup>113,160</sup> Another advantage of high fields is to improve the sensitivity of quadrupolar nuclei which is proportional to  $B_0^{11/4}$ .<sup>161</sup> Since the chemical shifts scale linearly with  $B_0$ , high magnetic fields provide a direct means to determine chemical shifts experimentally, and detect and evaluate the CSA with accuracy.<sup>97,162</sup>

The availability of high field NMR spectrometers ( $B_0 > 18.8$  T) is particularly useful for studying quadrupolar nuclei with lineshapes that are dominated by significant second-order quadrupole broadening.<sup>97</sup> More recently, the advent of ultra-high magnetic field of up to 35.2 T ( $^1\text{H}$  Larmor frequency of 1.5 GHz) with dramatically improved sensitivity and resolution,<sup>160</sup> opened a new stage for the study

of quadrupolar nuclei and make possible the observation of difficult low- $\gamma$  and/or low-abundance nuclei including  $^{95}\text{Mg}$ ,  $^{17}\text{O}$  and  $^{67}\text{Zn}$ .<sup>161,163,164</sup>

### 1.5.2 Population transfer

Another way to improve the sensitivity of quadrupolar nuclei involves population transfer methods. They are used to enhance the CT of a quadrupolar nucleus by perturbing the populations of the outer satellite transitions.<sup>165</sup> Generally, there are two mechanisms to describe this process: ST saturation and ST inversion. The ST saturation can be accomplished by equalizing the population of energy levels related to STs. The enhancements of the CT ( $I + 1/2$ ) that can be achieved are 2, 3, 4 and 5 for nuclei with spins of  $3/2$ ,  $5/2$ ,  $7/2$  and  $9/2$  respectively.<sup>166</sup> On the other hand, the magnetization of the ST can be also transferred to the CT by a series of ST inversions. Considering that all the outer STs are inverted before that the inner ones, this can lead to enhancements ( $2I$ ) equal to 3, 5, 7 and 9 for spins  $3/2$ ,  $5/2$ ,  $7/2$  and  $9/2$  respectively.<sup>166</sup> Different populations transfer methods for the saturation and inversion of spin populations have been suggested. They involve DFS (double frequency sweeps), RAPT (rotor-assisted population transfer) and HS (adiabatic inversion with hyperbolic secant pulses).<sup>166–168</sup>

#### DFS

DFS allows for signal enhancement by adiabatically inverting the STs so that the population of the outer spin levels are transferred to the CT energy levels before they are selectively excited.<sup>142,169</sup> The inversion of population between two energy levels can be accomplished by sweeping a continuous rf-field through the entire spectrum while keeping the amplitude of the pulse constant.<sup>168</sup> These pulses irradiate simultaneously the high- and low-frequency sides of the CT using waveform generators.<sup>168</sup> DFS schemes with a large sweep range gives the best signal enhancement for NMR spectra of stationary powdered samples.<sup>169</sup>

## **RAPT**

RAPT is a method to enhance the CT sensitivity by a selective saturation of the STs. It consists of pulse train with constant amplitude and alternating phase.<sup>170</sup> Unlike DFS that uses a frequency sweep, RAPT uses only a constant frequency offset. The advantage of RAPT over other methods is that can be applied to polycrystalline samples during MAS, thus allowing to obtain simultaneously CT enhancement for all crystalline orientations.<sup>171</sup>

## **HS**

Shaped adiabatic pulses are also used to invert the populations associated with the STs. For the hyperbolic secant pulse, the adiabatic pulses are created with both amplitude and phase modulation.<sup>172,173</sup> The pulse is smoothly turned on and off as the amplitude is modulated by a hyperbolic secant function, whereas the phase is modulated to induce a sweep with a hyperbolic tangent profile. Under MAS conditions, HS yields an enhancement of the CT that exceeds that obtained by DFS or RAPT.<sup>166,168</sup>

### **1.5.3 QCPMG**

The quadrupolar Carr–Purcell–Meiboom–Gill (QCPMG) method,<sup>95</sup> adapted from the CPMG sequence, is commonly used in solid-state NMR to enhance the sensitivity of half-integer quadrupolar nuclei.<sup>174</sup> The sensitivity enhancement is achieved by applying a train of CT selective  $\pi$  pulses that refocus the signal during acquisition, thus, allowing the spin-echo to be recorded several times in the full timescale of the transverse relaxation/dephasing.<sup>175</sup> After a Fourier transformation of the echo train, a spectrum is obtained consisting of narrow peaks, often called spikelets, whose manifold reproduces that of the conventional powder spectrum.<sup>174</sup>

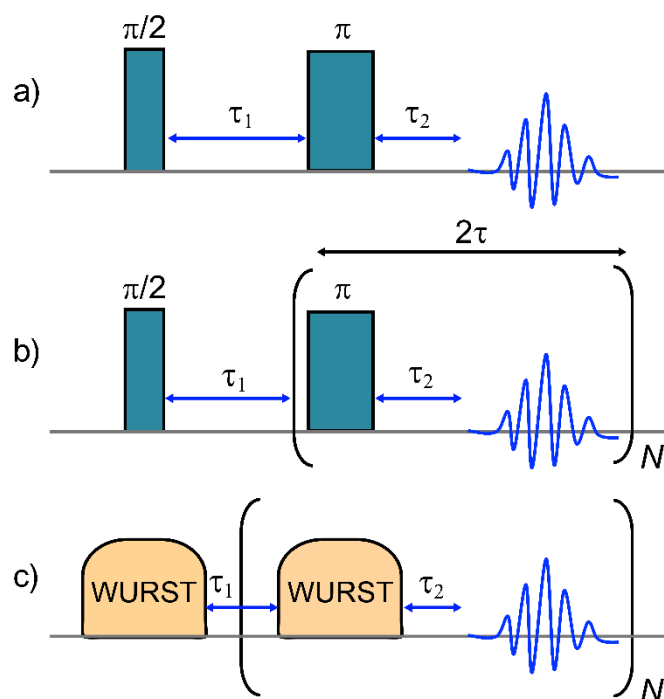


**Figure 8.** Pulse sequences of (a) Quadrupolar echo, (b) QCPMG and (c) WURST-QCPMG.

The origin of the sensitivity improvement from QCPMG compared to a conventional echo experiment (Figure 8a), comes from the acquisition of multiple echoes in every FID.<sup>166</sup> The QCPMG pulse sequence, presented in Figure 8b, is composed of two parts: a  $\pi/2$  pulse that is used for excitation and  $N$  successive  $\pi$  pulses, separated by  $2\tau$ , for refocusing. A train of echoes is collected in the time domain, which after a Fourier transformation results in a spectrum with narrow spikelets. The envelope of spikelets contains information on the inhomogeneous interactions, such as CSA, quadrupolar coupling, heteronuclear dipolar coupling, whereas each individual spikelet contains information regarding the homogeneous interactions, such as the homonuclear dipolar coupling and dynamics.<sup>166</sup> The resolution of the QCPMG spectrum is determined by the spikelet's spacing in the frequency domain  $(2\tau)^{-1}$  and their width, which is related to  $T_2'$ .<sup>176</sup>

The QCPMG approach is effective if the spin-spin relaxation time (i.e. the decay of the echo envelope  $T_2'$ ) is longer than the magnetization decay caused by local interactions.<sup>176</sup> Therefore, the maximum possible enhancement will depend on the value of  $T_2'$  of the sample, which determines how many echoes can be recorded in

each scan. The gain in S/N achieved with QCPMG, compared to a regular echo experiment, is determined by  $G_{S/N} = 2\sqrt{T_2'T_{\text{off}}}(2\tau)^{-1}$ , where  $T_2'$  is the effective spin-spin relaxation time and  $T_{\text{off}}$  is the time for the FID of the individual echo to become comparable with the noise level of a standard echo experiment.<sup>167</sup>

A modified version of the QCPMG sequence was developed by O'Dell and Schurko.<sup>177</sup> This sequence is similar to the standard QCPMG scheme but employs frequency sweep WURST (wideband uniform rate smooth truncated) pulses instead of rectangular pulses (Figure 8c). The frequency sweep of the WURST pulses is achieved by simultaneous modulation of the amplitude and phase of the pulses. The WURST-QCPMG sequence is useful for the acquisition of wide-line solid-state NMR spectra due to the high excitation bandwidths which affords a large reduction in the number of sub-spectra that must be acquired.<sup>178</sup>

#### 1.5.4 Dynamic Nuclear Polarization (DNP)

As shown in previous sections, solid-state NMR is a powerful tool for studying the surface of inorganic materials. It provides a unique insight into the atomic-level structure and dynamics of surface species, which is essential for establishing structure-activity relationships.<sup>179</sup> However, the inherent low sensitivity of solid-state NMR often prevents its application for the characterization of inorganic solids and the observation of their surfaces. NMR sensitivity is, thus, one of the main limitations for further developments in surface chemistry.<sup>180</sup> Such low sensitivity arises from the small magnetic moments of nuclear spins that yields small Boltzmann polarization, and slow longitudinal relaxation ( $T_1$ ), which ultimately results in weak NMR signals.<sup>181,182</sup>

Dynamic Nuclear Polarization (DNP) has emerged in the recent years as a technique to enhance the sensitivity of solid-state NMR experiments by 1-3 orders of magnitude.<sup>182</sup> DNP enhances the NMR signal by transferring the polarization from unpaired electrons to nearby NMR-active nuclei *via* microwave ( $\mu\text{w}$ ) irradiation, which is used to saturate the electron spins. To achieve this, DNP takes advantage of the large magnetic moments of electrons ( $\gamma_e$ ) and thus, a theoretical signal

enhancement of  $\sim 660$  ( $\gamma_e/\gamma_H$ ) is predicted for protons.<sup>181</sup> To perform a DNP experiment, an exogenous radical polarising agent (PA) is dispersed into the system of interest. This PA provides the unpaired electrons that are the source of the spin polarization. The choice of the PA highly depends on the magnetic field used for the experiment and the nucleus that will be polarized,  $^1\text{H}$  or a low- $\gamma$  nucleus.<sup>183</sup>

DNP experiments are typically performed at cryogenic sample temperatures of ca. 100 K and high-power gyrotron microwave sources ( $>10$  W) are required to successfully saturate the electron paramagnetic resonance (EPR) transitions of the PA.<sup>181</sup> The low temperatures increase electron and nuclear relaxation times, allowing for a higher accumulation of nuclear spin polarization and facilitate a more complete saturation of the electron spins.<sup>182</sup> In addition, a Boltzmann related signal enhancement is also obtained due to the cryogenic temperatures employed. The sensitivity of the DNP experiment is usually expressed in terms of DNP enhancement,  $\epsilon_{on/off}$ , and is determined by measuring the gain in signal intensity with and without microwave irradiation.<sup>182</sup>

### **Instrumentation**

The unique experimental conditions of DNP (cryogenic temperatures, high-power, high-frequency  $\mu\text{w}$  irradiation) require the implementation of specialized hardware.<sup>184</sup> In recent years, DNP has made important advances, and although the technique was initially developed for low magnetic fields, the scope has been extended to instruments operating at fields of 14.1 and 21.1 T.<sup>184</sup> The DNP NMR system consists of several components and it can be considered as an extension of the solid-state NMR spectrometer. A schematic drawing of typical DNP MAS spectrometer is presented in Figure 9. The principal components of the DNP NMR system are: gyrotron, transmission line and the NMR magnet.

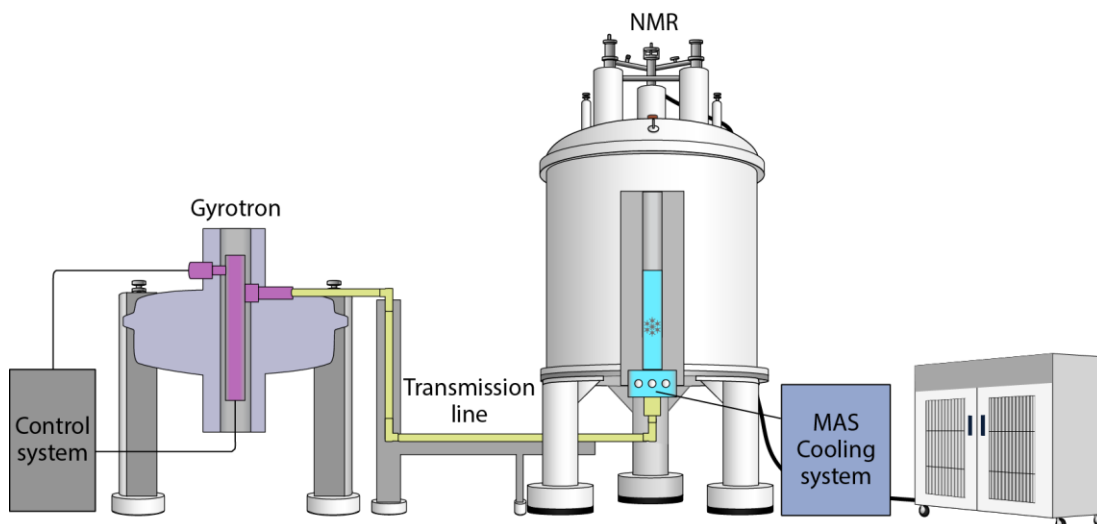


**Figure 9.** High-field DNP-NMR system with gyrotron microwave source (gyrotron tube indicated in purple), microwave transmission line (yellow) and low-temperature NMR probe (light blue).

The gyrotron is the instrument that generates high-power microwaves that are required for the polarization transfer from unpaired electrons to NMR-active nuclei. It consists of a gyrotron tube that is sealed inside a strong magnetic field and operates by transferring energy from an electron beam to an electric wave.<sup>184,185</sup> Gyrotrons can provide reliable continuous  $\mu\text{w}$  irradiation frequencies of up to 1 THz and deliver continuous  $\mu\text{w}$  power in the order of 10 W and above.<sup>56</sup> Such high-power conditions are necessary for MAS DNP as the size of the sample (in the order of a few millimetres) is comparable to the wavelength of the  $\mu\text{w}$ , therefore, excluding the use of DNP NMR probes with  $\mu\text{w}$  resonant structures.<sup>181</sup>

The  $\mu\text{w}$  transmission line, also called waveguide, consists of a series of interconnected aluminium tubes. Its purpose is to transfer the  $\mu\text{w}$  beam delivered by the gyrotron to the sample situated inside the NMR probe. At the end of the waveguide, the  $\mu\text{w}$  are diffracted and reflected by the RF coil, which have a pitch that is comparable to the wavelength of the  $\mu\text{w}$ . Due to the reflection of the  $\mu\text{w}$ , the distribution of the  $\mu\text{w}$  field within the sample is non-uniform, and hence, resulting in an inhomogeneous distribution of the DNP enhancement, with higher gains in the centre of the rotor. Furthermore, transparent sapphire rotors are preferred for DNP

MAS experiments because of their higher thermal conductivity and their  $\mu\text{w}$  transparency.<sup>181,185</sup>

In addition to the typical capabilities of regular solid-state NMR probes and  $\mu\text{w}$  transmission, DNP MAS probes are designed to operate at low temperature (LT) and provide stable MAS in this condition.<sup>56,184</sup> Besides cold bearing and drive gas, an additional cooling gas is used. This gas passes through a heat exchanger and is transported to the MAS stator *via* thermally isolated transfer lines. The LT MAS DNP probe is placed within an NMR magnet. The NMR magnets used for MAS DNP are similar to conventional wide-bore solid-state magnets. However, they are equipped with an additional sweep coil, that is used to adjust the static magnetic field in order to fulfill the DNP matching conditions for maximal DNP enhancements.<sup>181</sup>

### **Direct and Indirect DNP**

In general terms, DNP experiments can be carried out in two ways: *indirect* and *direct*. In an *indirect* DNP experiment, the  $^1\text{H}$  nuclei that are nearby the PA are first polarized, and the  $^1\text{H}$  spin diffusion mechanism distributes the magnetization through the sample.<sup>182</sup> Consequently, the enhanced polarization can be transferred to less receptive nuclei by using solid-state NMR methods like CP, or more recently introduced PRESTO and R-INEPT methods.<sup>186</sup> In a *direct* DNP method, the PA polarize directly the observed (low- $\gamma$ ) nuclei, and then, followed by homonuclear spin diffusion, the polarization is distributed to more remote nuclei (Figure 10). In these experiments, the NMR signal is measured by direct excitation experiment.<sup>187</sup> *Indirect* DNP is more commonly used than *direct* DNP. This is mainly due to the long build-up curves observed in *direct* DNP experiments because spin diffusion mechanism between low- $\gamma$  nuclei is not as efficient as that of  $^1\text{H}$ .<sup>182</sup> However, *direct* and *indirect* experiments have been proven to be complementary in surface science. *Indirect* DNP has shown to be selective to the first atomic layer whereas *direct* DNP probes the layers of the sub-surface.<sup>179</sup>



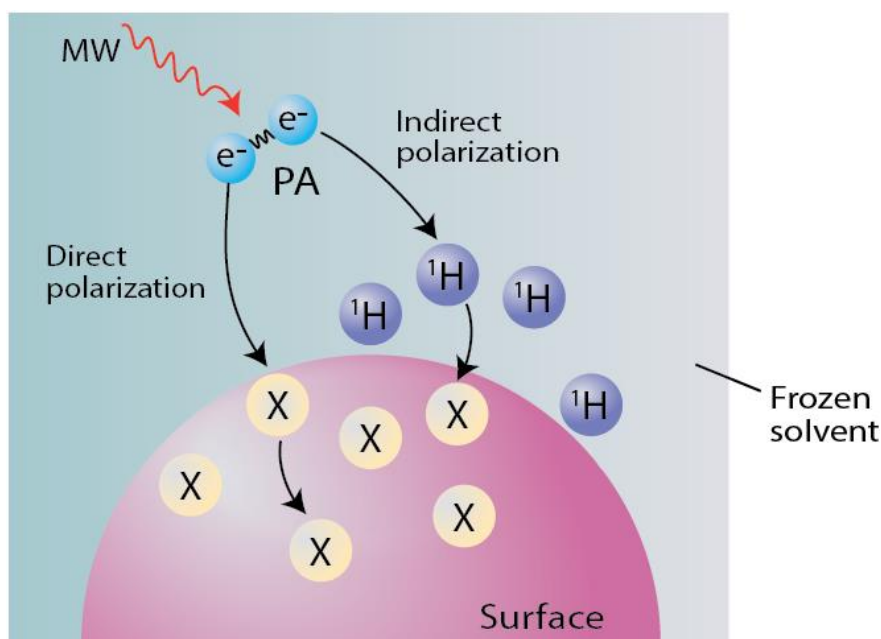


**Figure 10.** Schematic representation of indirect and direct DNP experiments. After microwave irradiation, polarization from electrons can be transferred directly to nuclei of the investigated materials (*direct* DNP) or indirectly, by transferring the polarization first to  $^1\text{H}$  and then to the detected nuclei by CP or other methods (*indirect* DNP).

### DNP SENS

Recent advances in instrumentation and the development of optimal radicals made it possible to apply DNP-enhanced solid-state NMR for the characterization of surfaces. Lesage *et al.* demonstrated for the first time in 2010, the successful application of DNP to enhance the surface signals of molecules immobilized on silica at 9.4 T.<sup>180</sup> This effect led to the development of ‘dynamic nuclear polarization surface-enhanced nuclear spectroscopy’ (DNP SENS).<sup>180</sup> The high sensitivity gains provided by DNP enable to selectively enhance the NMR signals from surfaces through a combination of incipient wetness impregnation and cross polarization methods (Figure 10).<sup>188</sup> DNP SENS has been shown to increase the signal intensity of conventional solid-state NMR spectra by one to three orders of magnitude at high-field and has been successfully applied to probe surfaces of a variety of materials.<sup>55,189,190</sup> DNP SENS has notably been applied to enhance the sensitivity of half-integer quadrupolar nuclei, such as  $^{27}\text{Al}$ <sup>191</sup> and  $^{17}\text{O}$ <sup>106,192</sup>. Very recently, DNP SENS approach has been successfully applied to enhance the NMR signal of low- $\gamma$  nuclei, such as

<sup>47,49</sup>Ti, <sup>95</sup>Mo and <sup>67</sup>Zn at the surfaces of MoO<sub>3</sub>/TiO<sub>2</sub> and Al-doped ZnO nanoparticles.<sup>193</sup>

### Sample formulation

Sample formulation is an essential step to ensure the success of a DNP SENS experiment. Incipient wetness impregnation (IWI) is often used to coat the surface of materials with PA solution.<sup>194</sup> This method requires the addition of stable radicals as source of unpaired electrons, usually nitroxide biradicals, such as AMUPol and TEKPol, which are dissolved in aqueous media (e.g. glycerol-d<sub>8</sub>/D<sub>2</sub>O/H<sub>2</sub>O 60/30/10 v:v:v, also called DNP-juice) or in organic solvents (e.g. 1,1,2,2-tetrachloroethane shorten as TCE), respectively. Impregnation process brings the PA molecules into close proximity with the NMR-active nuclei on the surface, thus, allowing them to be polarized faster by DNP than the bulk.<sup>108,182</sup> As DNP experiments are usually done at cryogenic temperatures, the polarizing matrix freezes to form a glassy solution. This frozen solution plays an important role in providing a rigid protonated matrix that diffuses hyperpolarization through the sample, which is advantageous for *indirect* DNP.<sup>182</sup> However, the frozen solvent dilutes the investigated material thus, reducing the effective amount of sample in the rotor. To circumvent this issue, DNP SENS experiments are often performed with a minimized amount of the frozen solvent.<sup>108</sup> Furthermore, in some cases, the radical solution can also modify the structure and dynamics of the surface.

The concentration of PA also influences the DNP sensitivity. For higher concentrations of PA, each unpaired electron polarizes fewer nuclei, and the build-up of the DNP-enhanced nuclear polarization occurs more rapidly, which tends to increase the sensitivity.<sup>56,181</sup> Nevertheless, high concentrations of PA can induce paramagnetic quenching of surface NMR signals and hence, decreases the absolute NMR sensitivity. In DNP SENS experiments, low concentrations of PA are preferred, especially for long polarization transfers.<sup>181</sup> Nevertheless, PAs can be physisorbed onto surfaces, thus, the concentration of the PA must be optimized in function of the specific surface area of the samples.<sup>189</sup> Typically, concentrations of 16 mM for TEKPol in TCE and 10 mM for AMUPol in DNP juice, have been found to be optimal for the impregnation of high-surface area porous materials.<sup>189</sup>

## Cross effect mechanism

DNP can occur in solid-state NMR through several mechanisms. The three most important mechanisms for MAS DNP transfers at  $B_0 \geq 5$  T are the solid effect (SE), Overhauser effect (OE) and cross effect (CE).<sup>160</sup> The SE and OE are the main mechanisms involved for DNP MAS using radicals with narrow EPR lines, for example trityl- and BDPA-type radicals. Conversely, polarization transfers with radicals with broad EPR line widths, which are the most commonly used radicals (e.g. nitroxide-based radicals), can be explained by the CE.<sup>108,195</sup>

The CE mechanism has been proven to be the most efficient one at high magnetic fields. It involves two unpaired electrons ( $S_a$  and  $S_b$ ), which are coupled by  $J$ -exchange or dipolar interactions, and one nucleus, typically  $^1\text{H}$ . The polarization transfer is achieved if the EPR frequency difference between the two electrons matches the Larmor frequency of the polarized nucleus, typically protons:  $|\omega_{ea} - \omega_{eb}| = \omega_{1H}$ .<sup>108</sup> The difference in polarization between the unpaired electrons can be generally enhanced by increasing the  $\mu\text{w}$  power.<sup>181</sup> High-energy and high-frequency  $\mu\text{w}$  generated by gyrotrons are used to saturate one of the EPR transitions, and consequently drive the polarization transfer from electron to the  $^1\text{H}$  through the three-spin “flip-flop-flip” process.<sup>56,195,196</sup> However, high-energy  $\mu\text{w}$  can cause sample heating and solvent melting, hence reducing the DNP enhancement.<sup>56</sup> The optimal  $\mu\text{w}$  power is thus optimized depending on the sample. In addition, cryogenic temperatures (c.a. 100 K) are required to slow down the electron spin relaxation rates and ensure efficient DNP polarization transfer.<sup>108,183</sup>

## Polarizing agents

Since CE requires two unpaired electrons dipolar coupled, most of high field DNP experiments have been carried out using exogeneous nitroxide-based biradicals.<sup>188</sup> The covalent link between the two nitroxide radicals in these molecules, results in an intramolecular dipolar coupling.<sup>181,197</sup> Generally, PAs with broad and anisotropic EPR spectra favour the CE mechanism since sufficient inter- or intramolecular electron-electron (e-e) dipolar coupling are present.<sup>56</sup> Nitroxide biradicals, such as TOTAPOL, AMUPol and TEKPol, have been proven to be efficient CE polarizing agents.<sup>181,197</sup> The efficiency of the PAs depends on various parameters as the solubility,

concentration and electron spin properties at operational temperatures.<sup>56</sup> Optimal DNP enhancements have been achieved with low concentration of biradicals thus reducing the paramagnetic quenching and the losses during the NMR sequence.<sup>181</sup>

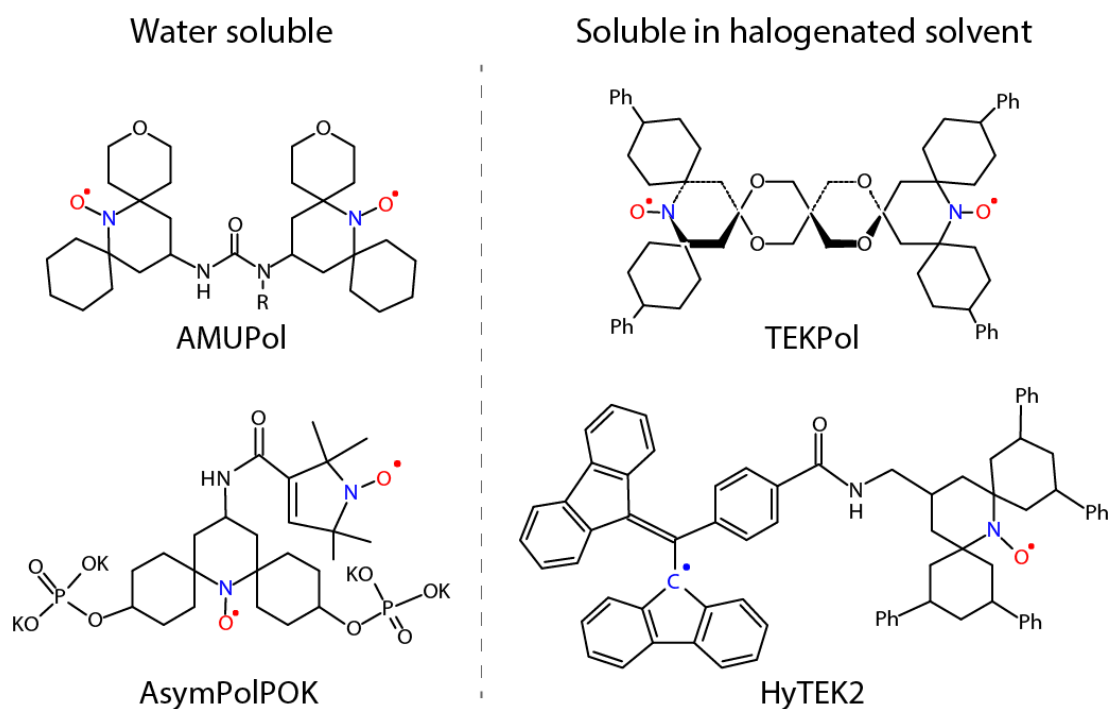


**Figure 11.** Structures of some of the organic radicals used as PA for high-field MAS DNP.

Generally, PAs are evaluated based on several factors, such as the homogeneous linewidth and inhomogeneous breadth of the EPR spectrum, its  $g$ -factor anisotropy, and the nuclear Larmor frequency.<sup>108,181</sup> The  $g$  anisotropy is the major cause of broadening at high magnetic fields. The structures of bi-nitroxides have been improved over the recent years by adjusting the length and rigidity of the organic tether, in order to optimize the e-e coupling and the relative orientation of their  $g$ -tensors. Other efforts have been made to change the functional groups to modulate the electron relaxation times and improve the solubility.<sup>198</sup> This has led to efficient polarizing agents as those presented in Figure 11. However, the performance of these radicals decreases significantly when increasing  $B_0$ . This is attributed to the fact that the efficiency of the CE scales with the inverse of the magnetic field strength.<sup>199</sup> Very recently, HyTEK2 radical has demonstrated high DNP efficiency and outstanding performance at both

18.8 and 21.1 T, compared to its widely used counterparts AMUPol and TEKPol.<sup>198,200</sup> The development and design of new PAs for efficient DNP transfer under MAS and high magnetic field are still active areas of research.<sup>56,201</sup>

## 1.6 OUTLINE OF THE THESIS

In chapter 1, we reviewed theory and methods which are helpful to understand the presented methodological achievements presented in Chapter 2 and 3 of this thesis.

Chapter 2 introduces new robust symmetry-based heteronuclear dipolar recoupling built from composite inversion pulses for PRESTO and *D*-RINEPT methods to transfer the polarization of protons to quadrupolar nuclei at MAS frequencies of 20 and 62.5 kHz.

Chapter 3 compare various symmetry-based homonuclear dipolar recouplings for DQ-SQ and SQ-SQ HOMCOR experiments between quadrupolar nuclei with spin  $I = 3/2$  and  $5/2$  at 20 kHz.

Chapter 4 presents new insights into the surface of boron nitride and oxide supported on dendritic fibrous nanosilica, DFNS/BN and DFNS/B<sub>2</sub>O<sub>3</sub>, through a combination of 1D and 2D multinuclear (<sup>1</sup>H, <sup>29</sup>Si and <sup>11</sup>B) solid-state NMR experiments.

The conclusions and perspectives finalize this document. The appendices further include SIMPSON input files (Appendix A), relevant pulse programs (Appendix B) and an AU program used for the shearing process for a 2D spectrum acquired with NUS (Appendix C).

## References

- (1) Somorjai, G. A.; Li, Y. Impact of Surface Chemistry. *Proc. Natl. Acad. Sci.* **2011**, *108* (3), 917–924. <https://doi.org/10.1073/pnas.1006669107>.
- (2) Tirrell, M.; Kokkoli, E.; Biesalski, M. The Role of Surface Science in Bioengineered Materials. *Surf. Sci.* **2002**, *500* (1–3), 61–83. [https://doi.org/10.1016/S0039-6028\(01\)01548-5](https://doi.org/10.1016/S0039-6028(01)01548-5).
- (3) Oetelaar, L. L. V. D. Surface and Interface Phenomena in Heterogeneous Metal Catalysis. **1997**. <https://doi.org/10.6100/IR475617>.
- (4) Delhaes, P. Surface and Interface Phenomena. In *Carbon-based Solids and Materials*; John Wiley & Sons, Inc.: Hoboken, NJ, USA, **2013**; pp 409–459. <https://doi.org/10.1002/9781118557617.ch11>.
- (5) Kolasinski, K. W. Introduction. In *Surface Science: Foundations of Catalysis and Nanoscience*; John Wiley & Sons, Ltd: Chichester, UK, **2012**; pp 1–8. <https://doi.org/10.1002/9781119941798.ch>.
- (6) Yates, J. T.; Campbell, C. T. Key to Control and Advance Myriad Technologies. *Proc. Natl. Acad. Sci.* **2011**, *108* (3), 911–916. <https://doi.org/10.1073/pnas.1006671107>.
- (7) Marchetti, A.; Chen, J.; Pang, Z.; Li, S.; Ling, D.; Deng, F.; Kong, X. Understanding Surface and Interfacial Chemistry in Functional Nanomaterials via Solid-State NMR. *Adv. Mater.* **2017**, *29* (14), 1605895. <https://doi.org/10.1002/adma.201605895>.
- (8) Baer, D. R. Introduction to Special Issue on Advances and Applications of Surface Analysis Methods. *Microsc. Today* **2016**, *24* (2), 12–15. <https://doi.org/10.1017/S1551929515001340>.
- (9) Li, J.; Holmberg, K. Surface Chemistry and Interface Science. *Phys. Chem. Chem. Phys.* **2017**, *19* (35), 23568–23569. <https://doi.org/10.1039/C7CP90152F>.
- (10) Biener, J.; Wittstock, A.; Baumann, T.; Weissmüller, J.; Bäumer, M.; Hamza, A. Surface Chemistry in Nanoscale Materials. *Materials* **2009**, *2* (4), 2404–2428. <https://doi.org/10.3390/ma2042404>.
- (11) Karakoti, A. S.; Shukla, R.; Shanker, R.; Singh, S. Surface Functionalization of Quantum Dots for Biological Applications. *Adv. Colloid Interface Sci.* **2015**, *215*, 28–45. <https://doi.org/10.1016/j.cis.2014.11.004>.
- (12) Liu, X.; Luo, Y. Surface Modifications Technology of Quantum Dots Based Biosensors and Their Medical Applications. *Chin. J. Anal. Chem.* **2014**, *42* (7), 1061–1069. [https://doi.org/10.1016/S1872-2040\(14\)60753-2](https://doi.org/10.1016/S1872-2040(14)60753-2).
- (13) Mishra, R.; Singh, S. K.; Gupta, H.; Srivastava, N.; Meghnani, D.; Tiwari, R. K.; Patel, A.; Tiwari, A.; Tiwari, V. K.; Singh, R. K. Surface Modification of Nano Na[Ni<sub>0.60</sub>Mn<sub>0.35</sub>Co<sub>0.05</sub>]O<sub>2</sub> Cathode Material by Dextran Functionalized RGO via Hydrothermal Treatment for High Performance Sodium Batteries. *Appl. Surf. Sci.* **2021**, *535*, 147695. <https://doi.org/10.1016/j.apsusc.2020.147695>.
- (14) Baer, D. R.; Engelhard, M. H.; Johnson, G. E.; Laskin, J.; Lai, J.; Mueller, K.; Munusamy, P.; Thevuthasan, S.; Wang, H.; Washton, N.; Elder, A.; Baisch, B. L.; Karakoti, A.; Kuchibhatla, S. V. N. T.; Moon, D. Surface Characterization of Nanomaterials and Nanoparticles: Important Needs and Challenging Opportunities. *J. Vac. Sci. Technol. Vac. Surf. Films* **2013**, *31* (5), 050820. <https://doi.org/10.1116/1.4818423>.

- (15) Somorjai, G. A.; Park, J. Y. Evolution of the Surface Science of Catalysis from Single Crystals to Metal Nanoparticles under Pressure. *J. Chem. Phys.* **2008**, *128* (18), 182504. <https://doi.org/10.1063/1.2888970>.
- (16) Le Ouay, B.; Stellacci, F. Antibacterial Activity of Silver Nanoparticles: A Surface Science Insight. *Nano Today* **2015**, *10* (3), 339–354. <https://doi.org/10.1016/j.nantod.2015.04.002>.
- (17) Boles, M. A.; Ling, D.; Hyeon, T.; Talapin, D. V. The Surface Science of Nanocrystals. *Nat. Mater.* **2016**, *15* (2), 141–153. <https://doi.org/10.1038/nmat4526>.
- (18) Mikkelsen, A.; Lundgren, E. Surface Science of Free-Standing Semiconductor Nanowires. *Surf. Sci.* **2013**, *607*, 97–105. <https://doi.org/10.1016/j.susc.2012.08.002>.
- (19) Klauber, C.; Smart, R. St. C. Solid Surfaces, Their Structure and Composition. In *Surface Analysis Methods in Materials Science*; O'Connor, D. J., Sexton, B. A., Smart, R. St. C., Eds.; Springer Berlin Heidelberg: Berlin, Heidelberg, **1992**; pp 3–65. [https://doi.org/10.1007/978-3-662-02767-7\\_1](https://doi.org/10.1007/978-3-662-02767-7_1).
- (20) Ertl, G. Reactions at Surfaces: From Atoms to Complexity (Nobel Lecture). *Angew. Chem. Int. Ed.* **2008**, *47* (19), 3524–3535. <https://doi.org/10.1002/anie.200800480>.
- (21) Woodruff, D. P. Surface Structure. In *Chemical Bonding at Surfaces and Interfaces*; Elsevier, **2008**; pp 1–56. <https://doi.org/10.1016/B978-044452837-7.50002-2>.
- (22) Zaera, F. Surface Chemistry at the Liquid/Solid Interface. *Surf. Sci.* **2011**, *605* (13), 1141–1145. <https://doi.org/10.1016/j.susc.2011.04.021>.
- (23) Starostina, N.; Brodsky, M.; Prikhodko, S.; Hoo, C. M.; Mecartney, M. L.; West, P. AFM Capabilities in Characterization of Particles and Surfaces: From Angstroms to Microns. *J. Cosmet. Sci.* **2008**, *59* (3), 225–232.
- (24) Inkson, B. J. 2 - Scanning Electron Microscopy (SEM) and Transmission Electron Microscopy (TEM) for Materials Characterization. In *Materials Characterization Using Nondestructive Evaluation (NDE) Methods*; Hübschen, G., Altpeter, I., Tschuncky, R., Herrmann, H.-G., Eds.; Woodhead Publishing, **2016**; pp 17–43. <https://doi.org/10.1016/B978-0-08-100040-3.00002-X>.
- (25) Alqaheem, Y.; Alomair, A. A. Microscopy and Spectroscopy Techniques for Characterization of Polymeric Membranes. *Membranes* **2020**, *10* (2), 33. <https://doi.org/10.3390/membranes10020033>.
- (26) Powell, C. J. Growth of Surface Analysis and the Development of Databases and Modeling Software for Auger-Electron Spectroscopy and X-Ray Photoelectron Spectroscopy. *Microsc. Today* **2016**, *24* (2), 16–23. <https://doi.org/10.1017/S1551929516000080>.
- (27) Swart, H. C. Surface Sensitive Techniques for Advanced Characterization of Luminescent Materials. *Materials* **2017**, *10* (8), 906. <https://doi.org/10.3390/ma10080906>.
- (28) MacDonald, R. J.; King, B. V. SIMS — Secondary Ion Mass Spectrometry. In *Surface Analysis Methods in Materials Science*; O'Connor, D. J., Sexton, B. A., Smart, R. St. C., Eds.; Springer Series in Surface Sciences; Springer: Berlin, Heidelberg, **1992**; pp 117–147. [https://doi.org/10.1007/978-3-662-02767-7\\_5](https://doi.org/10.1007/978-3-662-02767-7_5).
- (29) Browning, R. Auger Spectroscopy and Scanning Auger Microscopy. In *Surface Analysis Methods in Materials Science*; O'Connor, D. J., Sexton, B.

- A., Smart, R. St. C., Eds.; Springer Berlin Heidelberg: Berlin, Heidelberg, **1992**; pp 149–164. [https://doi.org/10.1007/978-3-662-02767-7\\_6](https://doi.org/10.1007/978-3-662-02767-7_6).
- (30) Kibel, M. H. X-Ray Photoelectron Spectroscopy. In *Surface Analysis Methods in Materials Science*; O'Connor, D. J., Sexton, B. A., Smart, R. St. C., Eds.; Springer Series in Surface Sciences; Springer: Berlin, Heidelberg, **1992**; pp 165–186. [https://doi.org/10.1007/978-3-662-02767-7\\_7](https://doi.org/10.1007/978-3-662-02767-7_7).
- (31) Greczynski, G.; Hultman, L. X-Ray Photoelectron Spectroscopy: Towards Reliable Binding Energy Referencing. *Prog. Mater. Sci.* **2020**, *107*, 100591. <https://doi.org/10.1016/j.pmatsci.2019.100591>.
- (32) Son, D.; Cho, S.; Nam, J.; Lee, H.; Kim, M. X-Ray-Based Spectroscopic Techniques for Characterization of Polymer Nanocomposite Materials at a Molecular Level. *Polymers* **2020**, *12* (5), 1053. <https://doi.org/10.3390/polym12051053>.
- (33) Pérez-Jiménez, A. I.; Lyu, D.; Lu, Z.; Liu, G.; Ren, B. Surface-Enhanced Raman Spectroscopy: Benefits, Trade-Offs and Future Developments. *Chem. Sci.* **2020**, *11* (18), 4563–4577. <https://doi.org/10.1039/D0SC00809E>.
- (34) Pilot, R.; Signorini, R.; Durante, C.; Orian, L.; Bhamidipati, M.; Fabris, L. A Review on Surface-Enhanced Raman Scattering. *Biosensors* **2019**, *9* (2), 57. <https://doi.org/10.3390/bios9020057>.
- (35) Langer, J.; Jimenez de Aberasturi, D.; Aizpurua, J.; Alvarez-Puebla, R. A.; Auguie, B.; Baumberg, J. J.; Bazan, G. C.; Bell, S. E. J.; Boisen, A.; Brolo, A. G.; Choo, J.; Cialla-May, D.; Deckert, V.; Fabris, L.; Faulds, K.; García de Abajo, F. J.; Goodacre, R.; Graham, D.; Haes, A. J.; Haynes, C. L.; Huck, C.; Itoh, T.; Käll, M.; Kneipp, J.; Kotov, N. A.; Kuang, H.; Le Ru, E. C.; Lee, H. K.; Li, J.-F.; Ling, X. Y.; Maier, S. A.; Mayerhöfer, T.; Moskovits, M.; Murakoshi, K.; Nam, J.-M.; Nie, S.; Ozaki, Y.; Pastoriza-Santos, I.; Perez-Juste, J.; Popp, J.; Pucci, A.; Reich, S.; Ren, B.; Schatz, G. C.; Shegai, T.; Schlücker, S.; Tay, L.-L.; Thomas, K. G.; Tian, Z.-Q.; Van Duyne, R. P.; Vo-Dinh, T.; Wang, Y.; Willets, K. A.; Xu, C.; Xu, H.; Xu, Y.; Yamamoto, Y. S.; Zhao, B.; Liz-Marzán, L. M. Present and Future of Surface-Enhanced Raman Scattering. *ACS Nano* **2020**, *14* (1), 28–117. <https://doi.org/10.1021/acsnano.9b04224>.
- (36) Hagenhoff, B. High Resolution Surface Analysis by TOF-SIMS. *Microchim. Acta* **2000**, *132* (2), 259–271. <https://doi.org/10.1007/s006040050019>.
- (37) Jayawardena, H. S. N.; Liyanage, S. H.; Rathnayake, K.; Patel, U.; Yan, M. Analytical Methods for Characterization of Nanomaterial Surfaces. *Anal. Chem.* **2021**, *93* (4), 1889–1911. <https://doi.org/10.1021/acs.analchem.0c05208>.
- (38) Conley, M. P.; Copéret, C. Solid-State NMR: An EYE Opener in Surface Chemistry. *Chim. Int. J. Chem.* **2012**, *66* (10), 752–758. <https://doi.org/10.2533/chimia.2012.752>.
- (39) Gutmann, T.; Grünberg, A.; Rothermel, N.; Werner, M.; Srouf, M.; Abdulhussain, S.; Tan, S.; Xu, Y.; Breitzke, H.; Buntkowsky, G. Solid-State NMR Concepts for the Investigation of Supported Transition Metal Catalysts and Nanoparticles. *Solid State Nucl. Magn. Reson.* **2013**, *55–56*, 1–11. <https://doi.org/10.1016/j.ssnmr.2013.06.004>.
- (40) Deng, F.; Yang, J.; Ye, C. Solid State NMR Characterization of Solid Surface of Heterogeneous Catalysts. In *Modern Magnetic Resonance*; Webb, G. A., Ed.; Springer Netherlands: Dordrecht, **2006**; pp 205–211. [https://doi.org/10.1007/1-4020-3910-7\\_25](https://doi.org/10.1007/1-4020-3910-7_25).



- (41) Szeto, K. C.; Merle, N.; Trébosc, J.; Taoufik, M.; Gauvin, R. M.; Pourpoint, F.; Delevoeye, L. Caveat on the Actual Robustness of Heteronuclear NMR Methods for Probing the Surface of  $\gamma$ -Alumina and Related Catalysts. *J Phys Chem C* **2019**, *9*.
- (42) Copéret, C.; Berkson, Z. J.; Chan, K. W.; de Jesus Silva, J.; Gordon, C. P.; Pucino, M.; Zhizhko, P. A. Olefin Metathesis: What Have We Learned about Homogeneous and Heterogeneous Catalysts from Surface Organometallic Chemistry? *Chem. Sci.* **2021**, *12* (9), 3092–3115. <https://doi.org/10.1039/D0SC06880B>.
- (43) Pallister, P. J.; Barry, S. T. Surface Chemistry of Group 11 Atomic Layer Deposition Precursors on Silica Using Solid-State Nuclear Magnetic Resonance Spectroscopy. *J. Chem. Phys.* **2016**, *146* (5), 052812. <https://doi.org/10.1063/1.4968021>.
- (44) Lee, S. K.; Ahn, C. W. Probing of 2-Dimensional Confinement-Induced Structural Transitions in Amorphous Oxide Thin Film. *Sci. Rep.* **2015**, *4* (1), 4200. <https://doi.org/10.1038/srep04200>.
- (45) Marple, M. A. T.; Wynn, T. A.; Cheng, D.; Shimizu, R.; Mason, H. E.; Meng, Y. S. Local Structure of Glassy Lithium Phosphorus Oxynitride Thin Films: A Combined Experimental and Ab Initio Approach. *Angew. Chem. Int. Ed.* **2020**, *59* (49), 22185–22193. <https://doi.org/10.1002/anie.202009501>.
- (46) Gutmann, T.; Buntkowsky, G. Solid-State NMR Studies of Supported Transition Metal Catalysts and Nanoparticles. In *Modern Magnetic Resonance*; Webb, G. A., Ed.; Springer International Publishing: Cham, **2017**; pp 1–21. [https://doi.org/10.1007/978-3-319-28275-6\\_39-1](https://doi.org/10.1007/978-3-319-28275-6_39-1).
- (47) Johnson, R. L.; Perras, F. A.; Kobayashi, T.; Schwartz, T. J.; Dumesic, J. A.; Shanks, B. H.; Pruski, M. Identifying Low-Coverage Surface Species on Supported Noble Metal Nanoparticle Catalysts by DNP-NMR. *Chem. Commun.* **2016**, *52* (9), 1859–1862. <https://doi.org/10.1039/C5CC06788J>.
- (48) Xu, M.; Chen, J.; Wen, Y.; Du, J.-H.; Lin, Z.; Peng, L.  $^{17}\text{O}$  Solid-State NMR Studies of  $\text{Ta}_2\text{O}_5$  Nanorods. *ACS Omega* **2020**, *5* (14), 8355–8361. <https://doi.org/10.1021/acsomega.0c00874>.
- (49) Chen, J.; Hope, M. A.; Lin, Z.; Wang, M.; Liu, T.; Halat, D. M.; Wen, Y.; Chen, T.; Ke, X.; Magusin, P. C. M. M.; Ding, W.; Xia, X.; Wu, X.-P.; Gong, X.-Q.; Grey, C. P.; Peng, L. Interactions of Oxide Surfaces with Water Revealed with Solid-State NMR Spectroscopy. *J. Am. Chem. Soc.* **2020**, *142* (25), 11173–11182. <https://doi.org/10.1021/jacs.0c03760>.
- (50) Deng, F.; Yang, J.; Ye, C. Solid State NMR Characterization of Solid Surface of Heterogeneous Catalysts. In *Modern Magnetic Resonance*; Webb, G. A., Ed.; Springer Netherlands: Dordrecht, **2006**; pp 205–211. [https://doi.org/10.1007/1-4020-3910-7\\_25](https://doi.org/10.1007/1-4020-3910-7_25).
- (51) Ong, T.-C.; Verel, R.; Copéret, C. Solid-State NMR: Surface Chemistry Applications. In *Encyclopedia of Spectroscopy and Spectrometry (Third Edition)*; Lindon, J. C., Tranter, G. E., Koppenaal, D. W., Eds.; Academic Press: Oxford, **2017**; pp 121–127. <https://doi.org/10.1016/B978-0-12-409547-2.12130-4>.
- (52) Gutmann, T.; Groszewicz, P. B.; Buntkowsky, G. Solid-State NMR of Nanocrystals. In *Annual Reports on NMR Spectroscopy*; Elsevier, **2019**; Vol. 97, pp 1–82. <https://doi.org/10.1016/bs.arnmr.2018.12.001>.

- (53) Casabianca, L. B. Solid-State Nuclear Magnetic Resonance Studies of Nanoparticles. *Solid State Nucl. Magn. Reson.* **2020**, *107*, 101664. <https://doi.org/10.1016/j.ssnmr.2020.101664>.
- (54) Hanrahan, M. P.; Fought, E. L.; Windus, T. L.; Wheeler, L. M.; Anderson, N. C.; Neale, N. R.; Rossini, A. J. Characterization of Silicon Nanocrystal Surfaces by Multidimensional Solid-State NMR Spectroscopy. *Chem. Mater.* **2017**, *29* (24), 10339–10351. <https://doi.org/10.1021/acs.chemmater.7b03306>.
- (55) Walder, B. J.; Berk, C.; Liao, W.-C.; Rossini, A. J.; Schwarzwälder, M.; Pradere, U.; Hall, J.; Lesage, A.; Copéret, C.; Emsley, L. One- and Two-Dimensional High-Resolution NMR from Flat Surfaces. *ACS Cent. Sci.* **2019**, *5* (3), 515–523. <https://doi.org/10.1021/acscentsci.8b00916>.
- (56) Lilly Thankamony, A. S.; Wittmann, J. J.; Kaushik, M.; Corzilius, B. Dynamic Nuclear Polarization for Sensitivity Enhancement in Modern Solid-State NMR. *Prog. Nucl. Magn. Reson. Spectrosc.* **2017**, *102–103*, 120–195. <https://doi.org/10.1016/j.pnmrs.2017.06.002>.
- (57) Li, Y.; Wu, X.-P.; Jiang, N.; Lin, M.; Shen, L.; Sun, H.; Wang, Y.; Wang, M.; Ke, X.; Yu, Z.; Gao, F.; Dong, L.; Guo, X.; Hou, W.; Ding, W.; Gong, X.-Q.; Grey, C. P.; Peng, L. Distinguishing Faceted Oxide Nanocrystals with  $^{17}\text{O}$  Solid-State NMR Spectroscopy. *Nat. Commun.* **2017**, *8* (1), 581. <https://doi.org/10.1038/s41467-017-00603-7>.
- (58) Chen, C.-H.; Gaillard, E.; Mentink-Vigier, F.; Chen, K.; Gan, Z.; Gaveau, P.; Rebière, B.; Berthelot, R.; Florian, P.; Bonhomme, C.; Smith, M. E.; Métro, T.-X.; Alonso, B.; Laurencin, D. Direct  $^{17}\text{O}$  Isotopic Labeling of Oxides Using Mechanochemistry. *Inorg. Chem.* **2020**, *59* (18), 13050–13066. <https://doi.org/10.1021/acs.inorgchem.0c00208>.
- (59) Reif, B.; Ashbrook, S. E.; Emsley, L.; Hong, M. Solid-State NMR Spectroscopy. *Nat. Rev. Methods Primer* **2021**, *1* (1), 2. <https://doi.org/10.1038/s43586-020-00002-1>.
- (60) Copéret, C.; Liao, W.-C.; Gordon, C. P.; Ong, T.-C. Active Sites in Supported Single-Site Catalysts: An NMR Perspective. *J. Am. Chem. Soc.* **2017**, *139* (31), 10588–10596. <https://doi.org/10.1021/jacs.6b12981>.
- (61) Polenova, T.; Gupta, R.; Goldbourn, A. Magic Angle Spinning NMR Spectroscopy: A Versatile Technique for Structural and Dynamic Analysis of Solid-Phase Systems. *Anal. Chem.* **2015**, *87* (11), 5458–5469. <https://doi.org/10.1021/ac504288u>.
- (62) Deschamps, M. Chapter Three - Ultrafast Magic Angle Spinning Nuclear Magnetic Resonance. In *Annual Reports on NMR Spectroscopy*; Webb, G. A., Ed.; Academic Press, **2014**; Vol. 81, pp 109–144. <https://doi.org/10.1016/B978-0-12-800185-1.00003-6>.
- (63) Protsak, I. S.; Morozov, Y. M.; Dong, W.; Le, Z.; Zhang, D.; Henderson, I. M. A  $^{29}\text{Si}$ ,  $^1\text{H}$  and  $^{13}\text{C}$  Solid-State NMR Study on the Surface Species of Various Depolymerized Organosiloxanes at Silica Surface. *Nanoscale Res. Lett.* **2019**, *14* (1), 160. <https://doi.org/10.1186/s11671-019-2982-2>.
- (64) Lapina, O. B.; Shubin, A. A.; Terskikh, V. V. Solid-State NMR of Oxide-Based Materials. In *Modern Magnetic Resonance*; Webb, G. A., Ed.; Springer International Publishing: Cham, **2018**; pp 1125–1160. [https://doi.org/10.1007/978-3-319-28388-3\\_105](https://doi.org/10.1007/978-3-319-28388-3_105).
- (65) Grekov, D.; Vancompernelle, T.; Taoufik, M.; Delevoye, L.; Gauvin, R. M. Solid-State NMR of Quadrupolar Nuclei for Investigations into Supported

- Organometallic Catalysts: Scope and Frontiers. *Chem. Soc. Rev.* **2018**, *47* (8), 2572–2590. <https://doi.org/10.1039/C7CS00682A>.
- (66) Wickramasinghe, A.; Wang, S.; Matsuda, I.; Nishiyama, Y.; Nemoto, T.; Endo, Y.; Ishii, Y. Evolution of CPMAS under Fast Magic-Angle-Spinning at 100kHz and Beyond. *Solid State Nucl. Magn. Reson.* **2015**, *72*, 9–16. <https://doi.org/10.1016/j.ssnmr.2015.10.002>.
- (67) Engelke, F.; Steuernagel, S. Cross Polarization in Rotating Solids: Spin-1/2 Nuclei \* Update Based on Original Article by Frank Engelke, Encyclopedia of Magnetic Resonance, 1996, John Wiley & Sons Ltd. In *eMagRes*; American Cancer Society, **2011**. <https://doi.org/10.1002/9780470034590.emrstm0102.pub2>.
- (68) Hartmann, S. R.; Hahn, E. L. Nuclear Double Resonance in the Rotating Frame. *Phys. Rev.* **1962**, *128* (5), 2042–2053. <https://doi.org/10.1103/PhysRev.128.2042>.
- (69) Metz, G.; Ziliox, M.; Smith, S. O. Towards Quantitative CP-MAS NMR. *Solid State Nucl. Magn. Reson.* **1996**, *7* (3), 155–160. [https://doi.org/10.1016/S0926-2040\(96\)01257-X](https://doi.org/10.1016/S0926-2040(96)01257-X).
- (70) Mijatovic, J.; Binder, W. H.; Gruber, H. Characterization of Surface Modified Silica Nanoparticles by <sup>29</sup>Si Solid State NMR Spectroscopy. *Mikrochim Acta* **2000**, *133*, 175–181. <https://doi.org/10.1007/s006040070089>
- (71) Wei, D.; Han, M.; Yu, L. Solid-State <sup>77</sup>Se NMR of Organoselenium Compounds through Cross Polarization Magic Angle Spinning (CPMAS) Method. *Sci. Rep.* **2017**, *7* (1), 6376. <https://doi.org/10.1038/s41598-017-06892-8>.
- (72) Jarlbring, M.; Sandström, D. E.; Antzutkin, O. N.; Forsling, W. Characterization of Active Phosphorus Surface Sites at Synthetic Carbonate-Free Fluorapatite Using Single-Pulse <sup>1</sup>H, <sup>31</sup>P, and <sup>31</sup>P CP MAS NMR. *Langmuir ACS J. Surf. Colloids* **2006**, *22* (10), 4787–4792. <https://doi.org/10.1021/la052837j>.
- (73) Faulkner, R. A.; DiVerdi, J. A.; Yang, Y.; Kobayashi, T.; Maciel, G. E. The Surface of Nanoparticle Silicon as Studied by Solid-State NMR. *Mater. Basel Switz.* **2012**, *6* (1), 18–46. <https://doi.org/10.3390/ma6010018>.
- (74) Davidowski, S. K.; Holland, G. P. Solid-State NMR Characterization of Mixed Phosphonic Acid Ligand Binding and Organization on Silica Nanoparticles. *Langmuir* **2016**, *32* (13), 3253–3261. <https://doi.org/10.1021/acs.langmuir.5b03933>.
- (75) Burum, D. P.; Bielecki, A. An Improved Experiment for Heteronuclear-Correlation 2D NMR in Solids. *J. Magn. Reson.* **1991**, *94* (3), 645–652. [https://doi.org/10.1016/0022-2364\(91\)90155-M](https://doi.org/10.1016/0022-2364(91)90155-M).
- (76) Kobayashi, T.; Nishiyama, Y.; Pruski, M. Chapter 1: Heteronuclear Correlation Solid-State NMR Spectroscopy with Indirect Detection under Fast Magic-Angle Spinning. In *Modern Methods in Solid-state NMR*; 2018; pp 1–38. <https://doi.org/10.1039/9781788010467-00001>.
- (77) Baccile, N.; Laurent, G.; Bonhomme, C.; Innocenzi, P.; Babonneau, F. Solid-State NMR Characterization of the Surfactant–Silica Interface in Templated Silicas: Acidic versus Basic Conditions. *Chem. Mater.* **2007**, *19* (6), 1343–1354. <https://doi.org/10.1021/cm062545j>.
- (78) Zhang, R.; Nishiyama, Y.; Ramamoorthy, A. Exploiting Heterogeneous Time Scale of Dynamics to Enhance 2D HETCOR Solid-State NMR Sensitivity. *J. Magn. Reson.* **2019**, *309*, 106615. <https://doi.org/10.1016/j.jmr.2019.106615>.

- (79) Mao, K.; Rapp, J. L.; Wiench, J. W.; Pruski, M. Characterization of Nanostructured Organic-Inorganic Hybrid Materials Using Advanced Solid-State NMR Spectroscopy. *MRS Online Proc. Libr.* **2009**, *1184* (1), 171–179. <https://doi.org/10.1557/PROC-1184-HH07-01>.
- (80) Swanson, H. L.; Guo, C.; Cao, M.; Addison, J. B.; Holland, G. P. Probing the Binding Modes and Dynamics of Histidine on Fumed Silica Surfaces by Solid-State NMR. *Phys. Chem. Chem. Phys.* **2020**, *22* (36), 20349–20361. <https://doi.org/10.1039/D0CP03472J>.
- (81) Zhang, R.; Pandey, M. K.; Nishiyama, Y.; Ramamoorthy, A. A Novel High-Resolution and Sensitivity-Enhanced Three-Dimensional Solid-State NMR Experiment Under Ultrafast Magic Angle Spinning Conditions. *Sci. Rep.* **2015**, *5* (1), 11810. <https://doi.org/10.1038/srep11810>.
- (82) Feike, M.; Demco, D. E.; Graf, R.; Gottwald, J.; Hafner, S.; Spiess, H. W. Broadband Multiple-Quantum NMR Spectroscopy. *J. Magn. Reson. A* **1996**, *122* (2), 214–221. <https://doi.org/10.1006/jmra.1996.0197>.
- (83) Sorte, E. G.; Rimsza, J. M.; Alam, T. M. Computational and Experimental  $^1\text{H}$ -NMR Study of Hydrated Mg-Based Minerals. *Molecules* **2020**, *25* (4), 933. <https://doi.org/10.3390/molecules25040933>.
- (84) Vancompernelle, T.; Merle, N.; Capet, F.; Rosal, I. D.; Laurent, M.; Delevoye, L.; Pourpoint, F.; Gauvin, R. M. Grafting of a New Bis-Silylamido Aluminum Species on Silica: Insight from Solid-State NMR into Interactions with the Surface. *Dalton Trans.* **2019**, *48* (16), 5243–5252. <https://doi.org/10.1039/C9DT00845D>.
- (85) Kobayashi, T.; Singappuli-Arachchige, D.; Wang, Z.; Slowing, I. I.; Pruski, M. Spatial Distribution of Organic Functional Groups Supported on Mesoporous Silica Nanoparticles: A Study by Conventional and DNP-Enhanced  $^{29}\text{Si}$  Solid-State NMR. *Phys. Chem. Chem. Phys.* **2017**, *19* (3), 1781–1789. <https://doi.org/10.1039/C6CP07642D>.
- (86) Zhao, E. W.; Maligal-Ganesh, R.; Mentink-Vigier, F.; Zhao, T. Y.; Du, Y.; Pei, Y.; Huang, W.; Bowers, C. R. Atomic-Scale Structure of Mesoporous Silica-Encapsulated Pt and PtSn Nanoparticles Revealed by Dynamic Nuclear Polarization-Enhanced  $^{29}\text{Si}$  MAS NMR Spectroscopy. *J. Phys. Chem. C* **2019**, *123* (12), 7299–7307. <https://doi.org/10.1021/acs.jpcc.9b01782>.
- (87) Hung, I.; Rossini, A. J.; Schurko, R. W. Application of the Carr–Purcell Meiboom–Gill Pulse Sequence for the Acquisition of Solid-State NMR Spectra of Spin-1/2 Nuclei. *J. Phys. Chem. A* **2004**, *108* (34), 7112–7120. <https://doi.org/10.1021/jp0401123>.
- (88) Ashbrook, S. E.; Duer, M. J. Structural Information from Quadrupolar Nuclei in Solid State NMR. *Concepts Magn. Reson. Part A* **2006**, *28A* (3), 183–248. <https://doi.org/10.1002/cmr.a.20053>.
- (89) Stone-Weiss, N.; Youngman, R. E.; Thorpe, R.; Smith, N. J.; Pierce, E. M.; Goel, A. An Insight into the Corrosion of Alkali Aluminoborosilicate Glasses in Acidic Environments. *Phys. Chem. Chem. Phys.* **2020**, *22* (4), 1881–1896. <https://doi.org/10.1039/C9CP06064B>.
- (90) Xu, J. H.; Jadhav, A. L.; Turney, D. E.; Messinger, R. J. Molecular-Level Environments of Intercalated Chloroaluminate Anions in Rechargeable Aluminum-Graphite Batteries Revealed by Solid-State NMR Spectroscopy. *J. Mater. Chem. A* **2020**, *8* (31), 16006–16017. <https://doi.org/10.1039/D0TA02611E>.

- (91) Greiser, S.; Gluth, G. J. G.; Sturm, P.; Jäger, C.  $^{29}\text{Si}$ ( $^{27}\text{Al}$ ),  $^{27}\text{Al}$ ( $^{29}\text{Si}$ ) and  $^{27}\text{Al}$ ( $^1\text{H}$ ) Double-Resonance NMR Spectroscopy Study of Cementitious Sodium Aluminosilicate Gels (Geopolymers) and Gel-Zeolite Composites. *RSC Adv.* **2018**, *8* (70), 40164–40171. <https://doi.org/10.1039/C8RA09246J>.
- (92) Ashbrook, S. E.; Sneddon, S. New Methods and Applications in Solid-State NMR Spectroscopy of Quadrupolar Nuclei. *J. Am. Chem. Soc.* **2014**, *136* (44), 15440–15456. <https://doi.org/10.1021/ja504734p>.
- (93) Walkley, B.; Provis, J. L. Solid-State Nuclear Magnetic Resonance Spectroscopy of Cements. *Mater. Today Adv.* **2019**, *1*, 100007. <https://doi.org/10.1016/j.mtadv.2019.100007>.
- (94) Smith, M. E. Low- $\gamma$  Nuclei in Solid Samples. In *Encyclopedia of Magnetic Resonance*; Harris, R. K., Ed.; John Wiley & Sons, Ltd: Chichester, UK, **2007**; p emrstm0278. <https://doi.org/10.1002/9780470034590.emrstm0278>.
- (95) Larsen, F. H.; Jakobsen, H. J.; Ellis, P. D.; Nielsen, N. Chr. Sensitivity-Enhanced Quadrupolar-Echo NMR of Half-Integer Quadrupolar Nuclei. Magnitudes and Relative Orientation of Chemical Shielding and Quadrupolar Coupling Tensors. *J. Phys. Chem. A* **1997**, *101* (46), 8597–8606. <https://doi.org/10.1021/jp971547b>.
- (96) Lin, X.; Ideta, K.; Miyawaki, J.; Nishiyama, Y.; Mochida, I.; Yoon, S.-H. High Magnetic Field Solid-State NMR Analyses by Combining MAS, MQ-MAS, Homo-Nuclear and Hetero-Nuclear Correlation Experiments. *Magn. Reson. Chem.* **2012**, *50* (4), 289–294. <https://doi.org/10.1002/mrc.3804>.
- (97) Gan, Z.; Gor'kov, P.; Cross, T. A.; Samoson, A.; Massiot, D. Seeking Higher Resolution and Sensitivity for NMR of Quadrupolar Nuclei at Ultrahigh Magnetic Fields. *J. Am. Chem. Soc.* **2002**, *124* (20), 5634–5635. <https://doi.org/10.1021/ja025849p>.
- (98) Amoureux, J.-P.; Pruski, M. MQMAS NMR: Experimental Strategies and Applications. In *Encyclopedia of Magnetic Resonance*; Harris, R. K., Ed.; John Wiley & Sons, Ltd: Chichester, UK, **2007**; p emrstm0319. <https://doi.org/10.1002/9780470034590.emrstm0319>.
- (99) Ashbrook, S. E.; Griffin, J. M.; Johnston, K. E. Recent Advances in Solid-State Nuclear Magnetic Resonance Spectroscopy. *Annu. Rev. Anal. Chem.* **2018**, *11* (1), 485–508. <https://doi.org/10.1146/annurev-anchem-061417-125852>.
- (100) Taoufik, M.; Szeto, K. C.; Merle, N.; Rosal, I. D.; Maron, L.; Trébosc, J.; Tricot, G.; Gauvin, R. M.; Delevoye, L. Heteronuclear NMR Spectroscopy as a Surface-Selective Technique: A Unique Look at the Hydroxyl Groups of  $\gamma$ -Alumina. *Chem. – Eur. J.* **2014**, *20* (14), 4038–4046. <https://doi.org/10.1002/chem.201304883>.
- (101) Xu, S.; Jaegers, N. R.; Hu, W.; Kwak, J. H.; Bao, X.; Sun, J.; Wang, Y.; Hu, J. Z. High-Field One-Dimensional and Two-Dimensional  $^{27}\text{Al}$  Magic-Angle Spinning Nuclear Magnetic Resonance Study of  $\theta$ -,  $\delta$ -, and  $\gamma$ - $\text{Al}_2\text{O}_3$  Dominated Aluminum Oxides: Toward Understanding the Al Sites in  $\gamma$ - $\text{Al}_2\text{O}_3$ . *ACS Omega* **2021**, *6* (5), 4090–4099. <https://doi.org/10.1021/acsomega.0c06163>.
- (102) Kaushik, M.; Leroy, C.; Chen, Z.; Gajan, D.; Willinger, E.; Müller, C. R.; Fayon, F.; Massiot, D.; Fedorov, A.; Copéret, C.; Lesage, A.; Florian, P. Atomic-Scale Structure and Its Impact on Chemical Properties of Aluminum Oxide Layers Prepared by Atomic Layer Deposition on Silica. *Chem. Mater.* **2021**, *33* (9), 3335–3348. <https://doi.org/10.1021/acs.chemmater.1c00516>.

- (103) Castiglione, F.; Mele, A.; Raos, G. Chapter Four -  $^{17}\text{O}$  NMR: A “Rare and Sensitive” Probe of Molecular Interactions and Dynamics. In *Annual Reports on NMR Spectroscopy*; Webb, G. A., Ed.; Academic Press, 2015; Vol. 85, pp 143–193. <https://doi.org/10.1016/bs.arnmr.2014.12.004>.
- (104) Ashbrook, S. E.; Davis, Z. H.; Morris, R. E.; Rice, C. M.  $^{17}\text{O}$  NMR Spectroscopy of Crystalline Microporous Materials. *Chem. Sci.* **2021**, *12* (14), 5016–5036. <https://doi.org/10.1039/D1SC00552A>.
- (105) Merle, N.; Trébosc, J.; Baudouin, A.; Rosal, I. D.; Maron, L.; Szeto, K.; Genelot, M.; Mortreux, A.; Taoufik, M.; Delevoye, L.; Gauvin, R. M.  $^{17}\text{O}$  NMR Gives Unprecedented Insights into the Structure of Supported Catalysts and Their Interaction with the Silica Carrier. *J. Am. Chem. Soc.* **2012**, *134* (22), 9263–9275. <https://doi.org/10.1021/ja301085m>.
- (106) Hope, M. A.; Halat, D. M.; Magusin, P. C. M. M.; Paul, S.; Peng, L.; Grey, C. P. Surface-Selective Direct  $^{17}\text{O}$  DNP NMR of CeO<sub>2</sub> Nanoparticles. *Chem. Commun.* **2017**, *53* (13), 2142–2145. <https://doi.org/10.1039/C6CC10145C>.
- (107) Chen, J.; Wu, X.-P.; Hope, M. A.; Qian, K.; Halat, D. M.; Liu, T.; Li, Y.; Shen, L.; Ke, X.; Wen, Y.; Du, J.-H.; Magusin, P. C. M. M.; Paul, S.; Ding, W.; Gong, X.-Q.; Grey, C. P.; Peng, L. Polar Surface Structure of Oxide Nanocrystals Revealed with Solid-State NMR Spectroscopy. *Nat. Commun.* **2019**, *10* (1), 5420. <https://doi.org/10.1038/s41467-019-13424-7>.
- (108) Liao, W.-C.; Ghaffari, B.; Gordon, C. P.; Xu, J.; Copéret, C. Dynamic Nuclear Polarization Surface Enhanced NMR Spectroscopy (DNP SENS): Principles, Protocols, and Practice. *Curr. Opin. Colloid Interface Sci.* **2018**, *33*, 63–71. <https://doi.org/10.1016/j.cocis.2018.02.006>.
- (109) Man, P. P. Quadrupolar Interactions. In *Encyclopedia of Magnetic Resonance*; Harris, R. K., Ed.; John Wiley & Sons, Ltd: Chichester, UK, **2011**; p emrstm0429.pub2. <https://doi.org/10.1002/9780470034590.emrstm0429.pub2>.
- (110) Pourpoint, F.; Lafon, O.; Gauvin, R.; Amoureux, J.-P.; Delevoye, L. Chapter 4: Two-Dimensional Methods for Half-Integer Quadrupolar Nuclei. In *Modern Methods in Solid-state NMR*; **2018**; pp 97–133. <https://doi.org/10.1039/9781788010467-00097>.
- (111) Ashbrook, S. E. Recent Advances in Solid-State NMR Spectroscopy of Quadrupolar Nuclei. *Phys. Chem. Chem. Phys.* **2009**, *11* (32), 6892. <https://doi.org/10.1039/b907183k>.
- (112) Brus, J.; Abbrent, S.; Kobera, L.; Urbanova, M.; Cuba, P. Chapter Two - Advances in  $^{27}\text{Al}$  MAS NMR Studies of Geopolymers. In *Annual Reports on NMR Spectroscopy*; Webb, G. A., Ed.; Academic Press, **2016**; Vol. 88, pp 79–147. <https://doi.org/10.1016/bs.arnmr.2015.11.001>.
- (113) Chen, K. A Practical Review of NMR Lineshapes for Spin-1/2 and Quadrupolar Nuclei in Disordered Materials. *Int. J. Mol. Sci.* **2020**, *21* (16), 5666. <https://doi.org/10.3390/ijms21165666>.
- (114) Leigh Spencer, T.; Goward, G. R.; Bain, A. D. Complete Description of the Interactions of a Quadrupolar Nucleus with a Radiofrequency Field. Implications for Data Fitting. *Solid State Nucl. Magn. Reson.* **2013**, *53*, 20–26. <https://doi.org/10.1016/j.ssnmr.2013.03.002>.
- (115) Vega, A. J. Quadrupolar Nuclei in Solids. In *eMagRes*; American Cancer Society, **2010**. <https://doi.org/10.1002/9780470034590.emrstm0431.pub2>.
- (116) Edén, M. Chapter Four - Update on  $^{27}\text{Al}$  NMR Studies of Aluminosilicate Glasses. In *Annual Reports on NMR Spectroscopy*; Atta-ur-Rahman, Ed.;

- Academic Press, **2020**; Vol. 101, pp 285–410. <https://doi.org/10.1016/bs.arnmr.2020.07.002>.
- (117) Mafra, L.; Vidal-Moya, J. A.; Blasco, T. Chapter Four - Structural Characterization of Zeolites by Advanced Solid-state NMR Spectroscopic Methods. In *Annual Reports on NMR Spectroscopy*; Webb, G. A., Ed.; Annual Reports on NMR Spectroscopy; Academic Press, **2012**; Vol. 77, pp 259–351. <https://doi.org/10.1016/B978-0-12-397020-6.00004-0>.
- (118) Man, P. P. Quadrupole Couplings in Nuclear Magnetic Resonance, General. In *Encyclopedia of Analytical Chemistry*; Meyers, R. A., Ed.; John Wiley & Sons, Ltd: Chichester, UK, **2006**; p a6111. <https://doi.org/10.1002/9780470027318.a6111>.
- (119) Wasylishen, R. E.; Bernard, G. M. Solid-State NMR Spectroscopy in Organometallic Chemistry. In *Comprehensive Organometallic Chemistry III*; Elsevier, **2007**; pp 451–482. <https://doi.org/10.1016/B0-08-045047-4/00019-4>.
- (120) Apperley, D. C.; Harris, R. K.; Hodgkinson, P. *Solid-State NMR: Basic Principles & Practice*; Momentum Press: New York, N.Y.] (222 East 46th Street, New York, NY 10017), **2012**.
- (121) Frydman, L.; Harwood, J. S. Isotropic Spectra of Half-Integer Quadrupolar Spins from Bidimensional Magic-Angle Spinning NMR. *J. Am. Chem. Soc.* **1995**, *117* (19), 5367–5368. <https://doi.org/10.1021/ja00124a023>.
- (122) Deschamps, M.; Massiot, D. Correlation Experiments Involving Half-Integer Quadrupolar Nuclei. In *eMagRes*; American Cancer Society, **2011**. <https://doi.org/10.1002/9780470034590.emrstm1207>.
- (123) Malicki, N.; Mafra, L.; Quoineaud, A.-A.; Rocha, J.; Thibault-Starzyk, F.; Fernandez, C. Multiplex MQMAS NMR of Quadrupolar Nuclei. *Solid State Nucl. Magn. Reson.* **2005**, *28* (1), 13–21. <https://doi.org/10.1016/j.ssnmr.2005.02.007>.
- (125) Samoson, A.; Lippmaa, E.; Pines, A. High Resolution Solid-State N.M.R.: Averaging of Second-Order Effects by Means of a Double-Rotor. *Mol. Phys.* **1988**, *65* (4), 1013–1018. <https://doi.org/10.1080/00268978800101571>.
- (125) Llor, A.; Virlet, J. Towards High-Resolution NMR of More Nuclei in Solids: Sample Spinning with Time-Dependent Spinner Axis Angle. *Chem. Phys. Lett.* **1988**, *152* (2), 248–253. [https://doi.org/10.1016/0009-2614\(88\)87362-7](https://doi.org/10.1016/0009-2614(88)87362-7).
- (126) Dupree, R. Double Rotation NMR. In *Encyclopedia of Magnetic Resonance*; Harris, R. K., Ed.; John Wiley & Sons, Ltd: Chichester, UK, **2011**; p emrstm1203. <https://doi.org/10.1002/9780470034590.emrstm1203>.
- (127) Wu, Y. Double Rotation. In *Encyclopedia of Magnetic Resonance*; Harris, R. K., Ed.; John Wiley & Sons, Ltd: Chichester, UK, **2007**; p emrstm0135. <https://doi.org/10.1002/9780470034590.emrstm0135>.
- (128) Chmelka, B. F.; Zwanziger, J. W. Solid-State NMR Line Narrowing Methods for Quadrupolar Nuclei: Double Rotation and Dynamic-Angle Spinning. In *Solid-State NMR IV Methods and Applications of Solid-State NMR*; Blümich, B., Ed.; Diehl, P., Fluck, E., Günther, H., Kosfeld, R., Seelig, J., Blümich, B., Series Eds.; NMR Basic Principles and Progress; Springer Berlin Heidelberg: Berlin, Heidelberg, **1994**; Vol. 33, pp 79–124. [https://doi.org/10.1007/978-3-642-79127-7\\_2](https://doi.org/10.1007/978-3-642-79127-7_2).
- (129) Goldbourt, A.; Madhu, P. K. Multiple-Quantum Magic-Angle Spinning: High-Resolution Solid-state NMR Spectroscopy of Half-Integer Quadrupolar

- Nuclei. *Monatshefte Fr Chem. Chem. Mon.* **2002**, *133* (12), 1497–1534. <https://doi.org/10.1007/s00706-002-0502-y>.
- (130) Martin, R. W.; Kelly, J. E.; Collier, K. A. Spatial Reorientation Experiments for NMR of Solids and Partially Oriented Liquids. *Prog. Nucl. Magn. Reson. Spectrosc.* **2015**, *90–91*, 92–122. <https://doi.org/10.1016/j.pnmrs.2015.10.001>.
- (131) Grandinetti, P. J. Dynamic Angle Spinning. In *eMagRes*; American Cancer Society, **2011**. <https://doi.org/10.1002/9780470034590.emrstm0137.pub2>.
- (132) Wu, G.; Rovnyank, D.; Sun, B.; Griffin, R. G. High-Resolution Multiple Quantum MAS NMR Spectroscopy of Half-Integer Quadrupolar Nuclei. *Chem. Phys. Lett.* **1996**, *249* (3), 210–217. [https://doi.org/10.1016/0009-2614\(95\)01376-8](https://doi.org/10.1016/0009-2614(95)01376-8).
- (133) Gan, Z. Isotropic NMR Spectra of Half-Integer Quadrupolar Nuclei Using Satellite Transitions and Magic-Angle Spinning. *J. Am. Chem. Soc.* **2000**, *122* (13), 3242–3243. <https://doi.org/10.1021/ja9939791>.
- (134) Ashbrook, S. E.; Wimperis, S. High-Resolution NMR of Quadrupolar Nuclei in Solids: The Satellite-Transition Magic Angle Spinning (STMAS) Experiment. *Prog. Nucl. Magn. Reson. Spectrosc.* **2004**, *45* (1), 53–108. <https://doi.org/10.1016/j.pnmrs.2004.04.002>.
- (135) Frydman, L. Fundamentals of Multiple-Quantum Magic-Angle Spinning NMR on Half-Integer Quadrupolar Nuclei. *ChemInform* **2003**, *34* (32). <https://doi.org/10.1002/chin.200332288>.
- (136) Colaun, H.; Dawson, D. M.; Ashbrook, S. E. Investigating FAM-N Pulses for Signal Enhancement in MQMAS NMR of Quadrupolar Nuclei. *Solid State Nucl. Magn. Reson.* **2017**, *84*, 89–102. <https://doi.org/10.1016/j.ssnmr.2017.01.001>.
- (136) Amoureux, J.-P.; Fernandez, C.; Steuernagel, S. Z Filtering in MQMAS NMR. *Journal of Magnetic Resonance, Series A* **1996**, *123* (1), 116–118. <https://doi.org/10.1006/jmra.1996.0221>.
- (138) Brown, S. P.; Wimperis, S. Two-Dimensional Multiple-Quantum MAS NMR of Quadrupolar Nuclei. Acquisition of the Whole Echo. *J. Magn. Reson.* **1997**, *124* (1), 279–285. <https://doi.org/10.1006/jmre.1996.1059>.
- (139) Millot, Y.; Man, P. P. Procedures for Labeling the High-Resolution Axis of Two-Dimensional MQ-MAS NMR Spectra of Half-Integer Quadrupole Spins. *Solid State Nucl. Magn. Reson.* **2002**, *21* (1), 21–43. <https://doi.org/10.1006/snmr.2001.0043>.
- (140) Srivastava, D.; Ramachandran, R. Nuances of Multi-Quantum Excitation in Solid State NMR of Quadrupolar Nuclei. *RSC Adv.* **2013**, *3* (47), 25231–25236. <https://doi.org/10.1039/C3RA45195J>.
- (141) Gan, Z.; Kwak, H.-T. Enhancing MQMAS Sensitivity Using Signals from Multiple Coherence Transfer Pathways. *J. Magn. Reson.* **2004**, *168* (2), 346–351. <https://doi.org/10.1016/j.jmr.2004.03.021>.
- (142) Iuga, D.; Schäfer, H.; Verhagen, R.; Kentgens, A. P. M. Population and Coherence Transfer Induced by Double Frequency Sweeps in Half-Integer Quadrupolar Spin Systems. *J. Magn. Reson.* **2000**, *147* (2), 192–209. <https://doi.org/10.1006/jmre.2000.2192>.
- (143) Goldbourn, A.; Kababya, S.; Vega, S.; Madhu, P. K. The Influence of the Radiofrequency Excitation and Conversion Pulses on the Lineshapes and Intensities of the Triple-Quantum MAS NMR Spectra of  $I = 3/2$  Nuclei. *Solid State Nucl. Magn. Reson.* **2000**, *18* (1–4), 1–16. <https://doi.org/10.1006/snmr.2000.0007>.



- (144) Siegel, R.; Nakashima, T. T.; Wasylishen, R. E. Sensitivity Enhancement of MQMAS NMR Spectra of Spin 3/2 Nuclei Using Hyperbolic Secant Pulses. *Chem. Phys. Lett.* **2005**, *403* (4–6), 353–358. <https://doi.org/10.1016/j.cplett.2005.01.023>.
- (145) Kwak, H.-T.; Prasad, S.; Yao, Z.; Grandinetti, P. J.; Sachleben, J. R.; Emsley, L. Enhanced Sensitivity in RIACT/MQ-MAS NMR Experiments Using Rotor Assisted Population Transfer. *J. Magn. Reson.* **2001**, *150* (1), 71–80. <https://doi.org/10.1006/jmre.2001.2313>.
- (146) Kwak, H.-T.; Prasad, S.; Clark, T.; Grandinetti, P. J. Selective Suppression and Excitation of Solid-State NMR Resonances Based on Quadrupole Coupling Constants. *J. Magn. Reson.* **2003**, *160* (2), 107–113. [https://doi.org/10.1016/S1090-7807\(02\)00139-8](https://doi.org/10.1016/S1090-7807(02)00139-8).
- (147) Sasaki, A.; Tsutsumi, Y.; Amoureux, J.-P. Accelerating High-Resolution NMR of Half-Integer Quadrupolar Nuclei in Solids: SPAM-MQMAS and SPAM-STMAS. *Solid State Nucl. Magn. Reson.* **2020**, *108*, 101668. <https://doi.org/10.1016/j.ssnmr.2020.101668>.
- (148) Lim, K. H.; Charpentier, T.; Pines, A. Efficient Triple-Quantum Excitation in Modified RIACT MQMAS NMR for I=3/2 Nuclei. *J. Magn. Reson.* **2002**, *154* (2), 196–204. <https://doi.org/10.1006/jmre.2001.2471>.
- (149) Hung, I.; Gan, Z. Isotropic Solid-State MQMAS NMR Spectra for Large Quadrupolar Interactions Using Satellite-Transition Selective Inversion Pulses and Low Rf Fields. *J. Magn. Reson.* **2021**, *324*, 106913. <https://doi.org/10.1016/j.jmr.2021.106913>.
- (150) Amoureux, J. P.; Trébosc, J.; Delevoye, L.; Lafon, O.; Hu, B.; Wang, Q. Correlation NMR Spectroscopy Involving Quadrupolar Nuclei. *Solid State Nucl. Magn. Reson.* **2009**, *35* (1), 12–18. <https://doi.org/10.1016/j.ssnmr.2008.11.004>.
- (151) Wiench, J. W.; Tricot, G.; Delevoye, L.; Trebosc, J.; Frye, J.; Montagne, L.; Amoureux, J.-P.; Pruski, M. SPAM-MQ-HETCOR: An Improved Method for Heteronuclear Correlation Spectroscopy between Quadrupolar and Spin-1/2 Nuclei in Solid-State NMR. *Phys. Chem. Chem. Phys.* **2006**, *8* (1), 144–150. <https://doi.org/10.1039/B512246E>.
- (152) Rocha, J.; Morais, C. M.; Fernandez, C. Novel Nuclear Magnetic Resonance Techniques for the Study of Quadrupolar Nuclei in Clays and Other Layered Materials. *Clay Miner.* **2003**, *38* (3), 259–278. <https://doi.org/10.1180/0009855033830094>.
- (153) Fernandez, C.; Lang, D. P.; Amoureux, J. P.; Pruski, M. Measurement of Heteronuclear Dipolar Interactions between Quadrupolar and Spin-1/2 Nuclei in Solids by Multiple-Quantum REDOR NMR. *J. Am. Chem. Soc.* **1998**, *120* (11), 2672–2673. <https://doi.org/10.1021/ja973311r>.
- (154) Ashbrook, S. E.; Wimperis, S. High-Resolution NMR Spectroscopy of Quadrupolar Nuclei in Solids: Satellite-Transition MAS with Self-Compensation for Magic-Angle Misset. *J. Am. Chem. Soc.* **2002**, *124* (39), 11602–11603. <https://doi.org/10.1021/ja0203869>.
- (155) Amoureux, J.-P.; Huguenard, C.; Engelke, F.; Taulelle, F. Unified Representation of MQMAS and STMAS NMR of Half-Integer Quadrupolar Nuclei. *Chem. Phys. Lett.* **2002**, *356* (5), 497–504. [https://doi.org/10.1016/S0009-2614\(02\)00398-6](https://doi.org/10.1016/S0009-2614(02)00398-6).
- (156) Trebosc, J.; Amoureux, J.-P.; Gan, Z. Comparison of High-Resolution Solid-State NMR MQMAS and STMAS Methods for Half-Integer Quadrupolar

- Nuclei. *Solid State Nucl. Magn. Reson.* **2007**, *31* (1), 1–9. <https://doi.org/10.1016/j.ssnmr.2006.09.002>.
- (157) Ashbrook, S. E.; Wimperis, S. Advances in STMAS. In *eMagRes*; American Cancer Society, **2008**. <https://doi.org/10.1002/9780470034590.emrstm1032>.
- (158) Kwak, H.-T.; Gan, Z. Double-Quantum Filtered STMAS. *J. Magn. Reson.* **2003**, *164* (2), 369–372. [https://doi.org/10.1016/S1090-7807\(03\)00246-5](https://doi.org/10.1016/S1090-7807(03)00246-5).
- (159) Hung, I.; Gan, Z. Low-Power STMAS – Breaking through the Limit of Large Quadrupolar Interactions in High-Resolution Solid-State NMR Spectroscopy. *Phys. Chem. Chem. Phys.* **2020**, *22* (37), 21119–21123. <https://doi.org/10.1039/D0CP04274A>.
- (160) Perras, F. A.; Paterson, A. L. High Field Solid-State NMR of Challenging Nuclei in Inorganic Systems. In *Reference Module in Chemistry, Molecular Sciences and Chemical Engineering*; Elsevier, **2021**. <https://doi.org/10.1016/B978-0-12-823144-9.00015-7>.
- (161) Li, S.; Lafon, O.; Wang, W.; Wang, Q.; Wang, X.; Li, Y.; Xu, J.; Deng, F. Recent Advances of Solid-State NMR Spectroscopy for Microporous Materials. *Adv. Mater.* **2020**, *32* (44), 2002879. <https://doi.org/10.1002/adma.202002879>.
- (162) Pallister, P. J.; Moudrakovski, I. L.; Ripmeester, J. A. Mg-25 Ultra-High Field Solid State NMR Spectroscopy and First Principles Calculations of Magnesium Compounds. *Phys. Chem. Chem. Phys.* **2009**, *11* (48), 11487–11500. <https://doi.org/10.1039/B916076K>.
- (163) Gan, Z. Perspectives on High-Field and Solid-State NMR Methods of Quadrupole Nuclei. *J. Magn. Reson.* **2019**, *306*, 86–90. <https://doi.org/10.1016/j.jmr.2019.07.028>.
- (164) Bryce, D. L. New Frontiers for Solid-State NMR across the Periodic Table: A Snapshot of Modern Techniques and Instrumentation. *Dalton Trans.* **2019**, *48* (23), 8014–8020. <https://doi.org/10.1039/C9DT01801H>.
- (165) Siegel, R.; Nakashima, T. T.; Wasylishen, R. E. Sensitivity Enhancement of NMR Spectra of Half-Integer Quadrupolar Nuclei in the Solid State via Population Transfer. *Concepts Magn. Reson. Part A* **2005**, *26A* (2), 47–61. <https://doi.org/10.1002/cmr.a.20037>.
- (166) Perras, F. A.; Viger-Gravel, J.; Burgess, K. M. N.; Bryce, D. L. Signal Enhancement in Solid-State NMR of Quadrupolar Nuclei. *Solid State Nucl. Magn. Reson.* **2013**, *51–52*, 1–15. <https://doi.org/10.1016/j.ssnmr.2012.11.002>.
- (167) Moudrakovski, I. L. Recent Advances in Solid-State NMR of Alkaline Earth Elements. In *Annual Reports on NMR Spectroscopy*; Elsevier, **2013**; Vol. 79, pp 129–240. <https://doi.org/10.1016/B978-0-12-408098-0.00004-5>.
- (168) Fernandez, C.; Pruski, M. Probing Quadrupolar Nuclei by Solid-State NMR Spectroscopy: Recent Advances. In *Solid State NMR*; Chan, J. C. C., Ed.; Topics in Current Chemistry; Springer: Berlin, Heidelberg, **2012**; pp 119–188. [https://doi.org/10.1007/128\\_2011\\_141](https://doi.org/10.1007/128_2011_141).
- (169) Goswami, M.; van Bentum, P. J. M.; Kentgens, A. P. M. Sensitivity Enhancement in MAS NMR of Half-Integer Quadrupolar Nuclei Using Sideband Selective Double-Frequency Sweeps. *Can. J. Chem.* **2011**, *89* (9), 1130–1137. <https://doi.org/10.1139/v11-053>.
- (170) Dey, K. K.; Prasad, S.; Ash, J. T.; Deschamps, M.; Grandinetti, P. J. Spectral Editing in Solid-State MAS NMR of Quadrupolar Nuclei Using Selective

- Satellite Inversion. *J. Magn. Reson.* **2007**, *185* (2), 326–330. <https://doi.org/10.1016/j.jmr.2006.12.013>.
- (171) Kwak, H.-T.; Prasad, S.; Clark, T.; Grandinetti, P. J. Enhancing Sensitivity of Quadrupolar Nuclei in Solid-State NMR with Multiple Rotor Assisted Population Transfers. *Solid-State Nucl. Magn. Reson.* **2003**, *24* (2–3), 71–77. [https://doi.org/10.1016/S0926-2040\(03\)00051-1](https://doi.org/10.1016/S0926-2040(03)00051-1).
- (172) Nakashima, T. T.; Wasylishen, R. E. Sensitivity and Resolution Enhancement of Half-Integer Quadrupolar Nuclei in Solid-State NMR. In *eMagRes*; American Cancer Society, 2011. <https://doi.org/10.1002/9780470034590.emrstm1200>.
- (173) Siegel, R.; Nakashima, T. T.; Wasylishen, R. E. Sensitivity Enhancement of NMR Spectra of Half-Integer Spin Quadrupolar Nuclei in Solids Using Hyperbolic Secant Pulses. *J. Magn. Reson. San Diego Calif 1997* **2007**, *184* (1), 85–100. <https://doi.org/10.1016/j.jmr.2006.09.007>.
- (174) Dey, K.; Ash, J.; Trease, N.; Grandinetti, P. Trading Sensitivity for Information: Carr-Purcell-Meiboom-Gill Acquisition in Solid-State NMR. *J. Chem. Phys.* **2010**, *133*, 054501. <https://doi.org/10.1063/1.3463653>.
- (175) O'Dell, L. A.; Ratcliffe, C. I. Quadrupolar NMR to Investigate Dynamics in Solid Materials. In *eMagRes*; American Cancer Society, 2011; pp 1–16. <https://doi.org/10.1002/9780470034590.emrstm1209>.
- (176) Smith, M. E. Recent Progress in Solid-State Nuclear Magnetic Resonance of Half-Integer Spin Low- $\gamma$  Quadrupolar Nuclei Applied to Inorganic Materials. *Magn. Reson. Chem. MRC* **2020**. <https://doi.org/10.1002/mrc.5116>.
- (177) O'Dell, L. A.; Schurko, R. W. QCPMG Using Adiabatic Pulses for Faster Acquisition of Ultra-Wideline NMR Spectra. *Chem. Phys. Lett.* **2008**, *464* (1), 97–102. <https://doi.org/10.1016/j.cplett.2008.08.095>.
- (178) Schurko, R. W. Ultra-Wideline Solid-State NMR Spectroscopy. *Acc. Chem. Res.* **2013**, *46* (9), 1985–1995. <https://doi.org/10.1021/ar400045t>.
- (180) Berruyer, P.; Emsley, L.; Lesage, A. DNP in Materials Science: Touching the Surface. In *eMagRes* (eds R.K. Harris and R.L. Wasylishen) **2018**, *7*, pp 93–104. <https://doi.org/10.1002/9780470034590.emrstm1554>
- (180) Lesage, A.; Lelli, M.; Gajan, D.; Caporini, M. A.; Vitzthum, V.; Miéville, P.; Alauzun, J.; Roussey, A.; Thieuleux, C.; Mehdi, A.; Bodenhausen, G.; Coperet, C.; Emsley, L. Surface Enhanced NMR Spectroscopy by Dynamic Nuclear Polarization. *J. Am. Chem. Soc.* **2010**, *132* (44), 15459–15461. <https://doi.org/10.1021/ja104771z>.
- (181) Rankin, A. G. M.; Trébosc, J.; Pourpoint, F.; Amoureux, J.-P.; Lafon, O. Recent Developments in MAS DNP-NMR of Materials. *Solid State Nucl. Magn. Reson.* **2019**, *101*, 116–143. <https://doi.org/10.1016/j.ssnmr.2019.05.009>.
- (182) Rossini, A. J. Materials Characterization by Dynamic Nuclear Polarization-Enhanced Solid-State NMR Spectroscopy. *J. Phys. Chem. Lett.* **2018**, *9* (17), 5150–5159. <https://doi.org/10.1021/acs.jpcclett.8b01891>.
- (183) Lee, D.; Hediger, S.; De Paëpe, G. Is Solid-State NMR Enhanced by Dynamic Nuclear Polarization? *Solid State Nucl. Magn. Reson.* **2015**, *66–67*, 6–20. <https://doi.org/10.1016/j.ssnmr.2015.01.003>.
- (184) Rosay, M.; Blank, M.; Engelke, F. Instrumentation for Solid-State Dynamic Nuclear Polarization with Magic Angle Spinning NMR. *J. Magn. Reson.* **2016**, *264*, 88–98. <https://doi.org/10.1016/j.jmr.2015.12.026>.

- (185) Matsuki, Y.; Idehara, T.; Fukazawa, J.; Fujiwara, T. Advanced Instrumentation for DNP-Enhanced MAS NMR for Higher Magnetic Fields and Lower Temperatures. *J. Magn. Reson.* **2016**, *264*, 107–115. <https://doi.org/10.1016/j.jmr.2016.01.022>.
- (186) Giovine, R.; Trébosc, J.; Pourpoint, F.; Lafon, O.; Amoureux, J.-P. Magnetization Transfer from Protons to Quadrupolar Nuclei in Solid-State NMR Using PRESTO or Dipolar-Mediated Refocused INEPT Methods. *J. Magn. Reson.* **2019**, *299*, 109–123. <https://doi.org/10.1016/j.jmr.2018.12.016>.
- (187) Kobayashi, T.; Perras, F. A.; Slowing, I. I.; Sadow, A. D.; Pruski, M. Dynamic Nuclear Polarization Solid-State NMR in Heterogeneous Catalysis Research. *ACS Catal.* **2015**, *5* (12), 7055–7062. <https://doi.org/10.1021/acscatal.5b02039>.
- (188) Lee, D.; Hediger, S.; Paëpe, G. D. High-Field Solid-State NMR with Dynamic Nuclear Polarization. In *Modern Magnetic Resonance*; Webb, G. A., Ed.; Springer International Publishing: Cham, 2017; pp 1–17. [https://doi.org/10.1007/978-3-319-28275-6\\_73-1](https://doi.org/10.1007/978-3-319-28275-6_73-1).
- (189) Pump, E.; Bendjeriou-Sedjerari, A.; Viger-Gravel, J.; Gajan, D.; Scotto, B.; Samantaray, M. K.; Abou-Hamad, E.; Gurinov, A.; Almaksoud, W.; Cao, Z.; Lesage, A.; Cavallo, L.; Emsley, L.; Basset, J.-M. Predicting the DNP-SENS Efficiency in Reactive Heterogeneous Catalysts from Hydrophilicity. *Chem. Sci.* **2018**, *9* (21), 4866–4872. <https://doi.org/10.1039/C8SC00532J>.
- (191) Lee, D.; Leroy, C.; Crevant, C.; Bonhomme-Courry, L.; Babonneau, F.; Laurencin, D.; Bonhomme, C.; De Paëpe, G. Interfacial Ca<sup>2+</sup> Environments in Nanocrystalline Apatites Revealed by Dynamic Nuclear Polarization Enhanced 43 Ca NMR Spectroscopy. *Nat. Commun.* **2017**, *8* (1), 14104. <https://doi.org/10.1038/ncomms14104>.
- (191) Vitzthum, V.; Miéville, P.; Carnevale, D.; Caporini, M. A.; Gajan, D.; Copéret, C.; Lelli, M.; Zagdoun, A.; Rossini, A. J.; Lesage, A.; Emsley, L.; Bodenhausen, G. Dynamic Nuclear Polarization of Quadrupolar Nuclei Using Cross Polarization from Protons: Surface-Enhanced Aluminium-27 NMR. *Chem. Commun.* **2012**, *48* (14), 1988–1990. <https://doi.org/10.1039/C2CC15905H>.
- (193) Perras, F. A.; Kobayashi, T.; Pruski, M. Natural Abundance <sup>17</sup>O DNP Two-Dimensional and Surface-Enhanced NMR Spectroscopy. *J. Am. Chem. Soc.* **2015**, *137* (26), 8336–8339. <https://doi.org/10.1021/jacs.5b03905>.
- (193) Nagashima, H.; Trébosc, J.; Kon, Y.; Sato, K.; Lafon, O.; Amoureux, J.-P. Observation of Low- $\gamma$  Quadrupolar Nuclei by Surface-Enhanced NMR Spectroscopy. *J. Am. Chem. Soc.* **2020**, *142* (24), 10659–10672. <https://doi.org/10.1021/jacs.9b13838>.
- (194) Perras, F. A.; Wang, L.-L.; Manzano, J. S.; Chaudhary, U.; Opembe, N. N.; Johnson, D. D.; Slowing, I. I.; Pruski, M. Optimal Sample Formulations for DNP SENS: The Importance of Radical-Surface Interactions. *Curr. Opin. Colloid Interface Sci.* **2018**, *33*, 9–18. <https://doi.org/10.1016/j.cocis.2017.11.002>.
- (195) Corzilius, B. Theory of Solid Effect and Cross Effect Dynamic Nuclear Polarization with Half-Integer High-Spin Metal Polarizing Agents in Rotating Solids. *Phys. Chem. Chem. Phys.* **2016**, *18* (39), 27190–27204. <https://doi.org/10.1039/C6CP04621E>.
- (196) Thurber, K. R.; Tycko, R. Theory for Cross Effect Dynamic Nuclear Polarization under Magic-Angle Spinning in Solid State Nuclear Magnetic

- Resonance: The Importance of Level Crossings. *J. Chem. Phys.* **2012**, *137* (8), 084508. <https://doi.org/10.1063/1.4747449>.
- (197) Mentink-Vigier, F.; Mathies, G.; Liu, Y.; Barra, A.-L.; Caporini, M. A.; Lee, D.; Hediger, S.; Griffin, R. G.; Paëpe, G. D. Efficient Cross-Effect Dynamic Nuclear Polarization without Depolarization in High-Resolution MAS NMR. *Chem. Sci.* **2017**, *8* (12), 8150–8163. <https://doi.org/10.1039/C7SC02199B>.
- (198) Lund, A.; Casano, G.; Menzildjian, G.; Kaushik, M.; Stevanato, G.; Yulikov, M.; Jabbour, R.; Wisser, D.; Renom-Carrasco, M.; Thieuleux, C.; Bernada, F.; Karoui, H.; Siri, D.; Rosay, M.; Sergeev, I. V.; Gajan, D.; Lelli, M.; Emsley, L.; Ouari, O.; Lesage, A. TinyPols: A Family of Water-Soluble Binitroxides Tailored for Dynamic Nuclear Polarization Enhanced NMR Spectroscopy at 18.8 and 21.1 T. *Chem. Sci.* **2020**, *11* (10), 2810–2818. <https://doi.org/10.1039/C9SC05384K>.
- (199) Chaudhari, S. R.; Wisser, D.; Pinon, A. C.; Berruyer, P.; Gajan, D.; Tordo, P.; Ouari, O.; Reiter, C.; Engelke, F.; Copéret, C.; Lelli, M.; Lesage, A.; Emsley, L. Dynamic Nuclear Polarization Efficiency Increased by Very Fast Magic Angle Spinning. *J. Am. Chem. Soc.* **2017**, *139* (31), 10609–10612. <https://doi.org/10.1021/jacs.7b05194>.
- (200) Wisser, D.; Karthikeyan, G.; Lund, A.; Casano, G.; Karoui, H.; Yulikov, M.; Menzildjian, G.; Pinon, A. C.; Pura, A.; Engelke, F.; Chaudhari, S. R.; Kubicki, D.; Rossini, A. J.; Moroz, I. B.; Gajan, D.; Copéret, C.; Jeschke, G.; Lelli, M.; Emsley, L.; Lesage, A.; Ouari, O. BDPA-Nitroxide Biradicals Tailored for Efficient Dynamic Nuclear Polarization Enhanced Solid-State NMR at Magnetic Fields up to 21.1 T. *J. Am. Chem. Soc.* **2018**, *140* (41), 13340–13349. <https://doi.org/10.1021/jacs.8b08081>.
- (201) Griffin, R. G.; Swager, T. M.; Temkin, R. J. High Frequency Dynamic Nuclear Polarization: New Directions for the 21st Century. *J. Magn. Reson.* **2019**, *306*, 128–133. <https://doi.org/10.1016/j.jmr.2019.07.019>.



---

## **CHAPTER 2**

---





# Chapter 2: Improved NMR transfer of magnetization from $^1\text{H}$ to half-integer quadrupolar nuclei at 20 and 62.5 kHz MAS

---

## 2.1 STATEMENT OF CONTRIBUTION

Chapter 2 of this thesis includes the outcome of a publication in *Magnetic Resonance*,<sup>1</sup> for which I am the first author and that has the following co-authors: Andrew G. M. Rankin, Julien Trébosc, Frédérique Pourpoint, Yu Tsutsumi, Hiroki Nagashima, Olivier Lafon and Jean-Paul Amoureux. In all cases, only my primary contribution towards this publication is included in this manuscript. I carried out the NMR experiments on  $\gamma$ -alumina and  $\text{AlPO}_4\text{-14}$ , analyzed the experimental data and assisted with the editing of the paper. I also performed some preliminary numerical simulations of spin dynamics using Simpson software in order to compare the performances of the different composite pulses. Nevertheless, these simulations are not included in the manuscript since they are performed under conditions different from those used in experiments. A. Rankin and J. Trébosc provided assistance in experimentation. Y. Tsutsumi contributed to the spin dynamics simulations and performed the NMR experiments on L-Histidine·HCl. H. Nagashima and F. Pourpoint contributed to the analysis and interpretation of the results. O. Lafon contributed to the experimental design, conducted the numerical evaluations of the average Hamiltonian theory for the recoupling schemes and assisted with the writing of the paper. J-P. Amoureux contributed to the analysis of the results, the experimental design and the writing of the paper. All authors contributed equally to the editing of the article.

## 2.2 INTRODUCTION

Half-integer quadrupolar nuclei ( $I = 3/2, 5/2, 7/2$  or  $9/2$ ) represent over 60% of the NMR-active isotopes.<sup>2</sup> They are in proximity with protons in a wide range of materials including nanoparticles, microporous and hybrid materials, heterogeneous catalysts and biomaterials.<sup>3-6</sup> In solid-state NMR, the proximities between these isotopes can be probed by transferring polarization from  $^1\text{H}$  to half-integer quadrupolar nuclei *via* heteronuclear dipolar couplings under MAS conditions.<sup>7-11</sup> In recent years, the

polarization transfer from protons, combined with dynamic nuclear polarization (DNP), have improved the sensitivity for the detection of quadrupolar nuclei. The sensitivity gain achieved with this approach has enabled the detection of quadrupolar nuclei, such as  $^{17}\text{O}$ ,  $^{27}\text{Al}$ ,  $^{67}\text{Zn}$ ,  $^{47,49}\text{Ti}$ ,  $^{95}\text{Mo}$  and  $^{43}\text{Ca}$ , near the surface of materials.<sup>12–20</sup>

The polarization transfer from  $^1\text{H}$  to half integer quadrupolar isotopes was first achieved by cross polarization (CP) under MAS conditions.<sup>21</sup> However, CPMAS lacks robustness and efficiency due to the spin-locking of the quadrupolar magnetization.<sup>22–24</sup> One of the main challenges of cross polarization involving quadrupolar nuclei is that it requires a careful adjustment of the applied RF-fields in order to fulfill one of the Hartmann-Hahn matching conditions:  $(S + 1/2)\nu_{1S} + \varepsilon\nu_{1H} = n\nu_R$ , where  $\nu_{1S}$  and  $\nu_{1H}$  denote the amplitudes of the RF-fields applied to the quadrupolar  $S$  isotope and to the  $^1\text{H}$ , respectively;  $\varepsilon = \pm 1$ ,  $n = \pm 1$  or  $\pm 2$  and  $\nu_R$  is the MAS frequency, while avoiding the rotatory resonance recoupling ( $R^3$ ) conditions,  $\nu_{1S} = p\nu_R/(S + 1/2)$  with  $p = 0, 1, 2$  and  $3$ .<sup>23,25</sup> In addition, the quadrupolar magnetization cannot be spin-locked efficiently for some crystallite orientations, which results in line-shape distortions.<sup>26–28</sup>

More recently, other schemes, such as PRESTO (phase shifted recoupling effects a smooth transfer of order)<sup>13,29,30</sup> (Fig. 13a,c) and  $D$ -RINEPT (through-space refocused INEPT)<sup>20,31</sup>, have facilitated the coherent transfer of polarization to half-integer quadrupolar isotopes and circumvent the limitations mentioned above. In these two techniques:

- i) No spin-lock is applied to the half-integer quadrupolar nucleus, which limits the polarization losses and improves the robustness to the  $C_Q$  value;
- ii) Only two or three CT selective pulses are applied on the quadrupolar nucleus, thus providing transfers that are robust to offsets on this channel;
- iii) Since they do not have to fulfill any RF-field matching condition, the transfers are robust to RF-field inhomogeneity.

Consequently, for these schemes the dipolar interactions between the proton and quadrupolar isotopes are reintroduced by symmetry-based  $\text{RN}_n^{\nu}$  recoupling schemes

that are applied on the  $^1\text{H}$  channel.<sup>32,33</sup> The PRESTO sequence uses  $\gamma$ -encoded recoupling schemes such as  $\text{R18}_2^5$ , which does not require the synchronization of the delays between successive recoupling periods with the MAS.<sup>34</sup> However, PRESTO sequence, like CPMAS, suffers from dipolar truncation, which prevents long-range transfers, and is sensitive to the  $^1\text{H}$  CSA.<sup>29</sup> In the case of  $D$ -RINEPT, non- $\gamma$ -encoded recoupling schemes, such as  $\text{SR4}_1^2$ ,<sup>33</sup> are used. Therefore, the recoupling periods must be rotor-synchronized. In addition,  $D$ -RINEPT is not affected by dipolar truncation, hence allowing for transfers over long distances. Furthermore, this sequence benefits from higher robustness to  $^1\text{H}$  CSA and RF-field inhomogeneities but, is more sensitive to  $^1\text{H}$ - $^1\text{H}$  dipolar interactions at low MAS frequencies owing to the low RF-field requirement of  $\text{SR4}_1^2$ ,  $\nu_1 = 2\nu_R$ .<sup>19,20,31</sup>

More recently, Nagashima *et al.* introduced a new variant of the  $D$ -RINEPT sequence which uses a novel variant of  $\text{SR4}_1^2$  recoupling and is more robust to the  $^1\text{H}$ - $^1\text{H}$  dipolar losses (Fig. 13b,c).<sup>19,20</sup> In this new sequence:

- (i) the  $\text{SR4}_1^2$  dipolar recoupling is built from tanh/tan (tt) adiabatic inversion pulses;
- (ii) continuous-wave (CW) irradiations are applied during the windows, in order to decouple  $^1\text{H}$ - $^1\text{H}$  interactions;
- (iii) composite  $\pi/2$  and  $\pi$  pulses are applied on the  $^1\text{H}$  channel to improve the robustness to RF inhomogeneities of the sequence and hence, its transfer efficiency.

This sequence, denoted as  $D$ -RINEPT-CWc- $\text{SR4}_1^2$ (tt) in the following, has proven to be more efficient than PRESTO and CPMAS at  $\nu_R = 12.5$  kHz, and has been combined with DNP to successfully detect the NMR signals of quadrupolar nuclei, especially those with small dipolar couplings with protons and/or small gyromagnetic ratios, such as  $^{47,49}\text{Ti}$ ,  $^{17}\text{O}$ ,  $^{95}\text{Mo}$  and  $^{67}\text{Zn}$ . In the case of quadrupolar nuclei with large coupling with protons,  $D$ -RINEPT-CWc- $\text{SR4}_1^2$ (tt) using only two pulses on the quadrupolar channel has shown to be more efficient than PRESTO.<sup>19</sup>

As mentioned above, polarization transfer methods like  $D$ -RINEPT can be applied for indirect DNP experiments where low spinning speeds are used (e.g.  $\nu_R = 12.5$

kHz). However, many experiments in solid-state NMR require the polarization transfer from  $^1\text{H}$  to half-integer quadrupolar isotopes at  $\nu_R > 12.5$  kHz. One reason for this, is that MAS frequencies greater than 20 kHz are required to avoid the overlapping of the bands of the CT and the spinning sidebands of STs, in particular for  $^{27}\text{Al}$  experiments recorded at 18.8 T. Second, through-space heteronuclear correlation (*D*-HETCOR) 2D spectra between  $^1\text{H}$  and the quadrupolar nucleus can be acquired at  $\nu_R \geq 60$  kHz with high resolution along the  $^1\text{H}$  dimension, since high MAS rates can average out the  $^1\text{H}$ - $^1\text{H}$  interactions.

The PRESTO and *D*-RINEPT recoupling schemes can be built from different composite pulses, which have been designed to improve their performances. Giovine *et al.* have demonstrated that the efficiency of PRESTO at  $\nu_R \geq 60$  kHz can be improved by using the  $\text{R16}_6^6$  recoupling built from composite  $\pi$  pulses, such as  $270_090_{180}$ .<sup>31</sup> This composite pulse, which is used as a basic inversion element, was proposed by Madhu *et al.* to improve the robustness to RF-field and offset.<sup>35</sup> Other recoupling schemes, such as  $\text{SR4}_1^2$  and  $\text{R12}_3^5$  built from  $90_{+45}90_{-45}90_{+45}$  composite pulses, have been proposed by Perras *et al.* recently to decrease the effect of  $^1\text{H}$ - $^1\text{H}$  interactions,<sup>36</sup> but up to now, have not been incorporated into the *D*-RINEPT transfers. Globally, no systematic study of the  $\text{RN}_n^v$  recouplings built from composite  $\pi$  pulses have been carried out.

This dissertation seeks to investigate the use of *D*-RINEPT-CWc pulse sequence with an adiabatic recoupling at the MAS frequencies of  $\nu_R = 20$  and 62.5 kHz. Through numerical simulations of spin dynamics and NMR experiments performed on  $\gamma$ -alumina and isopropylamine-templated microporous  $\text{AlPO}_4$ -14 (shorten  $\text{AlPO}_4$ -14 in the following), it was shown that the RF-field requirement of this sequence increases with the  $^1\text{H}$ - $^1\text{H}$  dipolar interactions present in the sample of study. In practice, this RF requirement is not compatible with most of the MAS probes specifications at  $\nu_R \geq 20$  kHz, even for moderate  $^1\text{H}$ - $^1\text{H}$  interactions. As an alternative, this study provides new variants of the PRESTO and *D*-RINEPT-CWc with recoupling schemes built from single rectangular or composite  $\pi$  pulses, that were selected by average Hamiltonian (AH) theory. Consequently, these new schemes were tested on  $\gamma$ -alumina and  $\text{AlPO}_4$ -14, which exhibit small and moderate  $^1\text{H}$ - $^1\text{H}$  dipolar interactions, respectively, and

identified the most efficient and robust  $^1\text{H}$ - $^{27}\text{Al}$  PRESTO and *D*-RINEPT transfers at  $B_0 = 18.8$  T with  $\nu_R = 20$  and 62.5 kHz. Finally, this study demonstrated how these magnetization transfers can be used to acquire 2D  $^1\text{H}$ - $^{27}\text{Al}$  HETCOR spectra at  $\nu_R = 62.5$  kHz using a non-uniform sampling (NUS)<sup>37</sup> scheme.

## 2.3 THEORETICAL BACKGROUND

### 2.3.1 Symmetry-based dipolar recouplings

Symmetry based elements are widely used in solid-state NMR under MAS conditions to achieve selective recoupling of the heteronuclear dipolar interactions.<sup>38</sup> The design of recoupling pulse sequences is based on the symmetry-based recoupling framework established by Levitt *et al.*<sup>38</sup> Two main families of pulse sequences are identified: The *C*- and *R*-type. In the *C*-type sequences, the basic element is a  $2\pi$  element, which is a RF cycle, and the pulse sequence is built by repeating this cycle with incremented phases. These cycles return the irradiated spins to their initial states in the absence of other interactions.<sup>32,39</sup> In the *R*-type sequences, the basic element is a  $\pi$  rotation element also known as  $\mathcal{R}$ . Recoupling of heteronuclear dipolar interaction by a  $CN_n^v$  or  $RN_n^v$  symmetry-based sequence requires to choose the *symmetry numbers*  $N$ ,  $n$  and  $v$ , which are integers, in order to recouple selectively the heteronuclear spin interactions, while decoupling other interactions, such as the effect of  $^1\text{H}$ - $^1\text{H}$  spin interactions, to first order in the AH theory.<sup>40</sup> The transformation properties of a given spin interaction with respect to the rotation of the samples and the rotation of the nuclear spin polarizations by RF pulses are described by the space and spin ranks, denoted  $l$  and  $\lambda$ , respectively.<sup>38</sup> The space rank  $l$  has  $2l+1$  components  $m$  that takes values between  $l$  and  $-l$ , whereas the spin rank  $\lambda$  has  $2\lambda+1$  components  $\mu$  ranging from  $-\lambda$  to  $\lambda$ . Therefore, different interaction Hamiltonians take different values of  $l$  and  $\lambda$ , which allows for the design of rotor synchronized pulse sequences in order to select the desired interaction and remove the unwanted ones.<sup>41</sup> For example, the CSA and heteronuclear dipolar coupling interactions both have  $(l, \lambda) = (2, 1)$ , whereas the homonuclear dipolar coupling has  $(l, \lambda) = (2, 2)$ .<sup>32</sup>

The recoupling sequences considered in this work correspond to the  $RN_n^V$  class, which have more selective selection rules than  $CN_n^V$  class. The  $RN_n^V$  scheme is obtained by repeating the pair  $\mathcal{R}_\phi \mathcal{R}'_{-\phi}$   $N/2$  times, with  $\phi = \pi\nu/N$  radians an overall phase shift.  $\mathcal{R}_\phi$  is an inversion pulse with a duration of  $nT_R/N$ , where  $T_R = 1/\nu_R$  is the rotor period, and  $\mathcal{R}'_{-\phi}$  is an inversion pulse derived from  $\mathcal{R}_\phi$  by changing the sign of all phases.  $\mathcal{R}$  and  $\mathcal{R}'$  are identical when they are amplitude-modulated, i.e. all phase shifts are multiple of  $\pi$ . The rf-field requirement of  $RN_n^V$  is equal to:

$$\nu_1 = \frac{N}{n} \frac{\xi^{tot}}{2\pi} \nu_R, \quad (1)$$

where  $\xi^{tot} = \sum_{i=1}^P \xi^i$  is the sum of the flip angles of the  $P$  individual pulses of the  $\mathcal{R}$  element. The element  $\mathcal{R}$  must rotate the resonant spins through the angle  $\pi$  about the x-axis of the rotating frame, in the absence of other spin interactions.<sup>42</sup> Consequently,  $\mathcal{R}$  can be a  $\pi$  pulse with phase  $\phi = 0$ , a composite pulse, or a pulse with shaped amplitude and modulated frequency.<sup>32</sup> Fig. 12 displays two of the recoupling schemes employed in this work: symmetry-based scheme  $R22_2^7$  built from  $180_0$  pulses and  $R16_7^6$  scheme built from composite  $270_0 90_{180}$  inversion pulses, where the phases of the individual rectangular pulses forming the composite pulse are indicated as subscripts. The  $R22_2^7$  scheme consists of a repetition of two-pulse element  $180_{57.27} 180_{-57.27}$  and the required RF-field strength corresponds to a nutation frequency of 5.5 times the MAS frequency. This  $R16_7^6$  scheme consists of a repetition of four-pulse element  $270_{67.5} 90_{247.5} 270_{-67.5} 90_{115.7}$  and its RF-field strength then corresponds to a nutation frequency of 2.28 times the MAS frequency.

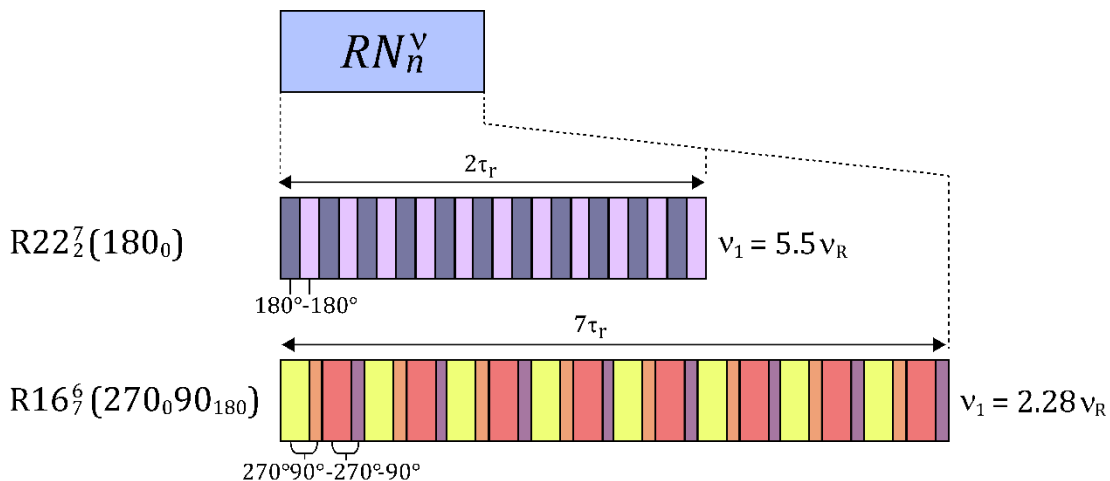


**Figure 12.** Schematic representation of two  $RN_n^v$  schemes employed in this work:  $R22_2^7$  built from rectangular  $180_0$  pulses and  $R16_7^6$  built from composite  $270_0 90_{180}$  pulses.

In general,  $RN_n^v$  schemes can be classified as non  $\gamma$ -encoded and  $\gamma$ -encoded. The definition of  $\gamma$ -encoding is derived from the fact that the amplitude of the recoupled AH does not depend on the  $\gamma$  Euler angle.<sup>34,40,43</sup> The non- $\gamma$ -encoded  $RN_n^v$  sequences are compatible with the use of supercycle, in order to improve the robustness to unwanted terms, such as  $^1\text{H}$ - $^1\text{H}$  dipolar interactions or  $^1\text{H}$  CSA. For example,  $SR4_1^2$  scheme, which uses a three-step multiple-quantum supercycle, is widely used for heteronuclear recoupling with protons in  $D$ -HMQC<sup>44</sup> and  $D$ -RINEPT<sup>31</sup> experiments. Conversely,  $\gamma$ -encoded  $RN_n^v$  sequences can provide a maximum transfer efficiency 25% higher than their non- $\gamma$ -encoded counterparts.<sup>45</sup> Furthermore, they do not require the synchronization with MAS of the delay between successive recoupling periods.

### 2.3.2 Scaling factor $\kappa$

The recoupling of heteronuclear dipolar interactions in  $RN_n^v$  scheme is scaled by a factor  $\kappa$ , which theoretically depends on the chosen symmetry numbers  $N$ ,  $n$  and  $v$  as well as the basic inversion element.<sup>38</sup> In order to accelerate the coherence transfer, it is desirable to use symmetry schemes providing large scaling factors.<sup>40,42</sup> In particular, this is important when carrying out experiments that involve the reintroduction of weak couplings  $b_{ij}$ , that carry valuable long-range structural information and therefore, require the application of the recoupling sequence over long-time intervals.<sup>42</sup>

### 2.3.3 Adiabatic pulses

Adiabatic RF pulses play an important role in spin inversion due to their robustness to RF-field inhomogeneity and resonance offsets.<sup>46</sup> They utilize the adiabatic principle wherein the magnetization vector  $\mathbf{M}$  is manipulated by a slow passage (adiabatic) of the effective magnetic field  $\mathbf{B}_{\text{eff}}$  through resonance. The advantage of this adiabatic passage (or sweep) is that spins having different resonant frequencies are inverted or manipulated at different times.<sup>47</sup> To achieve broadband inversion, this sweep rate must satisfy the adiabatic condition which is expressed by:<sup>48,49</sup>

$$|d\theta/dt| \ll \omega_{\text{eff}} \quad (2)$$

where  $\omega_{\text{eff}} = \gamma |\mathbf{B}_{\text{eff}}|$  is the effective field expressed in angular frequency units, given by the resultant of the applied radiofrequency field  $\omega_1 = \gamma |\mathbf{B}_1|$  and the resonance offset  $\Delta\omega = \gamma |\Delta\mathbf{B}|$ , and  $\theta$  is the angle made by  $\mathbf{B}_{\text{eff}}$  with the  $+x$  axis. This is often rearranged into an **adiabaticity factor**  $Q$  defined as:

$$Q = \omega_{\text{eff}} / |d\theta/dt| \quad (3)$$

which should be sufficiently larger than unity. Thus, the adiabatic condition can be met by ensuring that the sweep speed is sufficiently slow or that the magnitude of  $\mathbf{B}_{\text{eff}}$  is sufficiently large.<sup>50</sup>

Adiabatic pulses usually consist of a frequency- and amplitude modulated pulse, which creates  $\mathbf{B}_{\text{eff}}$  that sweeps adiabatically from an initial orientation parallel to the applied magnetic field  $\mathbf{B}_0$  to finish antiparallel to it (adiabatic full passage AFP).<sup>50,51</sup> These type of pulses can be implemented by means of tanh/tan pulses (denoted tt hereafter), which are relatively short, an advantage for solid-state NMR, and employs a hyperbolic tangent (tanh) modulation of the RF-field amplitude and a tangent (tan) sweep of the frequency.<sup>52</sup>

During the (tt) pulse, the instantaneous rf-amplitude is equal to:

$$\omega_1(t) = \omega_{1,\text{max}} \begin{cases} \tanh \left[ \frac{8\xi t}{T_R} \right] & 0 \leq t < T_R/8 \\ \tanh \left[ 2\xi \left( 1 - \frac{4t}{T_R} \right) \right] & T_R/8 \leq t < T_R/4 \end{cases} \quad (4)$$

where  $\omega_{1,\text{max}}$  is the peak amplitude of the rf-field,  $t$  refers to the time since the start of the pulse, which lasts  $T_R/4$  when incorporated into the SR4<sub>1</sub><sup>2</sup> recoupling scheme. The



parameter  $\xi$  determines the rise and fall times of the pulse. Hence, in the frequency-modulated (FM) frame,<sup>47</sup> the phase is

$$\phi_I(t) = \frac{\Delta\nu_{0,\max}}{2\theta\tan(\theta)} \ln \left\{ \cos \left[ \theta \left( 1 - 8 \frac{t}{T_R} \right) \right] \right\}. \quad (5)$$

where  $\Delta\nu_{0,\max}$  is the peak amplitude of the carrier frequency modulation and  $\theta$  determines the frequency sweep rate in the center of the pulse. Here,  $\xi = 10$  and  $\theta = 87^\circ = \text{atan}(20)$  were employed.<sup>20,53,54</sup>

However, one drawback of adiabatic pulses is that they require high RF power compared with rectangular pulses,<sup>55</sup> which is usually not compatible with the RF power specifications of most MAS probes.

### 2.3.4 PRESTO-III sequence

In the PRESTO sequence (Fig. 13a,c), symmetry-based  $\gamma$ -encoded  $RN_n^\gamma$  schemes applied to the  $^1\text{H}$  channel reintroduce the  $|m| = 2$  space components and the single-quantum (SQ) terms of the hetero-nuclear dipolar couplings between the protons and the quadrupolar nuclei, as well as the  $^1\text{H}$  CSA, while they suppress the contributions of  $^1\text{H}$  isotropic chemical shifts, the hetero-nuclear  $J$ -couplings with protons, and the  $^1\text{H}$ - $^1\text{H}$  dipolar couplings to the first-order AH.<sup>30</sup> As mentioned above, the hetero-nuclear dipolar interaction is characterized by a space rank  $l = 2$  and a spin rank  $\lambda = 1$ . A  $\gamma$ -encoded  $|m| = 2$  SQ hetero-nuclear dipolar recoupling must selectively reintroduce the two components  $\{l, m, \lambda, \mu\} = \{2, 2, 1, \mu\}$  and  $\{2, -2, 1, -\mu\}$  of the hetero-nuclear dipolar coupling and  $^1\text{H}$  CSA with  $\mu = \pm 1$ , while all other components must be suppressed.

During these recoupling schemes, the contribution of the dipolar coupling between  $I = ^1\text{H}$  and  $S$  nuclei to the first-order Hamiltonian is equal to<sup>30</sup>:

$$\bar{H}_{D,IS}^{(1)} = \omega_{D,IS} S_Z [I^+ \exp(i2\varphi) + I^- \exp(-i2\varphi)], \quad (6)$$

where  $I^\pm = I_x \pm iI_y$  are the shift operators, and the magnitude and phase of the recoupled  $I$ - $S$  dipolar coupling are given by

$$\omega_{D,IS} = -\kappa \frac{\sqrt{3}}{2} b_{IS} \sin^2(\beta_{PR}^{D,IS}) \quad (7)$$

$$\text{and } \varphi = \gamma_{PR}^{D,IS} - \omega_R t^0, \quad (8)$$

respectively, where  $b_{IS}$  is the dipolar coupling constant in rad/s, and  $\kappa$  is the scaling factor of the recoupled hetero-nuclear dipolar interaction, which depends on the  $RN_n^V$  symmetry and the  $\mathcal{R}$  element. The Euler angles  $\{0, \beta_{PR}^{D,IS}, \gamma_{PR}^{D,IS}\}$  relate the  $I$ - $S$  vector to the MAS rotor frame, and  $t^0$  refers to the starting time of the recoupling. The norm of  $\bar{H}_{D,IS}^{(1)}$  does not depend on the  $\gamma_{PR}^{D,IS}$  angle, since these recoupling schemes are  $\gamma$ -encoded.<sup>34,43</sup> The Hamiltonian of Eq. 6 does not commute among different spin pairs, and hence, the PRESTO sequence is affected by dipolar truncation, *i.e.*, the transfer to distant nuclei is attenuated by the stronger couplings with nearby spins<sup>56</sup>.

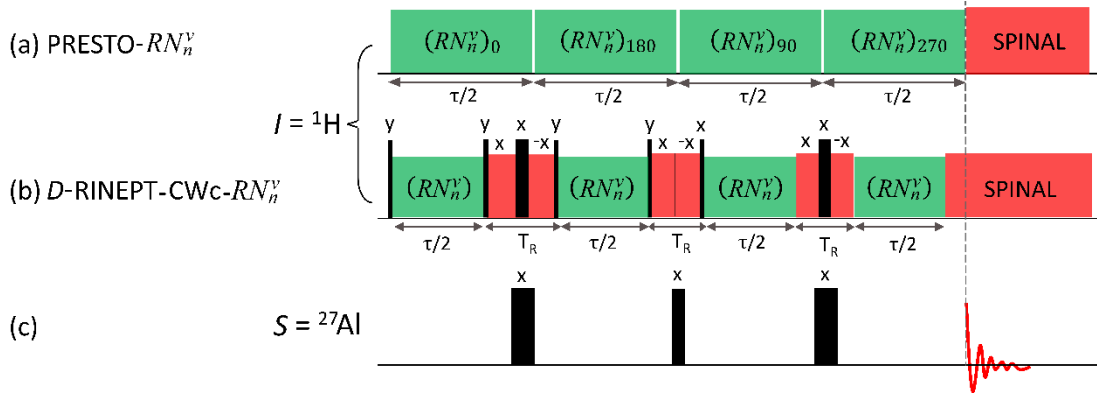


**Figure 13.**  $^1\text{H} \rightarrow ^{27}\text{Al}$  (a,c) PRESTO- $RN_n^V$  and (b,c) D-RINEPT-CWc- $RN_n^V$  pulse sequences. Those applied to  $^1\text{H}$  and  $^{27}\text{Al}$  channels are shown in (a,b) and (c), respectively. The narrow and broad black bars represent  $\pi/2$  and  $\pi$ -pulses, respectively. The acquisition of the FIDs (indicated with the vertical dashed line) starts after (a) the end of the  $RN_n^V$  block in the case of PRESTO or (b) on top of the echo shifted with  $\tau_R/2$  with respect to the end of the last recoupling block in the case of RINEPT.

As mentioned above, the SQ hetero-nuclear dipolar recoupling schemes also reintroduce the  $^1\text{H}$  CSA with the same scaling factor  $\kappa$ . However, this term does not commute with the recoupled  $^1\text{H}$ - $S$  dipolar interactions. Therefore, in the case of large  $^1\text{H}$  CSA, for instance at high magnetic fields, this interaction can interfere with the  $^1\text{H}$ - $S$  dipolar couplings, especially with the small ones. These interferences can be limited by the use of the PRESTO-III variant, depicted in Fig. 13a,c<sup>30</sup>, in which three CT-

selective pulses are applied to the  $S$  channel. Indeed, the CT-selective  $\pi$ -pulses partly refocus the  $^1\text{H}$  CSA, which limits these interferences.

### 2.3.5 Recoupling schemes for PRESTO

PRESTO using schemes, such as  $\text{R18}_1^7$  and  $\text{R18}_2^5$ , built from single rectangular  $\pi$ -pulses has been used for hetero-nuclear dipolar recoupling at moderate MAS frequencies ( $\nu_R \approx 10$  kHz)<sup>32</sup>. Other schemes, such as  $\text{R12}_5^4$ ,  $\text{R14}_6^5$ ,  $\text{R16}_7^6$ ,  $\text{R14}_8^5$ ,  $\text{R18}_8^7$ ,  $\text{R16}_9^6$ ,  $\text{R20}_9^8$  and  $\text{R18}_{10}^7$  using composite  $(270_090_{180})$  pulses, were applied for the measurement of  $^1\text{H}$  CSA at fast MAS frequencies,  $\nu_R \approx 60$ -70 kHz.<sup>57</sup> More recently, Giovine *et al.*, used PRESTO with  $\text{R16}_3^2$  recoupling built from a single rectangular  $\pi$ -pulse to transfer the  $^1\text{H}$  polarization to  $^{27}\text{Al}$  nuclei at  $\nu_R = 62.5$  kHz.<sup>31</sup>

In this work,  $\text{RN}_n^V$  schemes built from single rectangular and composite  $\pi$ -pulses to achieve  $\gamma$ -encoded  $|m| = 2$  hetero-nuclear SQ dipolar recoupling at  $\nu_R = 20$  or 62.5 kHz, were selected based on the AH and spin dynamics simulations. Three types of composite  $\pi$  pulses were tested:

- i)  $(270_090_{180})$ , which is designed to be offset compensated and amplitude modulated, thus improving the robustness to RF inhomogeneity. This composite pulse has been used as a basic element in several  $\text{RN}_n^V$  sequences;<sup>31,38,39,57</sup>
- ii)  $(90_0240_{90}90_0)$ , which compensates both RF inhomogeneity and offset;<sup>58,59</sup> and
- iii)  $(90_{-45}90_{45}90_{-45})$ , which was introduced by Madhu *et al.*, exhibits homo-nuclear decoupling properties.<sup>60</sup>

Adiabatic pulses cannot be employed for SQ hetero-nuclear dipolar recoupling since they yield vanishing scaling factors for the rotational components with  $\mu \neq 0$ <sup>54</sup>.

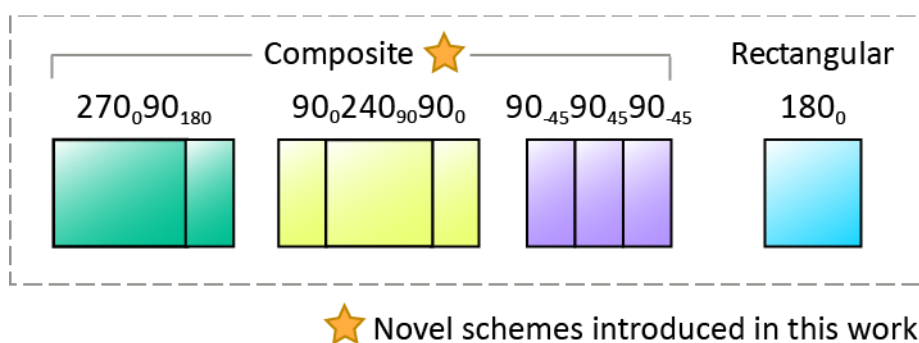


**Figure 14.** Type of pulses employed in  $RN_n^\nu$  sequences for PRESTO-III.

Regarding the  $RN_n^\nu$  symmetries, a total of 109 symmetries with  $2 \leq N \leq 30$ ,  $2 \leq n \leq 7$  and  $1 \leq \nu \leq 11$  were found which recouple the  $\{2, \pm 2, 1, \pm 1\}$  or  $\{2, \mp 2, 1, \pm 1\}$  rotational components of the  $^1\text{H-S}$  dipolar coupling and  $^1\text{H CSA}$ . The  $RN_n^\nu$  recouplings were selected based on those symmetries with RF-field limited to  $\nu_1 \leq 120$  and  $190$  kHz for  $\nu_R = 20$  and  $62.5$  kHz, respectively. The  $RN_n^\nu$  symmetries with  $45 \leq \phi \leq 135^\circ$  ( $\phi = \pi\nu/N$ ) were only considered since sequences with  $\phi$  close to  $90^\circ$  are better compensated for RF-field errors and inhomogeneities.<sup>61</sup> A schematic representation of this selection is presented in Fig. 15. The scaling factor,  $\kappa$ , of the recoupled  $^1\text{H-S}$  dipolar interaction was calculated using the ‘C and R symmetries’ Mathematica package<sup>39,62–64</sup>.

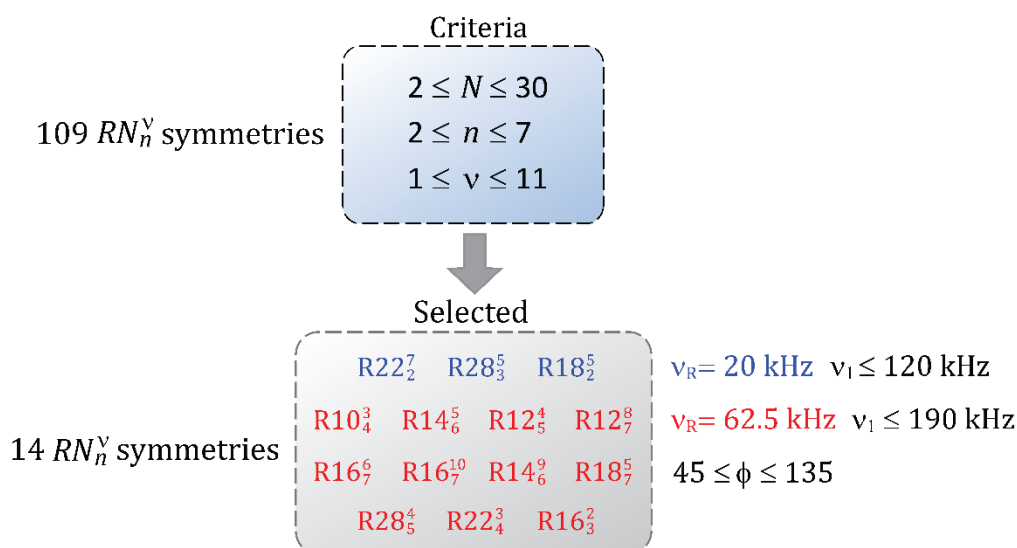


**Figure 15.** Schematic representation of the selection of  $RN_n^\nu$  schemes for PRESTO based on the symmetry numbers  $N$ ,  $n$  and  $\nu$ , the RF requirement and the  $\phi$  angle. The selected  $RN_n^\nu$  schemes are presented in Tables 3-5.

The corresponding selected  $RN_n^V$  sequences are listed in Tables 3 and 4 for  $\nu_R = 20$  and 62.5 kHz, respectively. These  $RN_n^V$  symmetries eliminate the contribution of  $^1\text{H}$ - $^1\text{H}$  dipolar interactions to the first-order Hamiltonian, but not their contribution to the second-order. The magnitude of the cross-terms between  $^1\text{H}$ - $^1\text{H}$  interactions in the second-order Hamiltonian was calculated with the Euclidean norm  $\|\kappa_{\{1,2\}}^{DD_1 \times DD_2}\|_2$ , for the selected symmetries (Annex 1).<sup>64</sup> Likewise, the magnitude of the cross terms between  $^1\text{H}$  CSA or offset were also calculated. with the Euclidean norms  $\|\kappa_{\{1,2\}}^{CSA \times CSA}\|_2$  and  $\|\kappa_{\{1,2\}}^{\delta iso \times \delta iso}\|_2$ , respectively. The calculated values of these three parameters are presented in the last three columns of the Tables 3 and 4.

For  $\nu_R = 20$  kHz, according to the AH, the  $RN_n^V$  sequence with the highest robustness to  $^1\text{H}$ - $^1\text{H}$  dipolar interactions is  $R22_2^7(180_0)$ . However, this recoupling is slightly less robust to  $^1\text{H}$  offset than  $R18_2^5(180_0)$ , which has already been reported. For this MAS frequency, the  $RN_n^V$  schemes using the chosen composite pulses either required RF-fields greater than 120 kHz, e.g.  $\nu_1 = 130$  and 173 kHz for the  $R26_3^7$  schemes built from  $(90_{-45}90_{45}90_{-45})$  and  $(270_090_{180})$  pulses, or did not suppress efficiently the second-order cross-terms between  $^1\text{H}$ - $^1\text{H}$  interactions because of small RF-field ( $\nu_1 \leq 62.5$  kHz).

**Table 3.** Selected  $RN_n^V$   $|m| = 2$  SQ hetero-nuclear dipolar recoupling for  $\nu_R = 20$  kHz.

$\mathcal{R}$	$RN_n^V$	$\phi^\circ$	$\nu_1/\nu_R$	$\kappa$	$\kappa/\ \kappa_{\{1,2\}}^{DD_1 \times DD_2}\ _2$	$\kappa/\ \kappa_{\{1,2\}}^{CSA \times CSA}\ _2$	$\kappa/\ \kappa_{\{1,2\}}^{\delta iso \times \delta iso}\ _2$
	$R22_2^7$	57	5.5	0.178	162	7.12	17.58
180 <sub>0</sub>	$R28_3^5$	51	4.67	0.176	156	5.08	18.29
	$R18_2^5$	50	4.5	0.175	140	7.20	18.49

For  $\nu_R = 62.5$  kHz, the  $RN_n^V$  sequences using composite  $\pi$ -pulses recouple the  $^1\text{H}$ -S dipolar interaction with a higher scaling factor than those built from single  $\pi$ -pulses. According to AH, the  $(90_0240_9090_0)$  basic element leads to the highest robustness to  $^1\text{H}$ - $^1\text{H}$  interferences. Even if the amplitude of the cross-terms is inversely proportional to the MAS frequency (Table 5), the amplitude of these terms is lower at  $\nu_R = 20$  than 62.5 kHz. The  $(270_090_{180})$  element is less robust to  $^1\text{H}$ - $^1\text{H}$  interferences, but benefits from a high robustness to offset. The selected  $RN_n^V$  symmetries for this element include

R14<sub>6</sub><sup>5</sup> and R16<sub>7</sub><sup>6</sup>, which have already been employed for the measurement of <sup>1</sup>H CSA and the transfer of <sup>1</sup>H polarization to half-integer quadrupolar nuclei at  $\nu_R \geq 60$  kHz.<sup>31,57</sup> The scaling factors  $\kappa$  of the <sup>1</sup>H-S dipolar interaction of the  $RN_n^V$  schemes built from single  $\pi$ -pulses are small with  $45 \leq \phi \leq 135^\circ$ , and hence the schemes given in Table 4 were also selected with an extended  $\phi$  range of 20-160°. These recoupling schemes are less robust to offset than the  $RN_n^V$  schemes built from (270<sub>0</sub>90<sub>180</sub>) element.

**Table 4.** Selected  $RN_n^V$   $|m| = 2$  SQ hetero-nuclear dipolar recoupling with  $45^\circ \leq \phi \leq 135^\circ$  for  $\nu_R = 62.5$  kHz.

$\mathcal{R}$	$RN_n^V$	$\phi^\circ$	$\nu_1/\nu_R$	$\kappa$	$\frac{\kappa}{\ \kappa_{\{1,2\}}^{DD_1 \times DD_2}\ _2}$	$\frac{\kappa}{\ \kappa_{\{1,2\}}^{CSA \times CSA}\ _2}$	$\frac{\kappa}{\ \kappa_{\{1,2\}}^{\delta iso \times \delta iso}\ _2}$
90 <sub>0</sub> 240 <sub>90</sub> 90 <sub>0</sub>	R10 <sub>4</sub> <sup>3</sup>	54	2.92	0.227	39.63	2.82	12.63
	R14 <sub>6</sub> <sup>5</sup>	64.3	2.72	0.232	36.33	1.87	12.39
	R12 <sub>5</sub> <sup>4</sup>	60	2.80	0.230	36.08	2.25	12.47
	R12 <sub>7</sub> <sup>8</sup>	120	2.00	0.227	35.96	1.61	7.72
270 <sub>0</sub> 90 <sub>180</sub>	R16 <sub>7</sub> <sup>6</sup>	67.5	2.28	0.150	17.96	1.85	$3.50 \times 10^{10}$
	R16 <sub>7</sub> <sup>10</sup>	112.5	2.28	0.150	17.96	1.85	$3.50 \times 10^{10}$
	R14 <sub>6</sub> <sup>5</sup>	64.3	2.33	0.150	15.90	2.33	$3.58 \times 10^{10}$
	R14 <sub>6</sub> <sup>9</sup>	115.7	2.33	0.150	15.90	2.15	$3.58 \times 10^{10}$
90 <sub>-45</sub> 90 <sub>45</sub> 90 <sub>-4</sub>	R10 <sub>4</sub> <sup>3</sup>	54	1.88	0.186	16.70	2.97	15.07
	R18 <sub>7</sub> <sup>5</sup>	50	1.93	0.189	15.73	1.98	25.49
	R14 <sub>6</sub> <sup>5</sup>	64.3	1.75	0.177	15.55	2.09	5.49
	R12 <sub>5</sub> <sup>4</sup>	60	1.80	0.181	15.17	2.47	8.11
180 <sub>0</sub>	R14 <sub>6</sub> <sup>5</sup>	64.3	1.16	0.085	5.35	2.26	1.34
	R14 <sub>6</sub> <sup>9</sup>	115.7	1.16	0.085	5.35	2.26	1.34
	R16 <sub>7</sub> <sup>6</sup>	67.5	1.14	0.082	4.90	1.98	1.09
	R16 <sub>7</sub> <sup>10</sup>	112.5	1.14	0.082	4.90	1.98	1.09

**Table 5.** Selected  $RN_n^V$   $|m| = 2$  SQ hetero-nuclear dipolar recoupling built from single  $\pi$  pulses with  $20^\circ \leq \phi \leq 160^\circ$  and  $\kappa \geq 0.15$  for  $\nu_R = 62.5$  kHz.

$\mathcal{R}$	$RN_n^V$	$\phi / ^\circ$	$\nu_1/\nu_R$	$\kappa$	$\kappa / \ \kappa_{\{1,2\}}^{DD_1 \times DD_2}\ _2$	$\kappa / \ \kappa_{\{1,2\}}^{CSA \times CSA}\ _2$	$\kappa / \ \kappa_{\{1,2\}}^{\delta iso \times \delta iso}\ _2$
180 <sub>0</sub>	R28 <sub>5</sub> <sup>4</sup>	25.7	2.75	0.163	24.42	3.34	26.42
	R22 <sub>4</sub> <sup>3</sup>	24.5	2.75	0.162	22.84	4.10	27.24
	R16 <sub>3</sub> <sup>2</sup>	22.5	2.67	0.161	16.26	5.21	28.89

### 2.3.6 *D*-RINEPT sequence

In the *D*-RINEPT sequence, the  $^1\text{H}$ -*S* dipolar interactions are reintroduced under MAS by applying a non- $\gamma$ -encoded two-spin order dipolar recoupling to the  $^1\text{H}$  channel. These schemes reintroduce the  $|m|=2$  space components and the zero-quantum (0Q) terms of the  $^1\text{H}$ -*S* dipolar interaction and  $^1\text{H}$  CSA, *i.e.*, the rotational components  $\{l, m, \lambda, \mu\} = \{2, \pm 2, 1, 0\}$ , while they suppress the contributions of  $^1\text{H}$  isotropic chemical shifts, the hetero-nuclear *J*-couplings with protons, and the  $^1\text{H}$ - $^1\text{H}$  dipolar couplings to the first-order AH.<sup>33,61</sup> The contribution of the  $^1\text{H}$ -*S* dipolar coupling to this Hamiltonian is equal to:<sup>31,33,65</sup>

$$\bar{H}_{D,IS}^{(1)} = 2\omega_{D,IS}I_zS_z \quad (9)$$

$$\text{where } \omega_{D,IS} = \kappa b_{IS} \sin^2(\beta_{PR}^{D,IS}) \cos(2\varphi). \quad (10)$$

The norm of  $\bar{H}_{D,IS}^{(1)}$  depends on the  $\varphi$  phase, given by Eq. 8, and hence on the  $\gamma_{PR}^{D,IS}$  angle. Therefore, these two-spin order dipolar recoupling schemes are non- $\gamma$ -encoded. The Hamiltonian of Eq. 9 commutes among different spin pairs and hence, these recoupling schemes are not affected by dipolar truncation. Similarly, the recoupled  $^1\text{H}$  CSA contribution to the first-order Hamiltonian is proportional to  $I_z$  and hence, also commutes with the recoupled  $^1\text{H}$ -*S* dipolar interactions and does not interfere with the hetero-nuclear dipolar recoupling.

The new *D*-RINEPT-CWc sequence introduced by Nagashima *et al.*,<sup>19,20</sup> is displayed in Fig. 13b,c. The  $^1\text{H}$ -*S* dipolar couplings are reintroduced by applying the  $RN_n^\nu$  schemes, such as  $\text{SR}4_1^2$ , during the defocusing and refocusing delays  $\tau$ , which are identical in this article, even if distinct delays can improve the transfer efficiency.<sup>19</sup> As the two-spin order recoupling schemes are non- $\gamma$ -encoded, they must be rotor-synchronized. A delay of  $T_R$  is used between two successive  $RN_n^\nu$  blocks. In the *D*-RINEPT-CWc sequence, a CW irradiation is applied during these delays in order to limit the losses due to  $^1\text{H}$ - $^1\text{H}$  dipolar interactions.<sup>19</sup> The nutation during this CW irradiation is eliminated by employing CW irradiations with opposite phases. Furthermore, the robustness to  $^1\text{H}$  rf-field inhomogeneity is improved by replacing the first  $\pi$  and second  $\pi/2$  pulses by composite  $(90_0180_{90}90_0)$  and  $(90_{90}90_0)$  pulses, respectively, the CW irradiation being applied between the individual pulses.<sup>58,66</sup>

### 2.3.7 Recoupling schemes for *D*-RINEPT

Different  $RN_n^\nu$  sequences have been proposed to achieve non- $\gamma$ -encoded  $|m| = 2$  two-spin order dipolar recoupling, including:

- i) symmetries  $R(4n)_n^{2n-1} = R12_3^5, R16_4^7, R20_5^9, R24_6^{11}, R28_7^{13}$  and  $R32_8^{15}$  for  $n = 3, 4, 5, 6, 7$  and  $8$  using single  $\pi$ -pulses as basic element, which have been employed to measure  $^1\text{H}$ - $^{17}\text{O}$  dipolar couplings at  $\nu_R = 50$  kHz,<sup>61</sup>
- ii)  $SR4_1^2$  recoupling built from a single  $\pi$ -pulse, which corresponds to the  $[R4_1^2R4_1^{-2}]_0[R4_1^2R4_1^{-2}]_{120}[R4_1^2R4_1^{-2}]_{240}$  sequence and has been employed in the RINEPT scheme,<sup>19,31</sup>
- iii)  $R12_3^5$  and  $SR4_1^2$  schemes using a  $(90_{-45}90_{45}90_{-45})$  composite  $\pi$ -pulse as a basic element, which have been incorporated into *D*-HMQC at  $\nu_R = 36$  kHz,<sup>36</sup> and
- iv)  $SR4_1^2$  schemes built from a (tt) adiabatic pulse, which have been used in the RINEPT sequence.<sup>19,20</sup>

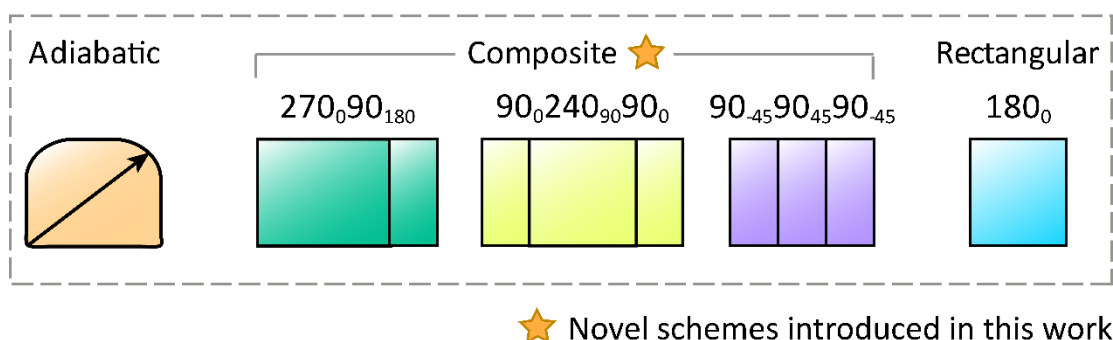


**Figure 16.** Type of pulses employed in  $RN_n^\nu$  sequences for *D*-RINEPT-CWc.

In this work, the  $RN_n^\nu$  schemes built from  $(180_0)$ ,  $(270_0 90_{180})$ ,  $(90_0 240_{90} 90_0)$  and  $(90_{-45} 90_{45} 90_{-45})$  inversion elements were selected. A total of 58  $RN_n^\nu$  symmetries with  $2 \leq N \leq 30$ ,  $2 \leq n \leq 7$  and  $1 \leq \nu \leq 11$  were found which recouple the  $\{2, \pm 2, 1, 0\}$  rotational components of the  $^1\text{H}$ -*S* dipolar coupling and  $^1\text{H}$  CSA. The  $RN_n^\nu$  symmetries with  $60 \leq \phi \leq 120^\circ$  were only considered since the currently employed non- $\gamma$ -encoded  $|m| = 2$  two-spin order hetero-nuclear dipolar recoupling schemes have  $75 \leq \phi \leq 90^\circ$ . A schematic representation of this selection is presented in Fig. 17.

The selected  $RN_n^\nu$  sequences are listed in Table 6, along with the parameters of the  $SR4_1^2$  schemes built from the different basic elements  $\mathcal{R}$  for the sake comparison. The



scaling factor,  $\kappa$ , of the recoupled  $^1\text{H}$ -S dipolar interaction was calculated using the ‘*C* and *R* symmetries’ Mathematica package.<sup>39,62–64</sup> In addition, the amplitudes of the cross-terms between  $^1\text{H}$ - $^1\text{H}$  interactions,  $^1\text{H}$  CSA and offset were calculated with the Euclidean norms  $\|\kappa_{\{1,2\}}^{DD_1 \times DD_2}\|_2$ ,  $\|\kappa_{\{1,2\}}^{CSA \times CSA}\|_2$  and  $\|\kappa_{\{1,2\}}^{\delta iso \times \delta iso}\|_2$ , respectively. They are presented in the last three columns of the Table 6.

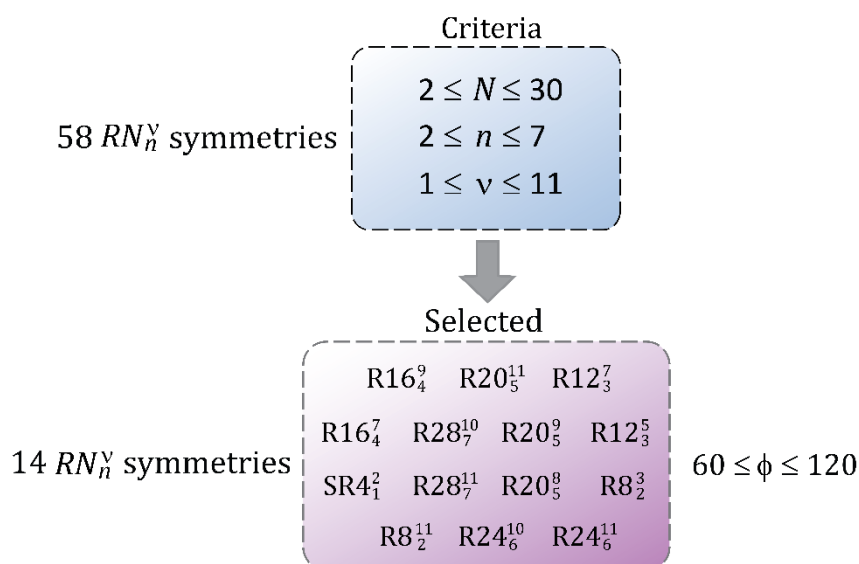


**Figure 17.** Schematic representation of the selection of  $RN_n^v$  schemes for *D*-RINEPT-CWc based on the symmetry numbers  $N$ ,  $n$  and  $v$ , and the  $\phi$  angle. The selected  $RN_n^v$  schemes are presented in Table 6.

According to the AH, the  $(90_0 240_{90} 90_0)$  composite  $\pi$ -pulse yields the highest robustness to  $^1\text{H}$ - $^1\text{H}$  dipolar interactions. However, the rf-field requirement of the  $RN_n^v$  sequences built from this composite pulse,  $v_1 = 1.16Nv_R/n$ , is not compatible at  $v_R = 62.5$  kHz with most 1.3 mm MAS probes (e.g.  $v_1 = 291$  kHz for  $SR4_1^2$ ). Furthermore, the highest robustness to  $^1\text{H}$  CSA and offset is achieved using the  $(270_0 90_{180})$  composite  $\pi$ -pulse. The  $SR4_1^2$  schemes benefit from the highest robustness to  $^1\text{H}$  CSA, because of the three-step multiple-quantum super-cycle.<sup>33,64</sup> Contrary to the  $RN_n^v$  with  $|m| = 2$  SQ hetero-nuclear dipolar recouplings, the rf-field of the  $RN_n^v$  with  $|m| = 2$  two-spin order schemes is always higher than  $2v_R$  since these symmetries with  $2n > N$ , such as  $R12_3^5$ , have smaller  $\kappa$  scaling factors for the basic elements employed here.

**Table 6.** Selected  $RN_n^V$   $|m| = 2$  two-spin order hetero-nuclear dipolar recoupling.

$\mathcal{R}$	$RN_n^V$	$\phi^\circ$	$v_I/v_R$	$\kappa$	$\kappa/\left\ \kappa_{\{1,2\}}^{DD_1 \times DD_2}\right\ _2$	$\kappa/\left\ \kappa_{\{1,2\}}^{CSA \times CSA}\right\ _2$	$\kappa/\left\ \kappa_{\{1,2\}}^{\delta iso \times \delta iso}\right\ _2$
$90_0 240_{90} 90_0$	R16 <sub>4</sub> <sup>9</sup>	101	4.66	0.131	63.17	16.48	9.31
	R20 <sub>5</sub> <sup>11</sup>	99	4.66	0.131	60.68	16.59	14.45
	R12 <sub>3</sub> <sup>7</sup>	105	4.66	0.131	51.25	16.11	9.70
	R16 <sub>4</sub> <sup>7</sup>	79	4.66	0.131	45.52	15.76	13.60
	R28 <sub>7</sub> <sup>10</sup>	64	4.66	0.131	44.55	14.06	11.98
	R20 <sub>5</sub> <sup>9</sup>	81	4.66	0.131	44.30	15.95	14.46
	R12 <sub>3</sub> <sup>5</sup>	75	4.66	0.131	43.91	15.40	12.83
	SR4 <sub>1</sub> <sup>2</sup>	90	4.66	0.131	42.37	22.65	10.48
$90_{-45} 90_{45} 90_{-4}$	R28 <sub>7</sub> <sup>11</sup>	71	3	0.191	39.81	10.05	6.10
	R20 <sub>5</sub> <sup>8</sup>	72	3	0.191	39.74	10.26	5.49
	R8 <sub>2</sub> <sup>3</sup>	67.5	3	0.191	39.43	9.42	7.88
	R8 <sub>2</sub> <sup>11</sup>	67.5	3	0.191	39.43	9.42	7.88
	R24 <sub>6</sub> <sup>10</sup>	75	3	0.191	39.32	10.66	4.22
	R28 <sub>7</sub> <sup>10</sup>	64.3	3	0.191	38.82	8.65	10.13
	R12 <sub>3</sub> <sup>5</sup>	75	3	0.191	38.33	10.66	4.22
	SR4 <sub>1</sub> <sup>2</sup>	90	3	0.191	19.95	19.48	1.33
$270_0 90_{180}$	R24 <sub>6</sub> <sup>11</sup>	82.5	4	0.212	33.12	25.46	$8.67 \times 10^{10}$
	R20 <sub>5</sub> <sup>9</sup>	81	4	0.212	31.85	25.19	$8.67 \times 10^{10}$
	R20 <sub>5</sub> <sup>11</sup>	99	4	0.212	31.85	25.19	$8.67 \times 10^{10}$
	R16 <sub>4</sub> <sup>7</sup>	78.8	4	0.212	28.56	24.69	$8.67 \times 10^{10}$
	R16 <sub>4</sub> <sup>9</sup>	101.2	4	0.212	28.56	24.69	$8.67 \times 10^{10}$
	R12 <sub>3</sub> <sup>5</sup>	75	4	0.212	20.84	23.58	$8.67 \times 10^{10}$
	R12 <sub>3</sub> <sup>7</sup>	105	4	0.212	20.84	23.58	$8.67 \times 10^{10}$
	SR4 <sub>1</sub> <sup>2</sup>	90	4	0.212	35.21	149.93	$8.67 \times 10^{10}$
$180_0$	R16 <sub>4</sub> <sup>7</sup>	78.8	2	0.25	19.65	10.52	2.78
	R16 <sub>4</sub> <sup>9</sup>	115.7	2	0.25	19.65	10.52	2.78
	R12 <sub>3</sub> <sup>5</sup>	75	2	0.25	18.9	9.89	3.74
	R12 <sub>3</sub> <sup>7</sup>	105	2	0.25	18.9	9.89	3.74
	SR4 <sub>1</sub> <sup>2</sup>	90	2	0.25	13.2	22.98	1.56

In the case of the adiabatic  $RN_n^y$  (tt) sequences, the determination of the scaling factors of the first- and second-order terms of the effective Hamiltonian is more complex since they depend on the  $\nu_{1,\max}$ ,  $\Delta\nu_{0,\max}$ ,  $\xi$  and  $\theta$  parameters.<sup>54</sup> For example, the scaling factor of the  $R12_3^5$  and  $SR4_1^2$  schemes is  $\kappa = 0.31$  for  $\nu_{1,\max}/\Delta\nu_{0,\max} = 0.685$ ,  $\xi = 10$  and  $\theta = 87^\circ$ , and this value monotonously decreases for increasing  $\nu_{1,\max}/\Delta\nu_{0,\max}$  ratios.

## 2.4 $^1\text{H} \rightarrow ^{27}\text{Al}$ PRESTO AND *D*-RINEPT NMR EXPERIMENTS

### 2.4.1 Samples and experimental conditions

Experiments were performed on isotopically unmodified  $\gamma$ -alumina purchased from Merck, and isopropylamine-templated  $\text{AlPO}_4$ -14, which was prepared as described by Antonijevic *et al.*<sup>67</sup>

All  $^1\text{H} \rightarrow ^{27}\text{Al}$  RINEPT-CWc and PRESTO-III NMR experiments were recorded at  $B_0 = 18.8$  T on a Bruker BioSpin Avance NEO spectrometer equipped with a 1.3 mm MAS probe spinning at  $\nu_R = 20$  (to test the  $RN_n^y$  schemes with large rf-field requirement) or 62.5 kHz. The tested recoupling schemes are listed in Tables 7 and 8 for experiments recorded at  $\nu_R = 20$  kHz and Tables 9 and 10 for  $\nu_R = 62.5$  kHz. The RF-field of the  $\pi/2$  and  $\pi$  pulses on the  $^1\text{H}$  channel, which do not belong to the recoupling scheme, was equal to 208 kHz, that of the continuous wave irradiation to 147 kHz, and that of  $^{27}\text{Al}$  CT-selective  $\pi/2$  and  $\pi$  pulses to 10 kHz. The defocusing and refocusing delays  $\tau$  are given in Tables 7 to 10. The pulses on the  $^1\text{H}$  channel were applied on-resonance, whereas those on  $^{27}\text{Al}$  channel were applied:

- (i) on-resonance with  $\text{AlO}_6$  signal of  $\gamma$ -alumina in Figs. 20 and 26, Tables 7 and 9, as well as in Figs. 21 and 27 when the offset is null,
- (ii) on-resonance with  $\text{AlO}_4$  signal of  $\text{AlPO}_4$ -14 in Figs. 24 and 28, Tables 8 and 10 as well as in Figs. 25 and 29 when the offset is null, and
- (iii) in the middle of the  $\text{AlO}_4$  and  $\text{AlO}_6$  peaks for the 1D spectra shown in Figs. 19 and 22.

These differences in offset explain some changes in the relative efficiencies of the recoupling between the figures. These 1D spectra resulted from averaging 64 transients with a relaxation delay of 1 s. The  $^{27}\text{Al}$  isotropic chemical shifts were referenced at 0 ppm to 1 mol.L $^{-1}$   $[\text{Al}(\text{H}_2\text{O})_6]^{3+}$  solution.

2D  $^1\text{H} \rightarrow ^{27}\text{Al}$  *D*-HETCOR spectra of  $\text{AlPO}_4\text{-14}$  using RINEPT-CWc-SR4 $_1^2$  were acquired with  $(180_0)$ ,  $(270_0 90_{180})$  and *tt* pulses as well as PRESTO-R16 $_7^6(270_0 90_{180})$ . These 2D spectra were acquired using a non-uniform sampling (NUS) with an exponentially biased sampling retaining 25% of the points with respect to uniform sampling. The 2D spectra resulted from 8 transients for each of the 500  $t_1$  increments with a recycle delay of 1 s, i.e. an acquisition time of 72 min.

The decay of the transverse proton magnetization of  $\text{AlPO}_4\text{-14}$  was also measured during a spin echo sequence (Fig. 18), in which the refocusing  $\pi$ -pulse was identical to that used in the defocusing part of the RINEPT-CWc sequence (Fig. 13b). This decay was measured at  $\nu_R = 20$  and 62.5 kHz either with no recoupling or by applying a SR4 $_1^2$  recoupling built from  $(180_0)$ ,  $(270_0 90_{180})$  and *tt* pulses during the delays of the spin echo sequence. The RF-fields applied during the two recoupling blocks were equal to their optimal values given in Tables 6 and 8.

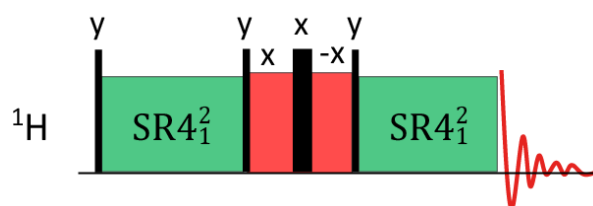


**Figure 18.** Spin echo sequence used to measure the decay of the transverse  $^1\text{H}$  magnetization.

#### 2.4.2 Performances of PRESTO and *D*-RINEPT at $\nu_R = 20$ kHz

##### $\gamma$ -alumina

The 1D spectra of  $\gamma$ -alumina acquired using  $^1\text{H} \rightarrow ^{27}\text{Al}$  RINEPT and PRESTO sequences, shown in Fig. 19, exhibit two resonances at 70 and 10 ppm, assigned to tetra- ( $\text{AlO}_4$ ) and hexa-coordinated ( $\text{AlO}_6$ ) resonances, respectively.<sup>68</sup>. The signal of penta-coordinated ( $\text{AlO}_5$ ) sites, which are mainly located in the first surface layer, is

barely detected because of the lack of sensitivity of conventional solid-state NMR spectroscopy.<sup>69</sup> The most intense peak,  $\text{AlO}_6$ , was used to compare the transfer efficiencies of RINEPT and PRESTO sequences with different recoupling schemes. Table 7 lists the measured performances of  $^1\text{H} \rightarrow ^{27}\text{Al}$  RINEPT-CWc and PRESTO transfers using various recoupling for  $\gamma$ -alumina at  $\nu_R = 20$  kHz. The PRESTO sequences using  $\text{R}22_2^7(180_0)$  and  $\text{R}18_2^5(180_0)$  recoupling were compared with the RINEPT-CWc scheme using  $\text{SR}4_1^2$  and  $\text{R}12_3^5$  with: single ( $180_0$ ), composite ( $270_090_{180}$ ) and ( $90_{-45}90_{45}90_{-45}$ ) or (tt) adiabatic pulses. A low transfer efficiency was obtained for RINEPT-CWc- $\text{SR}4_1^2(90_0240_{90}90_0)$  because of its low scaling factor,  $\kappa = 0.131$ , and hence its performances are not reported in Table 7. The recoupling schemes based on the symmetry  $\text{SC}2_1^0$ , corresponding to the  $[\text{C}2_1^0]_0[\text{C}2_1^0]_{120}[\text{C}2_1^0]_{240}$  sequence with a basic element  $\text{C} = (90_{45}90_{135}90_{45}90_{225}90_{315}90_{225})$ , or  $\text{C}6_3^0$  built from  $\text{C}' = (90_{30}90_{120}90_{30}90_{240}90_{330}90_{240})$  were also tested. These basic elements, which derive from ( $90_{-45}90_{45}90_{-45}$ ), have recently been proposed.<sup>36</sup>

As seen in Table 7 and Fig. 19a, the sequences yielding the highest transfer efficiencies are by decreasing order RINEPT-CWc with  $\text{SR}4_1^2(\text{tt})$  or  $\text{R}12_3^5(\text{tt}) > \text{PRESTO-R}22_2^7(180_0) > \text{RINEPT-CWc-SR}4_1^2(270_090_{180}) \approx \text{PRESTO-R}18_2^5(180_0) > \text{RINEPT-CWc-R}12_3^5(270_090_{180})$ . Figs. 20 and 21 display the signal intensity of these sequences as function of the RF-field amplitude and offset, respectively. The highest transfer efficiencies are obtained with the RINEPT-CWc sequence incorporating a (tt) adiabatic pulse. This recoupling also leads to the highest robustness to offset and RF inhomogeneity, and  $\text{SR}4_1^2(\text{tt})$  and  $\text{R}12_3^5(\text{tt})$  yield identical transfer efficiency and robustness. Hence, the three-step multiple-quantum super-cycle of the  $\text{SR}4_1^2$  symmetry does not improve the robustness in the case of a (tt) basic element. However, these recoupling schemes require maximum RF-fields of  $\nu_{1,\text{max}} \geq 8\nu_R = 160$  kHz, which may exceed the RF power specifications of most 3.2 mm MAS probes.

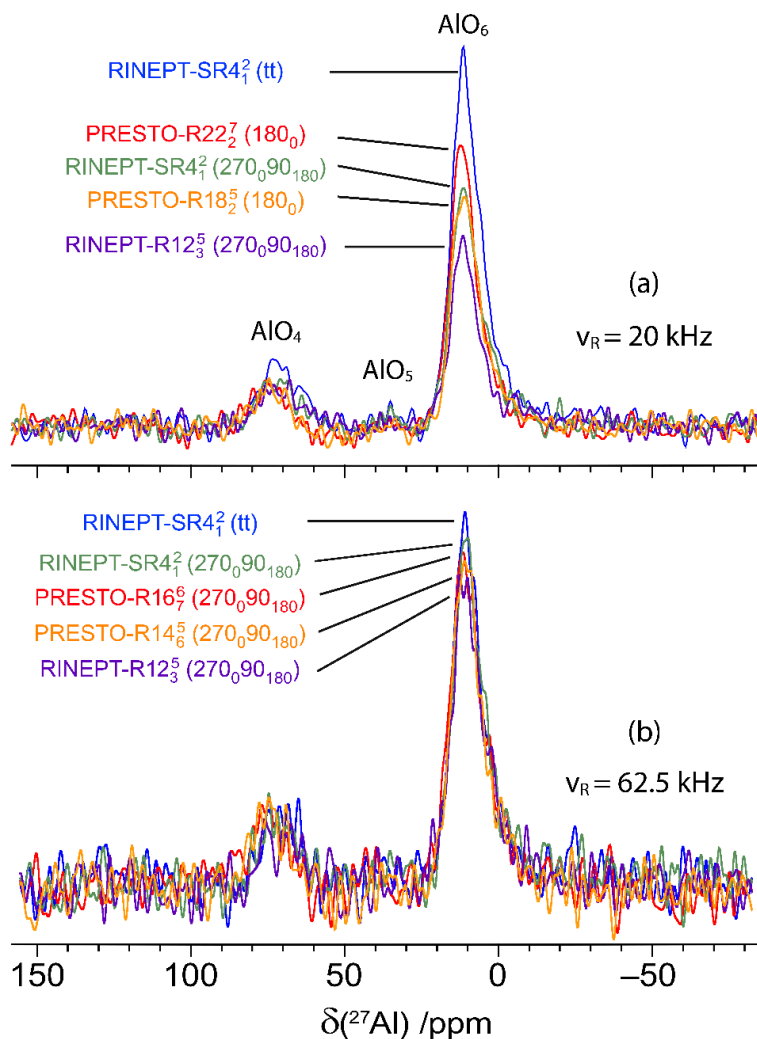


**Figure 19.**  $^{27}\text{Al}$  1D spectra of  $\gamma$ -alumina at 18.8 T with  $\nu_R = 20$  (a) and 62.5 (b) kHz acquired using  $^1\text{H} \rightarrow ^{27}\text{Al}$  transfers with RINEPT-CWc sequence and  $\text{SR4}_1^2(\text{tt})$ ,  $\text{SR4}_1^2(270_0 90_{180})$  and  $\text{R12}_3^5(270_0 90_{180})$  recoupling, or PRESTO scheme and (a)  $\text{R22}_2^7(180_0)$  or  $\text{R18}_2^5(180_0)$ , or (b)  $\text{R16}_7^6(270_0 90_{180})$  and  $\text{R14}_6^5(270_0 90_{180})$  recoupling. The  $\tau$  delays and  $\nu_1/\nu_{1,\text{max}}$  RF-fields were fixed to their optimum values given in Tables 7 and 9.

The PRESTO sequences using  $\text{R22}_2^7(180_0)$  and  $\text{R18}_2^5(180_0)$  recoupling also result in good transfer efficiencies, but lower than RINEPT-CWc- $\text{SR4}_1^2(\text{tt})$ . However, they use RF-fields of  $\nu_1/\nu_R = 5.5$  and 4.5, which are compatible with the specifications of 3.2 mm MAS probes. The higher transfer efficiency of  $\text{R22}_2^7(180_0)$  with respect to  $\text{R18}_2^5(180_0)$  stems from its weaker second-order cross-terms between  $^1\text{H}$ - $^1\text{H}$  interactions as shown in Table 3.

The efficiency of the RINEPT-CWc-SR4<sub>1</sub><sup>2</sup>(270<sub>0</sub>90<sub>180</sub>) sequence, with  $v_1 = 4v_R$ , is comparable to that of PRESTO-R18<sub>2</sub><sup>5</sup>(180<sub>0</sub>), but with a higher robustness to offset and RF inhomogeneity. We can notice that amplitude modulated recoupling schemes, for which the phase shifts are equal to 180°, such as SR4<sub>1</sub><sup>2</sup>(270<sub>0</sub>90<sub>180</sub>) and SR4<sub>1</sub><sup>2</sup>(180<sub>0</sub>), exhibit a high robustness to RF-field maladjustments (Fig. 20).<sup>39</sup> The use of (270<sub>0</sub>90<sub>180</sub>) composite pulses with SR4<sub>1</sub><sup>2</sup> symmetry, instead of single  $\pi$  pulses, improves its transfer efficiency as well as its robustness to offset and RF-field inhomogeneity.

In summary, for  $v_R = 20$  kHz in  $\gamma$ -alumina, the RINEPT-CWc-SR4<sub>1</sub><sup>2</sup>(270<sub>0</sub>90<sub>180</sub>) sequence achieves efficient and robust transfers of magnetization from protons to <sup>27</sup>Al nuclei using a moderate RF-field of  $v_1 = 4v_R$ . For <sup>1</sup>H spectra with a width smaller than 20 kHz and MAS probes with a good RF-homogeneity, PRESTO-R22<sub>2</sub><sup>7</sup>(180<sub>0</sub>) can result in slightly higher transfer efficiencies.

**Table 7.** Comparison of the performances of <sup>1</sup>H → <sup>27</sup>Al RINEPT-CWc and PRESTO transfers using various recouplings for AlO<sub>6</sub> signal of  $\gamma$ -alumina at  $v_R = 20$  kHz

PRESTO /RINEPT	Recoupling	$\tau$ / $\mu$ s	$v_1/v_{1,\max}$ /kHz	AlO <sub>6</sub> <sup>a,b</sup>	$\Delta v_0^c$ /kHz	$\Delta v_0/v_1$	$\Delta v_1^d$ /kHz	$\Delta v_1/v_1$
RINEPT	SR4 <sub>1</sub> <sup>2</sup> (tt)	400	160	1.00	110	0.68	> 100 <sup>e</sup>	> 0.62
	R12 <sub>3</sub> <sup>5</sup> (tt)	400	160	1.00	110	0.68	> 100 <sup>e</sup>	> 0.62
PRESTO	R22 <sub>2</sub> <sup>7</sup> (180 <sub>0</sub> )	400	110	0.73	30	0.27	39	0.35
RINEPT	SR4 <sub>1</sub> <sup>2</sup> (270 <sub>0</sub> 90 <sub>180</sub> )	400	80	0.63	50	0.63	44	0.55
PRESTO	R18 <sub>2</sub> <sup>5</sup> (180 <sub>0</sub> )	400	90	0.61	28	0.31	27	0.30
RINEPT	R12 <sub>3</sub> <sup>5</sup> (270 <sub>0</sub> 90 <sub>180</sub> )	400	80	0.50	40	0.50	35	0.44
	SR4 <sub>1</sub> <sup>2</sup> (90 <sub>-45</sub> 90 <sub>45</sub> 90 <sub>-45</sub> )	400	63	0.42	14	0.22	14	0.22
	SR4 <sub>1</sub> <sup>2</sup> (180 <sub>0</sub> )	400	45	0.40	17	0.38	24	0.53
	R12 <sub>3</sub> <sup>5</sup> (180 <sub>0</sub> )	400	45	0.35	10	0.22	15	0.33
	R12 <sub>3</sub> <sup>5</sup> (90 <sub>-45</sub> 90 <sub>45</sub> 90 <sub>-45</sub> )	400	66	0.35	11	0.17	18	0.27
	SC2 <sub>1</sub> <sup>0</sup> (C)	400	63	0.31	14	0.22	45	0.71
	C6 <sub>3</sub> <sup>0</sup> (C')	400	66	0.28	10	0.15	40	0.60

<sup>a</sup> AlO<sub>6</sub> signal normalized to that with <sup>1</sup>H → <sup>27</sup>Al RINEPT-CWc-SR4<sub>1</sub><sup>2</sup>(tt). <sup>b</sup> The relative error bars were determined from the S/N. For the AlO<sub>6</sub> signal intensity, they are equal to  $\pm 0.03$ . <sup>c</sup> FWHM of the robustness to offset. <sup>d</sup> FWHM of the robustness to RF-field. <sup>e</sup> Only a lower bound of RF-field could be determined due to probe RF specifications (Fig. 20).

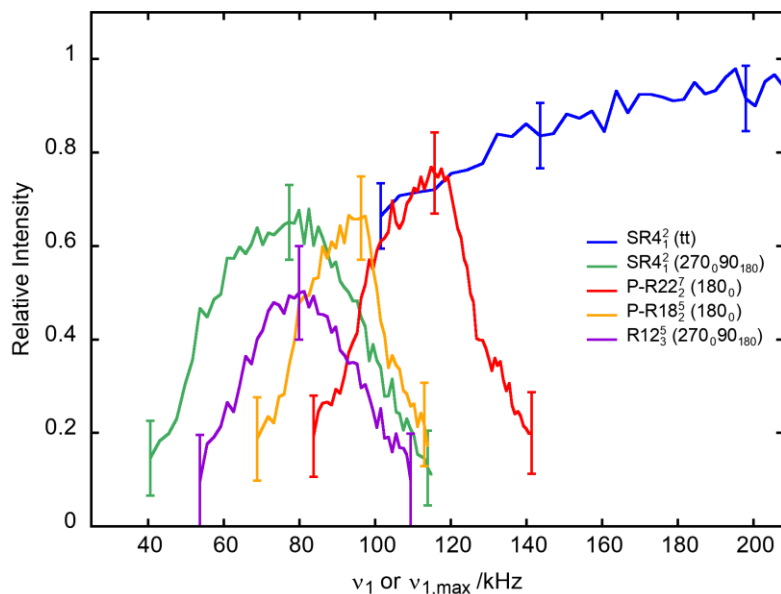


**Figure 20.**  $^{27}\text{AlO}_6$  on-resonance signal of  $\gamma$ -alumina at  $\nu_R = 20$  kHz as function of  $\nu_1$  or  $\nu_{1,\max}$  for PRESTO-R22 $_2^7(180_0)$  and -R18 $_2^5(180_0)$  as well as RINEPT-CWc-SR4 $_1^2(\text{tt})$ , -SR4 $_1^2(270_0 90_{180})$  and -R12 $_3^5(270_0 90_{180})$ . For each curve,  $\tau$  was fixed to its optimum value given in Table 7. Vertical bars correspond to the error on  $\text{AlO}_6$  intensity, determined by the inverse of the S/N of the optimum  $\nu_1$ .

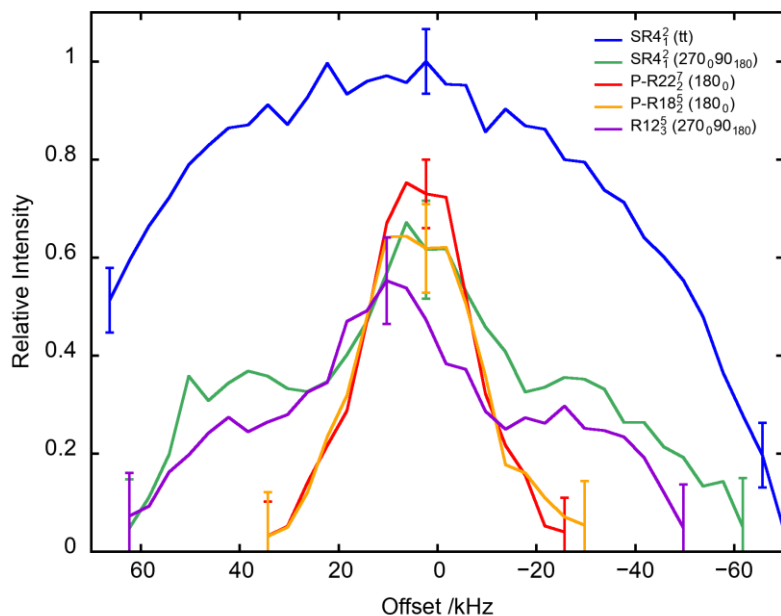


**Figure 21.**  $^{27}\text{AlO}_6$  signal of  $\gamma$ -alumina at  $\nu_R = 20$  kHz as function of offset for PRESTO-R22 $_2^7(180_0)$  and -R18 $_2^5(180_0)$  as well as RINEPT-CWc-SR4 $_1^2(\text{tt})$ , -SR4 $_1^2(270_0 90_{180})$  and -R12 $_3^5(270_0 90_{180})$ . For each curve,  $\tau$  and  $\nu_1$  or  $\nu_{1,\max}$  were fixed to their optimum values given in Table 7. Vertical bars correspond to the error on  $\text{AlO}_6$  intensity, determined by the inverse of the S/N of the optimum offset value.



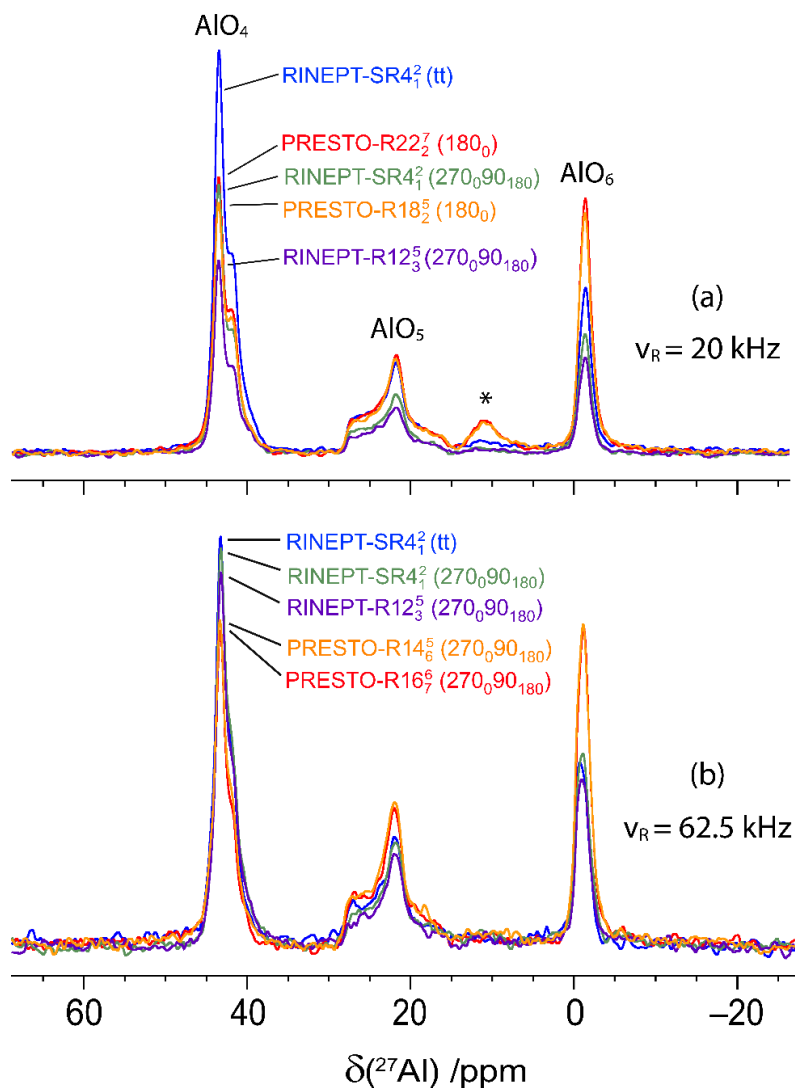
## AlPO<sub>4</sub>-14

Fig. 22a shows the  $^1\text{H} \rightarrow ^{27}\text{Al}$  RINEPT and PRESTO 1D spectra of AlPO<sub>4</sub>-14 recorded with  $\nu_R = 20$  kHz. They exhibit three  $^{27}\text{Al}$  resonances at 43, 21 and  $-2$  ppm assigned to AlO<sub>4</sub>, AlO<sub>5</sub> and AlO<sub>6</sub> sites, respectively.<sup>70</sup> The AlO<sub>5</sub> and AlO<sub>6</sub> sites are directly bonded to OH groups. The  $^1\text{H}$  MAS spectrum is shown in Fig. 23. According to the literature, the  $^{27}\text{AlO}_4$  signal subsumes the resonances of two AlO<sub>4</sub> sites with quadrupolar coupling constants  $C_Q = 1.7$  and  $4.1$  MHz, whereas those of AlO<sub>5</sub> and AlO<sub>6</sub> sites are equal to  $5.6$  and  $2.6$  MHz, respectively.<sup>67,71</sup> The  $^1\text{H}$ - $^1\text{H}$  dipolar couplings within the isopropylamine template molecule are larger than in  $\gamma$ -alumina. We used the most intense peak, AlO<sub>4</sub>, to compare the  $^1\text{H} \rightarrow ^{27}\text{Al}$  transfer efficiencies of RINEPT-CWc and PRESTO sequences with different recoupling schemes, and the results are given in Table 8. The six sequences yielding the highest transfer efficiencies are the same as for  $\gamma$ -alumina and their relative efficiencies are comparable for the AlO<sub>4</sub> peak of AlPO<sub>4</sub>-14 and the AlO<sub>6</sub> signal of  $\gamma$ -alumina.

**Table 8.** Comparison of the performances of  $^1\text{H} \rightarrow ^{27}\text{Al}$  RINEPT-CWc and PRESTO transfers with AlPO<sub>4</sub>-14 at  $\nu_R = 20$  kHz.

PRESTO /RINEPT	Recoupling	$\tau$ / $\mu\text{s}$	$\nu_1/\nu_{1,\text{max}}$ /kHz	Intensity <sup>a</sup>			$\Delta\nu_0$ /kHz	$\Delta\nu_0/\nu_1$	$\Delta\nu_1$ /kHz	$\Delta\nu_1/\nu_1$
				AlO <sub>6</sub> b	AlO <sub>5</sub> c	AlO <sub>4</sub> d				
RINEPT	SR4 <sub>1</sub> <sup>2</sup> (tt)	800	208	1.00	1.00	1.00	120	0.58	- <sup>e</sup>	- <sup>e</sup>
	R12 <sub>3</sub> <sup>5</sup> (tt)	800	208	0.99	0.99	0.98	120	0.58	- <sup>e</sup>	- <sup>e</sup>
PRESTO	R22 <sub>2</sub> <sup>7</sup> (180 <sub>0</sub> )	600	114	1.54	1.07	0.67	26	0.23	38	0.33
RINEPT	SR4 <sub>1</sub> <sup>2</sup> (270 <sub>0</sub> 90 <sub>180</sub> )	800	77	0.72	0.65	0.67	45	0.58	48	0.62
PRESTO	R18 <sub>2</sub> <sup>5</sup> (180 <sub>0</sub> )	600	94	1.45	1.03	0.62	25	0.27	26	0.28
	R12 <sub>3</sub> <sup>5</sup> (270 <sub>0</sub> 90 <sub>180</sub> )	800	77	0.58	0.50	0.48	46	0.60	36	0.47
	SR4 <sub>1</sub> <sup>2</sup> (180 <sub>0</sub> )	600	43	0.64	0.45	0.36	14	0.33	23	0.53
	SR4 <sub>1</sub> <sup>2</sup> (90 <sub>-45</sub> 90 <sub>45</sub> 90 <sub>-45</sub> )	800	61	0.56	0.43	0.25	16	0.26	20	0.32
RINEPT	SC2 <sub>1</sub> <sup>0</sup> (C)	800	68	0.54	0.41	0.24	18	0.26	52	0.73
	R12 <sub>3</sub> <sup>5</sup> (90 <sub>-45</sub> 90 <sub>45</sub> 90 <sub>-45</sub> )	600	61	0.43	0.30	0.21	8	0.13	18	0.29
	R12 <sub>3</sub> <sup>5</sup> (180 <sub>0</sub> )	600	45	0.34	0.28	0.21	8	0.18	18	0.40
	C6 <sub>3</sub> <sup>0</sup> (C')	600	68	0.52	0.36	0.21	10	0.15	42	0.61

<sup>a</sup> Intensities of AlO<sub>6</sub>, AlO<sub>5</sub> and AlO<sub>4</sub> resonances normalized to their intensities with  $^1\text{H} \rightarrow ^{27}\text{Al}$  RINEPT-CWc-SR4<sub>1</sub><sup>2</sup>(tt). <sup>b</sup> The absolute error on AlO<sub>6</sub> signal intensity is  $\pm 0.02$ . <sup>c</sup> The absolute error on AlO<sub>5</sub> signal intensity is  $\pm 0.03$ . <sup>d</sup> The absolute error on AlO<sub>4</sub> signal intensity is  $\pm 0.01$ . <sup>e</sup> FWHM of the robustness to RF-field was not measured for RINEPT-SR4<sub>1</sub><sup>2</sup>(tt) and -R12<sub>3</sub><sup>5</sup>(tt) (Fig. 24).



**Figure 22.**  $^{27}\text{Al}$  1D spectra of  $\text{AlPO}_4\text{-14}$  at 18.8 T with  $\nu_R = 20$  (a) and 62.5 (b) kHz acquired using  $^1\text{H} \rightarrow ^{27}\text{Al}$  transfers with RINEPT-CWc sequence and SR4<sub>1</sub><sup>2</sup>(tt), SR4<sub>1</sub><sup>2</sup>(270<sub>0</sub>90<sub>180</sub>) and R12<sub>3</sub><sup>5</sup>(270<sub>0</sub>90<sub>180</sub>) recoupling, or PRESTO sequence and (a) R22<sub>2</sub><sup>7</sup>(180<sub>0</sub>) and R18<sub>2</sub><sup>5</sup>(180<sub>0</sub>), or (b) R16<sub>7</sub><sup>6</sup>(270<sub>0</sub>90<sub>180</sub>) and R14<sub>6</sub><sup>5</sup>(270<sub>0</sub>90<sub>180</sub>) recoupling. The  $\tau$  delays and  $\nu_1/\nu_{1,\text{max}}$  RF-fields were fixed to their optimal values given in Tables 8 and 10. The resonance at *ca.* 11 ppm in (a) is due to an impurity.

Nevertheless, the RF requirement of the SR4<sub>1</sub><sup>2</sup>(tt) and R12<sub>3</sub><sup>5</sup>(tt) schemes is higher for  $\text{AlPO}_4\text{-14}$  than for  $\gamma$ -alumina because of the larger  $^1\text{H}\text{-}^1\text{H}$  dipolar couplings. This fact is in agreement with the numerical simulations (not shown) which demonstrate that higher  $^1\text{H}\text{-}^1\text{H}$  dipolar couplings require higher RF-field so that the (tt) pulses remain adiabatic.<sup>1</sup> This RF requirement prevents the use of these adiabatic recoupling schemes at  $\nu_R = 20$  kHz with most 3.2 mm MAS probes. The RF requirement of the

other sequences, and their robustness to offset and rf-field inhomogeneity are similar for both samples (Table 8 and Figs. 24 and 25).

In the case of  $\text{AlPO}_4\text{-14}$ , PRESTO sequence yields a higher efficiency than RINEPT for  $\text{AlO}_5$  and  $\text{AlO}_6$ , contrary to the  $\text{AlO}_4$  resonance, since (i) these Al sites are directly bonded to OH groups and (ii)  $\text{R}22\frac{7}{2}(180_0)$  and  $\text{R}18\frac{5}{2}(180_0)$  schemes are subject to dipolar truncation (section 2.3.4), which prevents to transfer the  $^1\text{H}$  magnetization of these OH groups to  $^{27}\text{AlO}_4$  nuclei.

Hence, at  $\nu_R = 20$  kHz, for both  $\text{AlPO}_4\text{-14}$  and  $\gamma$ -alumina, the RINEPT-CWc-SR4 $_1^2(270_090_{180})$  and PRESTO-R22 $_2^7(180_0)$  sequences are the best choices to transfer the  $^1\text{H}$  magnetization to  $^{27}\text{Al}$  nuclei.

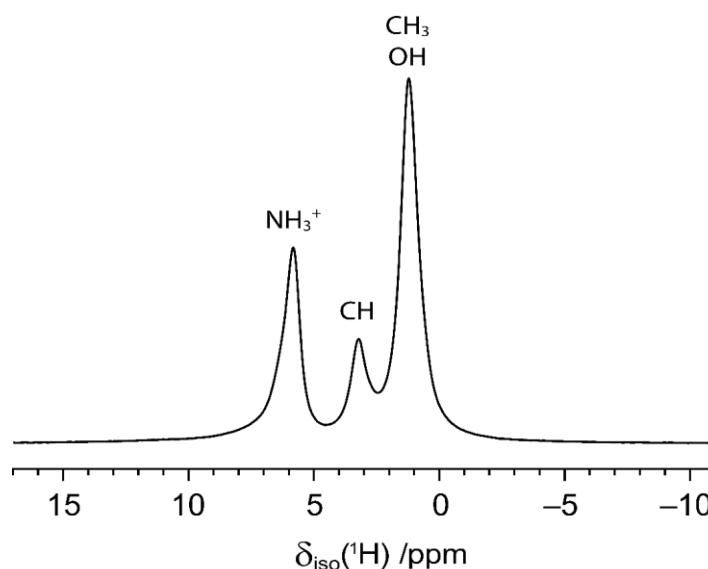


**Figure 23.**  $^1\text{H}$  MAS spectrum of  $\text{AlPO}_4\text{-14}$  acquired at  $B_0 = 18.8$  T and  $\nu_R = 20$  kHz by averaging 16 transients separated by a recycle interval of 1 s, using the DEPTH pulse sequence for probe background suppression, with  $\nu_1 \approx 208$  kHz.<sup>72</sup>

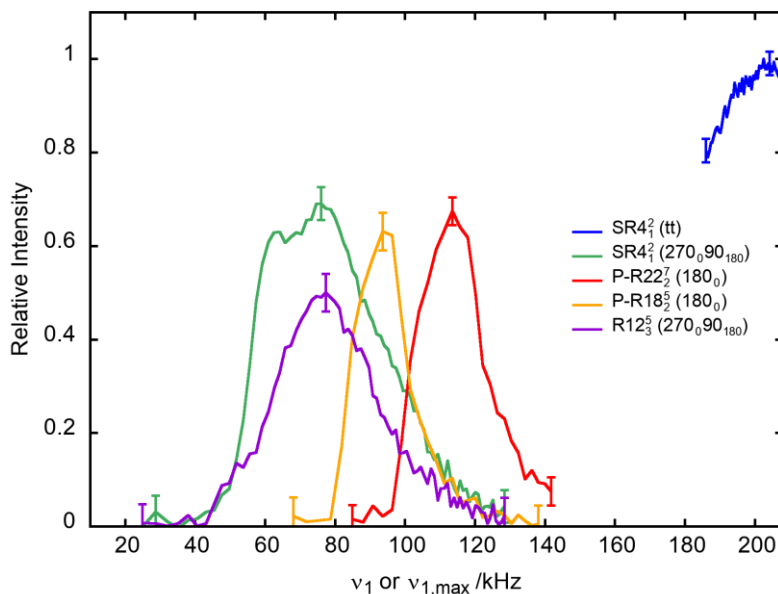


**Figure 24.**  $^{27}\text{AlO}_4$  signal of  $\text{AlPO}_4\text{-14}$  at  $\nu_R = 20$  kHz as function of  $\nu_1$  or  $\nu_{1,\text{max}}$  of the recoupling for PRESTO- $\text{R}22_2^7(180_0)$  and  $\text{-R}18_2^5(180_0)$  as well as RINEPT-CWc- $\text{SR}4_1^2(\text{tt})$ ,  $\text{-SR}4_1^2(270_0 90_{180})$  and  $\text{-R}12_3^5(270_0 90_{180})$ . For each curve,  $\tau$  was fixed to its optimum value given in Table 8. Vertical bars correspond to the error on  $\text{AlO}_4$  intensity, determined by the inverse of the S/N of the optimum  $\nu_1$ .

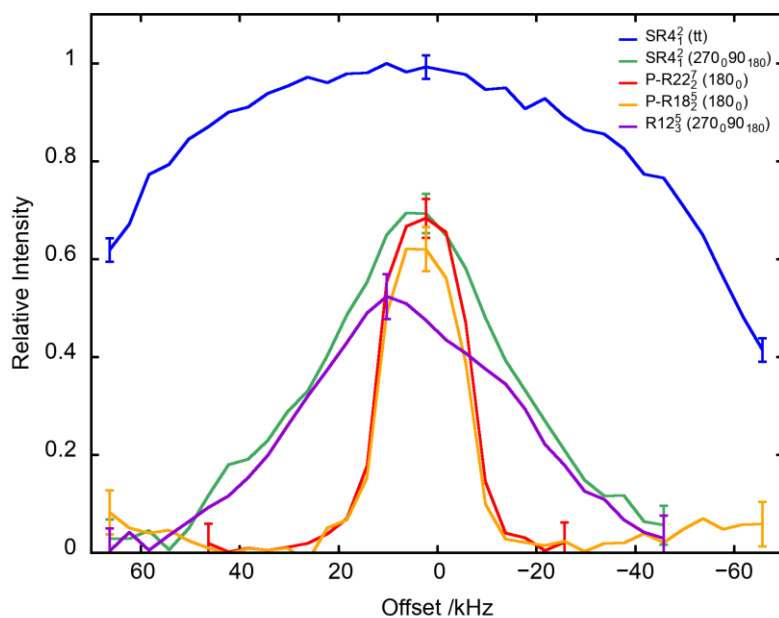


**Figure 25.**  $^{27}\text{AlO}_4$  signal of  $\text{AlPO}_4\text{-14}$  at  $\nu_R = 20$  kHz as function of offset of the recoupling for PRESTO- $\text{R}22_2^7(180_0)$  and  $\text{-R}18_2^5(180_0)$  as well as RINEPT-CWc- $\text{SR}4_1^2(\text{tt})$ ,  $\text{-SR}4_1^2(270_0 90_{180})$  and  $\text{-R}12_3^5(270_0 90_{180})$ . For each curve,  $\tau$  and  $\nu_1$  or  $\nu_{1,\text{max}}$  were fixed to their optimum values given in Table 8. Vertical bars correspond to the error on  $\text{AlO}_4$  intensity, determined by the inverse of the S/N of the optimum offset value.

### 2.4.3 Performances of PRESTO and *D*-RINEPT at $\nu_R = 62.5$ kHz

Similar comparisons of the performances of the various RINEPT-CWc and PRESTO sequences were performed for  $\gamma$ -alumina and AlPO<sub>4</sub>-14 at  $\nu_R = 62.5$  kHz.

#### $\gamma$ -alumina

The corresponding data for  $\gamma$ -alumina are given in Table 9. The sequences yielding the highest transfer efficiencies are by decreasing order: RINEPT-CWc with SR4<sub>1</sub><sup>2</sup>(tt) or R12<sub>3</sub><sup>5</sup>(tt) > RINEPT-CWc-SR4<sub>1</sub><sup>2</sup>(270<sub>0</sub>90<sub>180</sub>)  $\approx$  PRESTO-R16<sub>7</sub><sup>6</sup>(270<sub>0</sub>90<sub>180</sub>) > PRESTO-R14<sub>6</sub><sup>5</sup>(270<sub>0</sub>90<sub>180</sub>) > RINEPT-CWc-R12<sub>3</sub><sup>5</sup>(270<sub>0</sub>90<sub>180</sub>).

The nominal RF requirements of the RINEPT sequences using adiabatic or (270<sub>0</sub>90<sub>180</sub>) composite  $\pi$ -pulses correspond to  $\nu_{1\max} \approx 5\nu_R$  (313 kHz) or  $4\nu_R$  (250 kHz), which exceed the specifications of our 1.3 mm MAS probe, and the sequences were tested only up to  $\nu_{1\max} = 208$  kHz (Fig. 26). This suboptimal RF-field may limit the transfer efficiencies of these sequences.

The PRESTO-R16<sub>7</sub><sup>6</sup>(270<sub>0</sub>90<sub>180</sub>) and -R14<sub>6</sub><sup>5</sup>(270<sub>0</sub>90<sub>180</sub>) sequences yield transfer efficiencies comparable to those of RINEPT-CWc-SR4<sub>1</sub><sup>2</sup>(270<sub>0</sub>90<sub>180</sub>), but with a significantly lower RF-field,  $\nu_1 \approx 137$  kHz  $\approx 2.3\nu_R$ . Furthermore, the robustness to offset of these PRESTO sequences is comparable to that of RINEPT-CWc-SR4<sub>1</sub><sup>2</sup>(270<sub>0</sub>90<sub>180</sub>) (Fig. 27). PRESTO-R22<sub>4</sub><sup>3</sup>(180<sub>0</sub>) and -R16<sub>3</sub><sup>2</sup>(180<sub>0</sub>) sequences with a small phase shift of  $2\phi \leq 52^\circ$  are less efficient because they are sensitive to RF inhomogeneity.

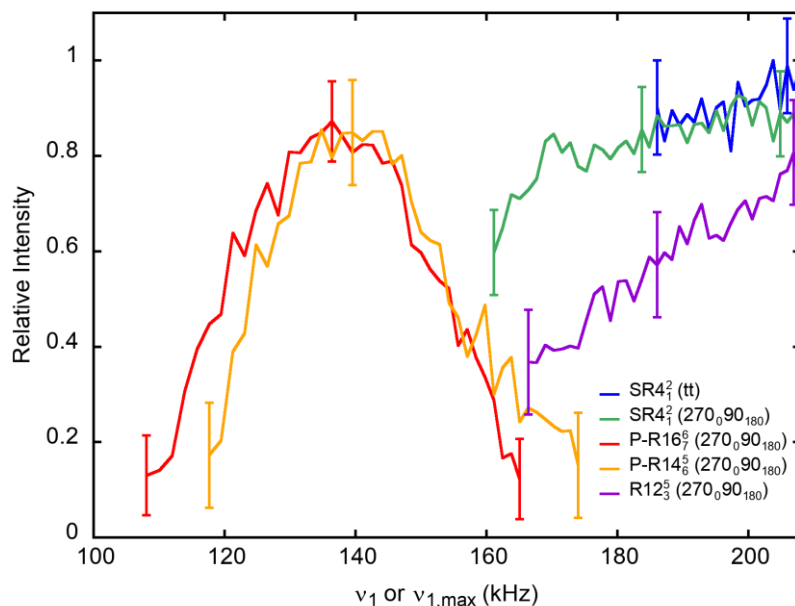


**Figure 26.**  $^{27}\text{AlO}_6$  on-resonance signal of  $\gamma$ -alumina at  $\nu_R = 62.5$  kHz as function of  $\nu_1$  or  $\nu_{1,\text{max}}$  for PRESTO-R16 $_7^6(270_0 90_{180})$  and -R14 $_6^5(270_0 90_{180})$  as well as RINEPT-CWc-SR4 $_1^2(\text{tt})$ , -SR4 $_1^2(270_0 90_{180})$  and -R12 $_3^5(270_0 90_{180})$ . For each curve,  $\tau$  was fixed to its optimum value given in Table 9. Vertical bars correspond to the error on  $\text{AlO}_6$  intensity, determined by the inverse of the S/N of the optimum  $\nu_1$ .

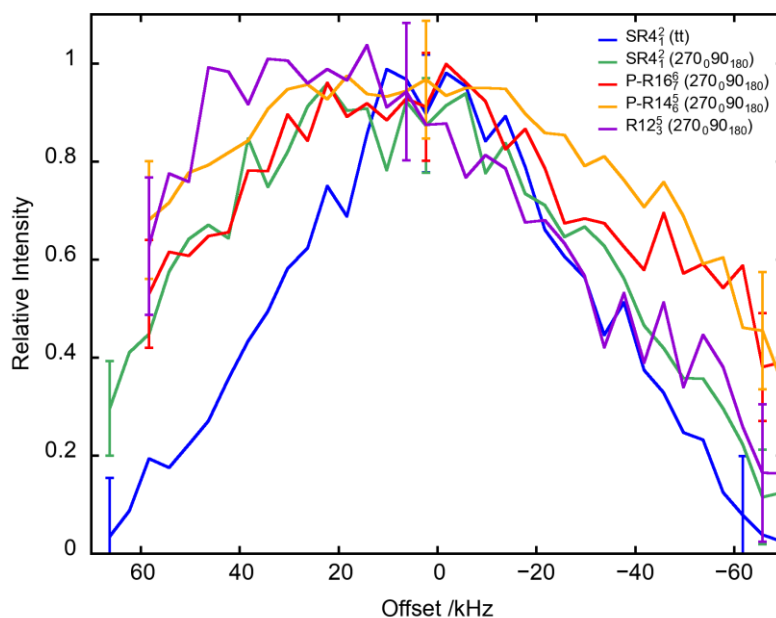


**Figure 27.**  $^{27}\text{AlO}_6$  signal of  $\gamma$ -alumina at  $\nu_R = 62.5$  kHz as function of offset for PRESTO-R16 $_7^6(270_0 90_{180})$  and -R14 $_6^5(270_0 90_{180})$  as well as RINEPT-CWc-SR4 $_1^2(\text{tt})$ , -SR4 $_1^2(270_0 90_{180})$  and -R12 $_3^5(270_0 90_{180})$ . For each curve,  $\tau$  and  $\nu_1$  or  $\nu_{1,\text{max}}$  were fixed to their optimum values given in Table 9. Vertical bars correspond to the error on  $\text{AlO}_6$  intensity, determined by the inverse of the S/N of the optimum offset value.

**Table 9.** Comparison of the performances of  $^1\text{H} \rightarrow ^{27}\text{Al}$  RINEPT-CWc and PRESTO transfers using various recouplings for the  $\text{AlO}_6$  signal of  $\gamma$ -alumina at  $\nu_{\text{R}} = 62.5$  kHz.

PRESTO/RINEPT	Recoupling	$\tau / \mu\text{s}$	$\nu_1/\nu_{1,\text{max}}$ /kHz	$\text{AlO}_6$ <sup>a,b</sup>	$\Delta\nu_0$ /kHz	$\Delta\nu_0/\nu_1$	$\Delta\nu_1$ /kHz	$\Delta\nu_1/\nu_1$
RINEPT	$\text{SR4}_1^2(\text{tt})$	256	208	1.00	74	0.36	- <sup>c</sup>	- <sup>c</sup>
	$\text{R12}_3^5(\text{tt})$	256	208	1.00	74	0.36	- <sup>c</sup>	- <sup>c</sup>
	$\text{SR4}_1^2(270_090_{180})$	320	208	0.92	96	0.46	- <sup>c</sup>	- <sup>c</sup>
PRESTO	$\text{R16}_7^6(270_090_{180})$	448	137	0.91	90	0.66	42	0.31
	$\text{R14}_6^5(270_090_{180})$	384	146	0.86	100	0.68	38	0.26
RINEPT	$\text{R12}_3^5(270_090_{180})$	320	208	0.82	86	0.41	- <sup>c</sup>	- <sup>c</sup>
	$\text{SR4}_1^2(180_0)$	320	125	0.75	52	0.42	88	0.70
	$\text{R12}_3^5(180_0)$	288	125	0.74	16	0.13	85	0.68
	PRESTO	$\text{R22}_4^3(180_0)$	256	157	0.67	68	0.43	20
$\text{R16}_5^2(180_0)$		384	155	0.51	48	0.31	40	0.26
RINEPT	$\text{SC2}_1^0(\text{C})$	256	186	0.34	50	0.27	84	0.45
	$\text{C6}_3^0(\text{C}')$	256	186	0.34	43	0.23	76	0.41
	$\text{SR4}_1^2(90_{-45}90_{45}90_{-45})$	256	186	0.32	47	0.25	70	0.38
	$\text{R12}_3^5(90_{-45}90_{45}90_{-45})$	256	186	0.32	40	0.22	70	0.38

<sup>a</sup>  $\text{AlO}_6$  signal normalized to that with  $^1\text{H} \rightarrow ^{27}\text{Al}$  RINEPT-CWc- $\text{SR4}_1^2(\text{tt})$ . <sup>b</sup> The absolute error on  $\text{AlO}_6$  signal intensity is  $\pm 0.08$ . <sup>c</sup> FWHM of the robustness to rf-field was not measured for RINEPT- $\text{SR4}_1^2(\text{tt})$  and  $-\text{R12}_3^5(\text{tt})$  (Fig. 26).

## AlPO<sub>4</sub>-14

In the case of  $\text{AlPO}_4$ -14, the relative transfer efficiencies for  $^{27}\text{AlO}_4$  species follow a similar order as for  $\gamma$ -alumina, except that the transfer efficiencies of PRESTO- $\text{R16}_7^6(270_090_{180})$  and  $-\text{R14}_6^5(270_090_{180})$  are significantly lower than that of RINEPT-CWc- $\text{SR4}_1^2(270_090_{180})$  (Table 10). This decreased efficiency of the PRESTO schemes for  $\text{AlO}_4$  stems notably from the dipolar truncation, which prevents the transfer of magnetization from the OH groups bonded to  $\text{AlO}_5$  and  $\text{AlO}_6$  sites to  $\text{AlO}_4$ , since these  $^{27}\text{AlO}_4$  nuclei are significantly more distant to protons as shown in Table 11. Furthermore, the amplitude-modulated  $\text{SR4}_1^2(270_090_{180})$  recoupling benefits from a higher robustness to RF-field inhomogeneity than the PRESTO schemes (Fig. 28). Conversely, the robustness to offset of these three sequences are comparable (Fig. 29),

whereas the RF requirements of  $R16_7^6(270_090_{180})$  and  $R14_6^5(270_090_{180})$  are much lower than that of  $SR4_1^2(270_090_{180})$ .

In summary, at  $\nu_R = 62.5$  kHz, for both  $\gamma$ -alumina and isopropylamine-templated  $AlPO_4$ -14, PRESTO- $R16_7^6(270_090_{180})$  and RINEPT-CWc- $SR4_1^2(270_090_{180})$  are the best methods to transfer the polarization of protons to quadrupolar nuclei. However, the first sequence requires a much lower rf-field than the second one.

**Table 10.** Comparison of the performances of  $^1H \rightarrow ^{27}Al$  RINEPT-CWc and PRESTO transfers using various recouplings for  $AlPO_4$ -14 at  $\nu_R = 62.5$  kHz.

PRESTO /RINEPT	Recoupling	$\tau$ / $\mu s$	$\nu_1/\nu_{1,max}$ /kHz	Intensity <sup>a</sup>			$\Delta\nu_0$ /kHz	$\Delta\nu_0/\nu_1$	$\Delta\nu_1$ /kHz	$\Delta\nu_1/\nu_1$
				$AlO_6$ <sub>b</sub>	$AlO_5$ <sub>c</sub>	$AlO_4$ <sub>d</sub>				
RINEPT	$SR4_1^2(tt)$	480	208	1.00	1.00	1.00	48	0.23	- <sup>e</sup>	- <sup>e</sup>
	$R12_3^5(tt)$	480	208	1.07	1.00	1.06	44	0.21	- <sup>e</sup>	- <sup>e</sup>
	$SR4_1^2(270_090_{180})$	480	208	1.05	0.95	0.97	85	0.41	90	0.43
	$R12_3^5(270_090_{180})$	480	208	0.91	0.84	0.91	80	0.38	68	0.33
PRESTO	$R16_7^6(270_090_{180})$	672	146	1.71	1.21	0.76	80	0.55	50	0.34
	$R14_6^5(270_090_{180})$	576	146	1.72	1.27	0.76	86	0.59	45	0.31
RINEPT	$SR4_1^2(180_0)$	480	129	0.84	0.79	0.75	48	0.37	64	0.49
	$R12_3^5(180_0)$	480	136	0.72	0.67	0.74	18	0.13	54	0.40
PRESTO	$R22_4^3(180_0)$	512	157	1.47	1.18	0.69	60	0.38	20	0.33
	$R16_3^2(180_0)$	480	147	1.17	0.83	0.52	64	0.44	20	0.31
RINEPT	$R12_3^5(90_{-45}90_{45}90_{-45})$	256	190	0.48	0.27	0.14	32	0.17	75	0.39
	$C6_3^0(C')$	256	193	0.47	0.28	0.14	28	0.15	78	0.40
	$SR4_1^2(90_{-45}90_{45}90_{-45})$	256	196	0.48	0.14	0.14	36	0.18	77	0.39
	$SC2_1^0(C)$	256	188	0.53	0.25	0.14	44	0.23	80	0.43

<sup>a</sup> Intensities of  $AlO_6$ ,  $AlO_5$  and  $AlO_4$  resonances normalized to their intensities with  $^1H \rightarrow ^{27}Al$  RINEPT-CWc- $SR4_1^2(tt)$ . <sup>b</sup> The absolute error on  $AlO_6$  signal intensity is  $\pm 0.04$ . <sup>c</sup> The absolute error on  $AlO_5$  signal intensity is  $\pm 0.06$ . <sup>d</sup> The absolute error on  $AlO_4$  signal intensity is  $\pm 0.02$ . <sup>e</sup> FWHM of the robustness to rf-field was not measured for RINEPT- $SR4_1^2(tt)$  and - $R12_3^5(tt)$  (Fig. 28).



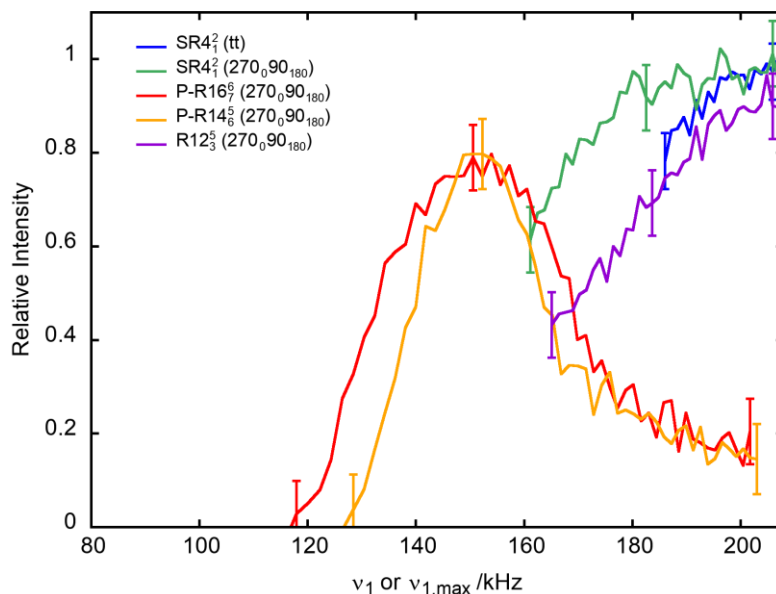


**Figure 28.**  $^{27}\text{AlO}_4$  signal of  $\text{AlPO}_4\text{-14}$  at  $\nu_R = 62.5$  kHz as function of  $\nu_1$  or  $\nu_{1,\text{max}}$  of the recoupling for PRESTO- $\text{R16}_7^6(270_0 90_{180})$  and  $\text{-R14}_8^5(270_0 90_{180})$  as well as RINEPT-CWc- $\text{SR4}_1^2(\text{tt})$ ,  $\text{-SR4}_1^2(270_0 90_{180})$  and  $\text{-R12}_3^5(270_0 90_{180})$ . For each curve,  $\tau$  was fixed to its optimum value given in Table 10. Vertical bars correspond to the error on  $\text{AlO}_4$  intensity, determined by the inverse of the S/N of the optimum  $\nu_1$ .

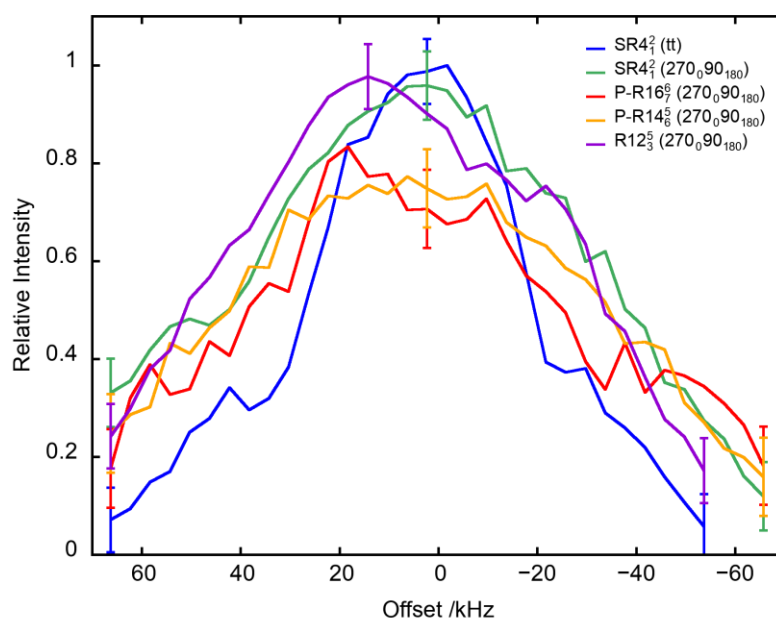


**Figure 29.**  $^{27}\text{AlO}_4$  signal of  $\text{AlPO}_4\text{-14}$  at  $\nu_R = 62.5$  kHz as function of offset of the recoupling for PRESTO- $\text{R16}_7^6(270_0 90_{180})$  and  $\text{-R14}_8^5(270_0 90_{180})$  as well as RINEPT-CWc- $\text{SR4}_1^2(\text{tt})$ ,  $\text{-SR4}_1^2(270_0 90_{180})$  and  $\text{-R12}_3^5(270_0 90_{180})$ . For each curve,  $\tau$  and  $\nu_1$  or  $\nu_{1,\text{max}}$  were fixed to their optimum values given in Table 10. Vertical bars correspond to the error on  $\text{AlO}_4$  intensity, determined by the inverse of the S/N of the optimum offset value.

**Table 11.** Distances between the different H atoms and their closest Al neighbours in the structure of isopropylamine templated AlPO<sub>4</sub>-14 determined from X-ray diffraction.<sup>73</sup> The H and Al atoms are numbered according to the cif file.

H	Al	$r_{\text{HAl}}/\text{\AA}$
H1 (OH)	Al4O <sub>6</sub>	2.496
	Al4O <sub>6</sub>	2.499
	Al1O <sub>5</sub>	2.503
	Al2O <sub>4</sub>	4.299
H2 (NH <sub>3</sub> )	Al4O <sub>6</sub>	3.069
	Al2O <sub>4</sub>	3.779
H3 (NH <sub>3</sub> )	Al3O <sub>4</sub>	3.778
	Al4O <sub>6</sub>	3.960
H4 (NH <sub>3</sub> )	Al2O <sub>4</sub>	3.479
	Al1O <sub>5</sub>	3.801
H5 (CH)	Al2O <sub>4</sub>	3.737
	Al1O <sub>5</sub>	4.850
H6 (CH <sub>3</sub> ) <sub>1</sub>	Al1O <sub>5</sub>	3.655
	Al3O <sub>4</sub>	4.594
H7 (CH <sub>3</sub> ) <sub>1</sub>	Al3O <sub>4</sub>	4.082
	Al1O <sub>5</sub>	4.320
H8 (CH <sub>3</sub> ) <sub>1</sub>	Al2O <sub>4</sub>	3.772
	Al3O <sub>4</sub>	4.651
H9 (CH <sub>3</sub> ) <sub>2</sub>	Al4O <sub>6</sub>	3.888
	Al3O <sub>4</sub>	4.124
H10 (CH <sub>3</sub> ) <sub>2</sub>	Al4O <sub>6</sub>	3.509
	Al3O <sub>4</sub>	4.502
H11 (CH <sub>3</sub> ) <sub>2</sub>	Al4O <sub>6</sub>	3.970
	Al3O <sub>4</sub>	4.048

## 2.5 2D $^1\text{H} \rightarrow ^{27}\text{Al}$ HETCOR EXPERIMENTS

Fig. 30 demonstrates the possibility to acquire 2D  $^1\text{H}$ - $^{27}\text{Al}$  *D*-HETCOR spectra using RINEPT-CWc-SR4<sub>1</sub><sup>2</sup>(270<sub>0</sub>,90<sub>180</sub>) transfer at  $\nu_R = 62.5$  kHz. This spectrum was recorded on AlPO<sub>4</sub>-14 using a NUS scheme retaining 25% of the  $t_1$  points, which would be acquired using the conventional uniform sampling. In this spectrum, the CH proton only correlates with the AlO<sub>4</sub> site since it is too distant from AlO<sub>5</sub> and AlO<sub>6</sub> sites as shown in Table 11. The other two  $^1\text{H}$  signals correlate with the three Al environments. Similar 2D spectra (not shown) were acquired using RINEPT-CWc transfer based on SR4<sub>1</sub><sup>2</sup>(180<sub>0</sub>) and SR4<sub>1</sub><sup>2</sup>(tt) recoupling as well as PRESTO-R16<sub>7</sub><sup>6</sup>(270<sub>0</sub>90<sub>180</sub>). Their skyline projections are shown in Fig. 31. The projections along F2 are in agreement with the results presented in Fig. 22b.

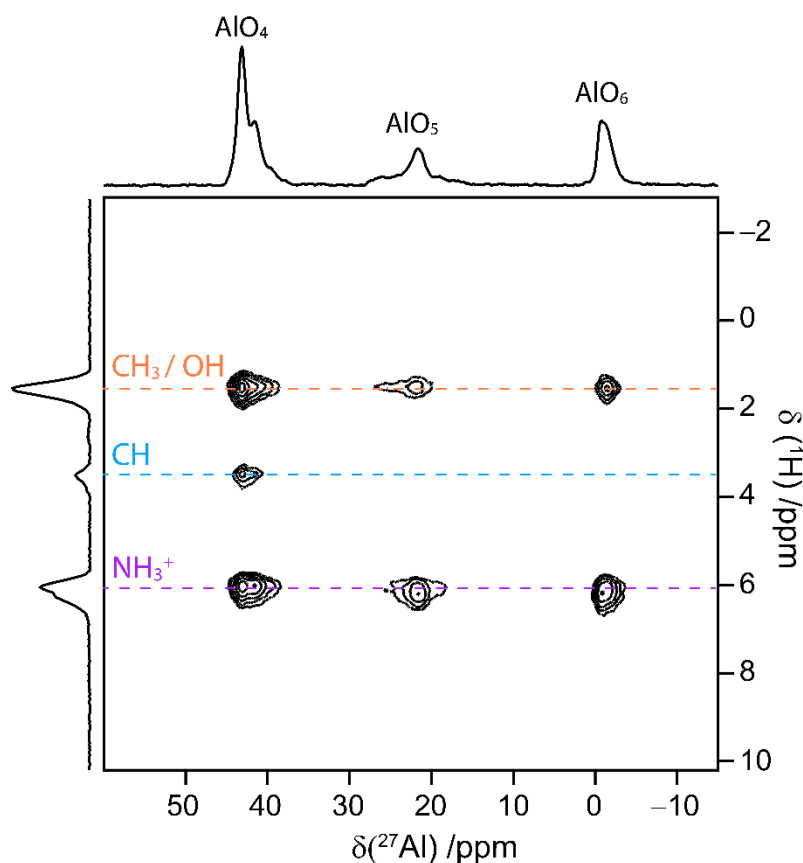


**Figure 30.**  $^1\text{H}$ - $^{27}\text{Al}$  *D*-HETCOR 2D spectrum of AlPO<sub>4</sub>-14, along with its skyline projections, at  $B_0 = 18.8$  T and  $\nu_R = 62.5$  kHz acquired in only 72 min with only ca. 2.5  $\mu\text{L}$  of active volume with NUS 25% using RINEPT-CWc-SR4<sub>1</sub><sup>2</sup>(270<sub>0</sub>90<sub>180</sub>) transfer.

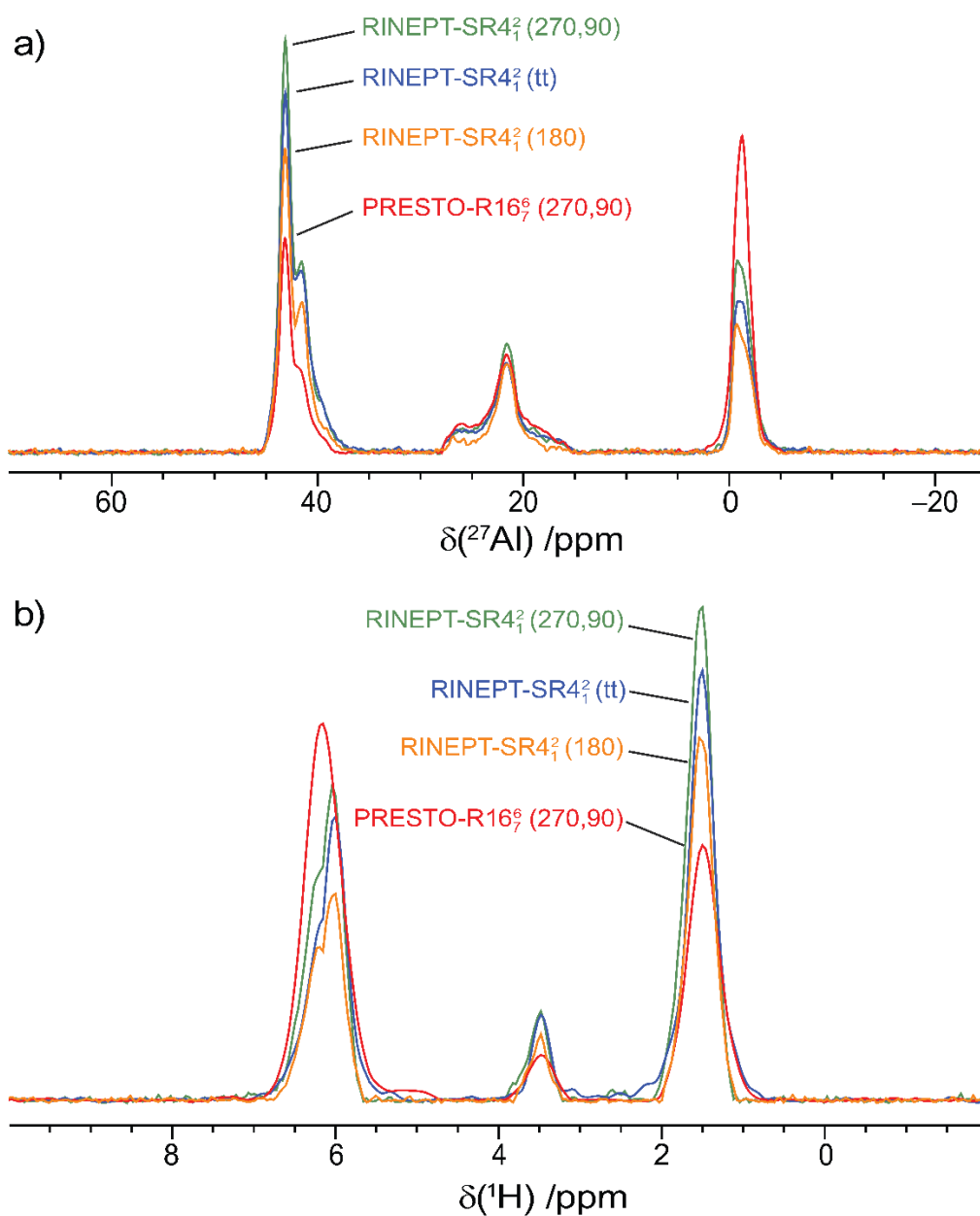


**Figure 31.** Skyline projections along a) F2 and b) F1 of  $^1\text{H}$ - $^{27}\text{Al}$  HETCOR 2D spectra of  $\text{AlPO}_4\text{-14}$  recorded with RINEPT-CWc- $\text{SR4}_1^2(270_090_{180})$ ,  $\text{SR4}_1^2(\text{tt})$ ,  $\text{SR4}_1^2(180_090_{180})$  and PRESTO- $\text{R16}_7^6(270_090_{180})$  transfers. All 2D spectra were acquired using NUS 25% in 72 min.

## 2.6 MEASUREMENT OF THE DECAY OF THE TRANSVERSE $^1\text{H}$ MAGNETIZATION DURING RECOUPLING

The decay of the  $^1\text{H}$  transverse magnetization was measured during a spin-echo experiment (Fig. 18), in which the refocusing  $\pi$ -pulse was the composite one employed in the defocusing part of the RINEPT-CW sequence (Fig. 13b). These experiments were performed on  $\text{AlPO}_4\text{-14}$  since the  $^1\text{H}$ - $^1\text{H}$  dipolar interactions are larger in this sample than in  $\gamma$ -alumina. This decay was measured either in the absence of any recoupling or under a  $\text{SR4}_1^2$  recoupling built from  $(180_0)$ ,  $(270_090_{180})$  or tt inversion element. The three  $^1\text{H}$  signals featured a mono-exponential decay with a time constant  $T_2'$  reported in Table 12.

**Table 12.**  $^1\text{H}$   $T_2'$  values of  $\text{AlPO}_4\text{-14}$  without recoupling or with  $\text{SR4}_1^2$  recoupling built from  $(180_0)$ ,  $(270_090_{180})$  or tt inversion element. The estimated error bars are equal to 7 %.

$\nu_R$ (kHz)	20			62.5		
$T_2'$ (ms)	$\text{NH}_3^+$	CH	$\text{CH}_3 + \text{OH}$	$\text{NH}_3^+$	CH	$\text{CH}_3 + \text{OH}$
No recoupling	1.6	1.6	1.4	4.0	4.2	4.4
$(180_0)$	0.6	0.4	0.6	0.9	0.5	0.7
$(270_090_{180})$	0.8	0.6	0.9	0.5	0.3	0.4
tt	52	1000	170	2.2	2.7	2.1

At  $\nu_R = 20$  kHz, the  $T_2'$  constants are significantly shorter under  $\text{SR4}_1^2(180_0)$  and  $\text{SR4}_1^2(270_090_{180})$  than without recoupling. This faster decay can stem from the reintroduction of  $^1\text{H}$ - $^1\text{H}$  dipolar interactions in the second- and higher-order terms of the AH by the recoupling as well as the effect of pulse transients<sup>74</sup>. Conversely, the  $T_2'$  constants under  $\text{SR4}_1^2(\text{tt})$  are much longer than without recoupling, showing that the adiabatic pulses using large RF-field efficiently decouple the  $^1\text{H}$ - $^1\text{H}$  dipolar interactions, whereas the continuous variation of the phase and amplitude during these pulses minimizes the transients.

At  $\nu_R = 62.5$  kHz, the  $T_2'$  constants without recoupling are lengthened with respect to those at  $\nu_R = 20$  kHz since faster MAS better averages the  $^1\text{H}$ - $^1\text{H}$  dipolar

interactions.<sup>75</sup> Conversely, the  $T_2'$  constants under  $\text{SR4}_1^2(270_090_{180})$  recoupling are shorter at  $\nu_R = 62.5$  than at 20 kHz. This counter-intuitive reduction may stem from the shorter pulse lengths at  $\nu_R = 62.5$  kHz, which results in a larger number of transients. For the same reason, the  $T_2'$  constants under  $\text{SR4}_1^2(180_0)$  are only slightly longer at high MAS frequency. The  $T_2'$  constants under  $\text{SR4}_1^2(\text{tt})$  recoupling are much shorter at  $\nu_R = 62.5$  than at 20 kHz because the adiabaticity criterion is not fulfilled at  $\nu_R = 62.5$  kHz and hence, the elimination of  $^1\text{H}$ - $^1\text{H}$  dipolar interactions is less effective (Fig. 28).

## 2.7 CONCLUSIONS

In this work, novel symmetry-based hetero-nuclear dipolar recoupling schemes were introduced, which can be incorporated into the RINEPT and PRESTO sequences to transfer the magnetization from  $^1\text{H}$  to half-integer quadrupolar nuclei at  $\nu_R = 20$  or 62.5 kHz. These new recouplings have been compared to the existing ones. It was shown that the RINEPT-CWc- $\text{SR4}_1^2(\text{tt})$  sequence with adiabatic pulses, which produces efficient and robust transfers at  $\nu_R \approx 10\text{-}15$  kHz,<sup>20</sup> requires rf-fields incompatible with the specifications of most MAS probes for  $\nu_R \geq 20$  kHz. Conversely, the introduced RINEPT-CWc- $\text{SR4}_1^2(270_090_{180})$  and PRESTO-R22 $_2^7(180_0)$  techniques with rf-fields of ca.  $4\nu_R$  and  $5.5\nu_R$ , respectively, are the methods of choice at  $\nu_R = 20$  kHz to transfer the magnetization from protons to quadrupolar nuclei. At  $\nu_R = 62.5$  kHz, the RINEPT-CWc- $\text{SR4}_1^2(270_090_{180})$  and PRESTO-R16 $_2^6(270_090_{180})$  sequences with RF-requirements of ca.  $4\nu_R$  and  $2.3\nu_R$ , respectively, result in the most robust and efficient transfers. At both MAS frequencies, the RINEPT and PRESTO techniques complement each other since the latter is dipolar truncated, whereas the former is not. As a result, the RINEPT sequences must be chosen to observe simultaneously protonated and unprotonated sites, whereas the PRESTO schemes can be employed for the selective observation of quadrupolar nuclei in proximity to protons. These techniques are expected to be useful for transferring the DNP-enhanced magnetization of protons to quadrupolar nuclei in indirect MAS DNP experiments at  $\nu_R \geq 20$  kHz, notably used at high magnetic fields.<sup>20,76,77</sup> It was demonstrated that they can be used to correlate the NMR signals of protons and quadrupolar nuclei at high MAS frequencies.

## References

- (1) Gómez, J. S.; Rankin, A. G. M.; Trébosc, J.; Pourpoint, F.; Tsutsumi, Y.; Nagashima, H.; Lafon, O.; Amoureux, J.-P. Improved NMR Transfer of Magnetization from Protons to Half-Integer Spin Quadrupolar Nuclei at Moderate and High Magic-Angle Spinning Frequencies. *Magn. Reson.* **2021**, *2* (1), 447–464. <https://doi.org/10.5194/mr-2-447-2021>.
- (2) Ashbrook, S. E.; Sneddon, S. New Methods and Applications in Solid-State NMR Spectroscopy of Quadrupolar Nuclei. *J. Am. Chem. Soc.* **2014**, *136* (44), 15440–15456. <https://doi.org/10.1021/ja504734p>.
- (3) Grekov, D.; Vancompernelle, T.; Taoufik, M.; Delevoye, L.; Gauvin, R. M. Solid-State NMR of Quadrupolar Nuclei for Investigations into Supported Organometallic Catalysts: Scope and Frontiers. *Chem. Soc. Rev.* **2018**, *47* (8), 2572–2590. <https://doi.org/10.1039/C7CS00682A>.
- (4) Stone-Weiss, N.; Youngman, R. E.; Thorpe, R.; Smith, N. J.; Pierce, E. M.; Goel, A. An Insight into the Corrosion of Alkali Aluminoborosilicate Glasses in Acidic Environments. *Phys. Chem. Chem. Phys.* **2020**, *22* (4), 1881–1896. <https://doi.org/10.1039/C9CP06064B>.
- (5) Xu, J. H.; Jadhav, A. L.; Turney, D. E.; Messinger, R. J. Molecular-Level Environments of Intercalated Chloroaluminate Anions in Rechargeable Aluminum-Graphite Batteries Revealed by Solid-State NMR Spectroscopy. *J. Mater. Chem. A* **2020**, *8* (31), 16006–16017. <https://doi.org/10.1039/D0TA02611E>.
- (5) Greiser, S.; Gluth, G. J. G.; Sturm, P.; Jäger, C.  $^{29}\text{Si}(^{27}\text{Al})$ ,  $^{27}\text{Al}(^{29}\text{Si})$  and  $^{27}\text{Al}(^1\text{H})$  Double-Resonance NMR Spectroscopy Study of Cementitious Sodium Aluminosilicate Gels (Geopolymers) and Gel–Zeolite Composites. *RSC Adv.* **2018**, *8* (70), 40164–40171. <https://doi.org/10.1039/C8RA09246J>.
- (7) Rocha, J.; Carr, S. W.; Klinowski, J.  $^{27}\text{Al}$  Quadrupole Nutation and  $^1\text{H}$ - $^{27}\text{Al}$  Cross-Polarization Solid-State NMR Studies of Ultrastable Zeolite Y with Fast Magic-Angle Spinning. *Chem. Phys. Lett.* **1991**, *187* (4), 401–408. [https://doi.org/10.1016/0009-2614\(91\)80272-Y](https://doi.org/10.1016/0009-2614(91)80272-Y).
- (8) Hwang, S.-J.; Chen, C.-Y.; Zones, S. I. Boron Sites in Borosilicate Zeolites at Various Stages of Hydration Studied by Solid State NMR Spectroscopy. *J. Phys. Chem. B* **2004**, *108* (48), 18535–18546. <https://doi.org/10.1021/jp0476904>.
- (9) Peng, L.; Huo, H.; Liu, Y.; Grey, C. P.  $^{17}\text{O}$  Magic Angle Spinning NMR Studies of Brønsted Acid Sites in Zeolites HY and HZSM-5. *J. Am. Chem. Soc.* **2007**, *129* (2), 335–346. <https://doi.org/10.1021/ja064922z>.
- (10) Vogt, F. G.; Yin, H.; Forcino, R. G.; Wu, L.  $^{17}\text{O}$  Solid-State NMR as a Sensitive Probe of Hydrogen Bonding in Crystalline and Amorphous Solid Forms of Diflunisal. *Mol. Pharm.* **2013**, *10* (9), 3433–3446. <https://doi.org/10.1021/mp400275w>.
- (11) Chen, J.; Wu, X.-P.; Hope, M. A.; Qian, K.; Halat, D. M.; Liu, T.; Li, Y.; Shen, L.; Ke, X.; Wen, Y.; Du, J.-H.; Magusin, P. C. M. M.; Paul, S.; Ding, W.; Gong, X.-Q.; Grey, C. P.; Peng, L. Polar Surface Structure of Oxide Nanocrystals Revealed with Solid-State NMR Spectroscopy. *Nat. Commun.* **2019**, *10* (1), 1–10. <https://doi.org/10.1038/s41467-019-13424-7>.
- (12) Blanc, F.; Sperrin, L.; Jefferson, D. A.; Pawsey, S.; Rosay, M.; Grey, C. P. Dynamic Nuclear Polarization Enhanced Natural Abundance  $^{17}\text{O}$

- Spectroscopy. *J. Am. Chem. Soc.* **2013**, *135* (8), 2975–2978. <https://doi.org/10.1021/ja4004377>.
- (13) Perras, F. A.; Kobayashi, T.; Pruski, M. Natural Abundance  $^{17}\text{O}$  DNP Two-Dimensional and Surface-Enhanced NMR Spectroscopy. *J. Am. Chem. Soc.* **2015**, *137* (26), 8336–8339. <https://doi.org/10.1021/jacs.5b03905>.
- (14) Perras, F. A.; Chaudhary, U.; Slowing, I. I.; Pruski, M. Probing Surface Hydrogen Bonding and Dynamics by Natural Abundance, Multidimensional,  $^{17}\text{O}$  DNP-NMR Spectroscopy. *J. Phys. Chem. C* **2016**, *120* (21), 11535–11544. <https://doi.org/10.1021/acs.jpcc.6b02579>.
- (15) Perras, F. A.; Wang, Z.; Naik, P.; Slowing, I. I.; Pruski, M. Natural Abundance  $^{17}\text{O}$  DNP NMR Provides Precise O–H Distances and Insights into the Brønsted Acidity of Heterogeneous Catalysts. *Angew. Chem. Int. Ed.* **2017**, *56* (31), 9165–9169. <https://doi.org/10.1002/anie.201704032>.
- (16) Hope, M. A.; Halat, D. M.; Magusin, P. C. M. M.; Paul, S.; Peng, L.; Grey, C. P. Surface-Selective Direct  $^{17}\text{O}$  DNP NMR of  $\text{CeO}_2$  Nanoparticles. *Chem. Commun.* **2017**, *53* (13), 2142–2145. <https://doi.org/10.1039/C6CC10145C>.
- (17) Lee, D.; Leroy, C.; Crevant, C.; Bonhomme-Coury, L.; Babonneau, F.; Laurencin, D.; Bonhomme, C.; Paëpe, G. D. Interfacial  $\text{Ca}^{2+}$  Environments in Nanocrystalline Apatites Revealed by Dynamic Nuclear Polarization Enhanced  $^{43}\text{Ca}$  NMR Spectroscopy. *Nat. Commun.* **2017**, *8*, 14104. <https://doi.org/10.1038/ncomms14104>.
- (18) Li, W.; Wang, Q.; Xu, J.; Aussenac, F.; Qi, G.; Zhao, X.; Gao, P.; Wang, C.; Deng, F. Probing the Surface of  $\gamma\text{-Al}_2\text{O}_3$  by Oxygen-17 Dynamic Nuclear Polarization Enhanced Solid-State NMR Spectroscopy. *Phys. Chem. Chem. Phys.* **2018**, *20* (25), 17218–17225. <https://doi.org/10.1039/C8CP03132K>.
- (18) Nagashima, H.; Trébosc, J.; Kon, Y.; Lafon, O.; Amoureux, J.-P. Efficient Transfer of  $^1\text{H}$  Magnetization to Half-Integer Quadrupolar Nuclei in Solids, Enhanced by Dynamic Nuclear Polarization at Moderate Spinning Rate. *Magn. Reson. Chem.* 2020. In press.
- (20) Nagashima, H.; Trébosc, J.; Kon, Y.; Sato, K.; Lafon, O.; Amoureux, J.-P. Observation of Low- $\gamma$  Quadrupolar Nuclei by Surface-Enhanced NMR Spectroscopy. *J. Am. Chem. Soc.* **2020**, *142* (24), 10659–10672. <https://doi.org/10.1021/jacs.9b13838>.
- (21) Harris, R. K.; Nesbitt, G. J. Cross Polarization for Quadrupolar Nuclei—Proton to Sodium-23. *J. Magn. Reson.* 1969 **1988**, *78* (2), 245–256. [https://doi.org/10.1016/0022-2364\(88\)90268-5](https://doi.org/10.1016/0022-2364(88)90268-5).
- (21) Vega, A. J. CPMAS of Quadrupolar  $S = 3/2$  Nuclei. *Solid State Nucl. Magn. Reson.* **1992**, *1* (1), 17–32. [https://doi.org/10.1016/0926-2040\(92\)90006-U](https://doi.org/10.1016/0926-2040(92)90006-U).
- (23) Amoureux, J.-P.; Pruski, M. Theoretical and Experimental Assessment of Single- and Multiple-Quantum Cross-Polarization in Solid State NMR. *Mol. Phys.* **2002**, *100* (10), 1595–1613. <https://doi.org/10.1080/00268970210125755>.
- (24) Tricot, G.; Lafon, O.; Trébosc, J.; Delevoye, L.; Méar, F.; Montagne, L.; Amoureux, J.-P. Structural Characterisation of Phosphate Materials: New Insights into the Spatial Proximities between Phosphorus and Quadrupolar Nuclei Using the D-HMQC MAS NMR Technique. *Phys. Chem. Chem. Phys.* **2011**, *13* (37), 16786–16794. <https://doi.org/10.1039/C1CP20993K>.
- (25) Ashbrook, S. E.; Wimperis, S. Spin-Locking of Half-Integer Quadrupolar Nuclei in Nuclear Magnetic Resonance of Solids: Second-Order Quadrupolar



- and Resonance Offset Effects. *J. Chem. Phys.* **2009**, *131* (19), 194509. <https://doi.org/10.1063/1.3263904>.
- (26) Barrie, P. J. Distorted Powder Lineshapes in  $^{27}\text{Al}$  CP / MAS NMR Spectroscopy of Solids. *Chem. Phys. Lett.* **1993**, *208* (5), 486–490. [https://doi.org/10.1016/0009-2614\(93\)87177-5](https://doi.org/10.1016/0009-2614(93)87177-5).
- (27) Hayashi, S.; Hayamizu, K. Line Shapes in CP/MAS NMR Spectra of Half-Integer Quadrupolar Nuclei. *Chem. Phys. Lett.* **1993**, *203* (4), 319–324. [https://doi.org/10.1016/0009-2614\(93\)85575-9](https://doi.org/10.1016/0009-2614(93)85575-9).
- (28) Ding, S. W.; Mcdowell, C. A. Theoretical Calculations of the CPMAS Spectral Lineshapes of Half-Integer Quadrupole Systems. *J. Magn. Reson. A* **1995**, *114* (1), 80–87. <https://doi.org/10.1006/jmra.1995.1108>.
- (29) Perras, F. A.; Kobayashi, T.; Pruski, M. PRESTO Polarization Transfer to Quadrupolar Nuclei: Implications for Dynamic Nuclear Polarization. *Phys. Chem. Chem. Phys.* **2015**, *17* (35), 22616–22622. <https://doi.org/10.1039/C5CP04145G>.
- (30) Zhao, X.; Hoffbauer, W.; Schmedt auf der Günne, J.; Levitt, M. H. Heteronuclear Polarization Transfer by Symmetry-Based Recoupling Sequences in Solid-State NMR. *Solid State Nucl. Magn. Reson.* **2004**, *26* (2), 57–64. <https://doi.org/10.1016/j.ssnmr.2003.11.001>.
- (31) Giovine, R.; Trébosc, J.; Pourpoint, F.; Lafon, O.; Amoureux, J.-P. Magnetization Transfer from Protons to Quadrupolar Nuclei in Solid-State NMR Using PRESTO or Dipolar-Mediated Refocused INEPT Methods. *J. Magn. Reson.* **2019**, *299*, 109–123. <https://doi.org/10.1016/j.jmr.2018.12.016>.
- (31) Zhao, X.; Ed, M.; Levitt, M. H. Recoupling of Heteronuclear Dipolar Interactions in Solid-State NMR Using Symmetry-Based Pulse Sequences. *Chem. Phys. Lett.* **2001**, *342* (July), 353–361.
- (32) Brinkmann, A.; Kentgens, A. P. M. Proton-Selective  $^{17}\text{O}$ – $^1\text{H}$  Distance Measurements in Fast Magic-Angle-Spinning Solid-State NMR Spectroscopy for the Determination of Hydrogen Bond Lengths. *J. Am. Chem. Soc.* **2006**, *128* (46), 14758–14759. <https://doi.org/10.1021/ja065415k>.
- (34) Pileio, G.; Concistrè, M.; McLean, N.; Gansmüller, A.; Brown, R. C. D.; Levitt, M. H. Analytical Theory of  $\gamma$ -Encoded Double-Quantum Recoupling Sequences in Solid-State Nuclear Magnetic Resonance. *J. Magn. Reson.* **2007**, *186* (1), 65–74. <https://doi.org/10.1016/j.jmr.2007.01.009>.
- (34) Madhu, P. K.; Zhao, X.; Levitt, M. H. High-Resolution  $^1\text{H}$  NMR in the Solid-State Using Symmetry-Based Pulse Sequences. *Chem. Phys. Lett.* **2001**, *346* (1), 142–148. [https://doi.org/10.1016/S0009-2614\(01\)00876-4](https://doi.org/10.1016/S0009-2614(01)00876-4).
- (35) Perras, F. A.; Goh, T. W.; Wang, L.-L.; Huang, W.; Pruski, M. Enhanced  $^1\text{H}$ -X D-HMQC Performance through Improved  $^1\text{H}$  Homonuclear Decoupling. *Solid State Nucl. Magn. Reson.* **2019**, *98*, 12–18. <https://doi.org/10.1016/j.ssnmr.2019.01.001>.
- (37) Lesot, P.; Kazimierczuk, K.; Trébosc, J.; Amoureux, J.-P.; Lafon, O. Fast Acquisition of Multidimensional NMR Spectra of Solids and Mesophases Using Alternative Sampling Methods. *Magn. Reson. Chem.* **2015**, *53* (11), 927–939. <https://doi.org/10.1002/mrc.4290>.
- (38) Levitt, M. H. Symmetry-Based Pulse Sequences in Magic-Angle Spinning Solid-State NMR. In *Encyclopedia of Nuclear Magnetic Resonance. Volume 9, Advances in NMR*; Grant, D. M., Harris, R. K., Eds.; Wiley, 2002; pp 165–196.

- (39) Carravetta, M.; Edén, M.; Zhao, X.; Brinkmann, A.; Levitt, M. H. Symmetry Principles for the Design of Radiofrequency Pulse Sequences in the Nuclear Magnetic Resonance of Rotating Solids. *Chem. Phys. Lett.* **2000**, *321* (3), 205–215. [https://doi.org/10.1016/S0009-2614\(00\)00340-7](https://doi.org/10.1016/S0009-2614(00)00340-7).
- (40) Nimerovsky, E.; Soutar, C. P. A Modification of  $\gamma$ -Encoded RN Symmetry Pulses for Increasing the Scaling Factor and More Accurate Measurements of the Strong Heteronuclear Dipolar Couplings. *J. Magn. Reson.* **2020**, *319*, 106827. <https://doi.org/10.1016/j.jmr.2020.106827>.
- (41) Kobayashi, T.; Perras, F. A.; Nishiyama, Y. Determination of the Chemical Shift Tensor Anisotropy and Asymmetry of Strongly Dipolar Coupled Protons under Fast MAS. *Solid State Nucl. Magn. Reson.* **2021**, *114*, 101743. <https://doi.org/10.1016/j.ssnmr.2021.101743>.
- (42) Edén, M. Enhanced Symmetry-Based Dipolar Recoupling in Solid-State NMR. *Chem. Phys. Lett.* **2003**, *378* (1), 55–64. [https://doi.org/10.1016/S0009-2614\(03\)01241-7](https://doi.org/10.1016/S0009-2614(03)01241-7).
- (43) Martineau, C.; Bouchevreau, B.; Taulelle, F.; Trébosc, J.; Lafon, O.; Amoureux, J. P. High-Resolution through-Space Correlations between Spin-1/2 and Half-Integer Quadrupolar Nuclei Using the MQ-D-R-INEPT NMR Experiment. *Phys. Chem. Chem. Phys.* **2012**, *14* (19), 7112–7119. <https://doi.org/10.1039/C2CP40344G>.
- (44) Hu, B.; Trébosc, J.; Amoureux, J. P. Comparison of Several Hetero-Nuclear Dipolar Recoupling NMR Methods to Be Used in MAS HMQC/HSQC. *J. Magn. Reson.* **2008**, *192* (1), 112–122. <https://doi.org/10.1016/j.jmr.2008.02.004>.
- (45) Nagashima, H.; Lilly Thankamony, A. S.; Trébosc, J.; Pourpoint, F.; Lafon, O.; Amoureux, J. P.  $\gamma$ -Independent through-Space Hetero-Nuclear Correlation between Spin-1/2 and Quadrupolar Nuclei in Solids. *Solid State Nucl. Magn. Reson.* **2017**, *84*, 216–226. <https://doi.org/10.1016/j.ssnmr.2017.06.002>.
- (46) Rosenfeld, D.; Panfil, S. L.; Zur, Y. Design of Selective Adiabatic Inversion Pulses Using the Adiabatic Condition. *J. Magn. Reson.* **1997**, *129* (2), 115–124. <https://doi.org/10.1006/jmre.1997.1263>.
- (47) Garwood, M.; DelaBarre, L. The Return of the Frequency Sweep: Designing Adiabatic Pulses for Contemporary NMR. *J. Magn. Reson.* **2001**, *153* (2), 155–177. <https://doi.org/10.1006/jmre.2001.2340>.
- (48) Heise, B.; Leppert, J.; Ramachandran, R. REDOR with Adiabatic Dephasing Pulses. *J. Magn. Reson.* **2000**, *146* (1), 181–187. <https://doi.org/10.1006/jmre.2000.2129>.
- (49) Kupce, E.; Freeman, R. Adiabatic Pulses for Wideband Inversion and Broadband Decoupling. *J. Magn. Reson. A* **1995**, *115* (2), 273–276. <https://doi.org/10.1006/jmra.1995.1179>.
- (49) O'Dell, L. A.; Klimm, K.; Freitas, J. C. C.; Kohn, S. C.; Smith, M. E.  $^{33}\text{S}$  MAS NMR of a Disordered Sulfur-Doped Silicate: Signal Enhancement via RAPT, QCPMG and Adiabatic Pulses. *Appl. Magn. Reson.* **2009**, *35* (2), 247–259. <https://doi.org/10.1007/s00723-008-0159-8>.
- (51) Tannús, A.; Garwood, M. Adiabatic Pulses. *NMR Biomed.* **1997**, *10* (8), 423–434. [https://doi.org/10.1002/\(SICI\)1099-1492\(199712\)10:8<423::AID-NBM488>3.0.CO;2-X](https://doi.org/10.1002/(SICI)1099-1492(199712)10:8<423::AID-NBM488>3.0.CO;2-X).
- (52) Hwang, T.-L.; van Zijl, P. C. M.; Garwood, M. Fast Broadband Inversion by Adiabatic Pulses. *J. Magn. Reson.* **1998**, *133* (1), 200–203. <https://doi.org/10.1006/jmre.1998.1441>.

- (53) Kervern, G.; Pintacuda, G.; Emsley, L. Fast Adiabatic Pulses for Solid-State NMR of Paramagnetic Systems. *Chem. Phys. Lett.* **2007**, *435* (1–3), 157–162. <https://doi.org/10.1016/j.cplett.2006.12.056>.
- (54) Nagashima, H.; Lilly Thankamony, A. S.; Trébosc, J.; Montagne, L.; Kerven, G.; Amoureux, J.-P.; Lafon, O. Observation of Proximities between Spin-1/2 and Quadrupolar Nuclei in Solids: Improved Robustness to Chemical Shielding Using Adiabatic Symmetry-Based Recoupling. *Solid State Nucl. Magn. Reson.* **2018**, *94*, 7–19. <https://doi.org/10.1016/j.ssnmr.2018.07.001>.
- (55) Shen, J. Use of Amplitude and Frequency Transformations to Generate Adiabatic Pulses of Wide Bandwidth and Low RF Power Deposition. *J. Magn. Reson. B* **1996**, *112* (2), 131–140. <https://doi.org/10.1006/jmrb.1996.0123>.
- (56) Bayro, M. J.; Huber, M.; Ramachandran, R.; Davenport, T. C.; Meier, B. H.; Ernst, M.; Griffin, R. G. Dipolar Truncation in Magic-Angle Spinning NMR Recoupling Experiments. *J. Chem. Phys.* **2009**, *130* (11), 114506. <https://doi.org/10.1063/1.3089370>.
- (57) Pandey, M. K.; Malon, M.; Ramamoorthy, A.; Nishiyama, Y. Composite-180° Pulse-Based Symmetry Sequences to Recouple Proton Chemical Shift Anisotropy Tensors under Ultrafast MAS Solid-State NMR Spectroscopy. *J. Magn. Reson.* **2015**, *250*, 45–54. <https://doi.org/10.1016/j.jmr.2014.11.002>.
- (58) Freeman, R.; Kempell, S. P.; Levitt, M. H. Radiofrequency Pulse Sequences Which Compensate Their Own Imperfections. *J. Magn. Reson.* **1980**, *38* (3), 453–479. [https://doi.org/10.1016/0022-2364\(80\)90327-3](https://doi.org/10.1016/0022-2364(80)90327-3).
- (58) Duong, N. T.; Trébosc, J.; Lafon, O.; Amoureux, J.-P. Improved Sensitivity and Quantification for <sup>29</sup>Si NMR Experiments on Solids Using UDEFT (Uniform Driven Equilibrium Fourier Transform). *Solid State Nucl. Magn. Reson.* **2019**, *100*, 52–62. <https://doi.org/10.1016/j.ssnmr.2019.03.007>.
- (59) Madhu, P. K.; Zhao, X.; Levitt, M. H. High-Resolution <sup>1</sup>H NMR in the Solid-State Using Symmetry-Based Pulse Sequences. *Chem. Phys. Lett.* **2001**, *346*, 142–148.
- (60) Brinkmann, A.; Kentgens, A. P. M. Sensitivity Enhancement and Heteronuclear Distance Measurements in Biological <sup>17</sup>O Solid State NMR. *J. Phys. Chem. B* **2006**, *110*, 16089–16101.
- (61) Brinkmann, A.; Levitt, M. H. Symmetry Principles in the Nuclear Magnetic Resonance of Spinning Solids: Heteronuclear Recoupling by Generalized Hartmann-Hahn Sequences. *J. Chem. Phys.* **2001**, *115*, 357–384.
- (62) Brinkmann, A.; Edén, M.; Levitt, M. H. Synchronous Helical Pulse Sequences in Magic-Angle Spinning Nuclear Magnetic Resonance: Double Quantum Recoupling of Multiple-Spin Systems. *J. Chem. Phys.* **2000**, *112*, 8539–8554.
- (63) Brinkmann, A.; Edén, M. Second Order Average Hamiltonian Theory of Symmetry-Based Pulse Schemes in the Nuclear Magnetic Resonance of Rotating Solids: Application to Triple-Quantum Dipolar Recoupling. *J. Chem. Phys.* **2004**, *120*, 11726–11745.
- (65) Lu, X.; Lafon, O.; Trébosc, J.; Tricot, G.; Delevoye, L.; Méar, F.; Montagne, L.; Amoureux, J. P. Observation of Proximities between Spin-1/2 and Quadrupolar Nuclei: Which Heteronuclear Dipolar Recoupling Method Is Preferable? *J. Chem. Phys.* **2012**, *137* (14), 144201. <https://doi.org/10.1063/1.4753987>.
- (66) Levitt, M. H.; Freeman, R. NMR Population Inversion Using a Composite Pulse. *J. Magn. Reson.* **1979**, *33* (2), 473–476. [https://doi.org/10.1016/0022-2364\(79\)90265-8](https://doi.org/10.1016/0022-2364(79)90265-8).

- (66) Antonijevic, S.; Ashbrook, S. E.; Biedasek, S.; Walton, R. I.; Wimperis, S.; Yang, H. Dynamics on the Microsecond Timescale in Microporous Aluminophosphate AlPO-14 as Evidenced by  $^{27}\text{Al}$  MQMAS and STMAS NMR Spectroscopy. *J. Am. Chem. Soc.* **2006**, *128* (24), 8054–8062. <https://doi.org/10.1021/ja057682g>.
- (68) Morris, H. D.; Ellis, P. D. Aluminum-27 Cross Polarization of Aluminas. The NMR Spectroscopy of Surface Aluminum Atoms. *J. Am. Chem. Soc.* **1989**, *111* (16), 6045–6049. <https://doi.org/10.1021/ja00198a012>.
- (68) Lee, D.; Duong, N. T.; Lafon, O.; De Paëpe, G. Primostrato Solid State NMR Enhanced by Dynamic Nuclear Polarization: Pentacoordinated  $\text{Al}^{3+}$  Ions Are Only Located at the Surface of Hydrated  $\gamma$ -Alumina. *J. Phys. Chem. C* **2014**, *118*, 25065–25076. <https://doi.org/10.1021/jp508009x>.
- (69) Ashbrook, S. E.; Cutajar, M.; Pickard, C. J.; Walton, R. I.; Wimperis, S. Structure and NMR Assignment in Calcined and As-Synthesized Forms of AlPO-14: A Combined Study by First-Principles Calculations and High-Resolution  $^{27}\text{Al}$ - $^{31}\text{P}$  MAS NMR Correlation. *Phys. Chem. Chem. Phys.* **2008**, *10* (37), 5754–5764. <https://doi.org/10.1039/B805681A>.
- (70) Fernandez, C.; Amoureux, J. P.; Chezeau, J. M.; Delmotte, L.; Kessler, H.  $^{27}\text{Al}$  MAS NMR Characterization of AlPO<sub>4</sub>-14 Enhanced Resolution and Information by MQMAS Dr. Hellmut G. Karge on the Occasion of His 65th Birthday. *Microporous Mater.* **1996**, *6* (5), 331–340. [https://doi.org/10.1016/0927-6513\(96\)00040-5](https://doi.org/10.1016/0927-6513(96)00040-5).
- (72) Cory, D. G.; Ritchey, W. M. Suppression of Signals from the Probe in Bloch Decay Spectra. *J. Magn. Reson.* **1988**, *80* (1), 128–132.
- (73) Broach, R. W.; Wilson, S. T.; Kirchner, R. M. Corrected Crystallographic Tables and Figure for As-Synthesized AlPO<sub>4</sub>-14. *Microporous Mesoporous Mater.* **2003**, *57* (2), 211–214. [https://doi.org/10.1016/S1387-1811\(02\)00563-2](https://doi.org/10.1016/S1387-1811(02)00563-2).
- (74) Wittmann, J. J.; Mertens, V.; Takeda, K.; Meier, B. H.; Ernst, M. Quantification and Compensation of the Influence of Pulse Transients on Symmetry-Based Recoupling Sequences. *J. Magn. Reson.* **2016**, *263*, 7–18. <https://doi.org/10.1016/j.jmr.2015.12.011>.
- (75) Mao, K.; Wiench, J. W.; Lin, V. S.-Y.; Pruski, M. Indirectly Detected Through-Bond Chemical Shift Correlation NMR Spectroscopy in Solids under Fast MAS: Studies of Organic–Inorganic Hybrid Materials. *J. Magn. Reson.* **2009**, *196* (1), 92–95. <https://doi.org/10.1016/j.jmr.2008.10.010>.
- (76) Rankin, A. G. M.; Trébosc, J.; Pourpoint, F.; Amoureux, J.-P.; Lafon, O. Recent Developments in MAS DNP-NMR of Materials. *Solid State Nucl. Magn. Reson.* **2019**, *101*, 116–143. <https://doi.org/10.1016/j.ssnmr.2019.05.009>.
- (77) Berruyer, P.; Björgvinsdóttir, S.; Bertarello, A.; Stevanato, G.; Rao, Y.; Karthikeyan, G.; Casano, G.; Ouari, O.; Lelli, M.; Reiter, C.; Engelke, F.; Emsley, L. Dynamic Nuclear Polarization Enhancement of 200 at 21.15 T Enabled by 65 KHz Magic Angle Spinning. *J. Phys. Chem. Lett.* **2020**, *11* (19), 8386–8391. <https://doi.org/10.1021/acs.jpcclett.0c02493>.

---

## **CHAPTER 3**

---



# Chapter 3: Comparison of double and single quantum dipolar NMR correlations of quadrupolar nuclei

---

## 3.1 STATEMENT OF CONTRIBUTION

Chapter 3 of this thesis incorporates unpublished material for a publication for which I will be the first author, and which will be co-authored with Julien Trébosc, Nghia Tuan Duong, Frédérique Pourpoint, Olivier Lafon and Jean-Paul Amoureux. In all cases, only my primary contribution towards this publication is included in this manuscript. I carried out the NMR experiments on  $\text{Li}_2\text{B}_4\text{O}_7$  and  $\text{AlPO}_4\text{-14}$ , analyzed the experimental data and assisted with the editing of the paper. I also performed some preliminary numerical simulations of spin dynamics using Simpson software in order to compare the performances of the different recoupling schemes. Nevertheless, these simulations are not included in the manuscript since they are under progress. J. Trébosc provided assistance in experimentation. Nghia Tuan Duong assisted with the spin dynamics simulations. F. Pourpoint contributed to the analysis and interpretation of the results. O. Lafon and J-P. Amoureux contributed to the experimental design, analysis and interpretation of the results and the writing of the paper. All authors contributed equally to the editing of the article.

## 3.2 INTRODUCTION

Dipolar homo-nuclear correlation (*D*-HOMCOR) 2D spectra are important tools for solid-state nuclear magnetic resonance (ssNMR) spectroscopy. They allow for the analysis of through-space proximities between different nuclei belonging to the same isotopes. This *D*-HOMCOR information is mostly acquired through single-quantum  $\leftrightarrow$  single-quantum (SQ-SQ) or double-quantum  $\leftrightarrow$  single-quantum (DQ-SQ) 2D spectra. To enhance the resolution, the experiments must be performed under magic-angle spinning (MAS) of the sample. Therefore, they require rotor-synchronized recoupling schemes to reintroduce the dipolar interactions, which are otherwise canceled by the sample rotation. A large armory of these two types of MAS experiments has been largely developed for spin-1/2 nuclei,<sup>1</sup> and presently these

methods can be considered as routine tools. However, the development of these *D*-HOMCOR sequences is still ongoing for quadrupolar nuclei with a spin value  $I > 1/2$ . The quadrupolar nuclei with a half-integer spin value ( $I = 3/2, 5/2, 7/2$  and  $9/2$ ) represent two-thirds of the NMR active isotopes. Several types of HOMCOR methods have been proposed for quadrupolar nuclei. They were initially based either on quadrupolar-driven<sup>2,3</sup> or proton-driven<sup>4-6</sup> dipolar recoupling mechanisms. However, the first methods are not very efficient, and the second require protonated samples. In the case of half-integer quadrupolar nuclei, several new homonuclear recoupling sequences have more recently been proposed.<sup>7-15</sup> They are based on the  $RN_n^N$  rotor-synchronized MAS schemes developed by Levitt and co-workers,<sup>16,17</sup> and they have largely been developed by Edén *et al.*, who have recently published several research and review articles on this topic.<sup>8-13</sup> However, to the best of our knowledge, there is no global comparison of the advantages and limitations of the two types of sequences (SQ-SQ and DQ-SQ) for half-integer quadrupolar nuclei. Moreover, the previously published *D*-HOMCOR analyses have mostly been performed either on spin-3/2 or 5/2 nuclei, and rarely on the two categories of nuclei simultaneously.

Starting from the conclusions provided in previous publications,<sup>8-13</sup> this work has sought to determine the best schemes for the aforementioned methods and provide a quantitative comparison of their efficiencies. In this work, the analysis has been simultaneously performed on nuclei with spin 3/2 (<sup>11</sup>B) or 5/2 (<sup>27</sup>Al). It is important to note that the theoretical explanations used in this manuscript have been developed for spin-1/2 nuclei, for the sake of ease of spin dynamics of these nuclei with respect to quadrupolar nuclei. This means (i) that they are only based on symmetry properties,<sup>17</sup> (ii) that the nuclei are not subject to the quadrupolar interaction, and (iii) hence that the rf-field is much larger than all other microscopic interactions. However, contrary to spin-1/2 nuclei, for half-integer quadrupolar nuclei the spins are often subject to large quadrupolar interactions, and hence the rf-field must be limited to a few kHz to control the trajectory of the magnetization, which limits the excitation bandwidth of the recoupling sequences.



### 3.3 PULSE SEQUENCES

In Fig. 32, the *D*-HOMCOR sequences applied to half-integer quadrupolar nuclei are presented. The purpose of these sequences is to correlate the signal of identical nuclei, which are coupled by dipolar interaction, and simultaneously cancel the signal created by the coherences that are developing within the same nucleus. To achieve this, perfect control of the transfers of the magnetizations is required, which practically means using rf-fields that are much larger than all microscopic interactions.

This is feasible for spin-1/2 nuclei, because dipolar and CSA interactions are often limited to a few tens of kHz, whereas MAS probes can deliver rf-fields up to ca. 100 kHz. However, these rf-fields cannot control the magnetization of the satellite transitions (ST,  $m \leftrightarrow m-1$  with  $m \neq 1/2$ ) of half-integer quadrupolar nuclei since these ST transitions are subject to the first-order quadrupolar interactions, which often extend over several MHz. In this case, the only way to control the magnetization transfers is to apply weak rf-fields of only a few kHz to manipulate selectively the magnetization of the Central-Transition (CT) between the  $\pm 1/2$  energy levels. This is possible because these levels are only subject to the much smaller second-order quadrupolar interaction. However, as a result, these weak CT-selective pulses lead to poor robustness to offsets. In this ‘fictitious spin-1/2 approximation’, the effective rf-field acting on these CT levels is the rf field strength multiplied by the factor  $(I + 1/2)$ . All the HOMCOR sequences presented derive from the HORROR condition,<sup>7,18-22</sup> which means that the nutation frequency of the pulses is given by

$$\nu_1 = \nu_R / (2I + 1), \quad (1)$$

where  $\nu_R = 1/T_R$  is the MAS spinning frequency. All following sequences are derived from the  $RN_n^y$  rotor synchronized recoupling schemes introduced by Levitt for spin-1/2 nuclei.<sup>16,17</sup> However, it is important to remind that these schemes follow symmetry considerations, but that they do not account for the quadrupolar interaction.

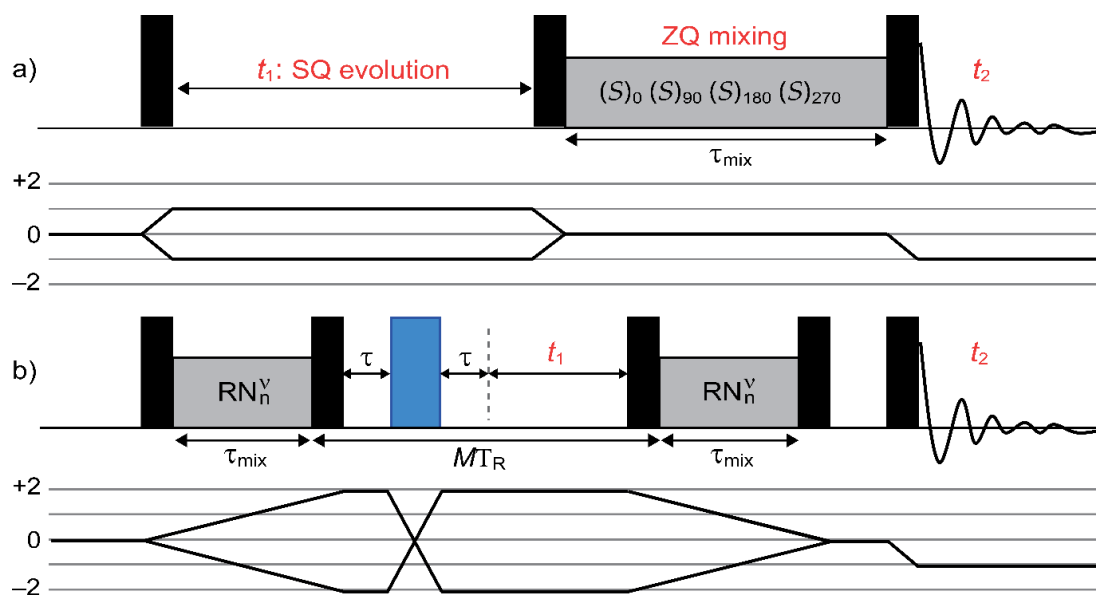


**Figure 32.** Pulse sequences used for (a) SQ-SQ and (b) DQ-SQ HOMCOR experiments of half-integer spin quadrupolar nuclei. All pulses are CT-selective with  $\nu_1 = \nu_R / (2I + 1)$ . The black squares are  $\pi/2$ -pulses, whereas the blue one in (b) is a  $\pi$ -pulse. In (b) a  $[RN_n^V]$  bracketed recoupling is shown with five  $\pi/2$ -pulses, whereas an un-bracketed version should only require the last reading  $\pi/2$ -pulse. The  $RN_n^V$  recoupling parts are represented with grey zones.

In the following,  $\tau_{\text{mix}}$  will be referred to the recoupling time either in the center of the SQ-SQ sequence or in the excitation and reconversion periods of the DQ-SQ scheme (Fig. 32).

The SQ-SQ sequence shown in Fig. 32a is identical to that applied to spin-1/2 nuclei. After a  $\pi/2$ -pulse, the CT coherence evolves during  $t_1$  on the  $\pm 1Q$  levels. Then, a second  $\pi/2$ -pulse transfers these magnetizations along z, where a zero-quantum (ZQ) mixing sequence is applied. A three or four steps super-cycling is used, which means that all phases of the ZQ mixing sequence are incremented every  $120^\circ$  or  $90^\circ$ . In the following, these super-cyclings will be labelled with the index  $M = 3$  or  $4$ , respectively. Then a third  $\pi/2$ -pulse is applied to transfer the magnetization onto the  $-1Q$  level for CT observation during  $t_2$  period.

The DQ-SQ sequences are composed of two recoupling periods of identical length,  $\tau_{\text{mix}}$ , one for excitation and one for reconversion (Fig. 32b). They transfer the magnetization from 0Q to  $\pm 2Q$  and from  $\pm 2Q$  to 0Q, respectively. The recoupling

periods are composed of symmetry-based schemes, bracketed or not with  $\pi/2$ -pulses. They are denoted as  $[RN_n^V]$  or  $RN_n^V$ , respectively. The DQ-SQ sequence shown in Fig. 32b differs from that applied to spin-1/2 nuclei by the blue  $\pi$ -pulse in the middle. By using a phase-cycling with at least 8 phases, the  $\pm 2Q \rightarrow \mp 2Q$  inversion pathways are selected. As a result, all single nucleus contributions are canceled and hence, only remain those between different nuclei, which contribute to the DQ-SQ HOMCOR signal. The  $\tau - 180 - \tau$  sorting part of the sequence does not introduce any dephasing for the detected signal. Each  $RN_n^V$  individual block lasts  $nT_R$  and hence,  $\tau_{\text{mix}}$  is a multiple number of rotor periods. Presently, all DQ recoupling schemes are not  $\gamma$ -encoded, which means that the starts of the excitation and reconversion blocks must be separated by an integer number of rotor periods. As a result, the delay between the end of the 1<sup>st</sup> and the beginning of the 2<sup>nd</sup>  $RN_n^V$  recoupling parts must also be rotor-synchronized (Fig. 32b:  $MT_R$ ). The DQ evolution time is also often rotor-synchronized,  $t_1 = jT_R$ , (i) to fold back all sidebands along  $F_1$  onto the center-band, to simplify the spectrum and enhance the  $S/N$  ratio, and (ii) to always keep rotor-synchronized the starts of excitation and reconversion parts. The spinning speed may not be sufficient for the frequency spread along  $F_1$ , which is the double of that along  $F_2$ . In that case, the position of the  $\pi$ -pulse (shown in blue in Fig. 32b) should be changed to decrease the required indirect spectra-width by redistributing the evolution time before and after this pulse.<sup>14,23</sup> To limit the losses, the  $\tau$  delay should be as small as possible, and thus equal to  $(T_R - \tau_{180} - \tau_{90})/2$  or  $(T_R - \tau_{180})/2$ , when respectively using or not bracketing  $\pi/2$ -pulses before and after the  $RN_n^V$  blocks. The two recoupling  $\tau_{\text{mix}}$  blocks use the same  $RN_n^V$  scheme, except with a  $90^\circ$  phase shift.

### 3.4 SYMMETRY-BASED MATHEMATICAL DESCRIPTION

It is important to remind here that the  $RN_n^V$  schemes follow symmetry considerations, but that they do not account for the quadrupole interactions, which are often much larger than the rf-field.

#### 3.4.1 SQ-SQ

Following the two most recent reviews,<sup>12,13</sup> the five best recoupling schemes for SQ-SQ experiments have been analyzed in this work. These schemes are described in

Fig. 33: S = (a)  $SR2_2^1$ , (b)  $SR2_4^1$ , (c)  $SR2_8^1$ , (d)  $SR4_4^1$  and (e) the block-cycled  $BR2_2^1$ . The first four sequences, called  $SRN_n^1$ , use a phase inversion super-cycle, which results from the combination of two inverse recoupling schemes,  $RN_n^1RN_n^{-1}$ . This super-cycling is often used with spin-1/2 nuclei to make the sequence more robust to CSA. The last sequence,  $BR2_2^1$ , can be written as  $(R2_2^1)_n(R2_2^{-1})_n$ . It uses a different super-cycling, introduced with the  $R^3$  recoupling,<sup>7</sup> which corresponds to a global phase reversal at the midpoint of the  $\tau_{mix}$  interval. All these sequences were initially developed for DQ-SQ experiments.<sup>8,9,24</sup>

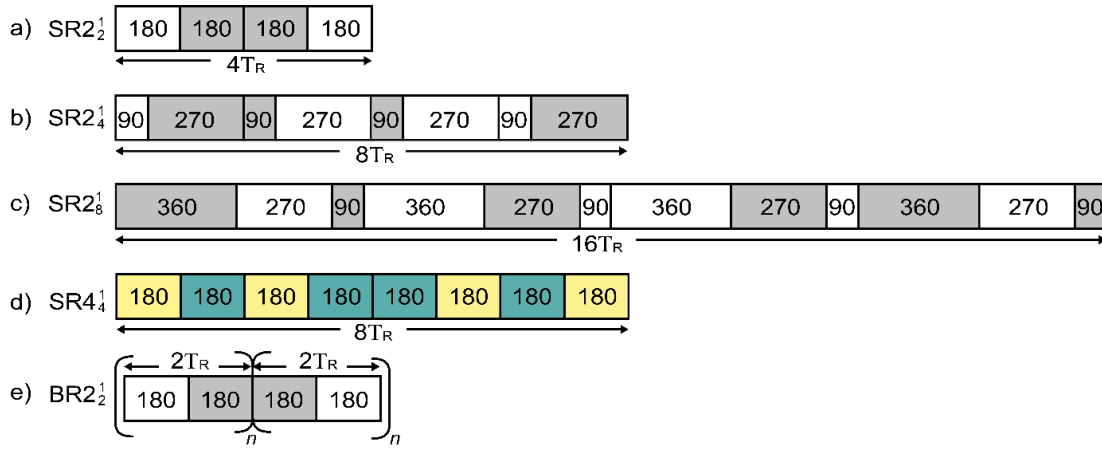


**Figure 33.** Minimum cycle times with (a)  $SR2_2^1$ , (b)  $SR2_4^1$ , (c)  $SR2_8^1$ , (d)  $SR4_4^1$ , and (e)  $BR2_2^1$ . In (a-c,e), white and grey colors mean phases of  $90^\circ$  and  $270^\circ$  respectively, and in (d) yellow and green colors mean phases of  $45^\circ$  and  $315^\circ$  respectively. In each case, the number is the flip-angle for the CT-selective pulse.

It must be noted that to fulfill the HORROR condition (Eq. 1), the  $SR2_4^1$  and  $SR2_8^1$  schemes replace the  $180^\circ$  square pulses of  $SR2_2^1$  with composite  $\pi$ -pulses, such as  $(90_0270_{180})$  pulses for  $SR2_4^1$  (Fig. 33b). In the following,  $\Sigma$  and  $\Delta$  will be referred to the sum and difference of chemical shifts for a pair of nuclei  $j$  and  $k$ .

The  $SRN_n^1$  recoupling schemes shown in Fig. 33a-d are periodic, and hence they can be described with an average Hamiltonian:<sup>8,25</sup>

$$H_S^{jk} = 0.5K \cdot F_{jk} \cdot \{I_j^+ I_k^+ + I_j^- I_k^- + I_j^+ I_k^- + I_j^- I_k^+ - 4I_{jz} I_{kz}\} \quad (2)$$

With  $F_{jk} = b_{jk} \sin(2\beta_{jk}) \cos(\gamma_{jk})$  where  $b_{jk}$  is the dipolar coupling constant and  $(\beta_{jk}, \gamma_{jk})$  are the Euler angles relating the  $jk$  inter-nuclear vector in the MAS rotor-fixed frame.  $K = 3/(8\sqrt{2})$  is the scaling factor of the homonuclear dipolar interaction.

All these sequences results in a Hamiltonian containing both DQ ( $I^+_j I^+_k + I^-_j I^-_k$ ) and ZQ ( $I^-_j I^+_k - 4I_{jz} I_{kz}$ ) operators, which can interfere in multi-spin systems. The sequence in Fig. 32a requires a ZQ recoupling, which can be obtained by filtering the DQ terms with a  $M \geq 3$  super-cycling, and the sequences are then noted  $(S)_{M \geq 3}$ . The super-cycled Hamiltonian is thus simplified with respect to Eq. 2:

$$H_{S(M \geq 3)}^{jk} = 0.5K \cdot F_{jk} \cdot \{ I^+_j I^-_k + I^-_j I^+_k - 4I_{jz} I_{kz} \} \quad (3)$$

This super-cycling concatenates  $M$  blocks of  $\text{SRN}_n^1$  schemes with the phases of all the pulses of a block shifted by  $360^\circ/M$  with respect to the previous block shown in Fig. 33. However, it must be noted that if on one hand it increases the robustness of the  $S$  schemes, on the other hand it multiplies by  $M$  their cycle times. Therefore, to limit the global cycle time, only the  $M = 3$  or  $4$  super-cyclings are used.

In the following, the conclusions obtained by Edén and co-workers for SQ-SQ HOMCOR analyses concerning half-integer quadrupolar nuclei are summarized.<sup>12,13</sup> These conclusions have been obtained with extensive simulations and experiments at 14.1 T and with  $\nu_R$  ranging from 10 to 30 kHz.

- First conclusion:  $\text{BR}2_{2}^1$  is not recommended as it requires a high-power  $^1\text{H}$  decoupling during the long  $\tau_{mix}$  time, because it also recouples the hetero-dipolar interactions.

- Second conclusion: an enhanced robustness to offset and rf-inhomogeneity is observed with  $(\text{SR}2_{2}^1)_M < (\text{SR}2_{4}^1)_M < (\text{SR}2_{8}^1)_M$  for increasing chemical shift difference,  $\Delta$ .

In the case of a small-moderate separation,  $\Delta \leq 3 - 4$  kHz,  $(SR2_{2}^{1})_M$  works better than  $(SR2_{4}^{1})_M$ ,  $(SR2_{8}^{1})_M$  and  $(SR4_{4}^{1})_M$ . As example, this was the case for  $^{11}\text{B}$  in a NCBS glass (Fig. 6g in ref. <sup>13</sup>).

In the case of a large separation,  $\Delta > 3 - 4$  kHz, from the simulations,  $(SR2_{8}^{1})_M$  is better than  $(SR2_{2}^{1})_M$  and  $(SR2_{4}^{1})_M$ . However, this was not confirmed experimentally, and hence the authors recommended  $(SR2_{4}^{1})_M$ . This was the case for  $^{27}\text{Al}$  in aluminophosphate AIPO-CJ19, where  $\Delta_{iso,max} \approx 9.6$  kHz and  $^{27}\text{Al}$ - $^{27}\text{Al}$  dipolar interactions are small (conclusion in ref. <sup>12</sup>).

### 3.4.2 DQ-SQ

The same  $SRN_n^1$  recoupling schemes shown in Fig. 33a-d can be applied to DQ-SQ sequences. Their Hamiltonian given in Eq. 2 are mixtures of DQ and ZQ operators. Pure DQ recoupling can be obtained with sandwiching these schemes with two  $90^\circ$  pulses, and the sequences, then denoted  $[SRN_n^1]$  double the scaling factor and eliminate the ZQ terms:

$$H_{[S]}^{jk} = K \cdot F_{jk} \cdot \{ I_j^+ I_k^+ + I_j^- I_k^- \} \quad (4)$$

The theoretical maximal efficiencies of  $SRN_n^1$  and  $[SRN_n^1]$  sequences are identical. However, practically,  $[SRN_n^1]$  is often slightly more efficient due to (i) increased losses in  $SRN_n^1$  related to lower scaling factor, and (ii) interferences of ZQ and DQ terms, which do not commute for distinct spin-pairs.

For the  $BR2_{2}^{1}$  sequence, no basic periodic unit can be defined, and therefore the conventional average Hamiltonian cannot be applied. However, a Magnus expansion can be applied to the Hamiltonians of the  $R2_{2}^{\pm 1}$  schemes, and after the  $n^{\text{th}}$  point of  $BR2_{2}^{1}$ , at  $4nT_R$ , it gives in an offset-toggling frame:<sup>15</sup>

$$H_{BR2_{2}^{1}}^{jk} = 0.5K \cdot F_{jk} \cdot \{ (1 - 0.5(S\Delta - S\Sigma))(I_j^+ I_k^- + I_k^+ I_j^-) - 2(S\Delta + S\Sigma)I_{jz}I_{kz} + 2(C\Sigma + C\Delta)2I_{jy}I_{ky} + 2(C\Sigma - C\Delta)I_{jz}I_{ky} + (1 + 0.5(S\Delta - S\Sigma))(I_j^+ I_k^+ + I_j^- I_k^-) \} \quad (5)$$

where  $S\Psi = \sin(8n\Psi T_R)/(8n\Psi T_R)$  and  $C\Psi = \{1 - \cos(8n\Psi T_R)/(8n\Psi T_R)\}$ , with  $\Psi = \Delta$  or  $\Sigma$ , and these terms tend to 0 when  $8n\Psi T_R \gg 1$ . In Eq. 5, the 1<sup>st</sup> and 2<sup>nd</sup>

terms are ZQ, the 3<sup>rd</sup> and 4<sup>th</sup> are SQ, and the 5<sup>th</sup> is the DQ contribution. These five terms depend on the length of the BR2<sub>2</sub><sup>1</sup> recoupling,  $4nT_R$ , and on the sum ( $\Sigma$ ), and difference ( $\Delta$ ) of chemical shifts of the two coupled spins. In the case of small dipolar couplings and hence large  $n$  values, if simultaneously  $nT_R \gg 1/(8\Delta)$  **and**  $1/(8\Sigma)$ , Eq. 5 simplifies and only remains

$$H_{BR2_2^1}^{jk} = 0.5K \cdot F_{jk} \cdot \{(I_j^+ I_k^- + I_k^+ I_j^-) + (I_j^+ I_k^+ + I_j^- I_k^-)\} \quad (6)$$

With  $(\Delta, \Sigma) = (\neq 0, 0)$ ,  $(0, \neq 0)$  or  $(\Delta, \pm\Delta)$ , it may also lead to the same DQ contribution multiplied by 0.5, 1.5 or 1, when  $nT_R \gg 1/(8\Delta)$  **or**  $1/(8\Sigma)$ . This shows that there is no constant DQ-SQ dipolar scaling factor for the BR2<sub>2</sub><sup>1</sup> recoupling, even in the simple case of spin-1/2 nuclei. Edén and co-workers have shown with simulations, that depending on the quadrupolar interaction and the dipolar value, the scaling factor is ‘intermediate in between the bracketed or not bracketed sequences’.<sup>11</sup>

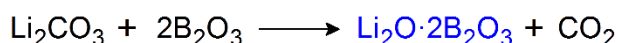
In the case of [BR2<sub>2</sub><sup>1</sup>], the Hamiltonian of Eq. 5 simplifies to Eq. 4, which leads to an increase of the scaling factor.

## 3.5 MATERIALS AND METHODS

### 3.5.1 Samples

Crystalline Li<sub>2</sub>O·2B<sub>2</sub>O<sub>3</sub> and isopropylamine templated AlPO<sub>4</sub>-14 (AlPO<sub>4</sub>-14 hereafter) were used for <sup>11</sup>B-<sup>11</sup>B and <sup>27</sup>Al-<sup>27</sup>Al HOMCOR experiments, respectively. Crystalline Li<sub>2</sub>B<sub>4</sub>O<sub>7</sub> was synthesized using the procedure detailed below whereas AlPO<sub>4</sub>-14 was prepared as described by Antonijevic *et al.*<sup>26</sup>

### 3.5.2 Synthesis of lithium diborate



Li<sub>2</sub>O·2B<sub>2</sub>O<sub>3</sub> was prepared by mixing lithium carbonate (Li<sub>2</sub>CO<sub>3</sub>) and boron oxide (B<sub>2</sub>O<sub>3</sub>) in appropriate proportions. The mixture was melted in a platinum crucible in a furnace at 1000 °C for 5 h before quenching it on an iron plate at room temperature. The glass sample was crystallized by heating it at 540 °C during 24 h and allowing it

to cold down slowly. The crystallization temperature was verified by Differential Thermal Analysis (DTA).

### 3.5.3 Phase identification

After synthesis, powder XRD measurements were performed to determine the phase purity of the crystal sample. The patterns were recorded at room temperature using a Bruker D8 Advance X-ray diffractometer working in the in the Bragg-Brentano geometry with Cu-K $\alpha$  ( $\lambda = 1.5406 \text{ \AA}$ ) radiation. The diffractometer was operated over the angular range of  $2\theta = 10\text{-}60^\circ$  with a scan step width of  $0.02^\circ$  and a scan rate of  $0.5 \text{ s/step}$ .

The XRD-patterns were analyzed using the DIFFRAC.EVA V4.0 software (Bruker). The profile-matching refinement of the crystal structures were carried out using the single crystal structural model for each compound imported in the JANA2006 crystallographic system.<sup>27</sup> The background was fitted using Chebyshev polynomial functions, and the peak shapes were described by a Pseudo-Voigt function.

The XRD pattern of the crystallized sample is shown in Fig. 34. It is in good agreement with that of reported  $\text{Li}_2\text{B}_4\text{O}_7$  crystal (JCPDS card 79-0963). The main high intensity reflections are assigned to the  $\text{Li}_2\text{B}_4\text{O}_7$  phase. However, some peaks with smaller intensities cannot be assigned to  $\text{Li}_2\text{B}_4\text{O}_7$ , which indicates that the sample contains an impurity. In order to identify this impurity, profile-matching refinement was done using the JANA2006<sup>27</sup> software.  $\alpha\text{-LiBO}_2$  (JCPDS card 51-0517) was identified as a secondary phase and can be attributed as the impurity of the crystallized sample (Fig. 36).



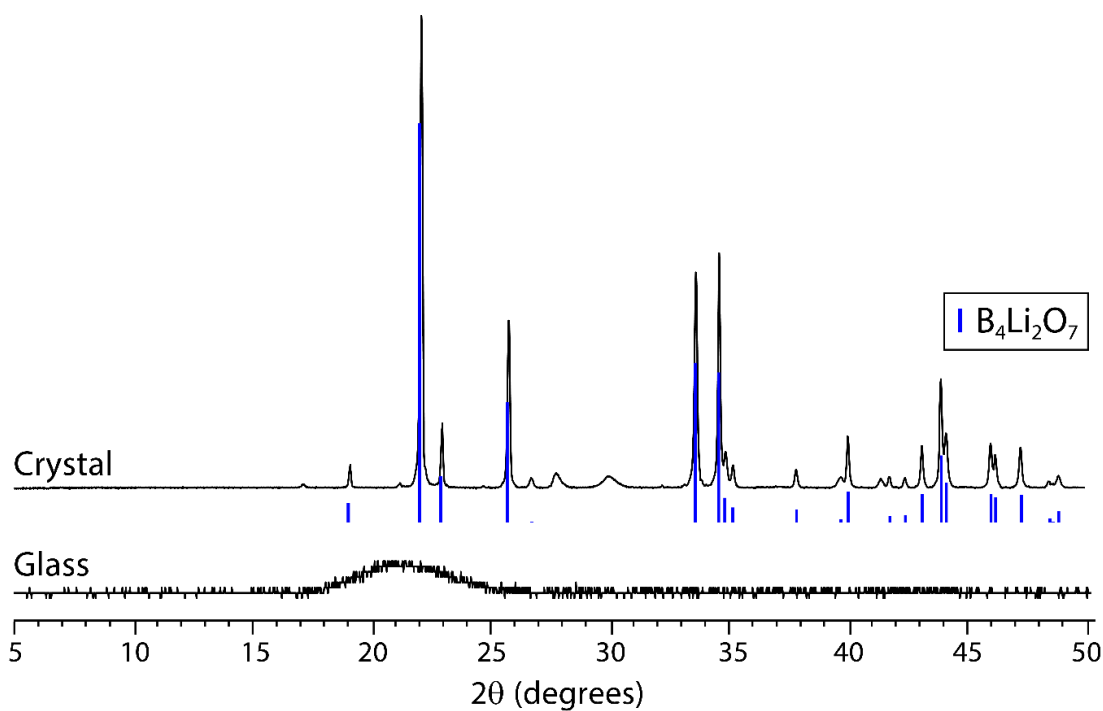


**Figure 34.** Comparison of powder XRD patterns of crystallized lithium diborate  $\text{Li}_2\text{O}\cdot 2\text{B}_2\text{O}_3$  and the glass sample initially prepared. Vertical lines represent the positions of diffraction lines of  $\text{B}_4\text{Li}_2\text{O}_7$ .

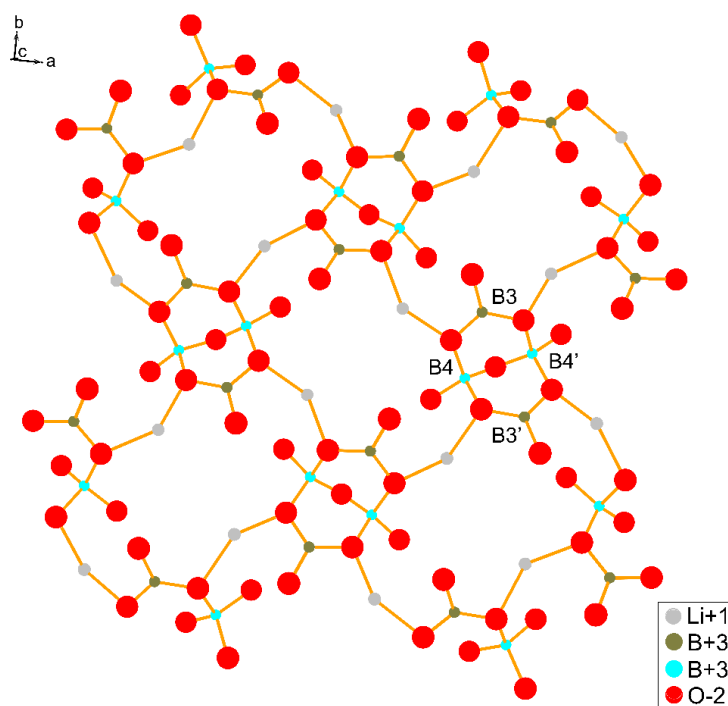


**Figure 35.** Crystalline structure of  $\text{Li}_2\text{B}_4\text{O}_7$  based on the cif file. The diborate unit is indicated with the atoms of boron tri- and four-coordinated, B3 and B4, respectively.

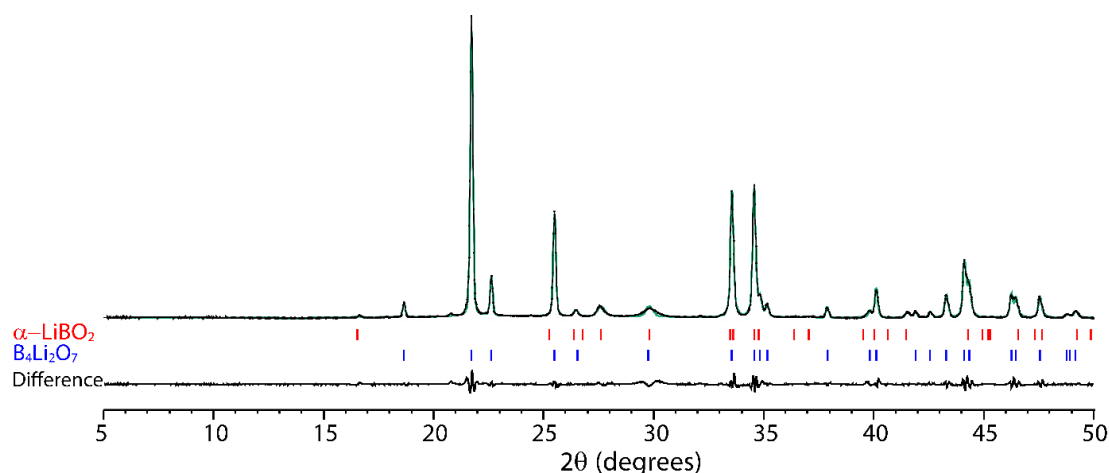


**Figure 36.** Comparison and difference between the powder XRD pattern of crystallized lithium diborate  $\text{Li}_2\text{O}\cdot 2\text{B}_2\text{O}_3$  and reference XRD patterns of  $\alpha\text{-LiBO}_2$  and  $\text{B}_4\text{Li}_2\text{O}_7$ .

### 3.5.4 NMR experiments

All experiments  $^{11}\text{B}$ - $^{11}\text{B}$  and  $^{27}\text{Al}$ - $^{27}\text{Al}$  through-space homonuclear correlation (*D*-HOMCOR) experiments have been recorded at two magnetic fields: 9.4 and 18.8 T, with 3.2 mm rotors spinning at  $\nu_R = 20$  kHz. They provided the same information, and hence the results obtained at 18.8 T are mainly presented in this dissertation because the resonances are four times more resolved than at 9.4 T, and hence much easier to explain.  $^{11}\text{B}$  chemical shifts were referenced using a solid sample of  $\text{NaBH}_4$  ( $\delta_{\text{iso}} = -42.05$  ppm), whereas  $^{27}\text{Al}$  chemical shifts were referenced at 0 ppm to 1 mol  $\text{L}^{-1}$   $[\text{Al}(\text{H}_2\text{O})_6]^{3+}$  solution.

#### 3.5.4.1 Experiments at 9.4 T

Experiments at  $B_0 = 9.4$  T ( $\nu_0 = 400$  MHz for  $^1\text{H}$ ) were recorded with a wide-bore magnet equipped with a Bruker AVANCE NEO console, using a 3.2 mm HXY magic angle spinning (MAS) probe operated in double-resonance mode.

Two-dimensional (2D)  $^{11}\text{B}$  MQMAS spectrum was obtained using the z-filtered sequence<sup>28</sup> at  $\nu_R = 16$  kHz. Excitation and conversion pulses lasted  $\tau_p = 6$  and 1.8  $\mu\text{s}$  with  $\nu_1 \approx 122$  kHz and the central transition (CT) selective pulse lasted 10  $\mu\text{s}$  with  $\nu_1 \approx 12.5$  kHz. The spectra are the result of averaging 12 transients (using a cogwheel

phase cycling COG12 for coherence pathway selection) separated by a recycle delay of 10 s for each of the 300  $t_1$  increments of 62.5  $\mu$ s. The quadrature detection method of States *et al.*<sup>29</sup> was used to achieve sign discrimination in the indirect dimension. After acquisition, a 2D Fourier transformation followed by a shearing transformation was performed to obtain a spectrum where the contour ridges were parallel to  $F_2$ , allowing the isotropic spectrum to be obtained directly from a projection onto  $F_1$ .<sup>30</sup>

#### 3.5.4.2 Experiments at 18.8 T

The experiments at  $B_0 = 18.8$  T were performed on a Bruker AVANCE NEO spectrometer equipped with a 3.2 mm double resonance  $^1\text{H}/\text{X}$  probe.

Quantitative  $^{11}\text{B}$  NMR spectra were acquired at  $\nu_R = 20$  kHz by using single-pulse NMR experiments with a pulse length of 1  $\mu$ s and an RF field strength of 120 kHz, corresponding to a short tip angle.<sup>31</sup> Quantitative  $^{11}\text{B}$  NMR spectra were acquired by averaging 4 transients, separated by a recycle interval of 20 s.

$^{11}\text{B}$  and  $^{27}\text{Al}$  SQ-SQ and DQ-SQ *D*-HOMCOR 2D spectra were acquired by using the pulse sequences displayed in Fig. 32a and b, respectively. The tested recoupling schemes for SQ-SQ experiments are  $\text{SR}2_{2}^1$ ,  $\text{SR}2_{4}^1$  and  $\text{SR}2_{8}^1$  (Fig. 33a-c) using the supercycle  $M = 4$ . For DQ-SQ sequences, the tested recouplings are  $\text{SR}2_{2}^1$  and  $\text{BR}2_{2}^1$  (Fig. 33a and e, respectively), and their bracketed counterparts,  $[\text{SR}2_{2}^1]$  and  $[\text{BR}2_{2}^1]$ , respectively. As said before, HOMCOR methods of half-integer quadrupolar nuclei are very sensitive to offsets. Therefore, the carrier frequency, which is then a very important parameter, will be indicated with an arrow in all spectra. The recycle delays were 1 s for all experiments. The spinning speed was  $\nu_R = 20$  kHz for each experiment. Additional experimental details are given in the figure captions.

## 3.6 RESULTS AND DISCUSSION

### 3.6.1 $^{11}\text{B}$ - $^{11}\text{B}$ *D*-HOMCOR experiments on $\text{Li}_2\text{B}_4\text{O}_7$

$^{11}\text{B}$  is a spin-3/2 isotope with a natural abundance of 80.1 % and a Larmor frequency of  $\nu_0 = 256.8$  MHz at  $B_0 = 18.8$  T. Boron species are either three- or four-coordinated, and they are named  $\text{B}^{\text{III}}$  and  $\text{B}^{\text{IV}}$ , respectively. These nuclei are subject to quadrupole interactions with  $C_Q$  values ranging between 2.4-2.9 MHz for  $\text{B}^{\text{III}}$  and 0.4 –0.8 MHz for  $\text{B}^{\text{IV}}$ .<sup>32–35</sup> The difference of chemical shifts between the  $\text{B}^{\text{III}}$  and  $\text{B}^{\text{IV}}$  sites is often limited to  $\Delta \leq 5$  kHz at  $B_0 = 18.8$  T. Nevertheless, these two types of species are resolved on the 1D spectra at this field, which simplifies the interpretation of the NMR spectra.

Borate glasses are important systems with various potential applications in optical, optoelectronic and biomedical devices.<sup>36–39</sup> Crystalline  $\text{Li}_2\text{B}_4\text{O}_7$  ( $\text{Li}_2\text{O} \cdot 2\text{B}_2\text{O}_3$ ) was chosen as a test sample. There are two boron species in this compound (JCPDS card 79-0963), one  $\text{B}_1^{\text{III}}$  and one  $\text{B}^{\text{IV}}$  sites, with a chemical separation of  $\Delta \approx 4.2$  kHz at  $B_0 = 18.8$  T.

The sample was obtained after a 24 h recrystallization process at 540 °C, from the glass obtained after melting during 5 h at 1000 °C of  $\text{Li}_2\text{B}_4\text{O}_7 \cdot 10\text{H}_2\text{O}$ . The crystalline sample contains 90% of  $\text{Li}_2\text{B}_4\text{O}_7$ ,<sup>40,41</sup> with 10% of another compound with only one  $\text{B}^{\text{III}}$  species (denoted  $\text{B}_2^{\text{III}}$  hereafter) (Fig. 38). A detailed analysis of the X-ray diffraction pattern has shown that the second species is  $\alpha\text{-LiBO}_2$  (Fig. 36).<sup>42–44</sup> The DMfit deconvolution of the 1D spectrum (Fig. 37) gives proportions of 45, 10 and 45 % for  $\text{B}_1^{\text{III}}$ ,  $\text{B}_2^{\text{III}}$  and  $\text{B}^{\text{IV}}$  species, with  $\delta_{\text{cs}}$  (ppm),  $C_Q$  (MHz),  $\eta_Q = (18.4, 2.63, 0.18)$ ,  $(16.5, 2.36, 0.60)$  and  $(2.1, 0.48, 0.51)$ , respectively (Table 13). It must be noted that the two  $\text{B}^{\text{III}}$  resonances are narrow and well separated in the MQMAS spectrum (Fig. 38), which means that the two different compounds form distinct crystallized phases. Hence, no spatial proximity between  $\text{B}_1^{\text{III}}$  and  $\text{B}_2^{\text{III}}$  species is expected.

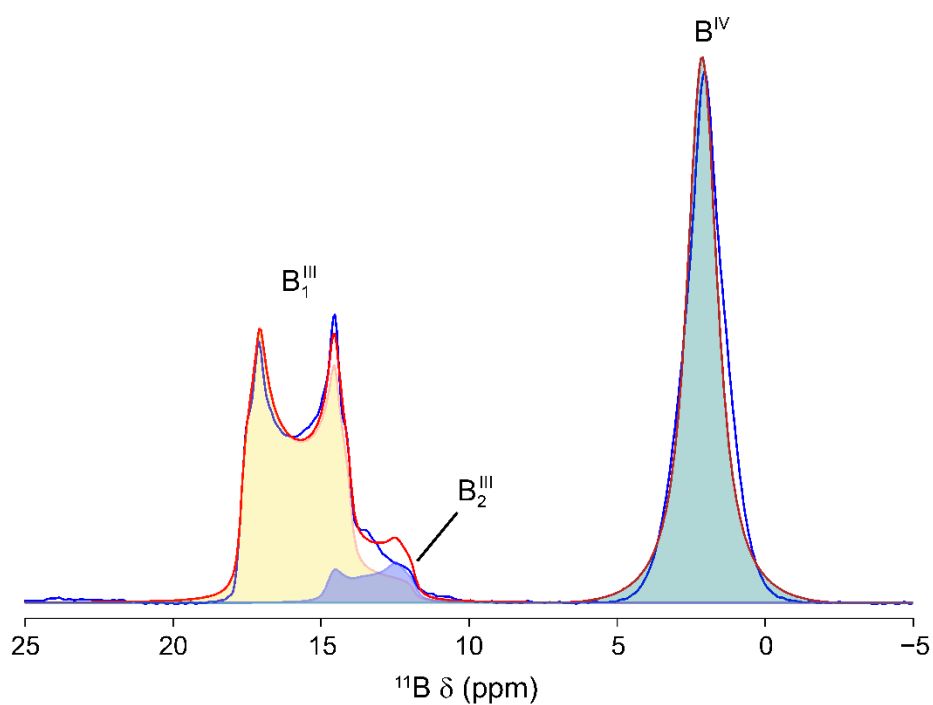


**Figure 37.** Lineshape deconvolution obtained from the  $^{11}\text{B}$  1D spectrum of the  $\text{Li}_2\text{B}_4\text{O}_7$  crystallized sample recorded at 18.8 T and  $\nu_R = 20$  kHz. Fitting was carried out using int2QUAD model in DMFit.<sup>45</sup> The relative amounts of  $\text{Li}_2\text{B}_4\text{O}_7$  and  $\alpha\text{-LiBO}_2$  phases are 90 and 10 %.

**Table 13.** Data obtained from the deconvolution of the  $^{11}\text{B}$  1D spectrum of the  $\text{Li}_2\text{B}_4\text{O}_7$  (using the int2QUAD model in DMFit.<sup>45</sup>) presented in Fig. 37.

B site	$\delta_{\text{cs}}$ (ppm)	$C_Q$ (MHz),	$\eta_Q$	Proportion (%)
$\text{B}_1^{\text{III}}$	18.4	2.63	0.18	45
$\text{B}_2^{\text{III}}$	16.5	2.36	0.60	10
$\text{B}^{\text{IV}}$	2.1	0.48	0.51	45

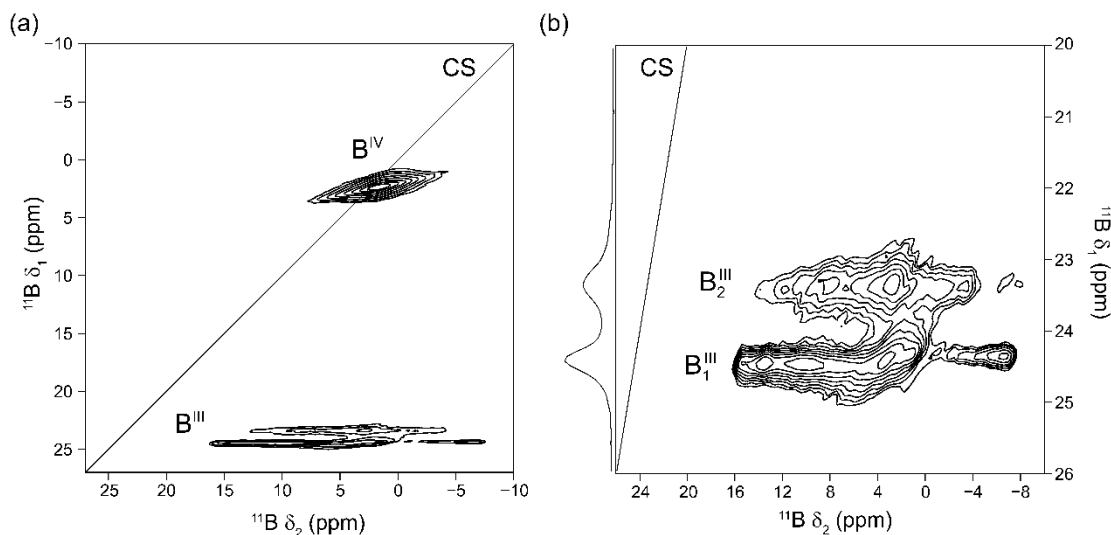


**Figure 38.** (a) 2D  $^{11}\text{B}$  z-filtered MQMAS spectrum of  $\text{Li}_2\text{B}_4\text{O}_7$  recorded at  $B_0 = 9.4$  T and  $\nu_R = 16$  kHz. Panel (b) is an expansion of panel (a). The oblique lines are the Chemical-Shift axes.

In crystalline  $\text{Li}_2\text{B}_4\text{O}_7$ , the closest B-B distances are equal to ca.  $2.46 \text{ \AA}$  ( $\text{B}_1^{\text{III}}\text{-B}^{\text{IV}}$ ) and  $2.36$  ( $\text{B}^{\text{IV}}\text{-B}^{\text{IV}}$ )  $\text{\AA}$ , which correspond to  $^{11}\text{B}\text{-}^{11}\text{B}$  dipolar coupling constants equal to ca. 820 and 937 Hz, respectively. The closest  $\text{B}_1^{\text{III}}\text{-B}_1^{\text{III}}$  species are more distant ( $3.57 \text{ \AA}$ ) and are thus related to a smaller dipolar coupling constant of 269 Hz.

In the following, the two  $\text{B}_1^{\text{III}}$  and  $\text{B}_2^{\text{III}}$  resonances are considered as a single one, and the sample will be called  $\text{Li}_2\text{B}_4\text{O}_7$ , neglecting the 10% impurity. Hereafter,  $\text{B}^3$  and  $\text{B}^4$  will denote the auto-correlation peaks of  $(\text{B}_1^{\text{III}} + \text{B}_2^{\text{III}})$  and  $\text{B}^{\text{IV}}$  species, and  $\text{B}^{34}$  and  $\text{B}^{43}$  the cross-peaks observed along  $F_2$  at  $(\text{B}_1^{\text{III}} + \text{B}_2^{\text{III}})$  and  $\text{B}^{\text{IV}}$  frequencies, respectively.

### 3.6.1.1 SQ-SQ

As previously demonstrated,  $M = 3$  and 4 provide similar robustness to offset and rf-inhomogeneity, but  $M = 4$  often performs slightly better<sup>7,12</sup>. So, following these conclusions, the three best  $(\text{SR}2_{\text{n}}^1)$  SQ-SQ recoupling schemes were tested on  $\text{Li}_2\text{B}_4\text{O}_7$  using this super-cycling:  $(\text{SR}2_{2}^1)_4$ ,  $(\text{SR}2_{4}^1)_4$  and  $(\text{SR}2_{8}^1)_4$ <sup>12,13</sup>. It must be noted that at  $\nu_R = 20$  kHz the mixing step of these  $(\text{SR}2_{\text{n}}^1)_4$  sequences is long:  $\Delta\tau_{\text{mix}} = 8nT_R = 0.8, 1.6$  and  $3.2$  ms with  $n= 2, 4$  and  $8$ , respectively.

2D SQ-SQ *D*-HOMCOR spectra exhibit large diagonal signals. However, these signals are produced by magnetization that is not transferred during the sequence or by transfers between nuclei with very close or identical resonance frequencies. Therefore, they do not provide information on the spatial proximities. In the case of the sample tested here, the B<sup>III</sup> and B<sup>IV</sup> resonances are well resolved at  $B_0 = 18.8$  T, and there is no spatial proximity between the B<sub>1</sub><sup>III</sup> and B<sub>2</sub><sup>III</sup> species. Nevertheless, the diagonal peaks can arise from magnetization, which is not transferred, as well as transfers of magnetization between nearby <sup>11</sup>B nuclei in the same environment.

Consequently, it is not easy to analyse the SQ-SQ spin dynamics with only 1D ( $t_1 = 0$ ) experiments, due to the superposition of useful (B<sup>34</sup> and B<sup>43</sup> cross-peaks) and useless (B<sup>3</sup> and B<sup>4</sup> auto-peaks) signals onto the F<sub>2</sub> axis. In Fig.39, a series of 2D spectra acquired with three different  $\tau_{\text{mix}}$  values are presented.

Two points can be noted by comparing the spectra displayed in Fig. 39: (i) the B<sup>34</sup> cross-peak is negative for  $v_{\text{offset}} = 3$  kHz in the case of (SR2<sub>8</sub><sup>1</sup>)<sub>4</sub>, which indicates a higher sensitivity to offset of this sequence and (ii) the B<sup>43</sup> cross peak is less intense than the B<sup>34</sup> peak owing to the faster decay of B<sup>III</sup> SQ coherences with respect to that of B<sup>IV</sup> SQ coherences. In particular, B<sup>43</sup> cross peak does not appear in the case of (SR2<sub>4</sub><sup>1</sup>)<sub>4</sub> and (SR2<sub>8</sub><sup>1</sup>)<sub>4</sub>. Conversely, with (SR2<sub>2</sub><sup>1</sup>)<sub>4</sub> recoupling the two cross-peaks are visible and positive.

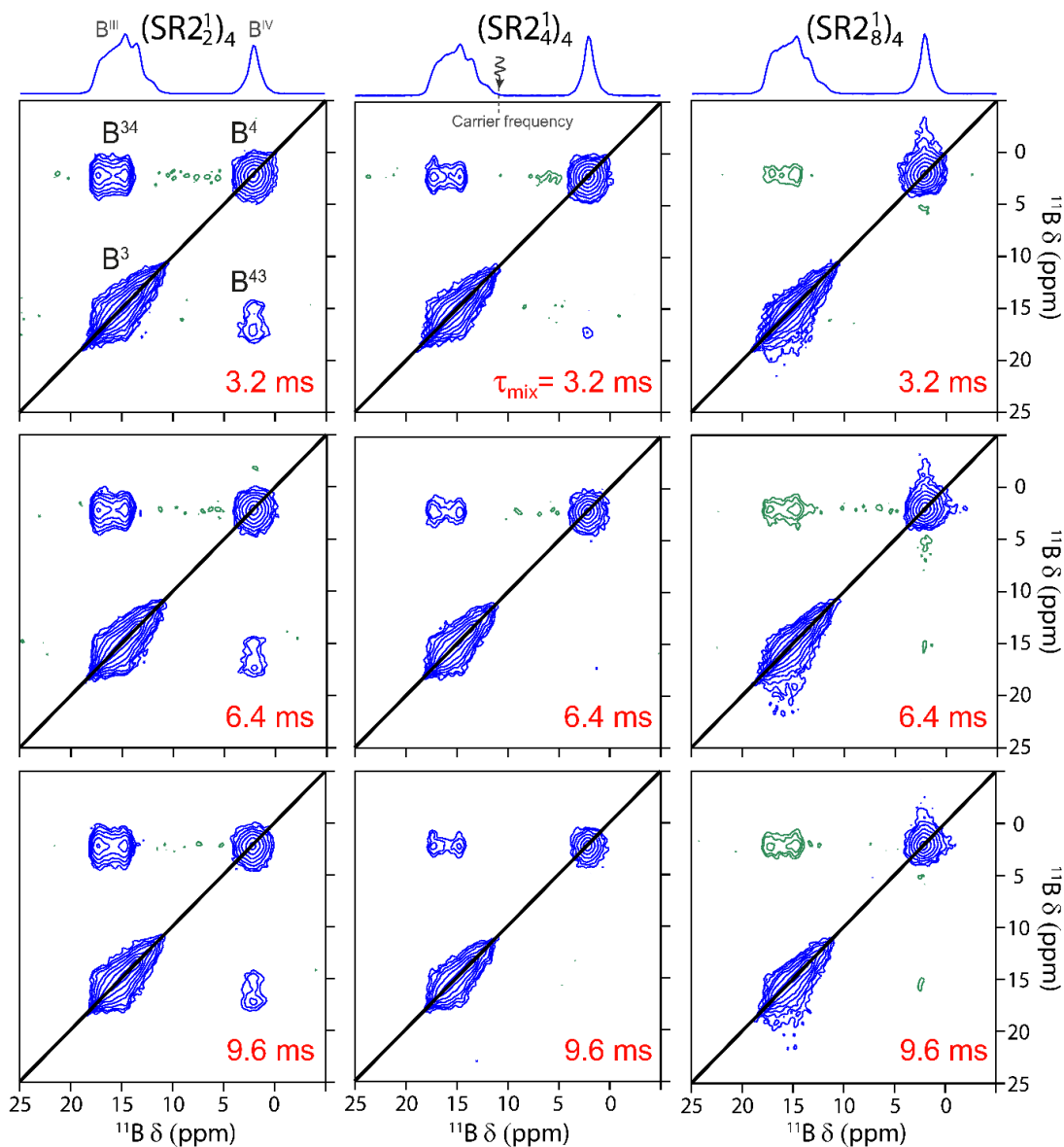


**Figure 39.** Series of 2D  $^{11}\text{B}$  SQ-SQ *D*-HOMCOR spectra of  $\text{Li}_2\text{B}_4\text{O}_7$  acquired at  $B_0 = 18.8$  T with a MAS frequency of 20 kHz and a non-uniform sampling (NUS) retaining 50% of the  $t_1$  points, with the carrier frequency optimized (Fig. 40) at  $\nu_{\text{offset}} = 3$  kHz (11.7 ppm), shown with an arrow between the  $\text{B}^{\text{III}}$  and  $\text{B}^{\text{IV}}$  resonances. The spectra acquired with recoupling schemes,  $(\text{SR}2_2^1)_4$ ,  $(\text{SR}2_4^1)_4$  and  $(\text{SR}2_8^1)_4$ , are shown in the first, second and third column, respectively. The negative cross-peaks are shown in green. The length of  $\tau_{\text{mix}} = 3.2, 6.4$  or  $9.6$  ms, is indicated in red on each panel. The top projections are those related to  $\tau_{\text{mix}} = 3.2$  ms. The 2D spectra result from averaging 48 transients using a relaxation delay  $\tau_{\text{RD}} = 1$  s for each of 120  $t_1$ -increments, leading to an experimental time  $T_{\text{exp}} = 48\text{-}55$  min.



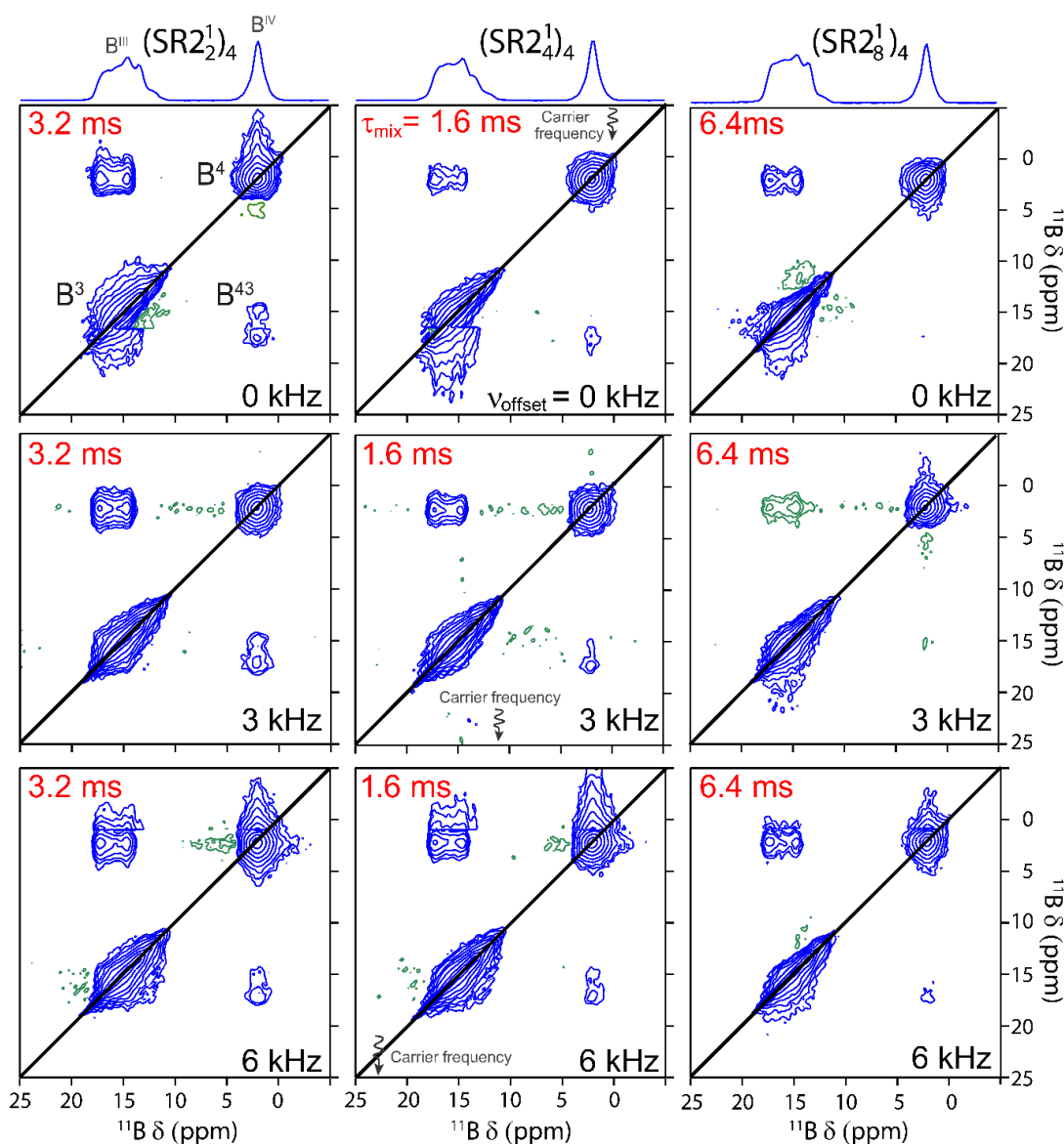


**Figure 40.** 2D  $^{11}\text{B}$  SQ-SQ *D*-HOMCOR spectra of  $\text{Li}_2\text{B}_4\text{O}_7$  acquired at  $B_0 = 18.8$  T with a MAS frequency of 20 kHz and a non-uniform sampling (NUS) retaining 50% of the  $t_1$  points with  $\nu_{\text{offset}} = 0, 3, 6$  kHz, as indicated in black and with arrows. The spectra acquired with recoupling schemes  $(\text{SR2}_2^1)_4$ ,  $(\text{SR2}_4^1)_4$  and  $(\text{SR2}_8^1)_4$  are shown in the first, second or third column, respectively. The negative signals are shown in green. The length of  $\tau_{\text{mix}} = 1.6, 3.2$  or  $6.4$  ms is indicated in red on each sub-figure. The top projections are those related to the spectra on the 1<sup>st</sup> line. The other experimental parameters are the same as in Fig. 39.

In Fig. 40, we show a series of 2D spectra acquired with three different offsets,  $\nu_{\text{offset}}$ , as indicated on the Figures. For each recoupling scheme, the  $\tau_{\text{mix}}$  value was chosen for optimum  $\text{B}^{34}$  cross-peak value. As observed in Fig. 39, whatever the offset

value, the  $B^{43}$  cross-peak either does not appear in Fig. 40 with  $(SR2\frac{1}{8})_4$  or is hardly visible with  $(SR2\frac{1}{4})_4$ . This is not the case with  $(SR2\frac{1}{2})_4$ . For this recoupling scheme, the maximum  $B^{34}$  signal with the least line-shape distortion is observed with  $\nu_{\text{offset}} = 3$  kHz.

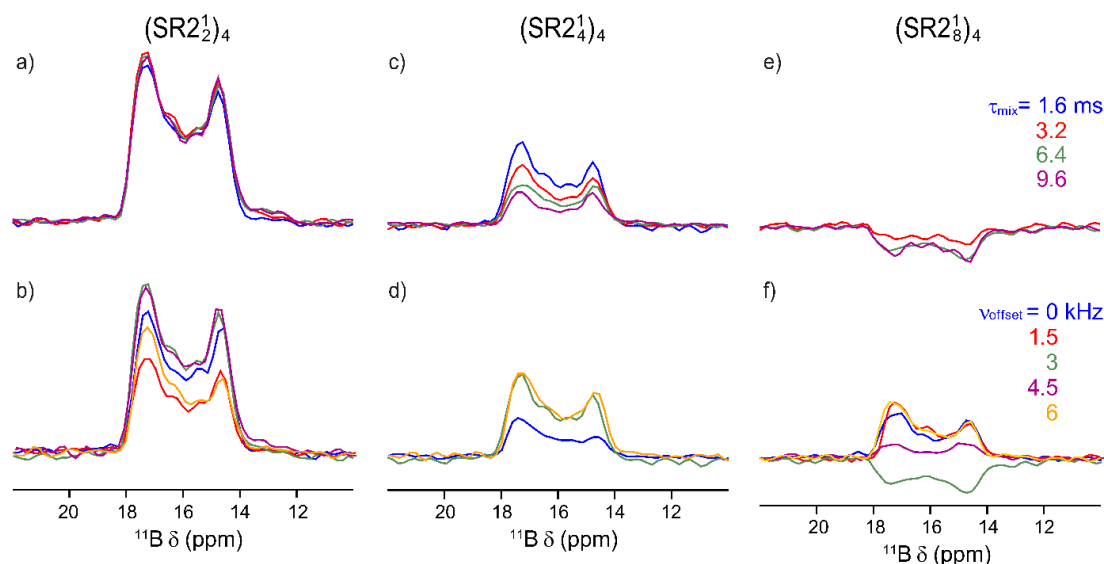


**Figure 41.** Slices of the 2D spectra corresponding to the  $B^{34}$  ( $B^{\text{III}}\text{-}B^{\text{IV}}$ ) cross-peak of  $\text{Li}_2\text{B}_4\text{O}_7$  observed with the  $^{11}\text{B}$  SQ-SQ  $D$ -HOMCOR sequence and  $(SR2\frac{1}{2})_4$ ,  $(SR2\frac{1}{4})_4$  and  $(SR2\frac{1}{8})_4$  recoupling schemes, shown in the first, second or third column, respectively. (a,c,e)  $\nu_{\text{offset}} = 3$  kHz and  $\tau_{\text{mix}} = 1.6, 3.2, 6.4$  and  $9.6$  ms; (b,d,f)  $\nu_{\text{offset}} = 0, 1.5, 3, 4.5, 6$  kHz and  $\tau_{\text{mix}} =$  (b)  $3.2$ , (d)  $1.6$  and (f)  $6.4$  ms. These slices are extracted from the 2D spectra shown in Figs. 39 and 40.

Fig. 41 presents slices of 2D spectra corresponding to the  $B^{34}$  cross-peak observed with the three recoupling schemes either (a,c,e) with  $\nu_{\text{offset}} = 3$  kHz versus  $\tau_{\text{mix}}$ , or (b,d,f) versus  $\nu_{\text{offset}}$  with  $\tau_{\text{mix}}$  optimized for best  $B^{34}$  amplitude. With  $(SR2\frac{1}{4})_4$ , and especially with  $(SR2\frac{1}{8})_4$  recoupling, large variations of the amplitude for this cross-peak are observed. This amplitude can even become negative for  $(SR2\frac{1}{8})_4$ . This is not the case with  $(SR2\frac{1}{2})_4$ , which is much more robust than the two other recoupling schemes. Fig. 41 is focused onto the behavior of the informative  $B^{34}$  cross-peak. However, it is very important to keep in mind that the observation of the informative cross-peaks is often hampered by the large amplitude of the useless diagonal signals, as shown in Fig. 42.

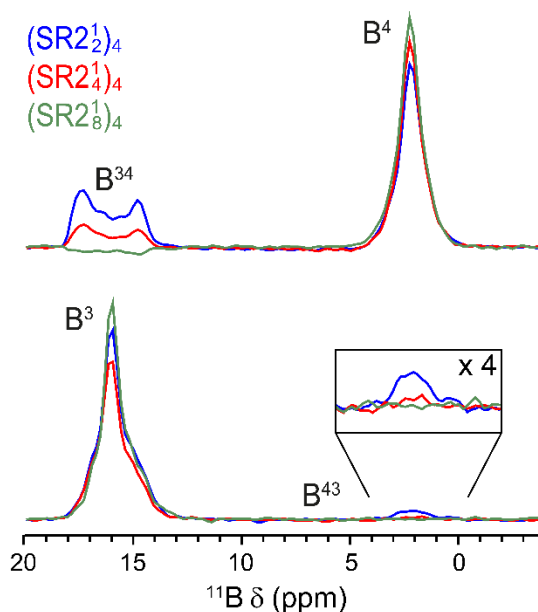


**Figure 42.** 1D slices of the  $^{11}\text{B}$  SQ-SQ *D*-HOMCOR spectra shown in Fig. 8 of  $\text{Li}_2\text{B}_4\text{O}_7$  with  $(\text{SR}2_{2}^1)_4$ ,  $(\text{SR}2_{4}^1)_4$  and  $(\text{SR}2_{8}^1)_4$  schemes, with  $v_{\text{offset}} = 3$  kHz (11.7 ppm) and  $\tau_{\text{mix}} = 3.2$  ms. These slices show that the  $\text{B}^{34}$  ( $\text{B}^{\text{III}}\text{-B}^{\text{IV}}$ ) and  $\text{B}^{43}$  ( $\text{B}^{\text{IV}}\text{-B}^{\text{III}}$ ) cross-peaks are hardly observable with  $(\text{SR}2_{4}^1)_4$ , and especially  $(\text{SR}2_{8}^1)_4$ .

### 3.6.1.2 DQ-SQ

The  $\text{SRN}_n^1$  schemes shown in Fig. 33a-d mostly differ in their behavior with respect to rf-inhomogeneity and offset due to the use of a small rf-field to fulfill the HORROR condition. From experiments and simulations, M. Edén and co-workers have made several conclusions concerning DQ-SQ experiments with  $\text{SRN}_n^1$  recoupling applied to half-integer quadrupolar nuclei.<sup>11</sup> The first one is that ‘an enhanced compensation for offsets can be observed following the order  $\text{SR}2_{2}^1 < \text{SR}2_{4}^1 \approx \text{SR}4_{4}^1$ ’.<sup>8,9</sup> The second point is that  $\text{SR}2_{2}^1$  is the most robust scheme to rf inhomogeneity, whereas  $\text{SR}2_{4}^1$  is the most robust to offset, but exhibits a low efficiency. The third point is that bracketed recoupling schemes are ‘favored, although their more rapid DQ excitation dynamics is sometimes a disadvantage’. The fourth conclusion is that ‘the strong sensitivity of  $\text{SR}2_{2}^1$  to the coupling of offset and rf-inhomogeneity restricts its application to  $\Delta$  smaller than a few kHz, yet encompassing many  $^{11}\text{B}$  and  $^{23}\text{Na}$  applications, and that  $\text{SR}2_{4}^1$  is recommended for larger  $\Delta$  values, which must remain lower than 10 kHz’.

Concerning the  $BR2_{\frac{1}{2}}^1$  scheme, Edén and co-workers concluded that ‘provided  $\tau_{mix}$  is sufficient, its robustness to offsets and rf-inhomogeneity is the best’. From numerical simulations, the dipolar scaling factor of  $BR2_{\frac{1}{2}}^1$  was found intermediate between bracketed or not bracketed sequences in Fig. 33a-d.<sup>11</sup> However, the bracketed  $[BR2_{\frac{1}{2}}^1]$  recoupling scheme has never been tested up to now.

Following these conclusions, the 2D  $^{11}B$  DQ-SQ *D*-HOMCOR spectra were recorded on the same test sample of  $Li_2B_4O_7$ , with  $SR2_{\frac{1}{2}}^1$ ,  $[SR2_{\frac{1}{2}}^1]$ ,  $BR2_{\frac{1}{2}}^1$  and  $[BR2_{\frac{1}{2}}^1]$ . A great advantage of DQ-SQ over SQ-SQ is that most 2D experiments can be easily optimized in a 1D way, with  $t_1 = 0$ , because all peaks are related to through-space proximities and are thus meaningful.

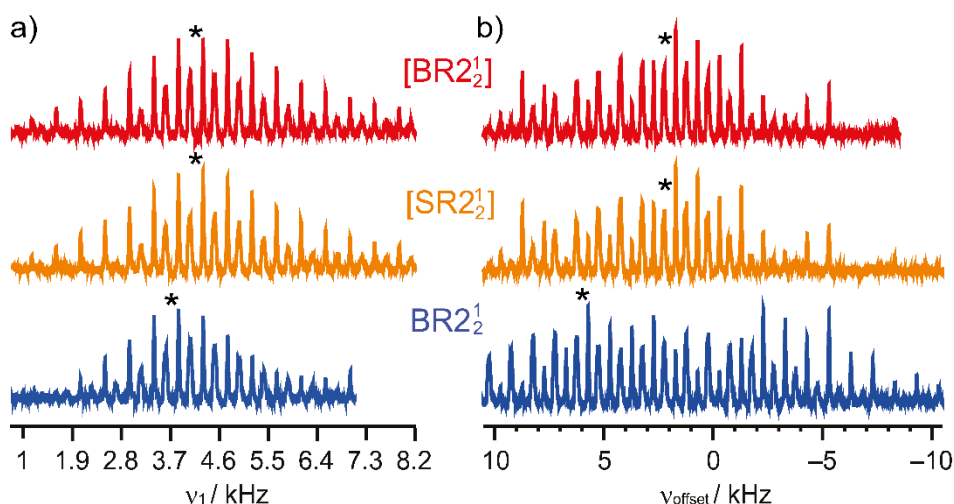


**Figure 43.** Experimental 1D  $^{11}B$  DQ-filtered signal of  $Li_2B_4O_7$  observed with a 1D ( $t_1 = 0$ ) version of the  $[SR2_{\frac{1}{2}}^1]$ ,  $[BR2_{\frac{1}{2}}^1]$  and  $BR2_{\frac{1}{2}}^1$ , sequences versus (a)  $v_1$  ranging from 1 to 8 kHz and (b)  $v_{offset}$  ranging from +10 to -10 kHz. The spectra obtained with  $SR2_{\frac{1}{2}}^1$  scheme are not shown because it is much less efficient than these three schemes (see Fig. 44). The optimum values are indicated with \*.

It must be first noted that the minimum mixing step of these four DQ-SQ sequences,  $\Delta\tau_{mix} = 200 \mu s$  at  $v_R = 20$  kHz, is much shorter than with the previous  $(SR2_{\frac{1}{n}}^1)_4$  recoupling employed in SQ-SQ *D*-HOMCOR schemes. Furthermore, a ratio of two was found between the optimum recoupling times for the bracketed and un-bracketed versions:  $\tau_{mix,opt} = 200$  and  $400 \mu s$ , for  $[SR2_{\frac{1}{2}}^1]$  /  $[BR2_{\frac{1}{2}}^1]$  and  $SR2_{\frac{1}{2}}^1$  /  $BR2_{\frac{1}{2}}^1$ , respectively (not shown). In Fig. 43, the robustness of the three most efficient sequences versus rf-field and offset is presented.

In Fig. 43a it is observed that the experimental optimum rf-fields are slightly smaller than the theoretical value of  $\nu_1 = 5$  kHz (Eq. 1). Moreover, the two bracketed schemes give similar rf-robustness, higher than their un-bracketed version. This is the opposite in Fig. 43b: the two bracketed versions give similar robustness to offset, but the highest one is achieved for  $\text{BR}2_{\frac{1}{2}}$ . It must be observed that the optimum offset values are not the same: 2 and 6 kHz (7.8 and 23.4 ppm) for the bracketed and un-bracketed versions, respectively, which means in the middle of the two resonances in the first case and off-resonance in the second case (Fig. 39).

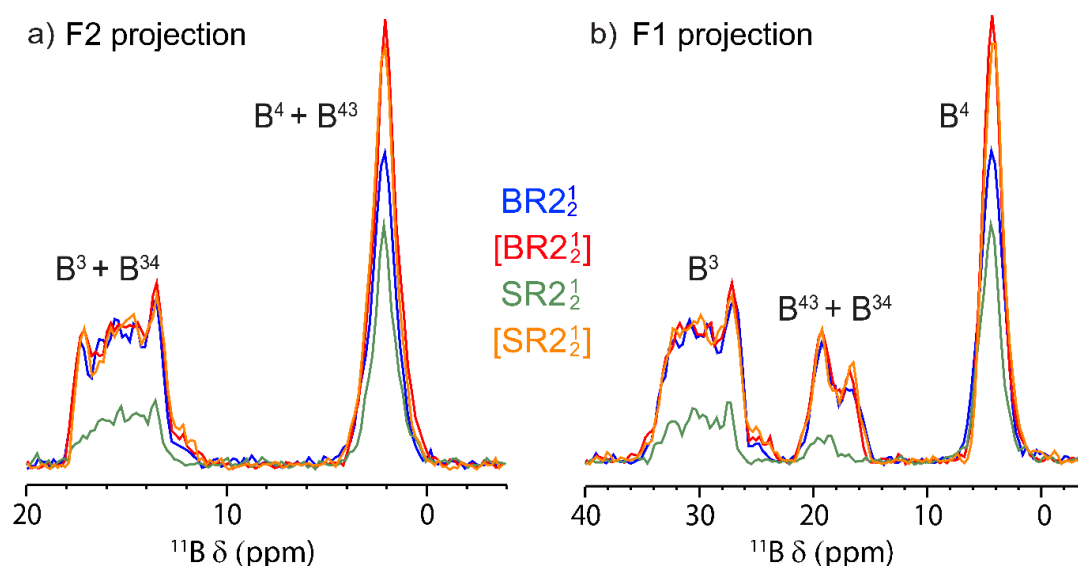


**Figure 44.** Comparison of the (a)  $F_2$  or (b)  $F_1$  projections of 2D DQ-SQ 2D spectra of  $\text{Li}_2\text{B}_4\text{O}_7$  acquired at  $B_0 = 18.8$  T with a MAS frequency of 20 kHz with NUS retaining 33% of the  $t_1$  points and recorded with  $[\text{SR}2_{\frac{1}{2}}]$ ,  $[\text{BR}2_{\frac{1}{2}}]$ ,  $\text{SR}2_{\frac{1}{2}}$  and  $\text{BR}2_{\frac{1}{2}}$  sequences. The 2D spectra result from averaging 64 transients using a relaxation delay  $\tau_{\text{RD}} = 1$  s for each of 120  $t_1$ -increments, leading to an experimental time  $T_{\text{exp}} = 45$ -50 min. We employed optimal rf field strength equal to  $\nu_1 = 3.7$  and 4.1 kHz for  $\text{BR}2_{\frac{1}{2}} / \text{SR}2_{\frac{1}{2}}$  and  $[\text{BR}2_{\frac{1}{2}}] / [\text{SR}2_{\frac{1}{2}}]$ , respectively.

Fig. 44 presents a comparison of the efficiencies of the four DQ-SQ recouplings, and the  $F_2$  and  $F_1$  projections of the four 2D spectra are shown. The two bracketed versions provide the same best signals for all peaks, whereas  $\text{BR}2_{\frac{1}{2}}$  provides a smaller signal for  $\text{B}^4$  auto-peak and  $\text{SR}2_{\frac{1}{2}}$  is much less efficient than the other schemes.

### 3.6.1.3 SQ-SQ vs DQ-SQ

In a last stage for the spin-3/2 analyses, in Fig. 45 is presented the comparison of the rows corresponding to the two species with the four most efficient sequences: SQ-SQ with  $(SR2\frac{1}{2})_4$ , and DQ-SQ with  $[BR2\frac{1}{2}]$ ,  $[SR2\frac{1}{2}]$  and  $BR2\frac{1}{2}$ . In order to make an easy comparison of the 2D spectra, the DQ-SQ ones were sheared by a factor of two in order to be displayed as SQ-SQ 2D spectra with the same scales on the two axes (not shown).

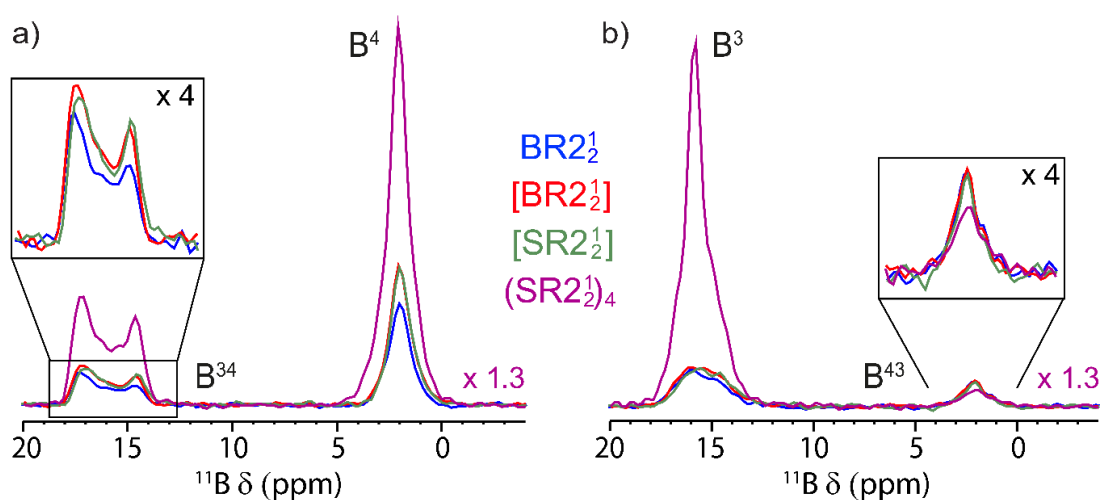


**Figure 45.** Comparison of  $F_2$  slices containing (a)  $B^4$  or (b)  $B^3$  diagonal peaks of 2D  $^{11}\text{B}$  the SQ-SQ and DQ-SQ  $D$ -HOMCOR spectra of  $\text{Li}_2\text{B}_4\text{O}_7$  using  $(SR2\frac{1}{2})_4$  recoupling for SQ-SQ scheme and  $[BR2\frac{1}{2}]$ ,  $[SR2\frac{1}{2}]$  and  $BR2\frac{1}{2}$  recoupling for DQ-SQ sequence at  $B_0 = 18.8$  T with a MAS frequency of 20 kHz. An expansion of the cross-peaks is also shown. All 2D spectra were acquired using uniform sampling. The 2D DQ-SQ and SQ-SQ spectra result from averaging 64 and 48 transients, respectively, using a relaxation delay  $\tau_{RD} = 1$  s for each of 120  $t_1$ -increments, leading to an experimental time  $T_{\text{exp}} = 2\text{h}30$  min and  $1\text{h}50$  min, respectively. The signal was normalized with respect to the number of transients. We employed optimal rf field strength equal to  $\nu_1 = 3.7$  kHz for  $BR2\frac{1}{2}$ , 4.1 kHz for  $[BR2\frac{1}{2}]$  and  $[SR2\frac{1}{2}]$  and  $\nu_1 = 3.9$  kHz for  $(SR2\frac{1}{2})_4$ .

The bracketed  $[SR2\frac{1}{2}]$  and  $[BR2\frac{1}{2}]$  sequences are the two most efficient DQ-SQ methods for the  $B^{34}$  cross-peak and  $B^4$  auto-peak (Fig. 45), whereas for the  $B^{43}$  and  $B^3$  peaks they give the same sensitivity as  $BR2\frac{1}{2}$ . The SQ-SQ method with  $(SR2\frac{1}{2})_4$  is twice more efficient than DQ-SQ methods for the  $B^{34}$  cross-peak, but the least efficient for the  $B^{43}$  cross-peak owing to the faster decay of  $B^{\text{III}}$  SQ coherences. Moreover, it

provides no through-space information through the  $B^3$  and  $B^4$  auto-peaks, which are mostly related to magnetizations that have not been transferred during the sequence.

As a conclusion for spin-3/2 nuclei with small or moderate chemical shift differences, such as  $^{11}\text{B}$ , the DQ-SQ sequence with  $[\text{BR}2\frac{1}{2}]$  and  $[\text{SR}2\frac{1}{2}]$  bracketed recouplings seem to be the better choices. Indeed, they deliver a good efficiency simultaneously for the cross- and auto-peaks, which both then provide an analysis of the spatial proximities. Conversely, the SQ-SQ sequences lead to cross-peaks with similar intensities as the DQ-SQ ones, but they do not allow analyzing the spatial proximities with resonances that have close or identical frequencies.

### 3.6.2 $^{27}\text{Al}$ - $^{27}\text{Al}$ experiments on $\text{AlPO}_4\text{-14}$

In  $^{27}\text{Al}$  NMR, the chemical shift range is much larger than for  $^{11}\text{B}$ . Indeed, the difference between the isotropic chemical shifts of  $\text{Al}^{\text{IV}}$  and  $\text{Al}^{\text{VI}}$  nuclei reaches  $\Delta \approx 10$  kHz at  $B_0 = 18.8$  T, which is approximately three-fold larger than that between those of  $\text{B}^{\text{III}}$  and  $\text{B}^{\text{IV}}$  nuclei. In this case of large  $\Delta$  values, Edén *et. al* have recommended the  $(\text{SR}2\frac{1}{2})_4$  and especially the  $(\text{SR}2\frac{1}{4})_4$  SQ-SQ sequence. This was the case for  $^{27}\text{Al}$  in CJ19, where  $\Delta_{\text{iso,max}} \approx 9.6$  kHz and  $^{27}\text{Al}$ - $^{27}\text{Al}$  dipolar interactions are small.<sup>13</sup> Therefore, the SQ-SQ sequences using  $(\text{SR}2\frac{1}{2})_4$  and  $(\text{SR}2\frac{1}{4})_4$  recoupling and the DQ-SQ schemes incorporating  $[\text{BR}2\frac{1}{2}]$  and  $\text{BR}2\frac{1}{2}$  recoupling will be compared in the following.

$\text{AlPO}_4\text{-14}$  presents four aluminum species: two tetrahedral  $\text{Al}^{\text{IV}}$  ( $\text{Al}^{\text{IV}}_1$ :  $\delta_{\text{iso}} = 42.7$  ppm,  $C_Q = 1.72$  MHz,  $\eta_Q = 0.57$ ;  $\text{Al}^{\text{IV}}_2$ :  $\delta_{\text{iso}} = 43.5$  ppm,  $C_Q = 3.90$  MHz,  $\eta_Q = 0.83$ ), one pentavalent  $\text{Al}^{\text{V}}$  ( $\delta_{\text{iso}} = 27.1$  ppm,  $C_Q = 5.61$  MHz,  $\eta_Q = 0.93$ ) and one octahedral  $\text{Al}^{\text{VI}}$  ( $\delta_{\text{iso}} = -1.3$  ppm,  $C_Q = 2.55$  MHz,  $\eta_Q = 0.67$ ) (Table 14).<sup>46</sup> Moreover, the tested sample contained an extra framework impurity at  $-2$  kHz indicated with a star. Along with Al-O-P-O-Al connectivities, which are common for all aluminophosphate molecular sieves, there also exist some Al-O-Al connectivities in  $\text{AlPO}_4\text{-14}$  due to edge sharing between  $\text{AlO}_6$  octahedra and vertex sharing between  $\text{AlO}_5$  and  $\text{AlO}_6$  polyhedra. As a result, the  $^{27}\text{Al}$ - $^{27}\text{Al}$  inter-nuclear distances are equal to 2.9, 3.6 and at least 4.3 Å for  $\text{Al}^{\text{VI}}\text{-Al}^{\text{VI}}$ ,  $\text{Al}^{\text{V}}\text{-Al}^{\text{VI}}$  and  $\text{Al}^{\text{IV}}_j\text{-Al}^{\text{IV}}_k$ , ( $j, k = 1, 2$ ), which correspond to

dipolar coupling constants  $|b_{\text{VI-VI}}|/(2\pi) = 333$ ,  $|b_{\text{V-VI}}|/(2\pi) = 174$ , and  $|b_{\text{IVj-IVk}}|/(2\pi) \leq 102$  Hz, respectively. All other distances are much larger and hence the dipolar interactions are much smaller than 100 Hz. To simplify the analysis, the 2D  $^{27}\text{Al}$  HOMCOR spectra are represented as those of  $^{11}\text{B}$  presented above. As example,  $\text{Al}^4$  and  $\text{Al}^{56}$  denote to the  $\text{Al}^{\text{IV}}\text{-Al}^{\text{IV}}$  auto-peak and the  $\text{Al}^{\text{V}}\text{-Al}^{\text{VI}}$  cross-peak, respectively. In addition, the two  $\text{Al}_1^{\text{IV}}$  and  $\text{Al}_2^{\text{IV}}$  overlapping resonances are not distinguished in the following.

**Table 14.** Aluminum species present in  $\text{AlPO}_4\text{-14}$  reported by Sasaki *et al.*<sup>46</sup>

Al site	$\delta_{\text{iso}}$ (ppm)	$C_Q$ (MHz),	$\eta_Q$
$\text{Al}^{\text{IV}}_1$	42.7	1.72	0.57
$\text{Al}^{\text{IV}}_2$	43.5	3.90	0.83
$\text{Al}^{\text{V}}$	27.1	5.61	0.93
$\text{Al}^{\text{VI}}$	-1.3	2.55	0.67

### 3.6.2.1 SQ-SQ

The  $(\text{SR}2_{2}^1)_4$  and  $(\text{SR}2_{4}^1)_4$  schemes were tested with the SQ-SQ sequences on  $\text{AlPO}_4\text{-14}$ . The optimized results were very similar. In Fig. 46 the best 2D spectrum recorded with the second scheme is shown. All cross-peaks are observed, even the  $\text{Al}^{\text{IV}}\text{-Al}^{\text{VI}}$  ones with a large chemical shift difference of 10 kHz and a small dipolar coupling of  $b_{\text{IV-VI}} = 52$  Hz related to the long inter-nuclear distance of 5.4 Å.



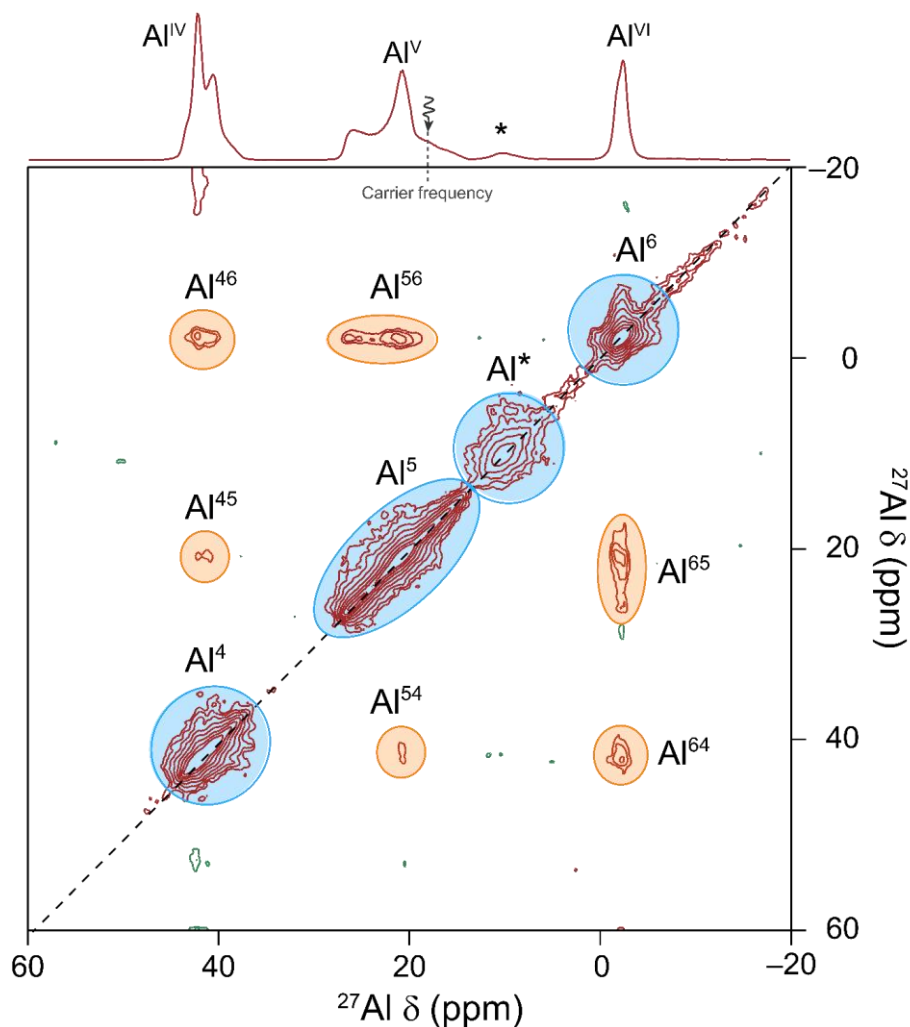


**Figure 46.** 2D  $^{27}\text{Al}$  SQ-SQ *D*-HOMCOR spectrum of  $\text{AlPO}_4\text{-14}$  using  $(\text{SR}2_4^1)_4$  recoupling at  $B_0 = 18.8$  T with a MAS frequency of 20 kHz acquired with NUS retaining 33% of the  $t_1$  points. Cross- and diagonal peaks are indicated with orange and blue ovals, respectively. The extra framework impurity at  $-2$  kHz is indicated with a star. We used  $\tau_{\text{mix}} = 3.2$  ms,  $\nu_1 = 2.4$  kHz and  $\nu_{\text{offset}} = 4$  kHz (19.2 ppm) for the recoupling. The 2D SQ-SQ spectrum results from averaging 48 transients using a relaxation delay  $\tau_{\text{RD}} = 1$  s for each of 330  $t_1$ -increments, leading to an experimental time  $T_{\text{exp}} = 1$  h 40 min.

In Fig. 47, the comparison of the cross-peaks observed with the two recoupling schemes is presented. The diagonal resonances, which are non-informative, have been largely truncated. These slices show that the informative cross-peaks only represent a few percent of the auto-peaks, and that the two recoupling schemes provide similar useful information.

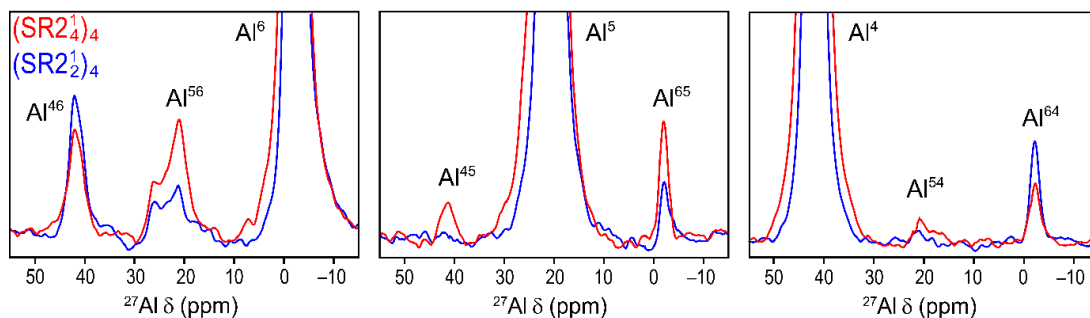


**Figure 47.** Comparison of the cross-peak intensities of the SQ-SQ spectra of  $\text{AlPO}_4\text{-14}$  at  $B_0 = 18.8$  T with a MAS frequency of 20 kHz acquired with NUS retaining 33% of the  $t_1$  point, obtained from 1D slices taken from the 2D spectra recorded with  $(\text{SR}2_{2}^1)_4$  ( $\tau_{\text{mix}} = 4.8$  ms,  $\nu_{\text{offset}} = 2.82$  kHz (13.5 ppm)) and  $(\text{SR}2_{4}^1)_4$  ( $\tau_{\text{mix}} = 3.2$  ms,  $\nu_{\text{offset}} = 4$  kHz (19.2 ppm)) recoupling schemes. The auto-peaks, which bring no information, have been truncated at 5 % of their maximum values. We employed rf field strength equal to  $\nu_1 = 2.4$  kHz. The other experimental parameters are identical to those of Fig. 46.

### 3.6.2.2 DQ-SQ

Because of the overlapping of the  $\text{Al}_1^{\text{IV}}$  and  $\text{Al}_2^{\text{IV}}$  resonances and of the very different dipolar values, the DQ-SQ spectra are mostly composed of only four main resonances: two auto-correlations ( $\text{Al}^4$  and  $\text{Al}^6$ :  $\text{Al}^{\text{IV}}\text{-Al}^{\text{IV}}$  and  $\text{Al}^{\text{VI}}\text{-Al}^{\text{VI}}$ ) and two pair of cross-peaks ( $\text{Al}^{56}$  and  $\text{Al}^{65}$ :  $\text{Al}^{\text{V}}\text{-Al}^{\text{VI}}$  and  $\text{Al}^{\text{VI}}\text{-Al}^{\text{V}}$ ). The other peaks are much smaller because they correspond to longer distances. This can be observed in Fig. 48, where is presented the best DQ-SQ spectrum, which was recorded with  $\text{BR}2_{2}^1$ . All peaks are observable, even the  $\text{Al}^{46}$  and  $\text{Al}^{64}$  ones ( $\text{Al}^{\text{IV}}\text{-Al}^{\text{VI}}$  and  $\text{Al}^{\text{VI}}\text{-Al}^{\text{IV}}$ ), which correspond to a large chemical shift difference ( $\Delta \approx 10$  kHz) and a small dipolar value of  $|b_{\text{IV-VI}}|/(2\pi) = 52$  Hz. Only the  $\text{Al}^5$  ( $\text{Al}^{\text{V}}\text{-Al}^{\text{V}}$ ) auto-peak is not observed, but it corresponds to a very large distance of 6.7 Å, and hence to the very small dipolar value of  $b_{\text{V-V}} = 27$  Hz.

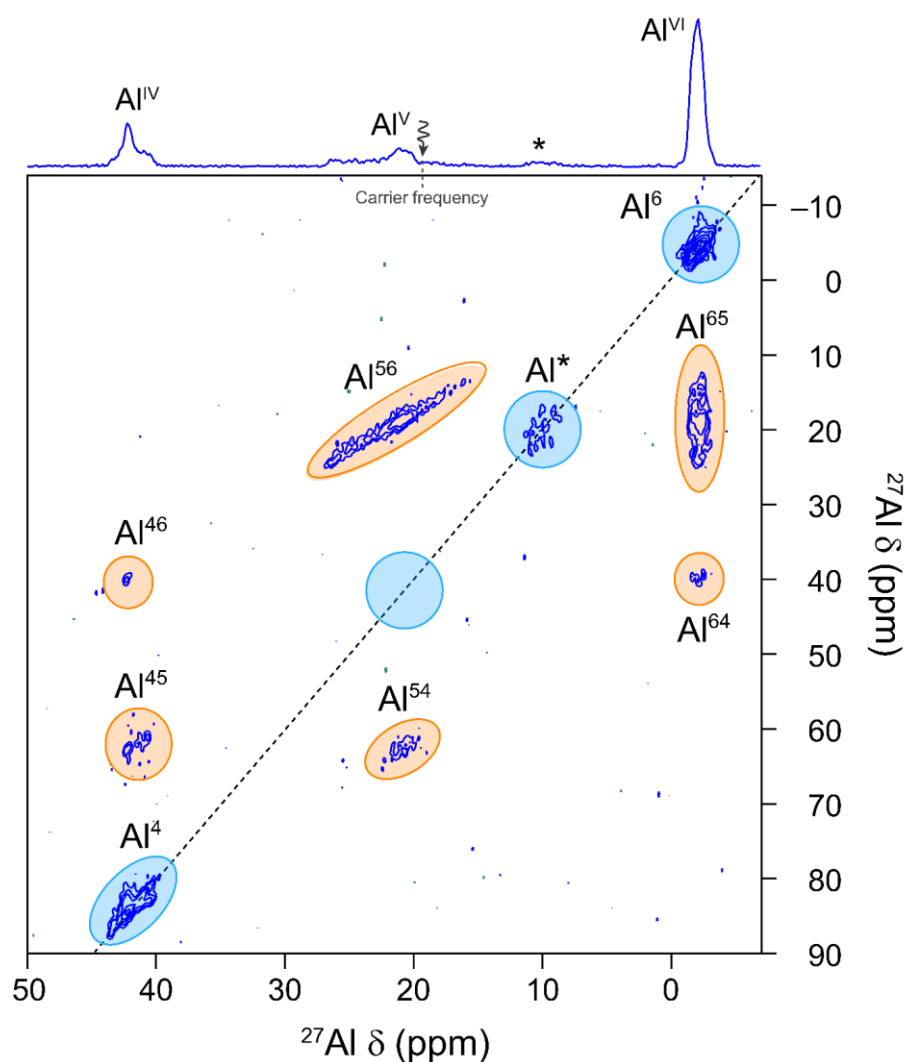


**Figure 48.** 2D  $^{27}\text{Al}$  DQ-SQ *D*-HOMCOR spectrum of  $\text{AlPO}_4\text{-14}$  using  $\text{BR}2\frac{1}{2}$  recoupling acquired with NUS retaining 33% of the  $t_1$  points at  $B_0 = 18.8$  T with a MAS frequency of 20 kHz. Cross- and auto-peaks are indicated with orange and blue circles, respectively. The 2D SQ-SQ spectrum results from averaging 64 transients using a relaxation delay  $\tau_{\text{RD}} = 1$  s for each of 330  $t_1$ -increments, leading to an experimental time  $T_{\text{exp}} = 2$  h. The recoupling used the following parameters:  $\nu_1 = 2.9$  kHz,  $\nu_{\text{offset}} = 4$  kHz (19.2 ppm) and  $\tau_{\text{mix}} = 0.8$  ms.

It is important to note that, due to the large differences of the dipolar couplings, the relative intensities of the peaks are largely changing depending whether the experiment is optimized for the shortest ( $\text{Al}^{\text{IV}}\text{-Al}^{\text{IV}}$ ,  $\text{Al}^{\text{VI}}\text{-Al}^{\text{VI}}$ ,  $\text{Al}^{\text{V}}\text{-Al}^{\text{VI}}$  and  $\text{Al}^{\text{VI}}\text{-Al}^{\text{V}}$ ) distances, as here, or longest (all other peaks) ones. It must also be noted that, owing to the weak rf-field used, the intensities of the peaks are strongly related to the offset value, as can be observed in Fig. 49.

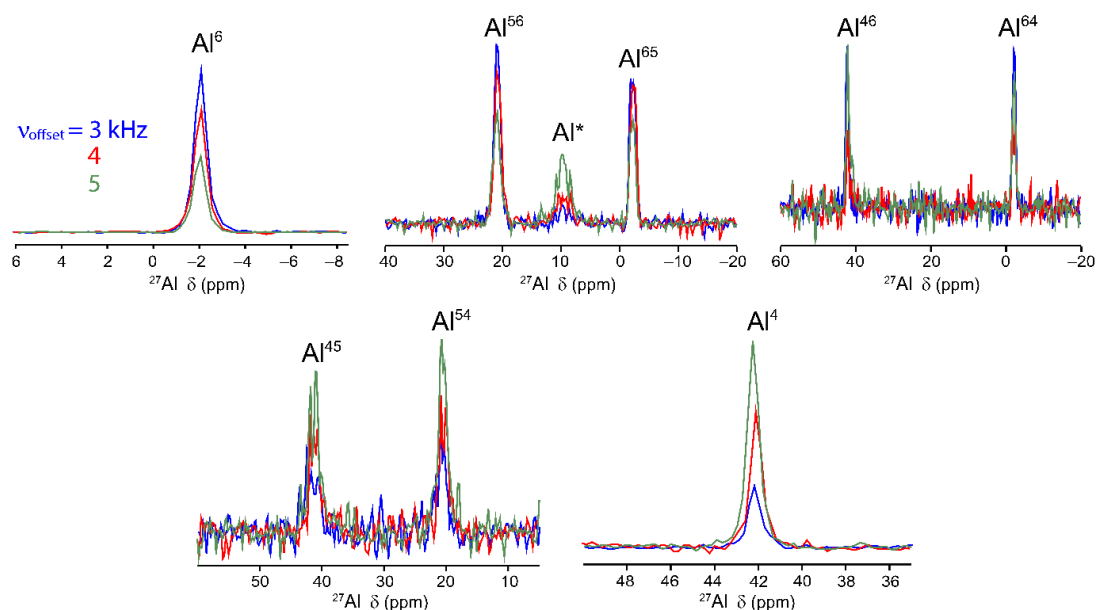


**Figure 49.**  $F_2$  slices of three 2D  $^{27}\text{Al}$  DQ-SQ  $D$ -HOMCOR spectra of  $\text{AlPO}_4\text{-14}$  acquired using  $\text{BR2}_2^1$  recoupling and NUS retaining 33% of the  $t_1$  points at  $B_0 = 18.8$  T with a MAS frequency of 20 kHz for  $v_{\text{offset}} = 3, 4$  or 5 kHz. The other experimental parameters are identical to those of Fig. 48.

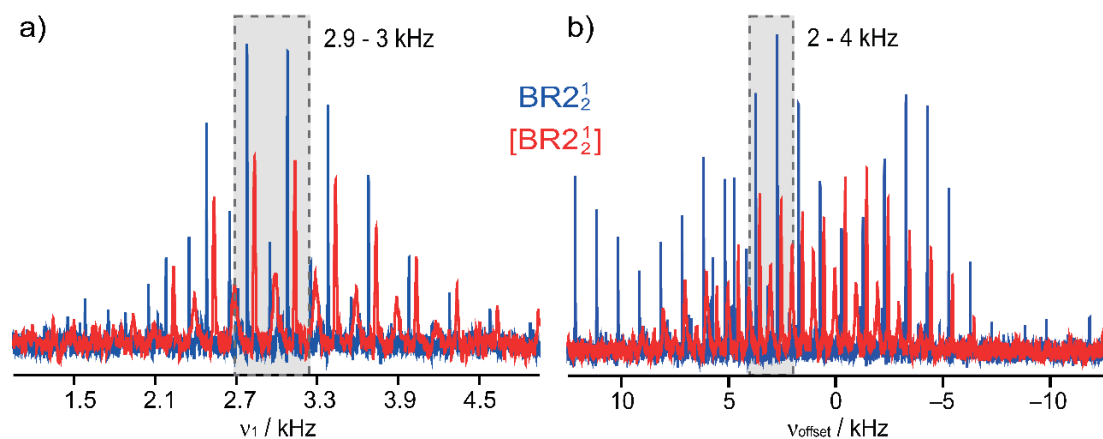


**Figure 50.** Robustness with respect to (a) rf-field and (b) offset of 1D  $^{27}\text{Al}$  DQ-filtered  $D$ -HOMCOR spectra of  $\text{AlPO}_4\text{-14}$ , recorded with  $\text{BR2}_2^1$  (blue,  $\tau_{\text{mix}} = 0.8$  ms) or  $[\text{BR2}_2^1]$  (red,  $\tau_{\text{mix}} = 0.4$  ms) recoupling at  $B_0 = 18.8$  T with a MAS frequency of 20 kHz. The 1D NMR spectra result from averaging 64 transients with  $\tau_{\text{RD}} = 1$  s. In panel (a),  $v_{\text{offset}} = 4$  kHz, whereas in panel (b),  $v_1 = 2.9$  and 3 kHz for  $\text{BR2}_2^1$  and  $[\text{BR2}_2^1]$ , respectively.

In Fig. 50, the sensitivity and the robustness to rf-field and offset of the  $\text{BR2}_2^1$  and  $[\text{BR2}_2^1]$  DQ-SQ sequences applied to  $\text{AlPO}_4\text{-14}$  are compared. As observed previously,  $\text{BR2}_2^1$  combines the advantages of being more efficient and more robust than  $[\text{BR2}_2^1]$ .

### 3.6.2.3 SQ-SQ vs DQ-SQ

In order to compare more easily the results obtained with SQ-SQ *D*-HOMCOR experiment using  $(\text{SR2}_4^1)_4$  recoupling and DQ-SQ using  $\text{BR2}_2^1$  recoupling, the 2D FIDs obtained in the second case has been sheared with a factor of two. The program used to perform such a shearing process for a 2D spectrum acquired with NUS is given in the Appendix C. After this data treatment, in Fig. 51 is presented the three slices along F2 obtained with the two types of 2D *D*-HOMCOR spectra. The signal of the useless auto-peaks has been truncated as indicated in each subfigure. These results demonstrate the poor efficiency of the HOMCOR sequences applied to spin-5/2 nuclei, even in the case of moderate dipolar values and small chemical shift differences, such as  $\text{Al}^{\text{VI}}\text{-Al}^{\text{VI}}$  ( $|b_{\text{VI-VI}}|/(2\pi) = 333$  Hz,  $\Delta\nu = 0$  Hz) and  $\text{Al}^{\text{V}}\text{-Al}^{\text{VI}}$  ( $|b_{\text{V-VI}}|/(2\pi) = 174$  Hz,  $\Delta\nu = 4800$  Hz). This efficiency only reaches a few percent in agreement with previous simulations.<sup>15</sup> The *S/N* ratio of these results is smaller than the one previously published on the same sample with the same spectrometer.<sup>14</sup> However, in this previous study an initial hyper-secant CT enhancing was used and the experiments were recorded using a 4 mm rotor instead of a 3.2 mm one, like in this dissertation. On one hand, using a 4 mm rotor allows increasing the *S/N* due to the larger sample amount, but on the other hand, it limits the spinning speed to ca. 15 kHz. For  $^{27}\text{Al}$  DQ-SQ experiments performed at  $B_0 = 18.8$  T, a MAS frequency of 15 kHz requires a rescaling of the evolution time  $t_1$  using the  $\pi$ -pulse displayed in blue in Fig. 32b.<sup>14</sup> Moreover, it has been shown that the offset robustness increases with the MAS frequency, since the rf-field of the recoupling is proportional to the MAS frequency (compare Figs. 3c and d of ref <sup>14</sup>). A better offset robustness is indeed observed at  $\nu_R = 20$  kHz (Fig. 40b), compared to 13.89 kHz (Fig. 3b of ref. <sup>15</sup>). In Fig. 51, it is observed that the cross-peak intensities for DQ-SQ *D*-HOMCOR scheme using  $\text{BR2}_2^1$  are always equal to or larger than those observed with SQ-SQ *D*-HOMCOR using  $(\text{SR2}_4^1)_4$  recoupling.

Therefore, as a conclusion, for  $^{27}\text{Al}$  ( $I = 5/2$ ) nuclei, the DQ-SQ *D*-HOMCOR variant using  $\text{BR2}_2^1$  sequence is recommended since it yields cross-peaks of higher

intensity and also allows analyzing the spatial proximities between resonances with close or identical frequencies.

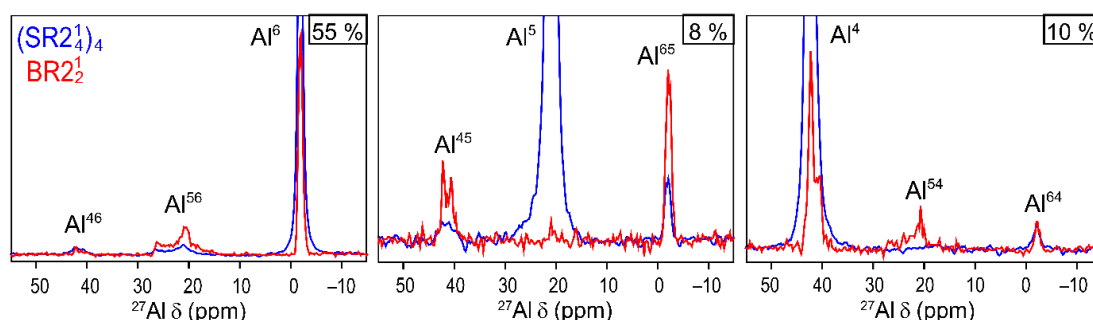


**Figure 51.** Comparison of three  $F_2$  slices of 2D  $^{27}\text{Al}$  DQ-SQ and SQ-SQ  $D$ -HOMCOR spectra of  $\text{AlPO}_4\text{-14}$  acquired using  $\text{BR}2\frac{1}{2}$  and  $(\text{SR}2\frac{1}{4})_4$  recoupling with  $\tau_{\text{mix}} = 0.8$  and 3.2 ms, respectively, and NUS retaining 33% of the  $t_1$  points at  $B_0 = 18.8$  T with a MAS frequency of 20 kHz. The offset of the recoupling schemes was equal to  $\nu_{\text{offset}} = 4$  kHz (19.2 ppm). The acquisition parameters of DQ-SQ and SQ-SQ experiments are identical to those of Figs. 46 and 48, respectively. The signal of the SQ-SQ spectrum has been multiplied by 1.33 to compensate for the difference in the number of transients. The auto-correlation peaks of SQ-SQ spectrum bring no information, and hence, these signals are truncated to the percentage of their maximal intensity indicated on each panel.

### 3.7 CONCLUSIONS

In this work, it has been analyzed and compared the efficiencies of HOMCOR experiments for half-integer quadrupolar nuclei, namely  $^{11}\text{B}$  and  $^{27}\text{Al}$ . For both isotopes, the DQ-SQ sequences are recommended, which deliver a good efficiency simultaneously for the cross- and auto-correlation peaks, hence providing a global analysis of the spatial proximities, even for resonances that have close or identical frequencies.

In the first case ( $^{11}\text{B}$ ,  $I = 3/2$ ), the chemical shift differences are small or moderate, and therefore, the  $[\text{SR}2\frac{1}{2}]$  or  $[\text{BR}2\frac{1}{2}]$  bracketed recoupling schemes are recommended. In the second case ( $^{27}\text{Al}$ ,  $I = 5/2$ ), the chemical shift differences are larger, and can reach ca. 10 kHz at 18.8 T. In this case, the  $\text{BR}2\frac{1}{2}$  un-bracketed recoupling scheme is recommended.

In any case, the acquisitions are time-consuming to obtain a reasonable signal-to-noise ratios. It must be noted that the experimental time can be largely decreased by using an initial CT enhancement obtained by the transfer of population from the STs to the CT.<sup>14</sup> The related gain increases with the spin value. The experimental time can also be decreased by a non-uniform sampling of the indirect dimension.<sup>47</sup>

## References

- (1) Teymoori, G.; Pahari, B.; Svensson, B.; Edén, M. Low-Power Broadband Homonuclear Dipolar Recoupling without Decoupling: Double-Quantum <sup>13</sup>C NMR Correlations at Very Fast Magic-Angle Spinning. *Chem. Phys. Lett.* **2012**, *547*, 103–109. <https://doi.org/10.1016/j.cplett.2012.07.053>.
- (2) Edén, M.; Frydman, L. Quadrupolar-Driven Recoupling of Homonuclear Dipolar Interactions in the Nuclear Magnetic Resonance of Rotating Solids. *J. Chem. Phys.* **2001**, *114* (9), 4116–4123. <https://doi.org/10.1063/1.1344886>.
- (3) Edén, M.; Frydman, L. Homonuclear NMR Correlations between Half-Integer Quadrupolar Nuclei Undergoing Magic-Angle Spinning. *J. Phys. Chem. B* **2003**, *107* (51), 14598–14611. <https://doi.org/10.1021/jp035794t>.
- (4) Ding, S.; McDowell, C. A. Spectral Spin Diffusion of a Spin-3/2 System in Rotating Solids. *Mol. Phys.* **1995**, *85* (2), 283–298. <https://doi.org/10.1080/00268979500101111>.
- (5) Dowell, N. G.; Ashbrook, S. E.; Wimperis, S. Relative Orientation of Quadrupole Tensors from High-Resolution NMR of Powdered Solids. *J. Phys. Chem. A* **2002**, *106* (41), 9470–9478. <https://doi.org/10.1021/jp021315z>.
- (6) Pandey, M. K.; Amoureux, J.-P.; Asakura, T.; Nishiyama, Y. Sensitivity Enhanced <sup>14</sup>N/<sup>14</sup>N Correlations to Probe Inter-Beta-Sheet Interactions Using Fast Magic Angle Spinning Solid State NMR in Biological Solids. *Phys. Chem. Chem. Phys.* **2016**, *18* (32), 22583–22589. <https://doi.org/10.1039/C6CP03848D>.
- (7) Mali, G.; Fink, G.; Taulelle, F. Double-Quantum Homonuclear Correlation Magic Angle Sample Spinning Nuclear Magnetic Resonance Spectroscopy of Dipolar-Coupled Quadrupolar Nuclei. *J. Chem. Phys.* **2004**, *120* (6), 2835–2845. <https://doi.org/10.1063/1.1638741>.
- (8) Edén, M.; Zhou, D.; Yu, J. Improved Double-Quantum NMR Correlation Spectroscopy of Dipolar-Coupled Quadrupolar Spins. *Chem. Phys. Lett.* **2006**, *431* (4), 397–403. <https://doi.org/10.1016/j.cplett.2006.09.081>.
- (9) Lo, A. Y. H.; Edén, M. Efficient Symmetry-Based Homonuclear Dipolar Recoupling of Quadrupolar Spins: Double-Quantum NMR Correlations in Amorphous Solids. *Phys. Chem. Chem. Phys.* **2008**, *10* (44), 6635–6644. <https://doi.org/10.1039/B808295B>.
- (10) Edén, M. Homonuclear Dipolar Recoupling of Half-Integer Spin Quadrupolar Nuclei: Techniques and Applications. *Solid State Nucl. Magn. Reson.* **2009**, *36* (1), 1–10. <https://doi.org/10.1016/j.ssnmr.2009.06.005>.
- (11) Edén, M. Recent Progress in Homonuclear Correlation Spectroscopy of Quadrupolar Nuclei. In *Modern Magnetic Resonance*; Webb, G. A., Ed.; Springer International Publishing: Cham, 2017; pp 1–33. [https://doi.org/10.1007/978-3-319-28275-6\\_104-1](https://doi.org/10.1007/978-3-319-28275-6_104-1).

- (12) Yu, Y.; Keil, P.; Stevansson, B.; Hansen, M. R.; Edén, M. Assessment of New Symmetry-Based Dipolar Recoupling Schemes for Homonuclear Magnetization Exchange between Quadrupolar Nuclei in Two-Dimensional Correlation MAS NMR. *J. Magn. Reson.* **2020**, *316*, 106734. <https://doi.org/10.1016/j.jmr.2020.106734>.
- (13) Yu, Y.; Keil, P.; Hansen, M. R.; Edén, M. Improved Magnetization Transfers among Quadrupolar Nuclei in Two-Dimensional Homonuclear Correlation NMR Experiments Applied to Inorganic Network Structures. *Molecules* **2020**, *25* (2), 337. <https://doi.org/10.3390/molecules25020337>.
- (14) Wang, Q.; Hu, B.; Lafon, O.; Trébosc, J.; Deng, F.; Amoureux, J. P. Double-Quantum Homonuclear NMR Correlation Spectroscopy of Quadrupolar Nuclei Subjected to Magic-Angle Spinning and High Magnetic Field. *J. Magn. Reson.* **2009**, *200* (2), 251–260. <https://doi.org/10.1016/j.jmr.2009.07.009>.
- (15) Duong, N. T.; Lee, D.; Mentink-Vigier, F.; Lafon, O.; De Paëpe, G. On the Use of Radio-Frequency Offsets for Improving Double-Quantum Homonuclear Dipolar Recoupling of Half-Integer-Spin Quadrupolar Nuclei. *Magn. Reson. Chem.* **2021**, *n/a* (n/a), 1–18. <https://doi.org/10.1002/mrc.5142>.
- (16) Carravetta, M.; Edén, M.; Zhao, X.; Brinkmann, A.; Levitt, M. H. Symmetry Principles for the Design of Radiofrequency Pulse Sequences in the Nuclear Magnetic Resonance of Rotating Solids. *Chem. Phys. Lett.* **2000**, *321* (3), 205–215. [https://doi.org/10.1016/S0009-2614\(00\)00340-7](https://doi.org/10.1016/S0009-2614(00)00340-7).
- (17) Levitt, M. H. Symmetry-Based Pulse Sequences in Magic-Angle Spinning Solid State NMR. In *Encyclopedia of Nuclear Magnetic Resonance. Volume 9, Advances in NMR*; Grant, D. M., Harris, R. K., Eds.; Wiley, 2002; pp 165–196.
- (18) Oas, T. G.; Griffin, R. G.; Levitt, M. H. Rotary Resonance Recoupling of Dipolar Interactions in Solid-state Nuclear Magnetic Resonance Spectroscopy. *J. Chem. Phys.* **1988**, *89* (2), 692–695. <https://doi.org/10.1063/1.455191>.
- (19) Fu, R.; Smith, S. A.; Bodenhausen, G. Recoupling of Heteronuclear Dipolar Interactions in Solid State Magic-Angle Spinning NMR by Simultaneous Frequency and Amplitude Modulation. *Chem. Phys. Lett.* **1997**, *272* (5), 361–369. [https://doi.org/10.1016/S0009-2614\(97\)00537-X](https://doi.org/10.1016/S0009-2614(97)00537-X).
- (20) Wi, S.; Logan, J. W.; Sakellariou, D.; Walls, J. D.; Pines, A. Rotary Resonance Recoupling for Half-Integer Quadrupolar Nuclei in Solid State Nuclear Magnetic Resonance Spectroscopy. *J. Chem. Phys.* **2002**, *117* (15), 7024–7033. <https://doi.org/10.1063/1.1506907>.
- (21) Baldus, M.; Rovnyak, D.; Griffin, R. G. Radio-Frequency-Mediated Dipolar Recoupling among Half-Integer Quadrupolar Spins. *J. Chem. Phys.* **2000**, *112* (13), 5902–5909. <https://doi.org/10.1063/1.481187>.
- (22) Painter, A. J.; Duer, M. J. Double-Quantum-Filtered Nuclear Magnetic Resonance Spectroscopy Applied to Quadrupolar Nuclei in Solids. *J. Chem. Phys.* **2002**, *116* (2), 710–722. <https://doi.org/10.1063/1.1425831>.
- (23) Wang, Q.; Hu, B.; Lafon, O.; Trébosc, J.; Deng, F.; Amoureux, J.-P. Homonuclear Dipolar Recoupling under Ultra-Fast Magic-Angle Spinning: Probing 19F–19F Proximities by Solid State NMR. *J. Magn. Reson.* **2010**, *203* (1), 113–128. <https://doi.org/10.1016/j.jmr.2009.12.009>.
- (24) Edén, M. Two-Dimensional MAS NMR Correlation Protocols Involving Double-Quantum Filtering of Quadrupolar Spin-Pairs. *J. Magn. Reson.* **2010**, *204* (1), 99–110. <https://doi.org/10.1016/j.jmr.2010.02.007>.



- (25) Bak, M.; Rasmussen, J. T.; Nielsen, N. C. SIMPSON: A General Simulation Program for Solid State NMR Spectroscopy. *J. Magn. Reson.* **2000**, *147* (2), 296–330. <https://doi.org/10.1006/jmre.2000.2179>.
- (26) Antonijevic, S.; Ashbrook, S. E.; Biedasek, S.; Walton, R. I.; Wimperis, S.; Yang, H. Dynamics on the Microsecond Timescale in Microporous Aluminophosphate AlPO-14 as Evidenced by <sup>27</sup>Al MQMAS and STMAS NMR Spectroscopy. *J. Am. Chem. Soc.* **2006**, *128* (24), 8054–8062. <https://doi.org/10.1021/ja057682g>.
- (27) Petříček, V.; Dušek, M.; Palatinus, L. Crystallographic Computing System JANA2006: General features. *Z. Für Krist. - Cryst. Mater.* **2014**, *229* (5), 345–352. <https://doi.org/10.1515/zkri-2014-1737>.
- (28) Amoureux, J.-P.; Fernandez, C.; Steuernagel, S. ZFiltering in MQMAS NMR. *J. Magn. Reson. A* **1996**, *123* (1), 116–118. <https://doi.org/10.1006/jmra.1996.0221>.
- (29) States, D. J.; Haberkorn, R. A.; Ruben, D. J. A Two-Dimensional Nuclear Overhauser Experiment with Pure Absorption Phase in Four Quadrants. *J. Magn. Reson.* **1982**, *48* (2), 286–292. [https://doi.org/10.1016/0022-2364\(82\)90279-7](https://doi.org/10.1016/0022-2364(82)90279-7).
- (30) Amoureux, J.-P.; Fernandez, C. Triple, Quintuple and Higher Order Multiple Quantum MAS NMR of Quadrupolar Nuclei. *Solid State Nucl. Magn. Reson.* **1998**, *10* (4), 211–223. [https://doi.org/10.1016/S0926-2040\(97\)00027-1](https://doi.org/10.1016/S0926-2040(97)00027-1).
- (31) Kentgens, A. P. M. A Practical Guide to Solid State NMR of Half-Integer Quadrupolar Nuclei with Some Applications to Disordered Systems. *Geoderma* **1997**, *80* (3), 271–306. [https://doi.org/10.1016/S0016-7061\(97\)00056-6](https://doi.org/10.1016/S0016-7061(97)00056-6).
- (32) Stebbins, J. F.; Du, L.-S.; Kroeker, S.; Neuhoff, P.; Rice, D.; Frye, J.; Jakobsen, H. J. New Opportunities for High-Resolution Solid-State NMR Spectroscopy of Oxide Materials at 21.1- and 18.8-T Fields. *Solid State Nucl. Magn. Reson.* **2002**, *21* (1–2), 105–115. <https://doi.org/10.1006/snrmr.2001.0051>.
- (33) Kroeker, S.; Stebbins, J. F. Three-Coordinated Boron-11 Chemical Shifts in Borates. *Inorg. Chem.* **2001**, *40* (24), 6239–6246. <https://doi.org/10.1021/ic010305u>.
- (34) Hansen, M. R.; Vosegaard, T.; Jakobsen, H. J.; Skibsted, J. <sup>11</sup>B Chemical Shift Anisotropies in Borates from <sup>11</sup>B MAS, MQMAS, and Single-Crystal NMR Spectroscopy. *J. Phys. Chem. A* **2004**, *108* (4), 586–594. <https://doi.org/10.1021/jp030939h>.
- (35) Sen, S. Density Functional Theory Calculations of <sup>11</sup>B NMR Parameters in Crystalline Borates. *Mol. Simul.* **2008**, *34* (10–15), 1115–1120. <https://doi.org/10.1080/08927020802258716>.
- (36) Liu, H.; Liu, Q.; Wang, M.; Zhao, X. Second-Order Non-Linear Optical Studies on CdS Microcrystallite-Doped Alkali Borosilicate Glasses. *J. Phys. Chem. Solids* **2007**, *68* (5), 963–967. <https://doi.org/10.1016/j.jpcs.2007.01.046>.
- (37) Bengisu, M. Borate Glasses for Scientific and Industrial Applications: A Review. *J. Mater. Sci.* **2016**, *51* (5), 2199–2242. <https://doi.org/10.1007/s10853-015-9537-4>.
- (38) Mariselvam, K.; Kumar, R. A. Borate Glasses for Luminescence Applications - Potential Materials for White LEDs and Laser Sources. *Univers. J. Chem.* **2016**, *4* (2), 55–64. <https://doi.org/10.13189/ujc.2016.040202>.

- (39) Adamiv, V. T.; Burak, Ya. V.; Gamernyk, R. V.; Romanyuk, G. M.; Teslyuk, I. M. Optical Properties, Electronic Polarizability and Optical Basicity of Lithium Borate Glasses. *Phys. Chem. Glas. - Eur. J. Glass Sci. And Technology Part B* **2011**, 52 (4), 152–156.
- (40) Chen, B.; Werner-Zwanziger, U.; Nascimento, M. L. F.; Ghussn, L.; Zanotto, E. D.; Zwanziger, J. W. Structural Similarity on Multiple Length Scales and Its Relation to Devitrification Mechanism: A Solid-State NMR Study of Alkali Diborate Glasses and Crystals. *J. Phys. Chem. C* **2009**, 113 (48), 20725–20732. <https://doi.org/10.1021/jp907259e>.
- (41) Barrow, N. S.; Yates, J. R.; Feller, S. A.; Holland, D.; Ashbrook, S. E.; Hodgkinson, P.; Brown, S. P. Towards Homonuclear J Solid-State NMR Correlation Experiments for Half-Integer Quadrupolar Nuclei: Experimental and Simulated  $^{11}\text{B}$  MAS Spin-Echo Dephasing and Calculated 2JBB Coupling Constants for Lithium Diborate. *Phys. Chem. Chem. Phys.* **2011**, 13 (13), 5778. <https://doi.org/10.1039/c0cp02343d>.
- (42) Kirfel, A.; Will, G.; Stewart, R. F. The Chemical Bonding in Lithium Metaborate,  $\text{LiBO}_2$ . Charge Densities and Electrostatic Properties. *Acta Crystallogr. B* **1983**, 39 (2), 175–185. <https://doi.org/10.1107/S0108768183002256>.
- (43) Vorotilova, L. S.; Dmitrieva, L. V.; Samoson, A. V. NMR Spectral Study of Two Crystalline Modifications of Lithium Metaborate,  $\text{LiBO}_2$ . *J. Struct. Chem.* **1989**, 30 (5), 756–759. <https://doi.org/10.1007/BF00763796>.
- (44) Kuhn, A.; Tobschall, E.; Heitjans, P. Li Ion Diffusion in Nanocrystalline and Nanoglassy  $\text{LiAlSi}_2\text{O}_6$  and  $\text{LiBO}_2$  - Structure Dynamics Relations in Two Glass Forming Compounds. *Z. Für Phys. Chem. 223 2009* **2009**, 223, 1359–1377. <https://doi.org/10.15488/2264>.
- (45) Massiot, D.; Fayon, F.; Capron, M.; King, I.; Calvé, S. L.; Alonso, B.; Durand, J.-O.; Bujoli, B.; Gan, Z.; Hoatson, G. Modelling One- and Two-Dimensional Solid-State NMR Spectra. *Magn. Reson. Chem.* **2002**, 40 (1), 70–76. <https://doi.org/10.1002/mrc.984>.
- (46) Fernandez, C.; Amoureux, J. P.; Chezeau, J. M.; Delmotte, L.; Kessler, H.  $^{27}\text{Al}$  MAS NMR Characterization of  $\text{AlPO}_4$ -14 Enhanced Resolution and Information by MQMAS Dr. Hellmut G. Karge on the Occasion of His 65th Birthday. *Microporous Mater.* **1996**, 6 (5), 331–340. [https://doi.org/10.1016/0927-6513\(96\)00040-5](https://doi.org/10.1016/0927-6513(96)00040-5).
- (47) Sasaki, A.; Trébosc, J.; Amoureux, J.-P. A Comparison of Through-Space Population Transfers from Half-Integer Spin Quadrupolar Nuclei to  $^1\text{H}$  Using MQ-HETCOR and MQ-SPAM-HETCOR under Fast MAS. *J. Magn. Reson.* **2021**, 329, 107028. <https://doi.org/10.1016/j.jmr.2021.107028>.

---

## **CHAPTER 4**

---



# Chapter 4: Boron nitride and oxide coated dendritic fibrous nanosilica for oxidative dehydrogenation: Insights into the catalytic sites from solid-state NMR

---

## 4.1 STATEMENT OF CONTRIBUTION

Chapter 4 of this thesis is based on a publication in *ACS Sustainable Chemistry and Engineering*,<sup>1</sup> for which I am a co-author together with: Andrew G. M. Rankin, Julien Trébosc and Olivier Lafon from the University of Lille, and our collaborators from the Tata Institute of Fundamental Research and the National Chemical Laboratory in India: Rajesh Belgamwar, Ayan Maity, Amit Kumar Mishra, Chathakudath P. Vinod and Vivek Polshettiwar. The co-authors from the University of Lille were in charge of carrying out the solid-state NMR characterization and strongly contributed to the writing of the article. My contribution to this article was to participate to the NMR experimentation, analysis of results and helping with the writing and editing of the paper. The co-authors from India, were in charge of the synthesis of DFNS/BN and DFNS/B<sub>2</sub>O<sub>3</sub> materials and their characterization by SEM, TEM, XRD and XPS, as well as performing the catalytic activity tests, and assisting with the writing of the article. All the authors contributed equally to the editing of the article.

This chapter focuses primary on the solid-state NMR study of the DFNS/BN and DFNS/B<sub>2</sub>O<sub>3</sub> catalysts along with insights into their structures.

## 4.2 INTRODUCTION

The catalytic oxidative dehydrogenation (ODH) of alkanes to produce alkenes is an important process in the modern chemical industry.<sup>2-5</sup> An important product of this reaction is propene, which is a very important building block for a large number of chemical products, such as the widely used poly(propylene) polymer. It is also used to produce a large quantity of other useful chemicals, such as acrolein, acrylonitrile, cumene, propylene oxide and butyraldehyde.<sup>2,6</sup> However, even after decades of research, propene selectivity remains too low due to over-oxidation of propene

producing CO<sub>2</sub> emission.<sup>4</sup> Consequently, there is an urgent need for a heterogeneous catalytic process which can convert propane to propene at low temperatures and with good selectivity. The discovery of boron-based catalysts, such as boron nitride (*h*-BN) and boron nitride nanotubes (BNNT), with highly favourable catalytic properties, provided an alternative route for the production of olefins from alkanes, which is more sustainable than the conventional protocol.<sup>7,8</sup>

For these boron-based catalysts, it was hypothesized that the oxidised edges were the catalytic active sites.<sup>6</sup> Additional studies on various boron-containing materials with oxidised surfaces supported that assumption.<sup>9–12</sup> In particular, <sup>11</sup>B solid-state NMR and in operando infrared spectroscopies showed the oxidation of *h*-BN surface under ODH conditions.<sup>10,12</sup> DFT calculations also proved that the formation of a disordered boron oxide phase at the surface of *h*-BN is feasible.<sup>13</sup> More recently it has been shown that boron oxide supported on mesoporous silica or silica nanoparticles can catalyze the ODH of propane.<sup>14,15</sup> Conversely, it was shown that zeolites containing isolated BO<sub>3</sub> units incorporated into the zeolite framework shows no catalytic activity for the ODH of propane to propene and the catalysis of ODH reaction requires the presence of aggregated boron sites.<sup>16</sup>

In this work, new boron nitride supported on dendritic fibrous nanosilica (DFNS/BN) catalysts are introduced for the ODH of propane. DFNS as support provides highly accessible large surface area owing to its unique fibrous morphology, for which the internal surface is more accessible than the porous structures found in, for example, in MCM-41 and SBA-15 type materials.<sup>17–19</sup> DFNS/BN showed increased catalytic properties with respect to *h*-BN, as well as improved stability and selectivity. DFNS/B<sub>2</sub>O<sub>3</sub> also showed catalytic activity for the ODH of propane but with decreased selectivity compared to DFNS/BN. This dissertation seeks to investigate the structures of both DFNS/BN and DFNS/B<sub>2</sub>O<sub>3</sub> by solid-state NMR through a combination of 1D and 2D multinuclear (<sup>1</sup>H, <sup>29</sup>Si, <sup>11</sup>B) solid-state NMR experiments. The local atomic environments of the DFNS supported BN and B<sub>2</sub>O<sub>3</sub> catalysts are studied by solid-state NMR spectroscopy, a technique that has been extensively demonstrated to be a powerful probe of the local structure of materials.<sup>20–24</sup> Indeed, the successful use of solid-state NMR to better understand catalytic sites and catalytic mechanisms has been proven.<sup>25–27</sup>

The present work has sought to determine which the active phase of DFNS/BN catalysts is and how the BN and B<sub>2</sub>O<sub>3</sub> phases are anchored in the SiO<sub>2</sub> support in these materials.

### 4.3 STATE OF THE ART

#### 4.3.1 Catalysts for ODH of light alkanes

The dehydrogenation reaction of alkanes to produce alkenes is an important process in the modern chemical industry.<sup>2,4</sup> The products from this reaction such as ethylene (named ethene according to IUPAC nomenclature) and propylene (also named propene) are the building blocks for various chemicals including polymers and fine chemicals.<sup>4,5</sup> Therefore, the amount of ethene or propene production is an indicator of the scale of a chemical industry.<sup>4</sup> Currently, 10% of the global propene production is obtained *via* propane dehydrogenation (PDH), which is considered economically and environmentally viable.<sup>3</sup> This reaction can be categorized in two routes depending on whether the oxidant is used or not, which are called oxidative or direct dehydrogenation, respectively.<sup>4</sup> The direct dehydrogenation (DH) is a thermodynamically limited reaction with endothermic properties. The conventional catalysts that are used for DH include Pt- and Cr-based oxides. However, the coke formation during the process deactivates the catalysts.<sup>5</sup> Conversely, for the oxidative dehydrogenation (ODH) (Fig. 52), which is an exothermic reaction, the introduction of an oxidant (e.g. O<sub>2</sub>) raises the thermodynamics limit and prevents coke formation. Nevertheless, the main drawback of ODH is its low selectivity of the desired olefin.<sup>4</sup>

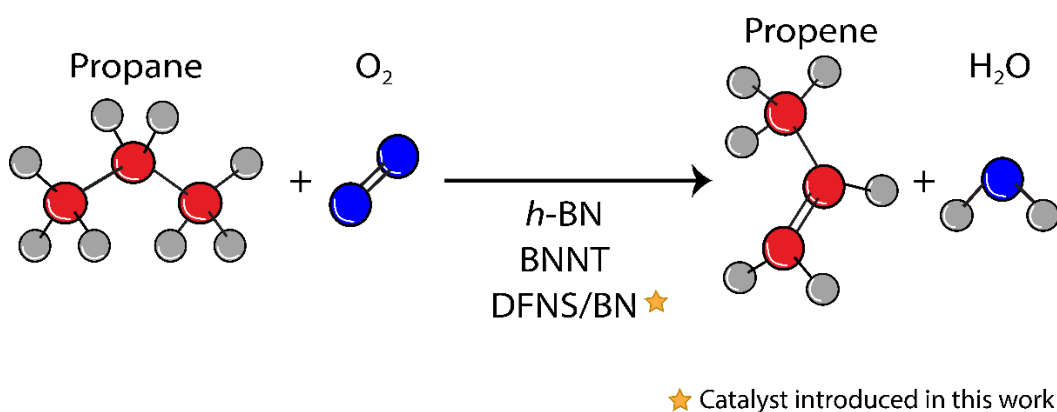


**Figure 52.** Schematic representation of the ODH of propane to propene.

In the past few decades, considerable efforts have been made to develop efficient catalytic systems for the ODH reaction of light alkanes, which mostly used transition metal oxides (e.g.,  $V_2O_5$ ,  $MoO_3$ , and  $NiO$ ) and alkaline-earth metal oxychlorides.<sup>3,4</sup> These metal-based catalysts displayed high reactivity towards the oxidative conversion of alkanes, but suffered from oxidation to  $CO_x$  and thus leading to  $CO_2$  emission.<sup>3</sup> The recent discovery of metal-free boron-based catalysts, such as *h*-BN and BNNTs, with high selectivity and activity to olefins and with reduced formation of  $CO_2$ , has revolutionized the catalytic oxidative dehydrogenation and paved a new route to the selective cleavage of C-H bonds.<sup>3,6,8,11</sup> Subsequently, a series of boron-based catalysts have been prepared with similar performance to *h*-BN which has been the referent for this reaction.<sup>8,9,15</sup> However, there is a need for further understanding of the catalytic mechanisms and nature of the active sites.<sup>3,4</sup>

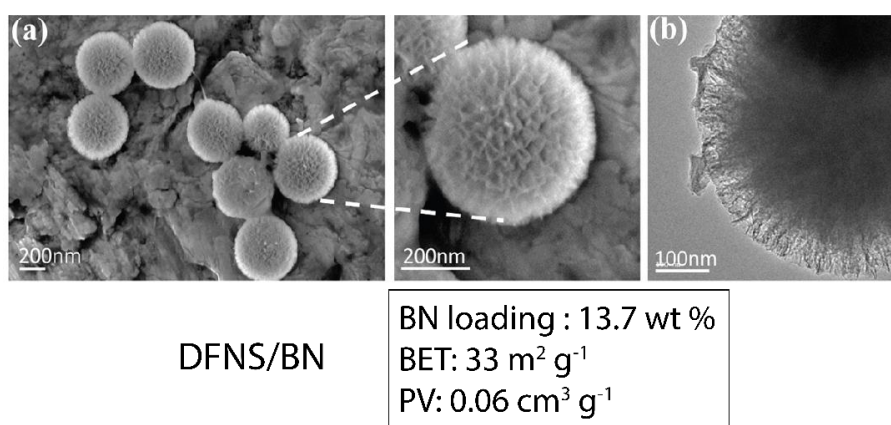


**Figure 53.** Fibrous morphology of DFNS/BN revealed by (a) SEM and (b) TEM. The BN loading and textural properties of this material is described below.

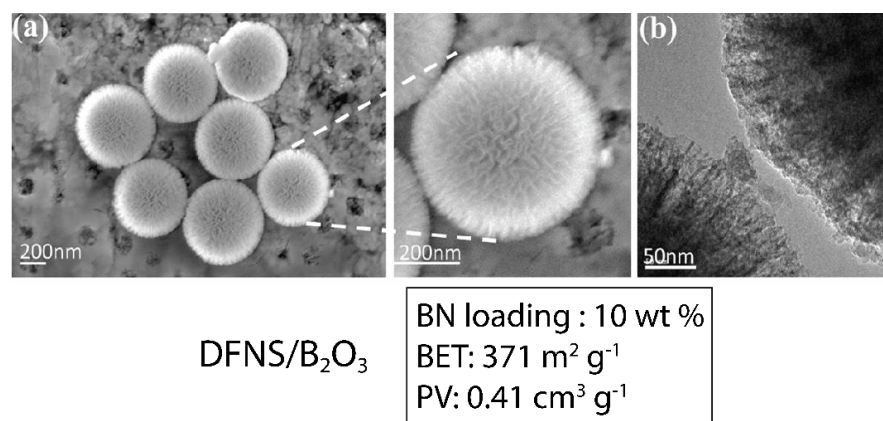


**Figure 54.** Fibrous morphology of DFNS/B<sub>2</sub>O<sub>3</sub> revealed by (a) SEM and (b) TEM. The BN loading and textural properties of this material is described below.



In this work, new boron-based catalysts supported on dendritic fibrous nanosilica DFNS are introduced for the oxidative dehydrogenation (ODH) of propane. BN supported on DFNS (hereafter DFNS/BN) and B<sub>2</sub>O<sub>3</sub> supported on DFNS (hereafter DFNS/B<sub>2</sub>O<sub>3</sub>) present unique fibrous morphology (Figs. 53 and 54) and their textural properties were studied (not shown). They were tested for the ODH of propane to propene (section 4.3.2) and their structures studied by solid-state NMR. (section 4.5).

### 4.3.2 Catalytic activity of DFNS/BN and DFNS/B<sub>2</sub>O<sub>3</sub>

The catalytic properties of DFNS/BN and DFNS/B<sub>2</sub>O<sub>3</sub> were examined for the oxidative dehydrogenation (ODH) of propane. They were studied using a fixed bed micro-activity flow reactor under atmospheric pressure (1 bar) at 490 °C. The catalytic activity of these samples was evaluated in terms of conversion and productivity. These measurements were performed by our collaborators in India.

It was found that during 19 h, DFNS/BN is moderately stable at the studied temperature (490 °C) and that the conversion percentage decreases by ~18%. This catalyst then exhibits a selectivity of around 59.4% for propene and around 16.5% for ethene (Fig. 55a). In terms of productivity, significant amounts of propene (38360 μmol.g<sub>cat</sub><sup>-1</sup>.h<sup>-1</sup>) and ethene (10657 μmol.g<sub>cat</sub><sup>-1</sup>.h<sup>-1</sup>) were produced. However, it was observed that the productivity towards propene decreased with the reaction time which indicates the formation of coke on the catalyst surface (Fig. 55b). It is required a separate study to understand this phenomenon, but it is not part of the scope of this manuscript.

On the other hand, it was observed that DFNS/B<sub>2</sub>O<sub>3</sub> was also stable for 19 h, with a selectivity around 17.9% for propene and 6.8% for ethene, and more than 70% for CO<sub>x</sub> with  $x = 1$  or 2, with a conversion rate of 24.8% (Fig. 55c). The high selectivity towards the CO when using DFNS/B<sub>2</sub>O<sub>3</sub> needs further investigation. However, this is not part of the scope of this manuscript. In terms of productivity, this catalyst showed a good performance towards propene (19520 μmol g<sub>cat</sub><sup>-1</sup> h<sup>-1</sup>) and ethene (7441 μmol.g<sub>cat</sub><sup>-1</sup>.h<sup>-1</sup>), which are almost half of the productivities obtained with DFNS/BN (Fig. 55d). This fact indicates that B<sub>2</sub>O<sub>3</sub> is catalytically active for propane dehydrogenation, although to a lesser extent than BN supported on DFNS.

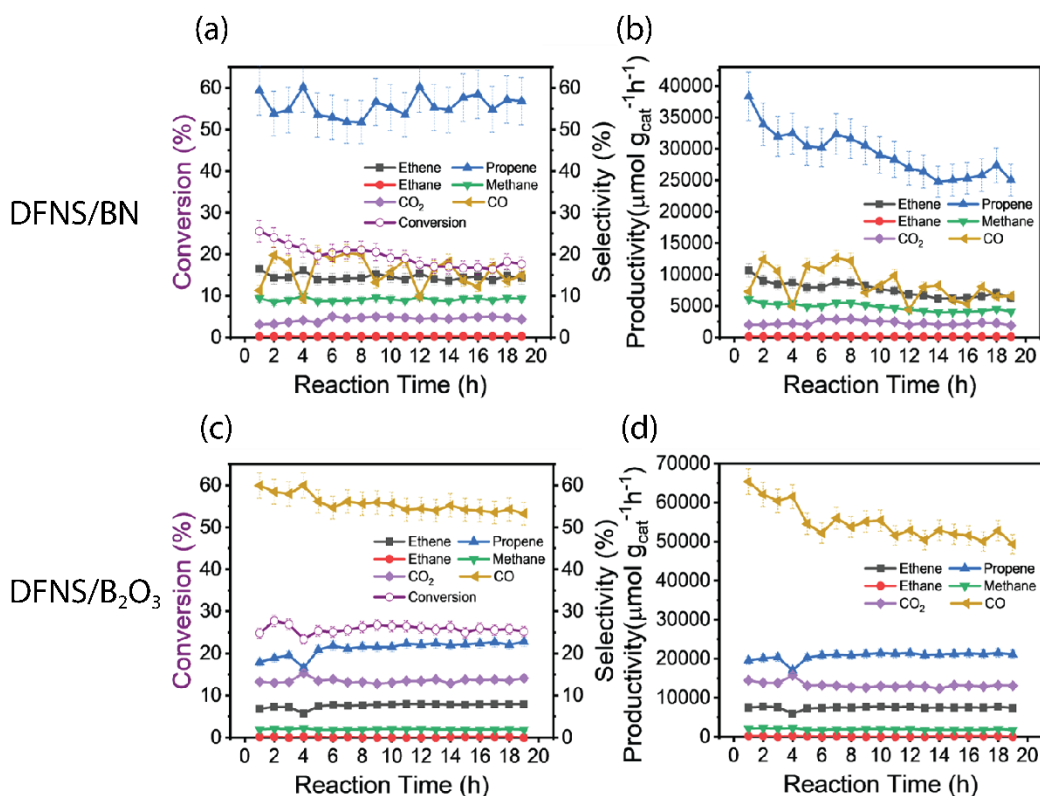


**Figure 55.** (a, c) Conversion and selectivity for propane dehydrogenation at 490 °C and (b, d) productivity for the same reaction and temperature using (a, b) DFNS/BN and (c, d) DFNS/B<sub>2</sub>O<sub>3</sub>.

The catalytic properties of DFNS/BN and DFNS/B<sub>2</sub>O<sub>3</sub> were compared with those of the other widely used catalysts for ODH of propane. *h*-BN catalysts can convert propane into propene with high selectivity, but the productivity is lower than that obtained with DFNS/BN and DFNS/B<sub>2</sub>O<sub>3</sub> or the other tested catalysts. It was found that DFNS/BN exhibits a better performance than *h*-BN in terms of propane conversion and propene productivity, while BNNT showed better propene productivity compared to DFNS/BN (Fig. 56). DFNS/B<sub>2</sub>O<sub>3</sub> also displayed better conversion and selectivity than *h*-BN, but in general, exhibits lower productivity towards propene compared to B<sub>2</sub>O<sub>3</sub> supported on SBA-15 (BOS-10) and BNNT. The better performance of both DFNS/BN and DFNS/B<sub>2</sub>O<sub>3</sub> for ODH of propane can be attributed to the highly accessible active sites as a result of the fibrous morphology and high surface area that DFNS provides as a support. Besides, these DFNS/BN and DFNS/B<sub>2</sub>O<sub>3</sub> supported catalysts showed better performance than vanadium (V) supported on silica, which is one of the best-known silica-supported catalysts for this

reaction (Table 15).<sup>2</sup> This result shows the high performance of the introduced catalysts and its potential application for the ODH of light alkanes.

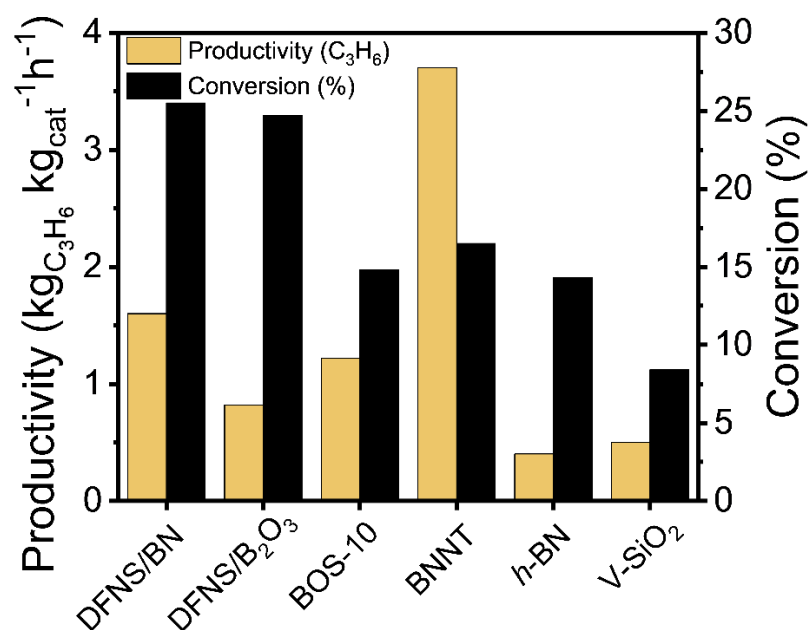


**Figure 56.** Comparison of DFNS/BN and DFNS/B<sub>2</sub>O<sub>3</sub> with a selection of previously reported unsupported and supported catalysts for propane dehydrogenation.<sup>6,14</sup>

**Table 15.** Comparison of conventional catalysts with DFNS/BN and DFNS/B<sub>2</sub>O<sub>3</sub> for propane dehydrogenation.<sup>6,14</sup>

Name of catalyst	Temperature (°C)	WHSV <sup>-1</sup> (kg <sub>cat</sub> mol <sub>C<sub>3</sub>H<sub>8</sub></sub> <sup>-1</sup> )	Conversion (%)	Productivity (g <sub>olefin</sub> g <sub>cat</sub> <sup>-1</sup> h <sup>-1</sup> )	Reference
DFNS/BN	490	1.47	25.5	1.9	This work
DFNS/B <sub>2</sub> O <sub>3</sub>	490	1.47	24.7	1.0	This work
BOS-10	450	0.18	14.8	1.2	78
BNNT	490	2-4	16.5	~4.1	5
h-BN	490	15-40	14.3	~0.4	5
V-SiO <sub>2</sub>	490	5-15	8.4	~0.5	5

As seen in Figs. 55 and 56, DFNS/BN displays higher catalytic activity than *h*-BN, while DFNS/B<sub>2</sub>O<sub>3</sub> also shows catalytic activity for ODH of propane, although with lower selectivity and productivity than DFNS/BN. This dissertation seeks to investigate the structures of both DFNS/BN and DFNS/B<sub>2</sub>O<sub>3</sub> by solid-state NMR through a combination of 1D and 2D experiments, in order to understand what the

active phase of DFNS/BN is and how the BN and B<sub>2</sub>O<sub>3</sub> phases are anchored on the SiO<sub>2</sub> support. The aim of this study is to correlate the atomic structures to the catalytic performance.

#### 4.4 SOLID-STATE NMR EXPERIMENTS

For all solid-state NMR experiments, rotors were packed inside an argon-atmosphere glovebox to prevent contact with moisture. <sup>11</sup>B chemical shifts were referenced using a solid sample of NaBH<sub>4</sub> ( $\delta_{\text{iso}} = -42.05$  ppm), whereas <sup>1</sup>H and <sup>29</sup>Si chemical shifts were referenced using neat tetramethylsilane (TMS) ( $\delta_{\text{iso}} = 0$  ppm).

##### 4.4.1 Samples

A set of three samples were used for the solid-state NMR analyses: i) boron nitride supported on dendritic fibrous nanosilica, which was prepared using a solution-phase deposition process (as-prepared DFNS/BN hereafter); ii) boron oxide supported on dendritic fibrous nanosilica, which was prepared using solid-phase deposition techniques (as-prepared DFNS/B<sub>2</sub>O<sub>3</sub> hereafter), and iii) DFNS/BN after catalysis. These samples were prepared by our collaborators in India.

##### 4.4.2 Experiments at 9.4 T

<sup>1</sup>H→<sup>29</sup>Si CP MAS NMR experiments were recorded at  $B_0 = 9.4$  T ( $\nu_0 = 400$  MHz for <sup>1</sup>H) with a wide-bore magnet equipped with a Bruker AVANCE II console, using a 3.2 mm triple-resonance HXY magic angle spinning (MAS) probe operated in double resonance mode. The samples were spun at a MAS rate,  $\nu_R = 10$  kHz. The initial  $\pi/2$  pulse lasted 2  $\mu$ s and was followed by a CP contact time equal to 8 ms. During the CP transfer, the RF nutation frequency on the <sup>29</sup>Si channel was constant and equal to 50 kHz, while the <sup>1</sup>H nutation frequency was linearly ramped from 36 to 40 kHz. The <sup>1</sup>H→<sup>29</sup>Si CP MAS spectra were recorded using recycle intervals of 1.95 s (as-prepared DFNS/BN), 17 s (as-prepared DFNS/B<sub>2</sub>O<sub>3</sub>) or 27.29 s (DFNS/BN after catalysis) and were the result of averaging 4096 (as-prepared DFNS/BN and DFNS/B<sub>2</sub>O<sub>3</sub>) or 7200 transients (DFNS/BN after catalysis). SPINAL <sup>1</sup>H decoupling<sup>28</sup> (~125 kHz) was applied during acquisition. The Hartmann-Hahn condition<sup>29,30</sup> was calibrated using a powdered sample of octakis(trimethylsiloxy)silsesquioxane (Q8M8).

### 4.4.3 Experiments at 18.8 T

All experiments at  $B_0 = 18.8$  T ( $\nu_0 = 800$  MHz for  $^1\text{H}$ ) were performed with a narrow-bore magnet equipped with a Bruker AVANCE NEO console. One-dimensional (1D)  $^1\text{H}$  and  $^{11}\text{B}$  experiments were acquired at  $\nu_R = 20$  kHz, using 3.2 mm double-resonance  $^{11}\text{B}$ - $^{31}\text{P}$  (featuring an MgO stator block to prevent  $^{11}\text{B}$  background signal) and 3.2 mm double-resonance HX probes for  $^{11}\text{B}$  and  $^1\text{H}$  experiments, respectively.  $^1\text{H}$  NMR spectra were acquired by averaging 16 transients separated by a recycle interval of 3 s, using the DEPTH pulse sequence for probe background suppression,<sup>31</sup> with  $\nu_1 \approx 93$  kHz. Quantitative  $^{11}\text{B}$  NMR spectra were acquired by using single-pulse NMR experiments with a pulse length of 0.5  $\mu\text{s}$  and an RF field strength of 71 kHz, corresponding to a short tip angle.<sup>32</sup> The quantitative  $^{11}\text{B}$  NMR spectra were acquired by averaging 2 (pure hexagonal (h) BN), 4096 (as-prepared DFNS/BN and DFNS/B<sub>2</sub>O<sub>3</sub>) or 16 (DFNS/BN after catalysis) transients, separated by a recycle interval of 1 (as-prepared DFNS/BN and DFNS/B<sub>2</sub>O<sub>3</sub>), 0.8 (DFNS/BN after catalysis) or 586 s (pure h-BN).

Two-dimensional (2D)  $^{11}\text{B}$  MQMAS spectra were obtained using the z-filtered sequence<sup>33</sup> at  $\nu_R = 20$  kHz, with a 3.2 mm HX probe. Excitation and conversion pulses lasted  $\tau_p = 6.5$  and 2  $\mu\text{s}$  with  $\nu_1 \approx 100$  kHz and the central transition (CT) selective pulse lasted 12.5  $\mu\text{s}$  with  $\nu_1 \approx 20$  kHz. SPINAL  $^1\text{H}$  decoupling<sup>28</sup> ( $\sim 100$  kHz) was applied during acquisition. Spectra are the result of averaging 240 (as-prepared DFNS/BN), 1032 (as-prepared DFNS/B<sub>2</sub>O<sub>3</sub>) or 1704 (DFNS/BN after catalysis) transients separated by a recycle delay of 1 (as-prepared DFNS/B<sub>2</sub>O<sub>3</sub> and DFNS/BN after catalysis) or 3.5 s (as-prepared DFNS/BN) for each of the 256 (as-prepared DFNS/BN) or 32 (as-prepared DFNS/B<sub>2</sub>O<sub>3</sub> and DFNS/BN after catalysis)  $t_1$  increments of 25 (as-prepared DFNS/BN) or 50  $\mu\text{s}$  (as-prepared DFNS/B<sub>2</sub>O<sub>3</sub> and DFNS/BN after catalysis). The quadrature detection method of States *et al.*<sup>34</sup> was used to achieve sign discrimination in the indirect dimension. After acquisition, a 2D Fourier transformation followed by a shearing transformation was performed to obtain a spectrum where the contour ridges were parallel to  $F_2$ , allowing the isotropic spectrum to be obtained directly from a projection onto  $F_1$ .<sup>35</sup>

$^{11}\text{B}\{-^1\text{H}\}$  *D*-HMQC experiments with  $^{11}\text{B}$  detection were acquired at  $\nu_{\text{R}} = 20$  kHz with a 3.2 mm triple-resonance HX probe.<sup>36,37</sup> The  $^1\text{H}\text{-}^{11}\text{B}$  dipolar couplings were reintroduced by applying SR4<sub>1</sub><sup>2</sup> scheme on the  $^1\text{H}$  channel.<sup>38</sup> The total duration of the two SR4<sub>1</sub><sup>2</sup> recoupling blocks was  $\tau_D = 0.75$  ms. The  $^1\text{H}$  RF nutation frequencies of the  $\pi/2$  pulses and SR4<sub>1</sub><sup>2</sup> recoupling were equal to  $\nu_1 \approx 100$  and 40 kHz, respectively.  $^{11}\text{B}$  CT selective pulses were applied with  $\nu_1 \approx 20$  kHz. Spectra are the result of averaging 16 (as-prepared DFNS/BN), 32 (as-prepared DFNS/B<sub>2</sub>O<sub>3</sub>) or 128 (DFNS/BN after catalysis) transients separated by a recycle interval of 2 (as-prepared DFNS/BN and DFNS/BN after catalysis) or 1 s (as-prepared DFNS/B<sub>2</sub>O<sub>3</sub>) for each of the 46 (as-prepared DFNS/BN), 100 (as-prepared DFNS/B<sub>2</sub>O<sub>3</sub>) or 44 (DFNS/BN after catalysis)  $t_1$  increments of 50  $\mu\text{s}$ . The States-TPPI quadrature detection method<sup>39</sup> was used to achieve sign discrimination in the indirect dimension.

2D  $^{11}\text{B}\{-^{29}\text{Si}\}$  *D*-HMQC experiments were acquired with a 3.2 mm triple-resonance HXY triple-gamma probe at  $\nu_{\text{R}} = 14.286$  kHz. The  $^{11}\text{B}\text{-}^{29}\text{Si}$  dipolar couplings were reintroduced the SFAM<sub>1</sub> dipolar recoupling scheme on the  $^{29}\text{Si}$  channel.<sup>40</sup> This experiment was calibrated using a sample of  $^{29}\text{Si}$ -enriched borosilicate glass.<sup>41</sup> The total duration of the two SFAM<sub>1</sub> recoupling blocks was  $\tau_D = 2$  ms.  $^{29}\text{Si}$   $\pi/2$  pulses were applied with  $\nu_1 \approx 59$  kHz and  $^{11}\text{B}$  CT selective pulses were applied with  $\nu_1 \approx 17$  kHz. The peak values of the frequency and amplitude sweeps of SFAM<sub>1</sub> on  $^{29}\text{Si}$  channel were  $(\nu_{\text{ref}}^{\text{max}}, \nu_1^{\text{max}}) = (70, 57)$  kHz. The double frequency sweep (DFS) method<sup>42</sup> was used in order to enhance the polarisation of the central transition (CT) by the manipulation of the populations of the satellite transitions (ST). The DFS pulse lasted 2 ms and used  $\nu_1 \approx 17$  kHz. During the DFS pulse, the frequencies of the rf spikelets were linearly swept in a symmetric manner from 1 to 85.8 kHz with respect to the CT. Spectra are the result of averaging 448 (DFNS/BN) or 1024 (DFNS/B<sub>2</sub>O<sub>3</sub>) transients separated by a recycle interval of 4 s for each of the 32 (DFNS/BN) or 42 (DFNS/B<sub>2</sub>O<sub>3</sub>)  $t_1$  increments of 35  $\mu\text{s}$ . The States-TPPI quadrature detection method<sup>39</sup> was used to achieve sign discrimination in the indirect dimension. Data processing was carried out using Bruker TopSpin (version 4.0.8) and ssNake (version 1.1).<sup>43</sup>

## 4.5 RESULTS AND DISCUSSION

### 4.5.1 Probing $^1\text{H}$ and $^{11}\text{B}$ environments and their proximities

The 1D  $^1\text{H}$  and  $^{11}\text{B}$  spectra on DFNS/BN (as-prepared and after catalysis) and as-prepared DFNS/ $\text{B}_2\text{O}_3$  are shown in Fig. 57. The  $^1\text{H}$  NMR spectrum of as-prepared DFNS/BN is dominated by a peak at 6.8 ppm and also exhibits a broad resonance with a maximal intensity at 4.3 ppm extending down to 0 ppm (Fig. 57a). The peak at 6.8 ppm is assigned to hydroxyl groups on the edge of BN sheets.<sup>44–46</sup> This signal can also subsume contributions from the  $\text{NB}_2\text{H}$  sites of the armchair edges of BN sheets as well as  $\text{BO}_3\text{OH}$  moieties since the reported isotropic chemical shifts,  $\delta_{\text{iso}}$ , of these sites are *ca.* 6 and 8 ppm, respectively.<sup>15,46</sup> The broad signal centred at 4.3 ppm subsumes the contributions of adsorbed water,<sup>47–50</sup>  $\text{BO}_2\text{OH}$  sites having  $\delta_{\text{iso}}$  values ranging from 5 to 2.7 ppm depending on the formation of hydrogen bonds and the nature of the second neighbour, B or Si,<sup>14–16,51,52</sup> the  $\text{NB}_2\text{H}$  sites of the zigzag edges of BN sheets resonating at *ca.* 3 ppm,<sup>46</sup> and silanol groups with  $\delta_{\text{iso}}$  values ranging from 3 to 1.6 ppm depending on the formation of hydrogen bonds and the nature of the second neighbour, B or Si.<sup>14–16,47,48,51,52</sup>

The  $^1\text{H}$  NMR spectrum of DFNS/BN after catalysis shown in Fig. 57b displays a broad peak centred at 4.4 ppm, which subsumes the contribution of adsorbed water,  $\text{BO}_2\text{OH}$  sites and silanol groups. The peak at 0.1 ppm arises from coke formation or the surface residual organic species. The marked reduction in the intensity of the resonance at 6.5 ppm indicates the conversion of BN into  $\text{B}_2\text{O}_3$ . This fact is in agreement with the results obtained with XPS and powder X-ray diffraction (PXRD) (not shown) and further confirms the conversion of BN into  $\text{B}_2\text{O}_3$ . The  $^1\text{H}$  spectrum of as-prepared DFNS/ $\text{B}_2\text{O}_3$  shown in Fig. 57c exhibits peaks at 2.9 and 1.7 ppm, which are ascribed to  $\text{BO}_2\text{OH}$  and isolated silanol sites, respectively. Silanol groups close to B atoms with  $\delta_{\text{iso}}$  values ranging from 2.2 to 2.7 ppm can contribute to the  $^1\text{H}$  signal.<sup>16,52–54</sup> The peak at 0 ppm is due to mobile residual organic species. The higher chemical shift of  $\text{BO}_2\text{OH}$  signal for DFNS/BN after catalysis than for as-prepared DFNS/ $\text{B}_2\text{O}_3$  could result from the larger amount of hydrogen-bonded  $\text{BO}_2\text{OH}$  sites.<sup>15</sup>

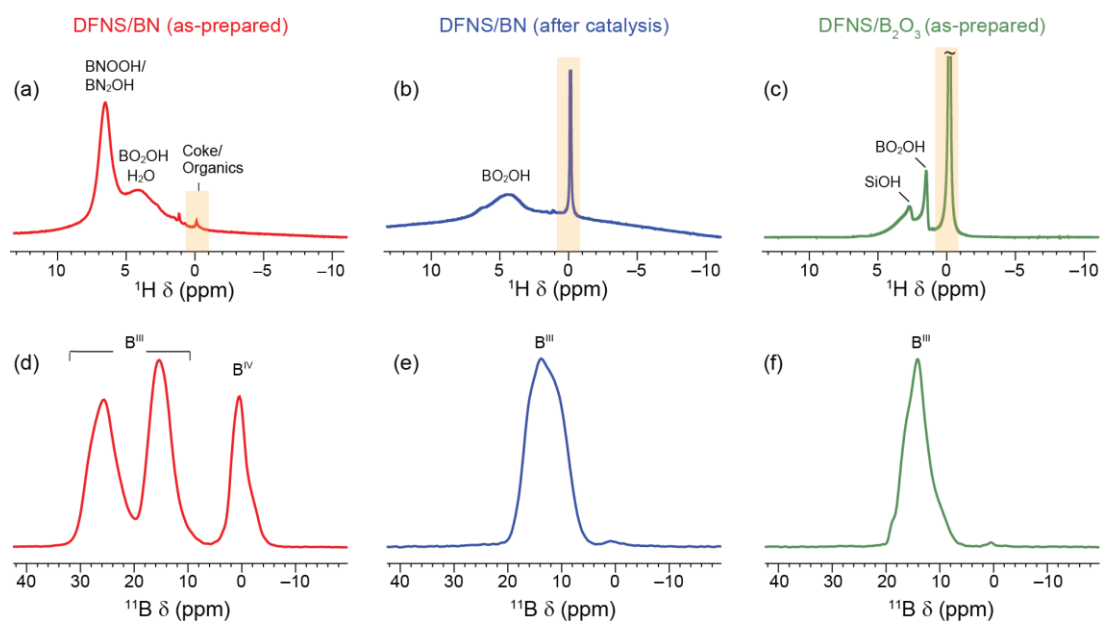


**Figure 57.** 1D (a, b, c)  $^1\text{H}$  DEPTH and (d, e, f)  $^{11}\text{B}$  quantitative (short tip angle) MAS NMR spectra of (a, d) as-prepared DFNS/BN, (b, e) DFNS/BN after catalysis and (c, f) as-prepared DFNS/ $\text{B}_2\text{O}_3$ . Experiments were recorded at  $B_0 = 18.8$  T with  $\nu_R = 20$  kHz.

1D  $^{11}\text{B}$  NMR data for the three aforementioned samples is presented in Figure 57d, e and f. The spectrum of as-prepared DFNS/BN (see Figure 57d) shows three broad signals with centres of gravity at *ca.* 0, 15 and 26 ppm. The signal at  $\sim 26$  ppm is assigned to tri-coordinated ( $\text{B}^{\text{III}}$ ) boron species of type  $\text{BN}_3$ ,  $\text{BN}_2\text{O}$  and  $\text{BNO}_2$  since these sites have  $\delta_{\text{iso}}$  values of 30, 27-28 and 20-24 ppm, respectively and quadrupolar coupling constant  $C_Q = 2.7\text{-}2.9$  MHz.<sup>10,15,55,56</sup> The  $\text{BN}_2\text{O}$  and  $\text{BNO}_2$  sites are located on the edges of the BN sheets. The signal at  $\sim 15$  ppm is assigned to tri-coordinated  $\text{BO}_3$  environments.<sup>14,15,52,54,57-61</sup> The signal at  $\sim 0$  ppm is assigned to tetra-coordinated ( $\text{B}^{\text{IV}}$ )  $\text{BO}_4$  environments.<sup>52,54,57,58,62</sup> The  $^{11}\text{B}$  spectrum being quantitative, the integrated intensities of the different signals indicates that BN sheets contains 37% of boron atoms, the remaining ones forming boron oxide phases as the result of the oxidation of BN sheets. The spectra of DFNS/BN after catalysis and as-prepared DFNS/ $\text{B}_2\text{O}_3$  (Fig. 57e and f) appear to be relatively similar. Both display lineshape components with centres of gravity at  $\sim 14$  ppm attributed to  $\text{BO}_3$  sites. This line is slightly broader for the DFNS/BN sample after catalysis. The signal at 26 ppm of  $\text{BN}_3$  and  $\text{BN}_2\text{O}$  sites has a very low intensity for the DFNS/BN sample after catalysis, which further confirms the oxidation of BN. As expected, this signal is not observed in the  $^{11}\text{B}$  spectrum of as-prepared DFNS/ $\text{B}_2\text{O}_3$ . Spectra of DFNS/BN after catalysis and as-prepared



DFNS/B<sub>2</sub>O<sub>3</sub> display a small peak at ~0 ppm that can be assigned to BO<sub>4</sub> environments. For sake of comparison, Fig. 58 compares the <sup>11</sup>B spectra of as-prepared DFNS/BN and DFNS/B<sub>2</sub>O<sub>3</sub> with that of the *h*-BN. The spectrum of *h*-BN displays a broad resonance with centre of gravity at ~28 ppm, which is assigned to boron species of type BN<sub>3</sub> with a quadrupolar coupling of  $C_Q = 2.9$  MHz, which is in agreement with previous investigations.<sup>10,56</sup> This feature of *h*-BN assisted in the identification of boron sites of as-prepared DFNS/BN.

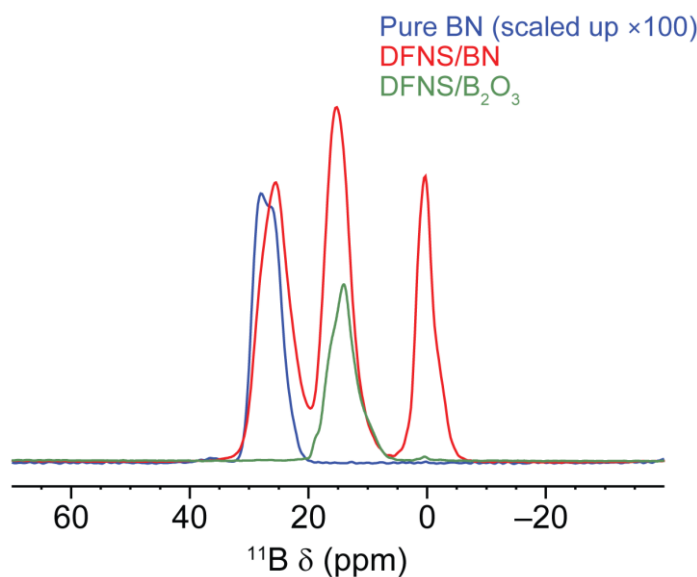


**Figure 58.** <sup>11</sup>B quantitative (*i.e.*, short tip angle) 1D NMR spectra of pure BN, as-prepared DFNS/BN and DFNS/B<sub>2</sub>O<sub>3</sub>. Experiments were recorded at  $B_0 = 18.8$  T with  $\nu_R = 20$  kHz.

To confirm the above assignment and probe <sup>1</sup>H-<sup>11</sup>B proximities, the 2D <sup>11</sup>B-<sup>1</sup>H through-space heteronuclear multiple-quantum coherence (*D*-HMQC) spectra of DFNS/BN (as-prepared and after catalysis) and as-prepared DFNS/B<sub>2</sub>O<sub>3</sub> were recorded (Fig. 59). The *D*-HMQC spectrum of as-prepared DFNS/BN (Fig. 59a) is dominated by a cross-peak between hydroxyl groups on the edge of BN sheets at 6.7 ppm and <sup>11</sup>BO<sub>3</sub> signal at 15 ppm. This observation is consistent with the formation of a disordered boron oxide phase at the surface of *h*-BN.<sup>10,13</sup> The BO<sub>3</sub> signal also correlates with the <sup>1</sup>H signal at 4 ppm assigned to BO<sub>2</sub>OH sites, which substantiates the presence of these sites in this sample. The lower intensity of the cross-peak at 4 ppm with respect to that at 6.7 ppm is consistent with the relative intensities of these signals in the 1D <sup>1</sup>H spectrum. The <sup>11</sup>B signals at ~0 ppm of BO<sub>4</sub> sites also exhibit weaker correlations with <sup>1</sup>H signals at 4 and 6.7 ppm, which indicates the close

proximity between  $\text{BO}_4$  environments and hydroxyl groups on the edge of BN sheets as well as  $\text{BO}_2\text{OH}$  sites. The  $^{11}\text{B}$  signal at 26 ppm exhibits further reduced correlations with  $^1\text{H}$  signals at 6.7 ppm, which could stem from  $\text{BN}_2(\text{OH})$  sites at the edge of BN sheets, as well as at 4 ppm, which indicates the close proximity between  $\text{BO}_2\text{OH}$  sites and BN sheets.

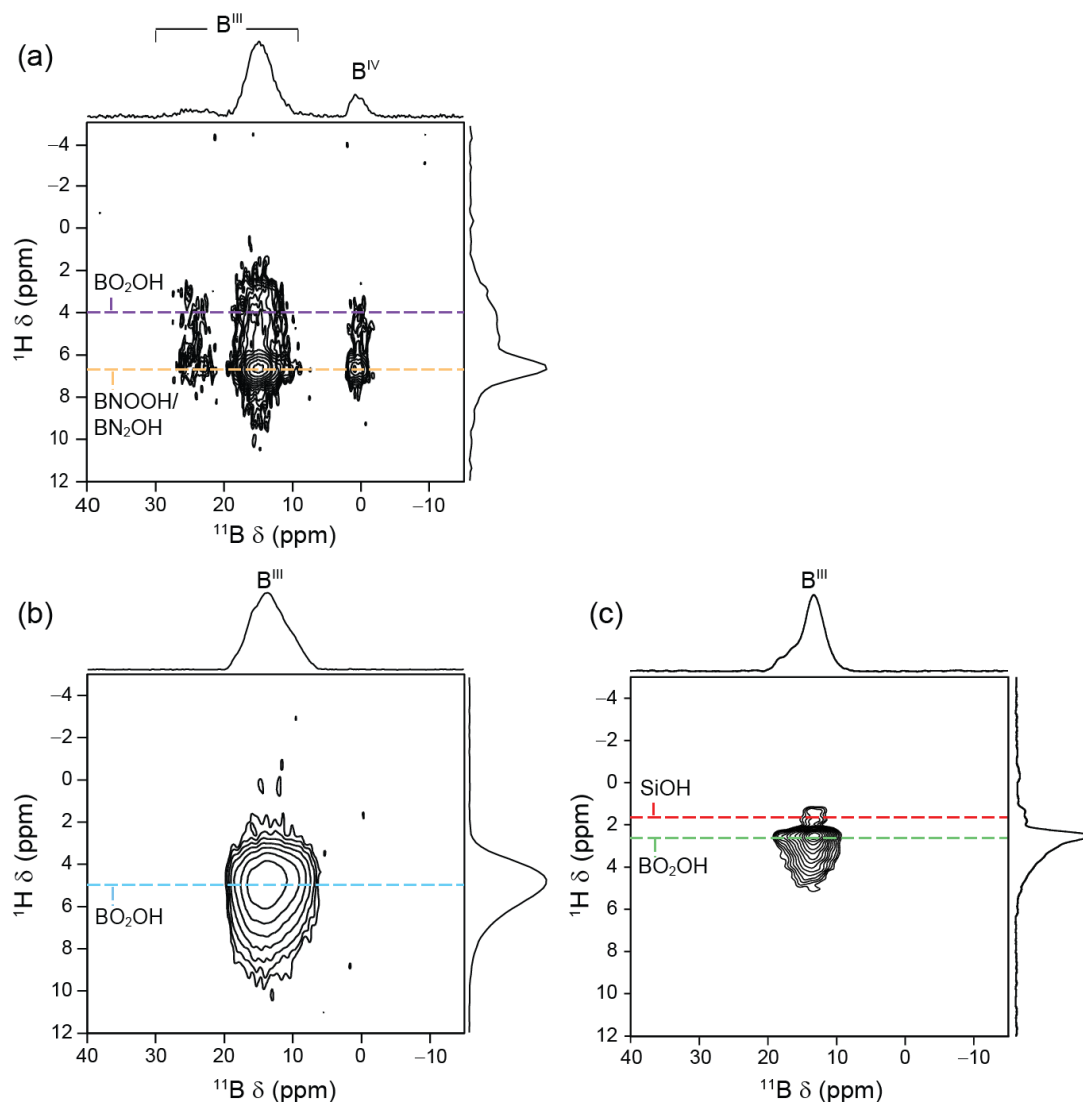


**Figure 59.** 2D  $^{11}\text{B}$ - $\{^1\text{H}\}$  *D*-HMQC (a) as-prepared DFNS/BN (b) DFNS/BN after catalysis and (c) as-prepared DFNS/ $\text{B}_2\text{O}_3$  along with their skyline projections in both dimensions. The spectra were acquired at  $B_0 = 18.8$  T and  $\nu_R = 20$  kHz.

Nevertheless, as seen in Fig. 60, the relative intensities of the sites  $\text{BN}_x\text{O}_{(3-x)}$  with  $x = 1, 2$  or  $3$  and  $\text{BO}_4$  with respect to that of  $\text{BO}_3$  environments are much smaller in the projection of the  $D$ -HMQC spectrum than in the quantitative spectrum. The weak cross peaks of  $\text{BO}_4$  sites indicate that they are more distant from that hydroxyl groups than  $\text{BO}_3$ . Furthermore, the correlations between protons and  $^{11}\text{B}$  nuclei of BN sheets are weak because they only arise from B atoms located at the edge of BN sheets.

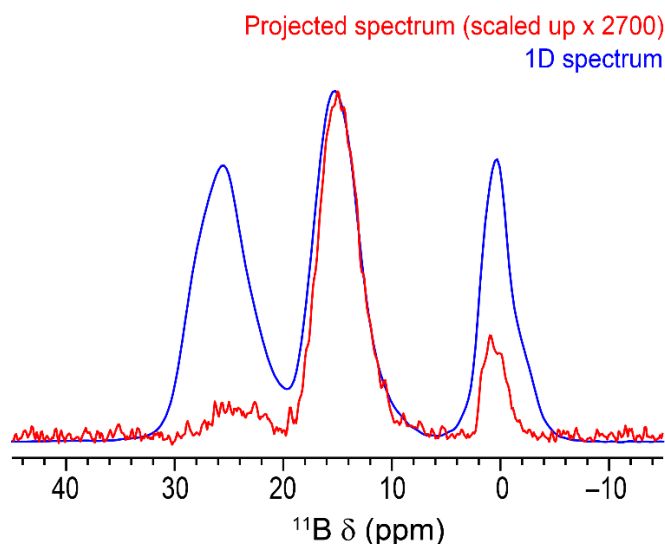


**Figure 60.** Comparison of 1D  $^{11}\text{B}$  quantitative (short tip angle) spectrum and the summation projection in the  $F_2$  dimension of the  $^{11}\text{B}$ - $\{^1\text{H}\}$   $D$ -HMQC spectrum of as-prepared DFNS/BN. The spectra were normalized to the intensity at 12 ppm.

The  $D$ -HMQC spectrum of DFNS/BN after catalysis (Fig. 59b) exhibits a broad correlation between the  $^{11}\text{B}$  signal at 14 ppm ascribed to  $\text{BO}_3$  sites and a  $^1\text{H}$  signal centered at 5 ppm. This  $^1\text{H}$  isotropic chemical shift corresponds to that of  $\text{BO}_2\text{OH}$  sites on the surface of oxidized  $h$ -BN phase.<sup>15</sup> The  $D$ -HMQC spectrum of as-prepared DFNS/ $\text{B}_2\text{O}_3$  (Fig. 59c) is dominated by a correlation between  $\text{BO}_3$  units and  $^1\text{H}$  signal ranging from 2.3 to 4 ppm, which is assigned to  $\text{BO}_2\text{OH}$  sites with second neighbours, B or Si, as well as silanol groups near  $\text{BO}_3$  moieties.<sup>14–16,51–53</sup> The comparison of Fig. 59b and c confirms the higher chemical shifts of  $\text{BO}_2\text{OH}$  protons in DFNS/BN after catalysis than as-prepared DFNS/ $\text{B}_2\text{O}_3$ . This shift could stem from a higher fraction of hydrogen-bonded  $\text{BO}_2\text{OH}$  sites. A cross-peak between the  $^1\text{H}$  signal at 1.7 ppm of isolated silanol and  $\text{BO}_3$  signal is also visible. Hence, the  $^{11}\text{B}$ - $\{^1\text{H}\}$   $D$ -HMQC spectrum confirms the close proximity between the silica surface and the boron atoms.

#### 4.5.2 Probing $^{29}\text{Si}$ environments and $^{29}\text{Si}$ - $^{11}\text{B}$ proximities

$1\text{D } ^1\text{H} \rightarrow ^{29}\text{Si}$  CP MAS experiments were also performed on DFNS/BN, DFNS/BN after catalysis and as-prepared DFNS/ $\text{B}_2\text{O}_3$  (Fig. 61). Spectral fitting was carried out using DMFit<sup>63</sup> (with a Gaussian/Lorentzian model) in order to identify the individual species present. Detailed information on these fits is presented in Table 16 and Fig. 62. The spectra of all three samples show the presence of  $\text{Si}(\text{SiO})_n(\text{OH})_{4-n}$  sites (denoted  $\text{Q}^n$ ) with  $n = 2, 3$  and  $4$ , characteristic of silica-type materials.<sup>27,64,65</sup> The spectrum of as-prepared DFNS/BN also displays a broad shoulder in the region attributable to  $\text{SiN}_n\text{O}_{4-n}$  sites with  $n = 1, 2$  or  $3$  (Fig. 61a and Fig. 62a), since the  $\text{SiN}_3\text{O}$ ,  $\text{SiN}_2\text{O}_2$  and  $\text{SiNO}_3$  sites resonate at *ca.*  $-63$ ,  $-75$  and  $-90$  ppm, respectively.<sup>66-71</sup> This signal indicates the presence of Si-N bonds in this material.

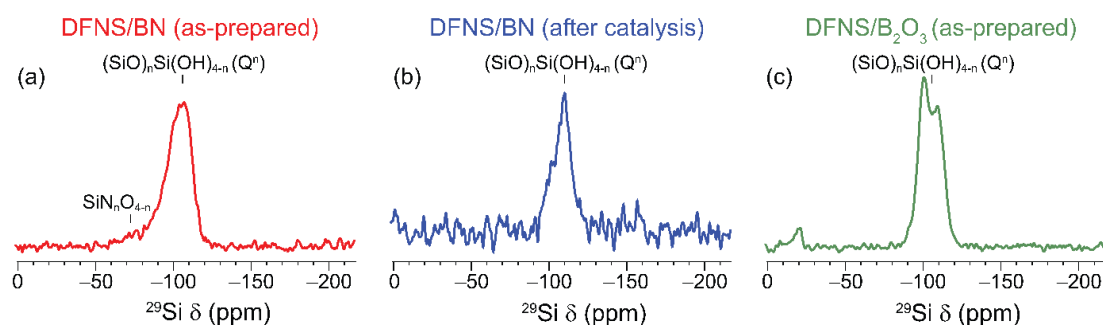


**Figure 61.**  $^1\text{H} \rightarrow ^{29}\text{Si}$  CP MAS NMR spectra of (a) as-prepared DFNS/BN, (b) DFNS/BN after catalysis and (c) as-prepared DFNS/ $\text{B}_2\text{O}_3$ . Experiments were recorded at  $B_0 = 9.4$  T with  $\nu_R = 10$  kHz.

The spectrum of DFNS/BN after catalysis (Fig. 61b and Fig. 62b) reveals that primarily  $\text{Q}^4$  species remain in this sample, indicating that most of the Si-OH surface groups have been consumed or transformed, likely as a result of the catalytic reaction process.<sup>72</sup> This reduced amount of surface hydroxyls also leads to a lower efficiency of the CP transfer and hence, lower signal-to-noise ratio for this sample, despite the collection of a larger number of transients.<sup>73,74</sup> The shoulder centred at *ca.*  $-73$  ppm (attributed to  $\text{SiN}_n\text{O}_{4-n}$  sites) is also no longer visible after catalysis, in agreement with the conversion of BN into  $\text{B}_2\text{O}_3$  inferred from PXRD and XPS (not shown) and  $^{11}\text{B}$  NMR. The spectrum of as-prepared DFNS/ $\text{B}_2\text{O}_3$  can be also fitted with three

components ( $Q^2$ ,  $Q^3$  and  $Q^4$ ) as shown in Table 16 and Fig. 62c, but with some differences in the integrated areas with respect to DFNS/BN after catalysis.

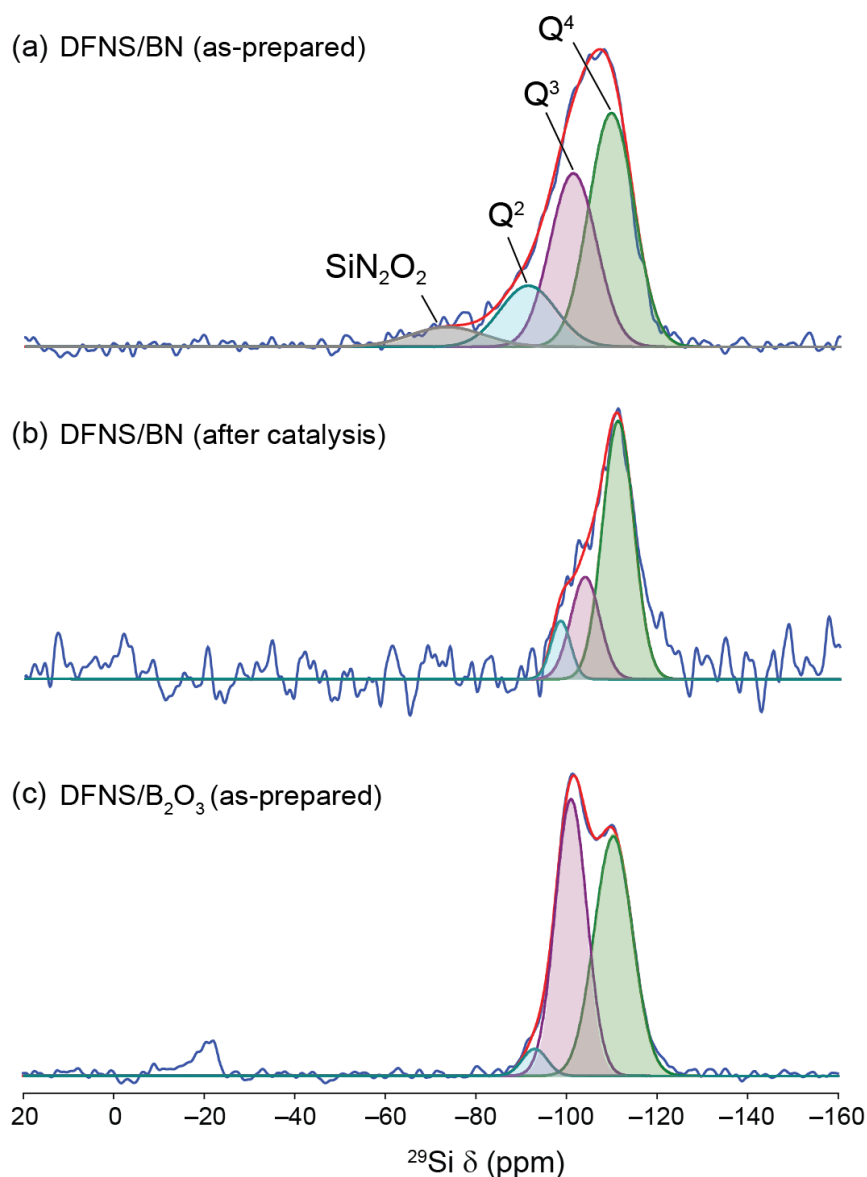


**Figure 62.** Deconvolutions of the lineshapes obtained from  $^1\text{H} \rightarrow ^{29}\text{Si}$  CP MAS experiments on (a) as-prepared DFNS/BN, (b) DFNS/BN after catalysis and (c) as-prepared DFNS/ $\text{B}_2\text{O}_3$ . Fitting was carried out using the Gaussian/Lorentzian model in DMFit.<sup>63</sup> In (c), the small peak at *ca.* -20 ppm in the  $^1\text{H} \rightarrow ^{29}\text{Si}$  CP MAS spectrum of as-prepared DFNS/ $\text{B}_2\text{O}_3$  is probably due to residual organic species, so was not included in the fitting process.

**Table 16.** Data obtained from the deconvolutions of the  $^1\text{H} \rightarrow ^{29}\text{Si}$  CP MAS NMR spectra (using the Gaussian/Lorentzian model in DMFit<sup>63</sup>). Parameters include: peak assignment,<sup>27,64–69,71,72,75,76</sup> chemical shift,  $\delta$ ; full width at half maximum, FWHM; absolute integrated area (%).

Sample	Assignment	$\delta$ (ppm)	FWHM (ppm)	Area (%)
	$\text{SiN}_2\text{O}_2$	-73.2	19.1	6.2
As-prepared	$\text{Q}^2$	-91.1	14.6	14.6
DFNS/BN	$\text{Q}^3$	-101.0	12.1	34.2
	$\text{Q}^4$	-109.5	11.8	45.0
DFNS/BN after catalysis	$\text{Q}^2$	-98.3	5.1	9.3
	$\text{Q}^3$	-103.7	7.6	24.4
	$\text{Q}^4$	-110.9	8.1	66.3
As-prepared DFNS/ $\text{B}_2\text{O}_3$	$\text{Q}^2$	-93.1	6.5	3.6
	$\text{Q}^3$	-101.0	8.2	47.1
	$\text{Q}^4$	-110.4	9.9	49.3

To further probe the interactions between the silica surface and the supported BN and  $\text{B}_2\text{O}_3$  phases, the 2D  $^{11}\text{B}\{-^{29}\text{Si}\}$  *D*-HMQC spectra were acquired. The corresponding spectrum of as-prepared DFNS/BN shown in Fig. 63a is dominated by a cross-peak between the  $\text{Q}^4$  site and the  $\text{BO}_3$  signal at  $\sim 12$  ppm assigned to  $\text{B}(\text{OSi})_x(\text{OB})_{3-x}$  environments with  $x = 1, 2$  or  $3$ .<sup>14,16,53,57</sup> These  $\text{B}(\text{OSi}(\text{Q}^4))_x(\text{OB})_{3-x}$  sites mainly corresponds to the subsurface region of the material. The spectrum also exhibit cross-peaks between the  $\text{Q}^4$  and  $\text{Q}^3$  site and the  $\text{BO}_3$  signal at  $\sim 14$  ppm as well as between the  $\text{Q}^3$  sites and the  $\text{BO}_3$  signal at  $\sim 16$  ppm, which are assigned to surface sites  $\text{B}(\text{OSi}(\text{Q}^{3,4}))_x(\text{OB})_{2-x}\text{OH}$  with  $x = 1$  or  $2$  and  $\text{BOSi}(\text{Q}^3)(\text{OH})_2$ , respectively.<sup>16,53,57</sup> Cross-peaks between the  $\text{BO}_4$  signal at  $\sim 0$  ppm and the  $\text{Q}^3$  sites as well as the  $\text{BO}_4$  signal at  $\sim -2$  ppm and the  $\text{Q}^4$  sites were observed. The cross-peak of the  $\text{B}^{\text{IV}}$  signal at  $\sim 0$  ppm can be ascribed to the surface  $\text{B}(\text{OSi}(\text{Q}^3))_x(\text{OB})_{3-x}\text{OH}$  site with  $x = 1, 2$  or  $3$ , whereas the cross-peak of the  $\text{B}^{\text{IV}}$  signal at  $\sim -2$  ppm can be ascribed to the subsurface  $\text{B}(\text{OSi}(\text{Q}^4))_x(\text{OB})_{4-x}$  sites with  $x = 1, 2, 3$  or  $4$ .<sup>13,54</sup> These cross-peaks between  $\text{BO}_3$  and  $\text{BO}_4$  signals and those of  $\text{Q}^4$  and  $\text{Q}^3$  sites demonstrate the presence of B–O–Si bonds in the as-prepared DFNS/BN. Furthermore, the  $\text{BN}_2\text{OH}$  signal at 26 ppm correlates with that of  $\text{SiN}_2\text{O}_2$  site at  $-73$  ppm. A weak cross-peak between the  $\text{BNO}_2$  sites at 23.5 ppm and the  $\text{SiNO}_3$  signal at  $-93$  ppm is also observed.<sup>46,67,69,71</sup> These cross-peaks

suggest the presence of B–N–Si bonds in the sample. The 2D  $^{11}\text{B}\text{-}\{^{29}\text{Si}\}$   $D$ -HMQC spectrum of DFNS/ $\text{B}_2\text{O}_3$  (Fig. 63b) is dominated by cross-peaks between the  $\text{BO}_2\text{OH}$  signal at  $\sim 14$  ppm and the  $\text{Q}^4$  and  $\text{Q}^3$  sites, which suggests the anchoring of  $\text{B}_2\text{O}_3$  phase on silica surface *via* B–O–Si bonds.<sup>14</sup>

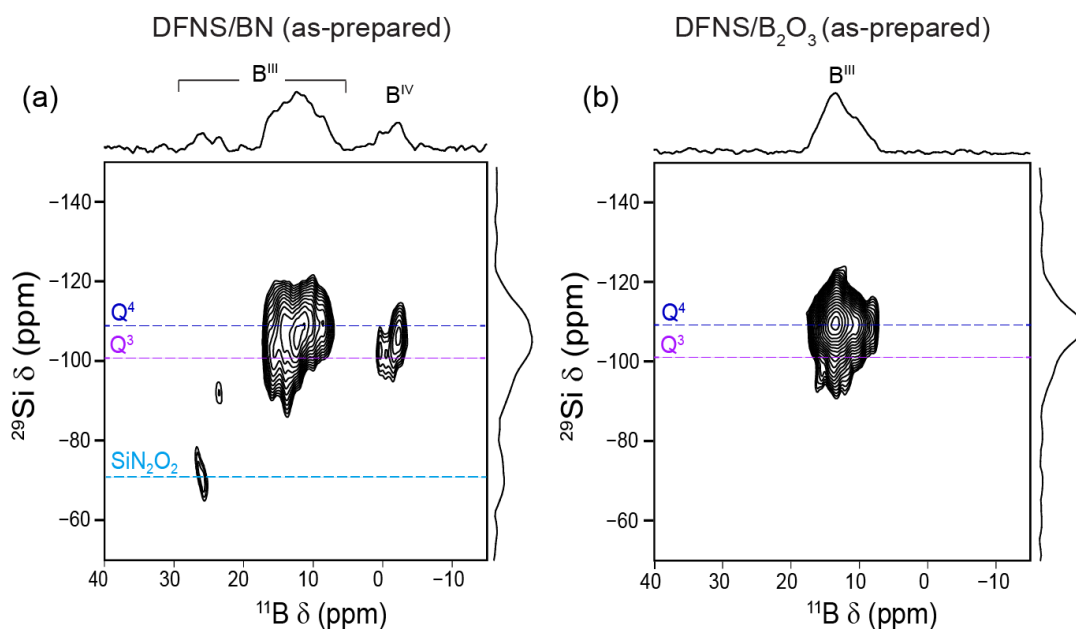


**Figure 63.** 2D  $^{11}\text{B}\text{-}\{^{29}\text{Si}\}$   $D$ -HMQC NMR spectra of (a) as-prepared DFNS/BN and (b) as-prepared DFNS/ $\text{B}_2\text{O}_3$  along with their skyline projections in both dimensions. The spectra were recorded at  $B_0 = 18.8$  T and  $\nu_R = 14.286$  kHz.

### 4.5.3 Insights into the boron species

To better resolve the  $^{11}\text{B}$  signals, 2D  $^{11}\text{B}$  MQMAS spectra of as-prepared DFNS/BN and DFNS/ $\text{B}_2\text{O}_3$  and DFNS/BN after catalysis (Fig. 64) were also acquired. These spectra correlate the anisotropic MAS spectra of the  $^{11}\text{B}$  central transitions shown along the direct  $\delta_2$  dimension to their isotropic shift detected along the indirect  $\delta_1$  dimension. The projection along the vertical isotropic direction indicates that each of the three  $^{11}\text{B}$  sites has a wide distribution of  $\delta_{\text{iso}}$  values, which stems from the distribution of local environments, as the second neighbour of boron atoms can be B, Si or H.<sup>44,49</sup>

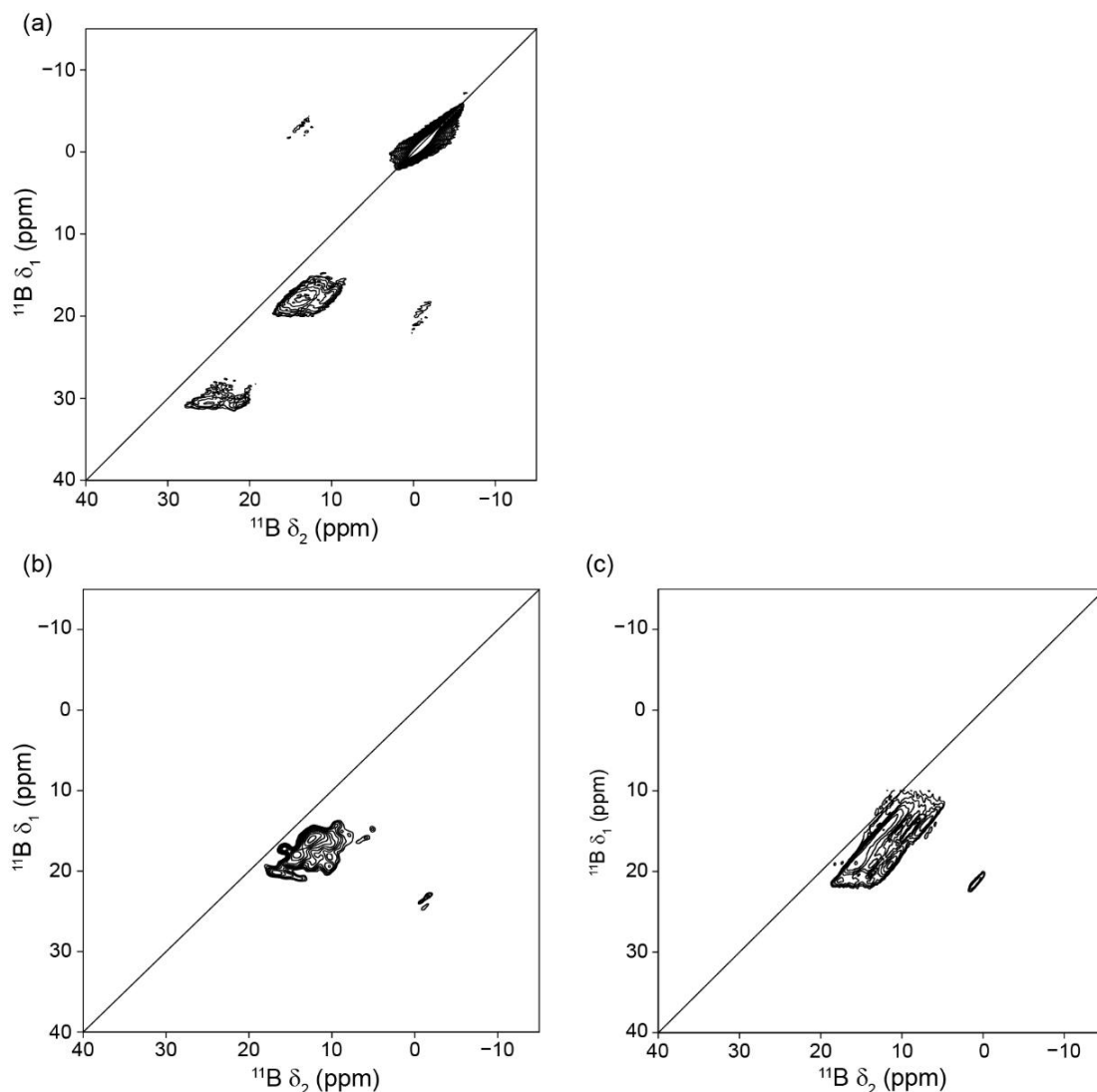


**Figure 64.** 2D  $^{11}\text{B}$  MQMAS spectra of (a) as-prepared DFNS/BN, (b) DFNS/BN after catalysis and (c) as-prepared DFNS/ $\text{B}_2\text{O}_3$ . The projections in  $F_1$  indirect dimension of MQMAS spectra along with their deconvolution are shown in Figs. 65 and 66. The MQMAS spectra were acquired at  $B_0 = 18.8$  T and  $\nu_R = 20$  kHz.

In order to obtain detailed insight into the distinct functional groups that were present in the boron surface layers, spectral fitting of the lineshapes in the  $F_1$  dimension of the acquired MQMAS spectra was performed using DMFit.<sup>63</sup> Since the  $F_1$  dimension of an MQMAS spectrum presents resonances that are free from the effects of quadrupolar broadening,<sup>23,63</sup> it was possible for a Gaussian/Lorentzian model to be employed. The simulated spectra are shown in Figs. 65 and 66. Table 17 lists the shifts,  $\delta_1$ , along the indirect dimension of the sheared MQMAS spectra of the simulated peaks for the three investigated samples. Due to the significant overlap of sites in these



MQMAS spectra, fitting of the total lineshapes to obtain  $\delta_{\text{iso}}$  and  $C_Q/P_Q$  values with a sufficient degree of accuracy was not possible.

In the 2D MQMAS spectrum of as-prepared DFNS/BN (Fig. 64a and 65), three peaks at  $\delta_1 = 30.5, 28.6$  and  $27.2$  ppm can be resolved in the most deshielded signals. The peak at  $30.5$  ppm is assigned to bulk  $\text{BN}_3$  sites, whereas the signals at  $28.6$  and  $27.2$  ppm are likely produced by  $\text{BN}_2\text{OH}$  and  $\text{BN}_2\text{O}$  sites, respectively, located at the edge of BN sheets, since the  $^{11}\text{B}$  chemical shift increases for decreasing number of bridging oxygen atoms.<sup>46,61,77</sup> The  $\text{BNO}_2$  signal may not be detected because of the lack of sensitivity of MQMAS experiments. The  $\text{BO}_3$  signal can be simulated by three peaks at  $\delta_1 = 18.4, 17.2$  and  $16.3$  ppm, assigned to  $\text{BO}_2\text{OH}(\text{ring}), \text{BO}_2\text{OH}(\text{non-ring})$  and  $\text{BO}_3(\text{ring})$ , respectively since for the same number of bridging oxygens,  $^{11}\text{B}$  nuclei residing in boroxol rings exhibit more deshielded signals as compared to those in the chain.<sup>14,61,77</sup>  $\text{BO}_3(\text{non-ring})$  sites resonating at  $\delta_1 \approx 14$  ppm (Fig. 64a) can also contribute to the signal at  $\delta_1 = 16.3$  ppm. Furthermore, according to the 2D  $^{11}\text{B}\{-^{29}\text{Si}\}$  *D*-HMQC spectrum (Fig. 63a), a fraction of the  $\text{BO}_3$  moieties are anchored to the silica surface. In particular, the peak at  $\delta_1 = 18.4$  ppm subsumes the signal of  $\text{BOSi}(\text{Q}^3)(\text{OH})_2$  and  $\text{B}(\text{OSi}(\text{Q}^{3,4}))_x(\text{OB})_{2-x}\text{OH}$  surface sites, whereas the signal of  $\text{B}(\text{OSi}(\text{Q}^4))_x(\text{OB})_{4-x}$  sites also overlaps with those of  $\text{BO}_2\text{OH}(\text{non-ring})$  and  $\text{BO}_3(\text{ring})$  environments. The  $\text{BO}_4$  signal can be deconvoluted as the sum of three peaks at  $\delta_1 = 0.1, -1$  and  $-1.9$  ppm, which may be ascribed to  $\text{B}(\text{OSi}(\text{Q}^3))_x(\text{OB})_{3-x}\text{OH}$ ,  $\text{B}(\text{OB})_4$  and  $\text{B}(\text{OSi}(\text{Q}^4))_x(\text{OB})_{4-x}$  sites, respectively (Fig. 65c), based on the 2D  $^{11}\text{B}\{-^1\text{H}\}$  and  $^{11}\text{B}\{-^{29}\text{Si}\}$  *D*-HMQC spectra (Fig. 59a and 63a).

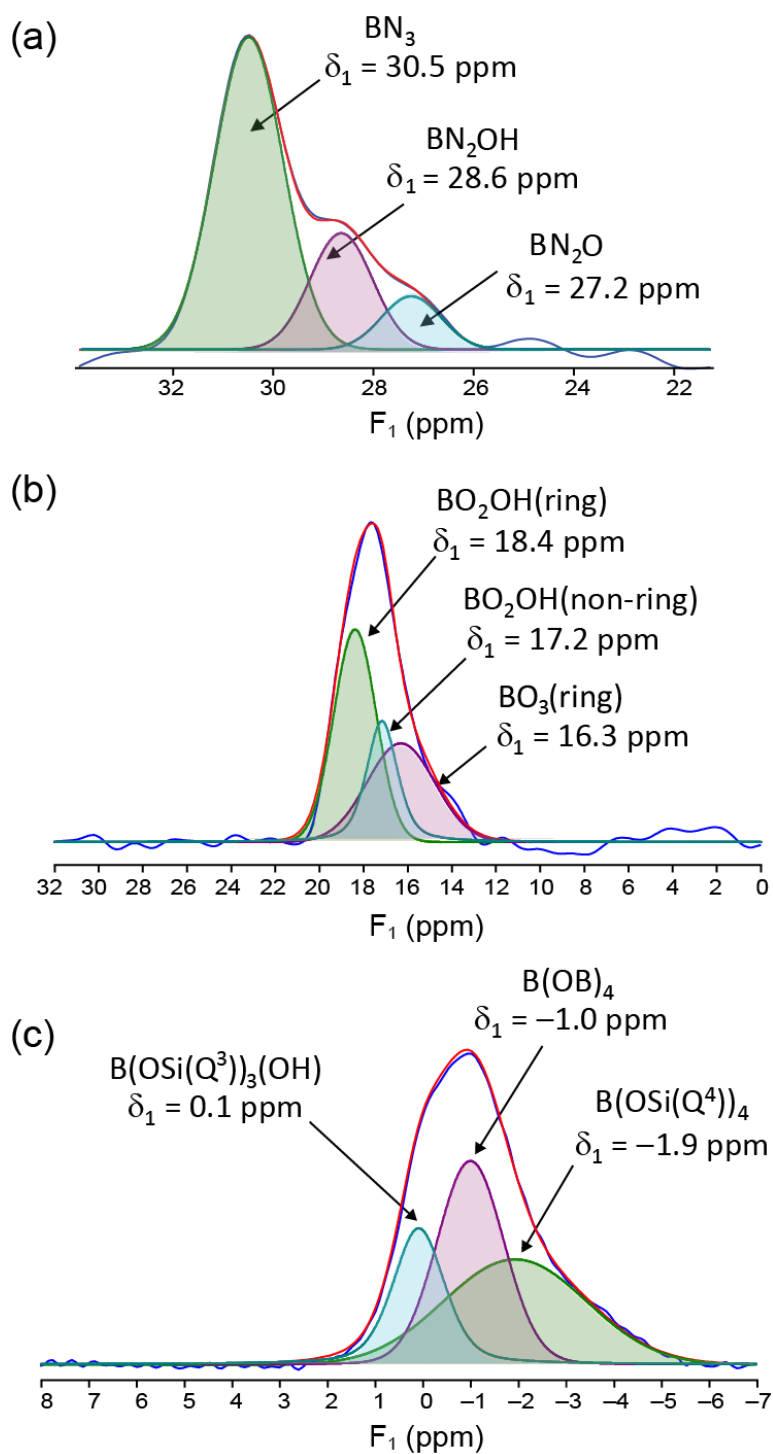


**Figure 65.** (a-c) Deconvolutions of the lineshapes obtained from total projections of the  $F_1$  dimension of the  $^{11}\text{B}$  MQMAS spectrum of as-prepared DFNS/BN. Fitting was carried out using the Gaussian/Lorentzian model in DMFit.<sup>63</sup>

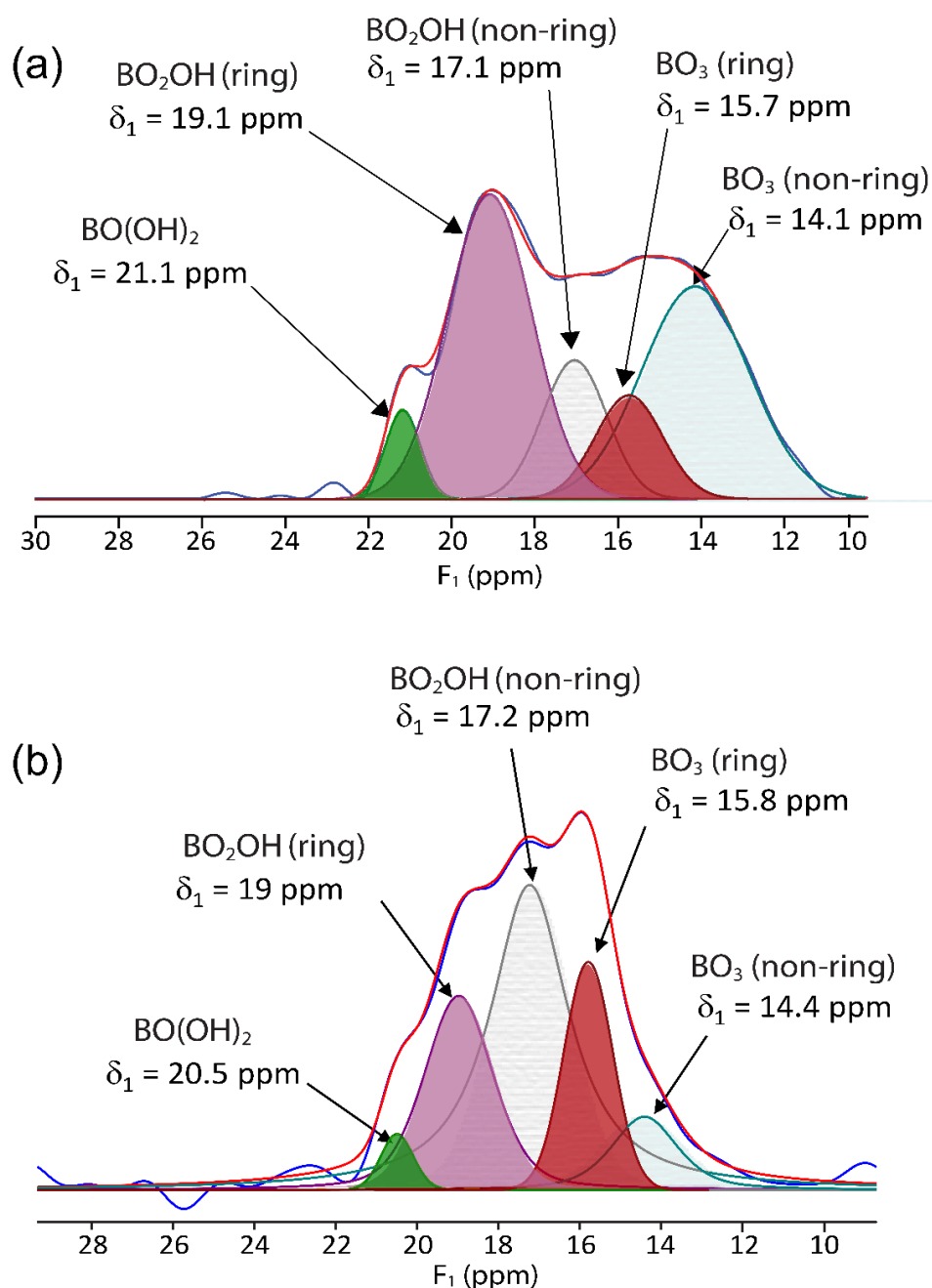


**Figure 66.** Deconvolutions of the lineshapes obtained from total projections of the  $F_1$  dimension of the  $^{11}\text{B}$  MQMAS spectrum of (a) DFNS/BN after catalysis and (b) as-prepared DFNS/ $\text{B}_2\text{O}_3$ . Fitting was carried out using the Gaussian/Lorentzian model in DMFit.<sup>17</sup> The  $\text{BO}_4$  peak is folded, and thus, not shown.

**Table 17.** Possible boron species present in DFNS supported catalysts obtained from fitting the  $F_1$  dimensions of MQMAS spectra of DFNS/BN before and after catalysis, and DFNS/B<sub>2</sub>O<sub>3</sub> before catalysis.<sup>10,14–16,46,51–62,77</sup> It should be noted that the  $\delta_1$  values presented here result from a linear combination of  $\delta_2$  and  $\delta_{1(\text{non-sheared})}$ . They do **not** directly correspond to  $\delta_{\text{iso}}$  (the isotropic chemical shift).<sup>35,78</sup>

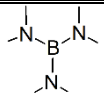
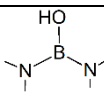
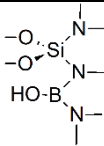
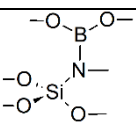
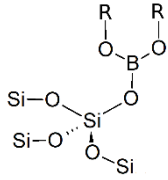
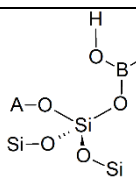
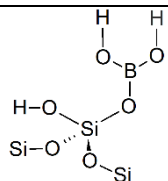
Sample	Species	$\delta_1$ (ppm)
As-prepared DFNS/BN	BN <sub>3</sub>	30.5
	BN <sub>2</sub> OH	28.6
	BN <sub>2</sub> O	27.2
	BO <sub>2</sub> OH(ring)	18.4
	BO <sub>2</sub> OH(non-ring)	17.2
	BO <sub>3</sub> (ring)	16.3
	B(OSi(Q <sup>3</sup> )) <sub>3</sub> OH	0.1
	B(OB) <sub>4</sub>	-1.0
	B(OSi(Q <sup>4</sup> )) <sub>4</sub>	-1.9
As-prepared DFNS/B <sub>2</sub> O <sub>3</sub>	BO(OH) <sub>2</sub>	20.5
	BO <sub>2</sub> OH(ring)	19.0
	BO <sub>2</sub> OH(non-ring)	17.2
	BO <sub>3</sub> (ring)	15.8
	BO <sub>3</sub> (non-ring)	14.4
	BO <sub>4</sub>	<sup>a</sup>
DFNS/BN after catalysis	BO(OH) <sub>2</sub>	21.1
	BO <sub>2</sub> OH(ring)	19.1
	BO <sub>2</sub> OH(non-ring)	17.1
	BO <sub>3</sub> (ring)	15.7
	BO <sub>3</sub> (non-ring)	14.1
	BO <sub>4</sub>	<sup>a</sup>

<sup>a</sup>Value not reported because peak was folded.<sup>78,79</sup>

As seen in Fig. 66a, the BO<sub>3</sub> signal in the projection of the 2D MQMAS spectrum of DFNS/BN after catalysis can be simulated as the sum of five components resonating at  $\delta_1 = 21.1, 19.1, 17.1, 15.7$  and  $14.1$  ppm, assigned to BO(OH)<sub>2</sub>, BO<sub>2</sub>OH(ring), BO<sub>2</sub>OH(non-ring), BO<sub>3</sub>(ring) and BO<sub>3</sub>(non-ring), respectively.<sup>14,61,77</sup> The projection also displays a folded BO<sub>4</sub> signal, which can be simulated as a single resonance (not shown). For DFNS/B<sub>2</sub>O<sub>3</sub>, the BO<sub>3</sub> signal in the projection of the 2D MQMAS spectrum can be simulated as the sum of five components at  $\delta_1 = 20.5, 19, 17.2, 15.8$  and  $14.4$  ppm (Fig. 66b). These shifts are similar to those used to simulate the BO<sub>3</sub> signal DFNS/BN after catalysis. The BO<sub>4</sub> signal of DFNS/ B<sub>2</sub>O<sub>3</sub> catalysis can also be simulated as a single resonance (not shown). A key difference between DFNS/BN after catalysis and DFNS/B<sub>2</sub>O<sub>3</sub> is the larger relative intensities of BO(OH)<sub>2</sub> and BO<sub>2</sub>OH(ring) sites as compared to BO<sub>3</sub>(ring) for the first sample, which is consistent

with the larger amount of hydrogen bonded hydroxyl groups attached to B for this material (the resonance of  $\text{BO}_3(\text{ring})$ , which is bonded to hydroxyl group, is represented in red in Fig. 66).<sup>15,16</sup> This structural difference could explain the difference in productivity between DFNS/BN after catalysis and DFNS/ $\text{B}_2\text{O}_3$ . Table 18 summarizes the main plausible local environments, which have been identified in the investigated samples on the basis of solid-state NMR data.

**Table 18.** Main plausible local environments in as prepared DFNS/BN, DFNS/BN after catalysis and as-prepared DFNS/ $\text{B}_2\text{O}_3$  based on solid-state NMR data.

Local environments	Sample	NMR data
	as-prepared DFNS/BN	Peak at $\delta_1 = 30.5$ ppm in $^{11}\text{B}$ MQMAS
	as-prepared DFNS/BN	Cross-peak $\{\delta(^1\text{H}), \delta(^{11}\text{B})\} = \{6.7 \text{ ppm}, 26 \text{ ppm}\}$ in <i>D</i> -HMQC
	as-prepared DFNS/BN	Cross-peak $\{\delta(^{29}\text{Si}), \delta(^{11}\text{B})\} = \{-73 \text{ ppm}, 26 \text{ ppm}\}$ in <i>D</i> -HMQC
	as-prepared DFNS/BN	Cross-peak $\{\delta(^{29}\text{Si}), \delta(^{11}\text{B})\} = \{-93 \text{ ppm}, 23.5 \text{ ppm}\}$ in <i>D</i> -HMQC
 with R = B or $\text{Si}(\text{Q}^4)$	as-prepared DFNS/BN as-prepared DFNS/ $\text{B}_2\text{O}_3$	Cross-peak $\{\delta(^{29}\text{Si}), \delta(^{11}\text{B})\} = \{-110 \text{ ppm}, 12 \text{ ppm}\}$ in <i>D</i> -HMQC
 with R = B or $\text{Si}(\text{Q}^4)$ and A = H or Si	as-prepared DFNS/BN as-prepared DFNS/ $\text{B}_2\text{O}_3$	Cross-peak $\{\delta(^{29}\text{Si}), \delta(^{11}\text{B})\} = \{-101 \text{ and } -110 \text{ ppm}, 14 \text{ ppm}\}$ in <i>D</i> -HMQC
	as-prepared DFNS/BN as-prepared DFNS/ $\text{B}_2\text{O}_3$	Cross-peak $\{\delta(^{29}\text{Si}), \delta(^{11}\text{B})\} = \{-101 \text{ ppm}, 16 \text{ ppm}\}$ in <i>D</i> -HMQC

	as-prepared DFNS/BN	Cross-peak $\{\delta(^{29}\text{Si}), \delta(^{11}\text{B})\} = \{-110 \text{ ppm}, -2 \text{ ppm}\}$ in <i>D</i> -HMQC
with A = B or Si(Q <sup>4</sup> )		
	as-prepared DFNS/BN	Cross-peak $\{\delta(^{29}\text{Si}), \delta(^{11}\text{B})\} = \{-101 \text{ ppm}, 0 \text{ ppm}\}$ in <i>D</i> -HMQC
with A = B or Si(Q <sup>3</sup> )		
	as-prepared DFNS/BN DFNS/BN after catalysis as-prepared DFNS/B <sub>2</sub> O <sub>3</sub>	Peak at $\delta_1 \approx 16$ (BO <sub>3</sub> ) and 19 (BO <sub>2</sub> OH) ppm in <sup>11</sup> B MQMAS
with A = B or Si		
	as-prepared DFNS/BN DFNS/BN after catalysis	Cross-peak $\{\delta(^1\text{H}), \delta(^{11}\text{B})\} = \{4 \text{ ppm}, 15 \text{ ppm}\}$ in <i>D</i> -HMQC Peak at $\delta_1 = 17.1$ ppm in <sup>11</sup> B MQMAS
with A = B or Si		
	as-prepared DFNS/B <sub>2</sub> O <sub>3</sub>	Cross-peak $\{\delta(^1\text{H}), \delta(^{11}\text{B})\} = \{2.7 \text{ ppm}, 15 \text{ ppm}\}$ in <i>D</i> -HMQC
with A = B or Si		

## 4.6 CONCLUSIONS

Through a combination of analytical techniques, notably 1D and 2D multinuclear ( $^1\text{H}$ ,  $^{29}\text{Si}$ ,  $^{11}\text{B}$ ) solid-state NMR experiments, it has been shown that the supported BN phase undergoes a transformation to  $\text{B}_2\text{O}_3$  (oxidation) during the propane dehydrogenation process, whilst avoiding deactivation (up to 19 h). This has been attributed to the stabilising effect of DFNS through the covalent linkage of silica and  $\text{B}_2\text{O}_3$  via Si-O-B bonding, allowing  $\text{B}_2\text{O}_3$  to remain on the DFNS surface and act as a catalyst. The presence of these linkages was confirmed by solid-state NMR spectroscopy. Furthermore, 2D  $^1\text{H}$ - $^{11}\text{B}$  heteronuclear correlation and  $^{11}\text{B}$  high resolution spectra acquired at  $B_0 = 18.8$  T indicate a larger fraction of hydrogen-bonded BOH groups at the surface of oxidised DFNS/BN with respect to as-prepared DFNS/ $\text{B}_2\text{O}_3$ . This structural difference could explain the higher selectivity towards propene of oxidised DFNS/BN.

## References

- (1) Belgamwar, R.; Rankin, A. G. M.; Maity, A.; Mishra, A. K.; Gómez, J. S.; Trébosc, J.; Vinod, C. P.; Lafon, O.; Polshettiwar, V. Boron Nitride and Oxide Supported on Dendritic Fibrous Nanosilica for Catalytic Oxidative Dehydrogenation of Propane. *ACS Sustain. Chem. Eng.* **2020**, *8* (43), 16124–16135. <https://doi.org/10.1021/acssuschemeng.0c04148>.
- (2) Grant, J. T.; Venegas, J. M.; McDermott, W. P.; Hermans, I. Aerobic Oxidations of Light Alkanes over Solid Metal Oxide Catalysts. *Chem. Rev.* **2018**, *118* (5), 2769–2815. <https://doi.org/10.1021/acs.chemrev.7b00236>.
- (3) Sheng, J.; Yan, B.; Lu, W.-D.; Qiu, B.; Gao, X.-Q.; Wang, D.; Lu, A.-H. Oxidative Dehydrogenation of Light Alkanes to Olefins on Metal-Free Catalysts. *Chem. Soc. Rev.* **2021**, *50* (2), 1438–1468. <https://doi.org/10.1039/D0CS01174F>.
- (4) Sun, X.; Han, P.; Li, B.; Mao, S.; Liu, T.; Ali, S.; Lian, Z.; Su, D. Oxidative Dehydrogenation Reaction of Short Alkanes on Nanostructured Carbon Catalysts: A Computational Account. *Chem. Commun.* **2018**, *54* (8), 864–875. <https://doi.org/10.1039/C7CC06941C>.
- (5) Dai, Y.; Gao, X.; Wang, Q.; Wan, X.; Zhou, C.; Yang, Y. Recent Progress in Heterogeneous Metal and Metal Oxide Catalysts for Direct Dehydrogenation of Ethane and Propane. *Chem. Soc. Rev.* **2021**, *50* (9), 5590–5630. <https://doi.org/10.1039/D0CS01260B>.
- (6) Grant, J. T.; Carrero, C. A.; Goeltl, F.; Venegas, J.; Mueller, P.; Burt, S. P.; Specht, S. E.; McDermott, W. P.; Chierigato, A.; Hermans, I. Selective Oxidative Dehydrogenation of Propane to Propene Using Boron Nitride Catalysts. *Science* **2016**, *354* (6319), 1570–1573. <https://doi.org/10.1126/science.aaf7885>.

- (7) Sattler, J. J. H. B.; Ruiz-Martinez, J.; Santillan-Jimenez, E.; Weckhuysen, B. M. Catalytic Dehydrogenation of Light Alkanes on Metals and Metal Oxides. *Chem. Rev.* **2014**, *114* (20), 10613–10653. <https://doi.org/10.1021/cr5002436>.
- (8) Guo, F.; Yang, P.; Pan, Z.; Cao, X.-N.; Xie, Z.; Wang, X. Carbon-Doped BN Nanosheets for the Oxidative Dehydrogenation of Ethylbenzene. *Angew. Chem. Int. Ed.* **2017**, *56* (28), 8231–8235. <https://doi.org/10.1002/anie.201703789>.
- (9) Grant, J. T.; McDermott, W. P.; Venegas, J. M.; Burt, S. P.; Micka, J.; Phivilay, S. P.; Carrero, C. A.; Hermans, I. Boron and Boron-Containing Catalysts for the Oxidative Dehydrogenation of Propane. *ChemCatChem* **2017**, *9* (19), 3623–3626. <https://doi.org/10.1002/cctc.201701140>.
- (10) Love, A. M.; Thomas, B.; Specht, S. E.; Hanrahan, M. P.; Venegas, J. M.; Burt, S. P.; Grant, J. T.; Cendejas, M. C.; McDermott, W. P.; Rossini, A. J.; Hermans, I. Probing the Transformation of Boron Nitride Catalysts under Oxidative Dehydrogenation Conditions. *J. Am. Chem. Soc.* **2019**, *141* (1), 182–190. <https://doi.org/10.1021/jacs.8b08165>.
- (11) Shi, L.; Wang, Y.; Yan, B.; Song, W.; Shao, D.; Lu, A.-H. Progress in Selective Oxidative Dehydrogenation of Light Alkanes to Olefins Promoted by Boron Nitride Catalysts. *Chem. Commun.* **2018**, *54* (78), 10936–10946. <https://doi.org/10.1039/C8CC04604B>.
- (12) Huang, R.; Zhang, B.; Wang, J.; Wu, K.-H.; Shi, W.; Zhang, Y.; Liu, Y.; Zheng, A.; Schlögl, R.; Su, D. S. Direct Insight into Ethane Oxidative Dehydrogenation over Boron Nitrides. *ChemCatChem* **2017**, *9* (17), 3293–3297. <https://doi.org/10.1002/cctc.201700725>.
- (13) Zhang, Z.; Jimenez-Izal, E.; Hermans, I.; Alexandrova, A. N. Dynamic Phase Diagram of Catalytic Surface of Hexagonal Boron Nitride under Conditions of Oxidative Dehydrogenation of Propane. *J. Phys. Chem. Lett.* **2019**, *10* (1), 20–25. <https://doi.org/10.1021/acs.jpcclett.8b03373>.
- (14) Lu, W.-D.; Wang, D.; Zhao, Z.; Song, W.; Li, W.-C.; Lu, A.-H. Supported Boron Oxide Catalysts for Selective and Low-Temperature Oxidative Dehydrogenation of Propane. *ACS Catal.* **2019**, *9* (9), 8263–8270. <https://doi.org/10.1021/acscatal.9b02284>.
- (15) Love, A. M.; Cendejas, M. C.; Thomas, B.; McDermott, W. P.; Uchupalanun, P.; Kruszynski, C.; Burt, S. P.; Agbi, T.; Rossini, A. J.; Hermans, I. Synthesis and Characterization of Silica-Supported Boron Oxide Catalysts for the Oxidative Dehydrogenation of Propane. *J. Phys. Chem. C* **2019**, *123* (44), 27000–27011. <https://doi.org/10.1021/acs.jpcc.9b07429>.
- (16) Altvater, N. R.; Dorn, R. W.; Cendejas, M. C.; McDermott, W. P.; Thomas, B.; Rossini, A. J.; Hermans, I. B-MWW Zeolite: The Case Against Single-Site Catalysis. *Angew. Chem. Int. Ed.* **2020**, *59*, 6546–6550. <https://doi.org/10.1002/anie.201914696>.
- (17) Maity, A.; Polshettiwar, V. Dendritic Fibrous Nanosilica for Catalysis, Energy Harvesting, Carbon Dioxide Mitigation, Drug Delivery, and Sensing. *ChemSusChem* **2017**, *10* (20), 3866–3913. <https://doi.org/10.1002/cssc.201701076>.
- (18) Maity, A.; Belgamwar, R.; Polshettiwar, V. Facile Synthesis to Tune Size, Textural Properties and Fiber Density of Dendritic Fibrous Nanosilica for Applications in Catalysis and CO<sub>2</sub> Capture. *Nature Protocols* **2019**, *14* (7), 2177–2204. <https://doi.org/10.1038/s41596-019-0177-z>.



- (19) Mishra, A. K.; Belgamwar, R.; Jana, R.; Datta, A.; Polshettiwar, V. Defects in Nanosilica Catalytically Convert CO<sub>2</sub> to Methane without Any Metal and Ligand. *Proc. Natl. Acad. Sci. USA* **2020**, *117* (12), 6383–6390. <https://doi.org/10.1073/pnas.1917237117>.
- (20) Bonhomme, C.; Gervais, C.; Laurencin, D. Recent NMR Developments Applied to Organic–Inorganic Materials. *Prog. Nucl. Magn. Reson. Spectrosc.* **2014**, *77*, 1–48. <https://doi.org/10.1016/j.pnmrs.2013.10.001>.
- (21) Copéret, C.; Liao, W.-C.; Gordon, C. P.; Ong, T.-C. Active Sites in Supported Single-Site Catalysts: An NMR Perspective. *J. Am. Chem. Soc.* **2017**, *139* (31), 10588–10596. <https://doi.org/10.1021/jacs.6b12981>.
- (22) Grekov, D.; Vancompernelle, T.; Taoufik, M.; Delevoye, L.; Gauvin, R. M. Solid-State NMR of Quadrupolar Nuclei for Investigations into Supported Organometallic Catalysts: Scope and Frontiers. *Chem. Soc. Rev.* **2018**, *47* (8), 2572–2590. <https://doi.org/10.1039/C7CS00682A>.
- (23) Ashbrook, S. E.; Hodgkinson, P. Perspective: Current Advances in Solid-State NMR Spectroscopy. *J. Chem. Phys.* **2018**, *149* (4), 040901. <https://doi.org/10.1063/1.5038547>.
- (24) Massiot, D.; Messinger, R. J.; Cadars, S.; Deschamps, M.; Montouillout, V.; Pellerin, N.; Veron, E.; Allix, M.; Florian, P.; Fayon, F. Topological, Geometric, and Chemical Order in Materials: Insights from Solid-State NMR. *Acc. Chem. Res.* **2013**, *46* (9), 1975–1984. <https://doi.org/10.1021/ar3003255>.
- (25) Lilly Thankamony, A. S.; Lion, C.; Pourpoint, F.; Singh, B.; Perez Linde, A. J.; Carnevale, D.; Bodenhausen, G.; Vezin, H.; Lafon, O.; Polshettiwar, V. Insights into the Catalytic Activity of Nitridated Fibrous Silica (KCC-1) Nanocatalysts from <sup>15</sup>N and <sup>29</sup>Si NMR Spectroscopy Enhanced by Dynamic Nuclear Polarization. *Angew. Chem. Int. Ed.* **2015**, *54* (7), 2190–2193. <https://doi.org/10.1002/anie.201406463>.
- (26) Singh, B.; Mote, K. R.; Gopinath, C. S.; Madhu, P. K.; Polshettiwar, V. SBA-15-Oxynitrides as a Solid-Base Catalyst: Effect of Nitridation Temperature on Catalytic Activity. *Angew. Chem. Int. Ed.* **2015**, *54* (20), 5985–5989. <https://doi.org/10.1002/anie.201501015>.
- (27) Singh, R.; Bayal, N.; Maity, A.; Pradeep, D. J.; Trébosc, J.; Madhu, P. K.; Lafon, O.; Polshettiwar, V. Probing the Interfaces in Nanosilica-Supported TiO<sub>2</sub> Photocatalysts by Solid-State NMR and In Situ FTIR. *ChemNanoMat* **2018**, *4* (12), 1231–1239. <https://doi.org/10.1002/cnma.201800338>.
- (28) Fung, B. M.; Khitrin, A. K.; Ermolaev, K. An Improved Broadband Decoupling Sequence for Liquid Crystals and Solids. *J. Magn. Reson.* **2000**, *142* (1), 97–101. <https://doi.org/10.1006/jmre.1999.1896>.
- (29) Stejskal, E. O.; Schaefer, J.; Waugh, J. S. Magic-Angle Spinning and Polarization Transfer in Proton-Enhanced NMR. *J. Magn. Reson. (1969)* **1977**, *28* (1), 105–112. [https://doi.org/10.1016/0022-2364\(77\)90260-8](https://doi.org/10.1016/0022-2364(77)90260-8).
- (30) Meier, B. H. Cross Polarization under Fast Magic Angle Spinning: Thermodynamical Considerations. *Chem. Phys. Lett.* **1992**, *188* (3), 201–207. [https://doi.org/10.1016/0009-2614\(92\)90009-C](https://doi.org/10.1016/0009-2614(92)90009-C).
- (31) Cory, D. G.; Ritchey, W. M. Suppression of Signals from the Probe in Bloch Decay Spectra. *J. Magn. Reson. (1969)* **1988**, *80* (1), 128–132. [https://doi.org/10.1016/0022-2364\(88\)90064-9](https://doi.org/10.1016/0022-2364(88)90064-9).
- (32) Kentgens, A. P. M. A Practical Guide to Solid-State NMR of Half-Integer Quadrupolar Nuclei with Some Applications to Disordered Systems.

- Geoderma* **1997**, *80* (3), 271–306. [https://doi.org/10.1016/S0016-7061\(97\)00056-6](https://doi.org/10.1016/S0016-7061(97)00056-6).
- (33) Amoureux, J.-P.; Fernandez, C.; Steuernagel, S. ZFiltering in MQMAS NMR. *J. Magn. Reson. A* **1996**, *123* (1), 116–118. <https://doi.org/10.1006/jmra.1996.0221>.
- (34) States, D. J.; Haberkorn, R. A.; Ruben, D. J. A Two-Dimensional Nuclear Overhauser Experiment with Pure Absorption Phase in Four Quadrants. *J. Magn. Reson. (1969)* **1982**, *48* (2), 286–292. [https://doi.org/10.1016/0022-2364\(82\)90279-7](https://doi.org/10.1016/0022-2364(82)90279-7).
- (35) Amoureux, J.-P.; Fernandez, C. Triple, Quintuple and Higher Order Multiple Quantum MAS NMR of Quadrupolar Nuclei. *Solid State Nucl. Magn. Reson.* **1998**, *10* (4), 211–223. [https://doi.org/10.1016/S0926-2040\(97\)00027-1](https://doi.org/10.1016/S0926-2040(97)00027-1).
- (36) Hu, B.; Trébosc, J.; Amoureux, J. P. Comparison of Several Hetero-Nuclear Dipolar Recoupling NMR Methods to Be Used in MAS HMQC/HSQC. *J. Magn. Reson.* **2008**, *192* (1), 112–122. <https://doi.org/10.1016/j.jmr.2008.02.004>.
- (37) Lu, X.; Lafon, O.; Trébosc, J.; Tricot, G.; Delevoye, L.; Méar, F.; Montagne, L.; Amoureux, J. P. Observation of Proximities between Spin-1/2 and Quadrupolar Nuclei: Which Heteronuclear Dipolar Recoupling Method Is Preferable? *J. Chem. Phys.* **2012**, *137* (14), 144201. <https://doi.org/10.1063/1.4753987>.
- (38) Brinkmann, A.; Kentgens, A. P. M. Proton-Selective  $^{17}\text{O}$ - $^1\text{H}$  Distance Measurements in Fast Magic-Angle-Spinning Solid-State NMR Spectroscopy for the Determination of Hydrogen Bond Lengths. *J. Am. Chem. Soc.* **2006**, *128* (46), 14758–14759. <https://doi.org/10.1021/ja065415k>.
- (39) Marion, D.; Ikura, M.; Tschudin, R.; Bax, A. Rapid Recording of 2D NMR Spectra without Phase Cycling. Application to the Study of Hydrogen Exchange in Proteins. *J. Magn. Reson. 1969* **1989**, *85* (2), 393–399. [https://doi.org/10.1016/0022-2364\(89\)90152-2](https://doi.org/10.1016/0022-2364(89)90152-2).
- (40) Fu, R.; Smith, S. A.; Bodenhausen, G. Recoupling of Heteronuclear Dipolar Interactions in Solid State Magic-Angle Spinning NMR by Simultaneous Frequency and Amplitude Modulation. *Chem. Phys. Lett.* **1997**, *272* (5), 361–369. [https://doi.org/10.1016/S0009-2614\(97\)00537-X](https://doi.org/10.1016/S0009-2614(97)00537-X).
- (41) Wegner, S.; van Wüllen, L.; Tricot, G. The Structure of Phosphate and Borosilicate Glasses and Their Structural Evolution at High Temperatures as Studied with Solid State NMR Spectroscopy: Phase Separation, Crystallisation and Dynamic Species Exchange. *Solid State Sci.* **2010**, *12* (4), 428–439. <https://doi.org/10.1016/j.solidstatesciences.2009.03.021>.
- (42) Kentgens, A. P. M.; Verhagen, R. Advantages of Double Frequency Sweeps in Static, MAS and MQMAS NMR of Spin  $I=3/2$  Nuclei. *Chem. Phys. Lett.* **1999**, *300* (3), 435–443. [https://doi.org/10.1016/S0009-2614\(98\)01402-X](https://doi.org/10.1016/S0009-2614(98)01402-X).
- (43) van Meerten, S. G. J.; Franssen, W. M. J.; Kentgens, A. P. M. SsNake: A Cross-Platform Open-Source NMR Data Processing and Fitting Application. *J. Magn. Reson.* **2019**, *301*, 56–66. <https://doi.org/10.1016/j.jmr.2019.02.006>.
- (44) Torii, S.; Jimura, K.; Hayashi, S.; Kikuchi, R.; Takagaki, A. Utilization of Hexagonal Boron Nitride as a Solid Acid–Base Bifunctional Catalyst. *J. Catal.* **2017**, *355*, 176–184. <https://doi.org/10.1016/j.jcat.2017.09.013>.
- (45) Wu, J.; Qin, L.; Wang, C.; Lv, B.; Wang, L.; Chen, J.; Xu, Y. Ultrathin N-Rich Boron Nitride Nanosheets Supported Iron Catalyst for Fischer–Tropsch

- Synthesis. *RSC Adv.* **2016**, *6* (44), 38356–38364. <https://doi.org/10.1039/C6RA05517F>.
- (46) Dorn, R. W.; Ryan, M. J.; Kim, T.-H.; Goh, T. W.; Venkatesh, A.; Heintz, P. M.; Zhou, L.; Huang, W.; Rossini, A. J. Identifying the Molecular Edge Termination of Exfoliated Hexagonal Boron Nitride Nanosheets with Solid-State NMR Spectroscopy and Plane-Wave DFT Calculations. *Chem. Mater.* **2020**. <https://doi.org/10.1021/acs.chemmater.0c00104>.
- (47) Hartmeyer, G.; Marichal, C.; Lebeau, B.; Rigolet, S.; Caullet, P.; Hernandez, J. Speciation of Silanol Groups in Precipitated Silica Nanoparticles by  $^1\text{H}$  MAS NMR Spectroscopy. *J. Phys. Chem. C* **2007**, *111* (26), 9066–9071. <https://doi.org/10.1021/jp071490l>.
- (48) Kim, H. N.; Lee, S. K. Atomic Structure and Dehydration Mechanism of Amorphous Silica: Insights from  $^{29}\text{Si}$  and  $^1\text{H}$  Solid-State MAS NMR Study of  $\text{SiO}_2$  Nanoparticles. *Geochim. Cosmochim. Acta* **2013**, *120*, 39–64. <https://doi.org/10.1016/j.gca.2013.05.047>.
- (49) Trébosc, J.; Wiench, J. W.; Huh, S.; Lin, V. S.-Y.; Pruski, M. Solid-State NMR Study of MCM-41-Type Mesoporous Silica Nanoparticles. *J. Am. Chem. Soc.* **2005**, *127* (9), 3057–3068. <https://doi.org/10.1021/ja043567e>.
- (50) Vega, A. J.; Scherer, G. W. Study of Structural Evolution of Silica Gel Using  $^1\text{H}$  and  $^{29}\text{Si}$  NMR. *J. Non-Cryst. Solids* **1989**, *111* (2), 153–166. [https://doi.org/10.1016/0022-3093\(89\)90276-7](https://doi.org/10.1016/0022-3093(89)90276-7).
- (51) Koller, H.; Fild, C.; Lobo, R. F. Variable Anchoring of Boron in Zeolite Beta. *Microporous Mesoporous Mater.* **2005**, *79* (1), 215–224. <https://doi.org/10.1016/j.micromeso.2004.10.035>.
- (52) Hwang, S.-J.; Chen, C.-Y.; Zones, S. I. Boron Sites in Borosilicate Zeolites at Various Stages of Hydration Studied by Solid State NMR Spectroscopy. *J. Phys. Chem. B* **2004**, *108* (48), 18535–18546. <https://doi.org/10.1021/jp0476904>.
- (53) Wiper, P. V.; Amelse, J.; Mafra, L. Multinuclear Solid-State NMR Characterization of the Brønsted/Lewis Acid Properties in the BP HAMS-1B (H-[B]-ZSM-5) Borosilicate Molecular Sieve Using Adsorbed TMPO and TBPO Probe Molecules. *J. Catal.* **2014**, *316*, 240–250. <https://doi.org/10.1016/j.jcat.2014.05.017>.
- (54) Tong, H. T. T.; Koller, H. Control of Al for B Framework Substitution in Zeolite Beta by Counterions. *Microporous Mesoporous Mater.* **2012**, *148* (1), 80–87. <https://doi.org/10.1016/j.micromeso.2011.07.021>.
- (55) Marchetti, P. S.; Kwon, D.; Schmidt, W. R.; Interrante, L. V.; Maciel, G. E. High-Field Boron-11 Magic-Angle Spinning NMR Characterization of Boron Nitrides. *Chem. Mater.* **1991**, *3* (3), 482–486. <https://doi.org/10.1021/cm00015a023>.
- (56) Jeschke, G.; Hoffbauer, W.; Jansen, M. A Comprehensive NMR Study of Cubic and Hexagonal Boron Nitride. *Solid State Nucl. Magn. Reson.* **1998**, *12* (1), 1–7. [https://doi.org/10.1016/S0926-2040\(98\)00045-9](https://doi.org/10.1016/S0926-2040(98)00045-9).
- (57) Chen, C. Y.; Zones, S. I.; Hwang, S. J.; Bull, L. M. Studies on Physicochemical and Catalytic Properties of Borosilicate Zeolites. In *Studies in Surface Science and Catalysis*; van Steen, E., Claeys, M., Callanan, L. H., Eds.; Recent Advances in the Science and Technology of Zeolites and Related Materials Part B; Elsevier, 2004; Vol. 154, pp 1547–1554. [https://doi.org/10.1016/S0167-2991\(04\)80676-1](https://doi.org/10.1016/S0167-2991(04)80676-1).

- (58) Hough, A.; Routh, A. F.; Clarke, S. M.; Wiper, P. V.; Amelse, J. A.; Mafra, L. Boron Removal and Reinsertion Studies in  $^{10}\text{B}$ - $^{11}\text{B}$  Exchanged HAMS-1B (H-[B]-ZSM-5) Borosilicate Molecular Sieves Using Solid-State NMR. *J. Catal.* **2016**, *334*, 14–22. <https://doi.org/10.1016/j.jcat.2015.11.006>.
- (59) Koller, H. An Improved  $^1\text{H}$  NMR Spectra Interpretation of B and Al Zeolites with Dipolar Methods. *Stud. Surf. Sci. Catal.* **2004**, *154*, 1380–1384. [https://doi.org/10.1016/S0167-2991\(04\)80653-0](https://doi.org/10.1016/S0167-2991(04)80653-0).
- (60) Fild, C.; Shantz, D. F.; Lobo, R. F.; Koller, H. Cation-Induced Transformation of Boron-Coordination in Zeolites. *Phys. Chem. Chem. Phys.* **2000**, *2* (13), 3091–3098. <https://doi.org/10.1039/B002134M>.
- (61) Kroeker, S.; Stebbins, J. F. Three-Coordinated Boron-11 Chemical Shifts in Borates. *Inorg. Chem.* **2001**, *40* (24), 6239–6246. <https://doi.org/10.1021/ic010305u>.
- (62) Garaga, M. N.; Hsieh, M.-F.; Nour, Z.; Deschamps, M.; Massiot, D.; Chmelka, B. F.; Cadars, S. Local Environments of Boron Heteroatoms in Non-Crystalline Layered Borosilicates. *Phys. Chem. Chem. Phys.* **2015**, *17* (33), 21664–21682. <https://doi.org/10.1039/C5CP03448E>.
- (63) Massiot, D.; Fayon, F.; Capron, M.; King, I.; Calvé, S. L.; Alonso, B.; Durand, J.-O.; Bujoli, B.; Gan, Z.; Hoatson, G. Modelling One- and Two-Dimensional Solid-State NMR Spectra. *Magn. Reson. Chem.* **2002**, *40* (1), 70–76. <https://doi.org/10.1002/mrc.984>.
- (64) Liu, C. C.; Maciel, G. E. The Fumed Silica Surface: A Study by NMR. *J. Am. Chem. Soc.* **1996**, *118* (21), 5103–5119. <https://doi.org/10.1021/ja954120w>.
- (65) Lippmaa, E.; Maegi, M.; Samoson, A.; Engelhardt, G.; Grimmer, A. R. Structural Studies of Silicates by Solid-State High-Resolution Silicon-29 NMR. *J. Am. Chem. Soc.* **1980**, *102* (15), 4889–4893. <https://doi.org/10.1021/ja00535a008>.
- (66) Dupree, R.; Lewis, M. H.; Leng-Ward, G.; Williams, D. S. Co-Ordination of Si Atoms in Silicon-Oxynitrides Determined by Magic-Angle-Spinning NMR. *J. Mater. Sci. Lett.* **1985**, *4* (4), 393–395. <https://doi.org/10.1007/BF00719726>.
- (67) Wu, G.; Jiang, S.; Li, L.; Zhang, F.; Yang, Y.; Guan, N.; Mihaylov, M.; Knözinger, H. Physico-Chemical Characterization of Nitrided Mesoporous Silicon MCM-41. *Microporous Mesoporous Mater.* **2010**, *135* (1), 2–8. <https://doi.org/10.1016/j.micromeso.2010.06.003>.
- (68) Chino, N.; Okubo, T. Nitridation Mechanism of Mesoporous Silica: SBA-15. *Microporous Mesoporous Mater.* **2005**, *87* (1), 15–22. <https://doi.org/10.1016/j.micromeso.2005.07.034>.
- (69) Weeren, R. van; Leone, E. A.; Curran, S.; Klein, L. C.; Danforth, S. C. Synthesis and Characterization of Amorphous  $\text{Si}_2\text{N}_2\text{O}$ . *J. Am. Ceram. Soc.* **1994**, *77* (10), 2699–2702. <https://doi.org/10.1111/j.1151-2916.1994.tb04664.x>.
- (70) Asefa, T.; Kruk, M.; Coombs, N.; Grondey, H.; MacLachlan, M. J.; Jaroniec, M.; Ozin, G. A. Novel Route to Periodic Mesoporous Aminosilicas, PMAs: Ammonolysis of Periodic Mesoporous Organosilicas. *J. Am. Chem. Soc.* **2003**, *125* (38), 11662–11673. <https://doi.org/10.1021/ja036080z>.
- (71) Hayashi, F.; Ishizu, K.; Iwamoto, M. Fast and Almost Complete Nitridation of Mesoporous Silica MCM-41 with Ammonia in a Plug-Flow Reactor. *J. Am. Ceram. Soc.* **2010**, *93* (1), 104–110. <https://doi.org/10.1111/j.1551-2916.2009.03375.x>.

- (72) Cheng, R.; Liu, X.; Fang, Y.; Terano, M.; Liu, B. High-Resolution  $^{29}\text{Si}$  CP/MAS Solid State NMR Spectroscopy and DFT Investigation on the Role of Geminal and Single Silanols in Grafting Chromium Species over Phillips Cr/Silica Catalyst. *Appl. Catal. Gen.* **2017**, *543*, 26–33. <https://doi.org/10.1016/j.apcata.2017.05.011>.
- (73) Rankin, A. G. M.; Webb, P. B.; Dawson, D. M.; Viger-Gravel, J.; Walder, B. J.; Emsley, L.; Ashbrook, S. E. Determining the Surface Structure of Silicated Alumina Catalysts *via* Isotopic Enrichment and Dynamic Nuclear Polarization Surface-Enhanced NMR Spectroscopy. *J. Phys. Chem. C* **2017**, *121* (41), 22977–22984. <https://doi.org/10.1021/acs.jpcc.7b08137>.
- (74) Chuang, I. S.; Kinney, D. R.; Maciel, G. E. Interior Hydroxyls of the Silica Gel System as Studied by Silicon-29 CP-MAS NMR Spectroscopy. *J. Am. Chem. Soc.* **1993**, *115* (19), 8695–8705. <https://doi.org/10.1021/ja00072a024>.
- (75) Harris, R. K.; Leach, M. J.; Thompson, D. P. Synthesis and Magic-Angle Spinning Nuclear Magnetic Resonance of Nitrogen-15-Enriched Silicon Nitrides. *Chem. Mater.* **1990**, *2* (3), 320–323. <https://doi.org/10.1021/cm00009a025>.
- (76) Zujovic, Z. D.; Etzion, R.; Metson, J. B. Solid-State NMR Characterization of Silicon Nitride Bonded Silicon Carbide Refractories. *Ind. Eng. Chem. Res.* **2008**, *47* (24), 9913–9918. <https://doi.org/10.1021/ie800759c>.
- (77) Angel Wong, Y.-T.; Bryce, D. L. Chapter Four - Recent Advances in  $^{11}\text{B}$  Solid-State Nuclear Magnetic Resonance Spectroscopy of Crystalline Solids. In *Annual Reports on NMR Spectroscopy*; Webb, G. A., Ed.; Academic Press, 2018; Vol. 93, pp 213–279. <https://doi.org/10.1016/bs.arnmr.2017.08.005>.
- (78) Amoureux, J.-P.; Pruski, M. MQMAS NMR: Experimental Strategies and Applications. In *Encyclopedia of Magnetic Resonance*; Harris, R. K., Ed.; John Wiley & Sons, Ltd: Chichester, UK, 2007; p emrstm0319. <https://doi.org/10.1002/9780470034590.emrstm0319>.
- (79) Keeler, J. *Understanding NMR Spectroscopy*. 2nd ed., Chichester, U.K.: John Wiley and Sons, 2010.



# General conclusions

---

This PhD work focused on the development of novel solid-state NMR methods to detect half-integer quadrupolar nuclei near surfaces of materials. These methods are notably based on hetero- and homo-nuclear dipolar recoupling schemes. The main achievements and new insights can be summarized as follows.

Novel symmetry-based heteronuclear recoupling schemes built from single and composite  $\pi$  pulses have been introduced for PRESTO and *D*-RINEPT sequences. Their performances have been tested for the  $^1\text{H} \rightarrow ^{27}\text{Al}$  transfers at  $\nu_{\text{R}} = 20$  and 62.5 kHz in two samples, notably  $\gamma\text{-Al}_2\text{O}_3$  and  $\text{AlPO}_4\text{-14}$ , which exhibit low and moderate  $^1\text{H}\text{-}^1\text{H}$  dipolar interactions. As a result,  $^1\text{H}$  magnetization can be efficiently transferred to  $^{27}\text{Al}$  nuclei using *D*-RINEPT with  $\text{SR4}_1^2(270_090_{180})$  and PRESTO with  $\text{R22}_2^7(180_0)$  at  $\nu_{\text{R}} = 20$  kHz. These new recouplings have been compared to *D*-RINEPT-  $\text{SR4}_1^2$  with adiabatic pulses, which still produce efficient and robust transfers, but requires large rf fields that may not be compatible with the specifications of most MAS probes. Therefore, the introduced recouplings will prove useful in indirect DNP experiments at  $\nu_{\text{R}} = 20$  kHz and high-magnetic fields to enhance the signal of quadrupolar nuclei *via* protons. On the other hand, transfers at high MAS are also required for many NMR experiments, including indirect DNP as well as HETCOR experiments between protons and half-integer quadrupolar nuclei. *D*-RINEPT with  $\text{SR4}_1^2(270_090_{180})$  and PRESTO with  $\text{R16}_7^6(270_090_{180})$  produce robust and efficient transfers at  $\nu_{\text{R}} = 62.5$  kHz. These recouplings were demonstrated to be useful to acquire 2D  $^1\text{H}\text{-}^{27}\text{Al}$  HETCOR spectra, allowing for the correlation of the NMR signals of protons and quadrupolar nuclei. At both MAS frequencies, the RINEPT and PRESTO techniques complement each other since the latter is dipolar truncated, whereas the former is not. Consequently, the RINEPT sequences must be chosen to observe simultaneously protonated and unprotonated sites, whereas the PRESTO schemes can be employed for the selective observation of quadrupolar nuclei in proximity to protons. Further research might explore the use of these techniques using the composite  $(270_090_{180})$  pulse to detect other challenging quadrupolar nuclei with low receptivity such as  $^{17}\text{O}$  (small N.A), and/or  $^{47,49}\text{Ti}$ ,  $^{67}\text{Zn}$  and  $^{33}\text{S}$  (low gyromagnetic ratio  $\gamma$ ).

Several symmetry-based homonuclear recoupling schemes used for SQ-SQ and DQ-SQ HOMCOR sequences were analysed and compared. Their performances were evaluated simultaneously for half-integer quadrupolar nuclei with spin value  $I = 3/2$  ( $^{11}\text{B}$ ) or  $5/2$  ( $^{27}\text{Al}$ ). Notably,  $^{11}\text{B}$ - $^{11}\text{B}$  and  $^{27}\text{Al}$ - $^{27}\text{Al}$  HOMCOR experiments were performed at  $\nu_{\text{R}} = 20$  kHz on two samples,  $\text{Li}_2\text{B}_4\text{O}_7$  and  $\text{AlPO}_4$ -14, respectively. For both isotopes, the DQ-SQ sequences are recommended, which yields a good efficiency for both the cross- and auto-correlation peaks, hence providing a global analysis of the spatial proximities, even for resonances that have close or identical frequencies. In the case of  $^{11}\text{B}$ , the chemical shift differences are small or moderate, and therefore, the  $[\text{SR}2_{\frac{1}{2}}^1]$  or  $[\text{BR}2_{\frac{1}{2}}^1]$  bracketed recoupling schemes are recommended. Conversely, for  $^{27}\text{Al}$ , the chemical shift differences are larger, and can reach ca. 10 kHz at 18.8 T. In this case, the  $\text{BR}2_{\frac{1}{2}}^1$  un-bracketed recoupling scheme is recommended. The insights gained from this study may be of assistance to the observation of homonuclear correlations between half-integer quadrupolar nuclei at high magnetic fields. Before this study, the efficiency of the SQ-SQ and DQ-SQ experiments were analyzed separately. Therefore, this work appears to be the first comprehensive study that compares the performances of SQ-SQ and DQ-SQ simultaneously. However, further simulations of the spin dynamics of the spins  $I = 3/2$  and  $5/2$  are needed to understand the results obtained here and to explain the differences between the two spins. One of the possible extensions to this work would be to decrease the experimental time by using an initial CT enhancement obtained by the transfer of population from the STs to the CT.

The aim of the last part of this thesis was to investigate the surface of catalysts for the oxidative dehydrogenation of propane, notably BN and  $\text{B}_2\text{O}_3$  supported on dendritic fibrous nanosilica (DFNS). A combination of 1D and 2D multinuclear ( $^1\text{H}$ ,  $^{29}\text{Si}$  and  $^{11}\text{B}$ ) solid-state NMR methods provided new insights into the structure of both materials. These findings suggest that the supported BN phase undergoes a transformation to  $\text{B}_2\text{O}_3$  (oxidation) during the propane dehydrogenation process, whilst avoiding deactivation. The results of this study support the idea that DFNS offers a stabilizing effect through the covalent linkage of silica and  $\text{B}_2\text{O}_3$  *via* Si-O-B bonding, allowing  $\text{B}_2\text{O}_3$  to remain on the DFNS surface and act as a catalyst. The NMR methods used for this research confirmed the presence of these linkages. These findings have significant implications for the understanding of how the oxidized boron



phase is anchored to the support and how this affects the stability of the catalyst. The second major finding was the larger fraction of hydrogen-bonded BOH groups at the surface of oxidized DFNS/BN with respect to as-prepared DFNS/B<sub>2</sub>O<sub>3</sub>, evidenced by 2D <sup>1</sup>H-<sup>11</sup>B HETCOR and <sup>11</sup>B MQMAS spectra. This structural difference could explain the higher selectivity towards propene of oxidized DFNS/BN. This study has raised important questions about the nature of the hydroxyl groups and should serve as a guide for the synthesis of more efficient catalysts for the oxidative dehydrogenation of propane.

A combination of above developed solid-state NMR techniques could contribute to a better characterization of homo- and hetero-nuclear through-space proximities in various materials, notably near their surface. Therefore, this improved characterization of surfaces of materials will facilitate the rational improvement of their properties.



# Perspectives

---

## DNP-ENHANCED MQMAS EXPERIMENTS USING *D*-RINEPT TRANSFER

This thesis has focused on the development of methods to improve the detection of quadrupolar nuclei near surfaces. Chapter 2 was dedicated to the study of the transfer of polarization from  $^1\text{H}$  to quadrupolar nuclei, such as  $^{27}\text{Al}$ , based on the PRESTO and *D*-RINEPT-CWc sequences. In particular, this variant of *D*-RINEPT, *D*-RINEPT-CWc-SR4 $_1^2$ (tt), has proven to be efficient for the indirect DNP of quadrupolar nuclei of low natural abundance, such as  $^{17}\text{O}$ , or low gyromagnetic ratio, such as  $^{47,49}\text{Ti}$ , in DNP experiments at 9.4 T. In addition, it has been demonstrated that this new technique is more sensitive than both direct and indirect DNP experiments using PRESTO. Nevertheless, the CT in these *D*-RINEPT spectra are broadened by second-order quadrupolar interactions, which can mask differences in isotropic chemical shifts.

We have presented in Chapter 1 the available methods for acquiring high-resolution NMR spectra of quadrupolar nuclei, notably the MQMAS and STMAS sequences. In general, MQMAS scheme produces high-resolution spectra and is more robust and easier to set up than STMAS experiment, but its low efficiency leads to low sensitivity. In order to circumvent this issue, we explored how the MQMAS scheme can be combined with MAS-DNP. The results shown below correspond to unpublished material, which is in development, and for this reason were not included in the central work of this thesis.

The *D*-RINEPT sequence (introduced in this thesis) use on the *S* channel three CT-selective pulses: two  $\pi$ -pulses to refocus the  $^1\text{H}$  CSA and one  $\pi/2$ -pulse in the middle for the coherence transfer. At the end of the sequences, the detected *S* signal is that of the single-quantum (SQ) of the CT between energy levels  $m_I = -1/2$  and  $+1/2$ . These SQ-CT coherences are broadened by the 2<sup>nd</sup>-order quadrupolar interaction ( $H_{Q2}$ ) of *S* isotopes. This broadening can be refocused by converting the SQ-CT coherences into

triple-quantum (3Q) coherences using FAM- $N$  scheme (see Fig. 67). These 3Q coherences are converted back into SQ-CT coherences by another FAM- $N$ . The signal can be detected using QCPMG scheme in order to enhance the NMR signal.

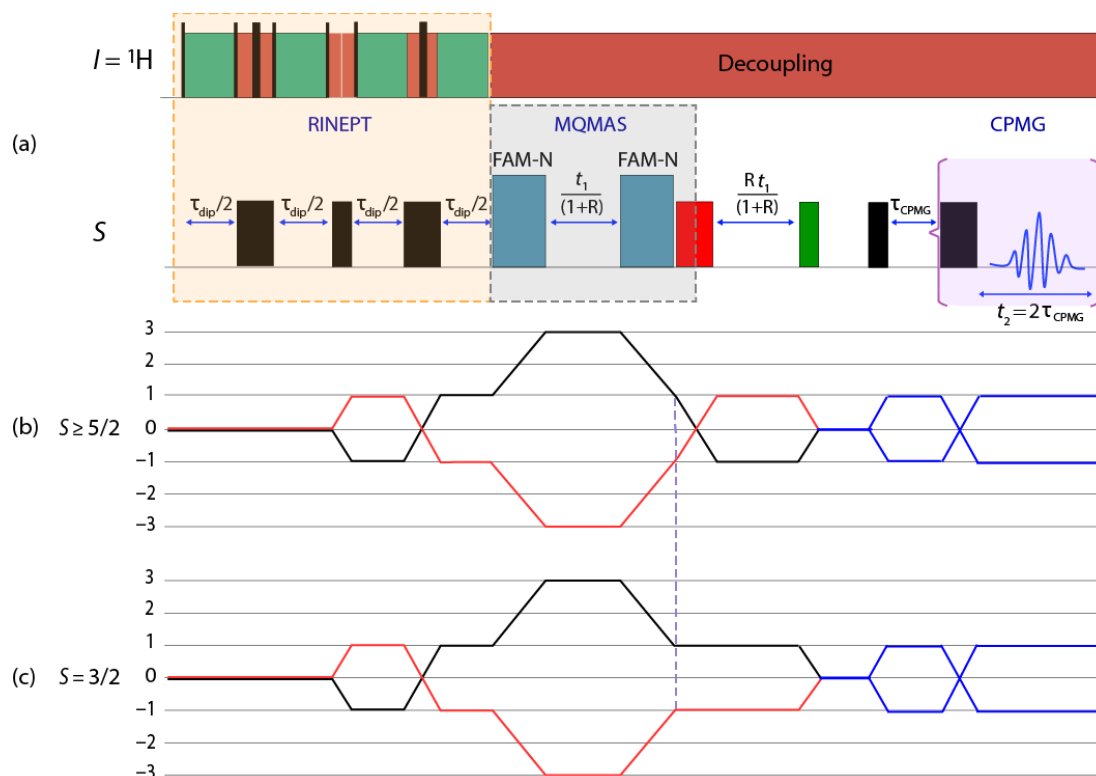


**Figure 67.**  ${}^1\text{H} \rightarrow S$   $D$ -RINEPT-MQMAS-QCPMG. (a) Pulse sequence, with the red selective  $\pi$ -pulse, just after the 2<sup>nd</sup> FAM- $N$  pulse, omitted in the case of  $S = 3/2$ . (b,c) Coherence transfer pathways for quadrupolar spin in the case of  $S \geq 5/2$  (b) or  $S = 3/2$  (c).  $R = 7/9, 19/12, 101/45, 91/36$  for  $S = 3/2, 5/2, 7/2, 9/2$ , respectively.

This  $D$ -RINEPT-MQMAS-QCPMG method was used to acquire  ${}^{11}\text{B}$  high-resolution spectra of DFNS/BN material, which were investigated in Chapter 4. The  ${}^{11}\text{B}$  MQMAS spectra presented in Fig. 68 allowed to observe NMR signals of the  ${}^{11}\text{B}$  nuclei with high resolution for this material. The isotropic projections of these 2D spectra are presented in Fig. 69. It is observed that the  $\text{BN}_3$  signal is detected in the spectrum acquired with direct excitation using the split- $t_1$  MQMAS pulse sequence, but it is absent in the  $D$ -RINEPT-MQMAS-QCPMG spectra (Fig. 68). This finding suggests that  $\text{BN}_3$  sites are remote from protons by several angstroms so that  $D$ -RINEPT cannot efficiently transfer the DNP-enhanced polarization of protons to the  $\text{BN}_3$  sites. Likewise,  $\text{BN}_2\text{OH}$  groups are not observed in the RINEPT-MQMAS

spectrum. This result can be attributed to the fact that they are not present at the surface or because their signal is too low to be detected. Therefore, these findings suggest that the  $\text{BN}_3$  and  $\text{BN}_2\text{OH}$  sites may not be found on the outermost surface of the material. For the  $^{11}\text{B}$  high-resolution MQMAS spectra acquired *D*-RINEPT-MQMAS-QCPMG with short recoupling time ( $\tau_{\text{dip}} = 320 \mu\text{s}$ ), it is possible to observe the signals of groups  $\text{BO}_2\text{OH}$  and  $\text{B}(\text{OSi}(\text{Q}^3))_x(\text{OB})_{3-x}\text{OH}$ , indicating that these sites are located on the surface of this material and are responsible of the catalytic activity of DFNS/BN. Conversely, for long recoupling time ( $\tau_{\text{dip}} = 1440 \mu\text{s}$ ), the signals of protonated  $\text{BO}_3$  sites decay, whereas only the signal of  $\text{BO}_3$  sites not bonded to OH groups are detected in the 2D  $^{11}\text{B}$  *D*-RINEPT-MQMAS spectra. These sites must be located in the subsurface of the material. Therefore, these results are of great importance and support those presented in Chapter 4.

These results demonstrate the efficiency and usefulness of the newly developed sequence and open a new way for the observation of surface and subsurface species in various materials with high resolution.

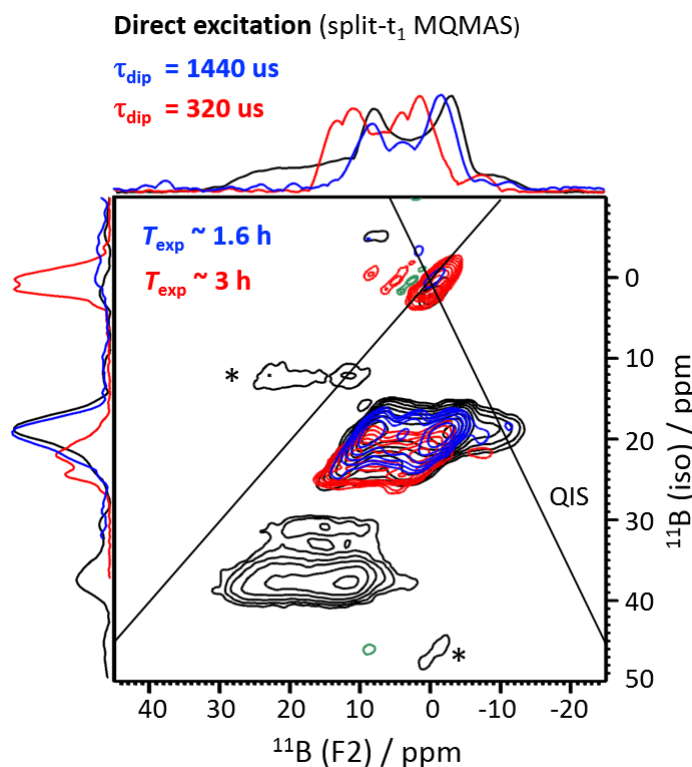


**Figure 68.** 2D  $^{11}\text{B}$  high-resolution MQMAS spectra of DFNS/BN acquired at  $\nu_{\text{R}}=10$  kHz and 9.4 T with direct excitation (split- $t_1$  MQMAS pulse sequence - in black) and

*D*-RINEPT-MQMAS-QCPMG sequence with recoupling time  $\tau_{\text{dip}} = 1440 \mu\text{s}$  (in blue) and  $320 \mu\text{s}$  (in red).

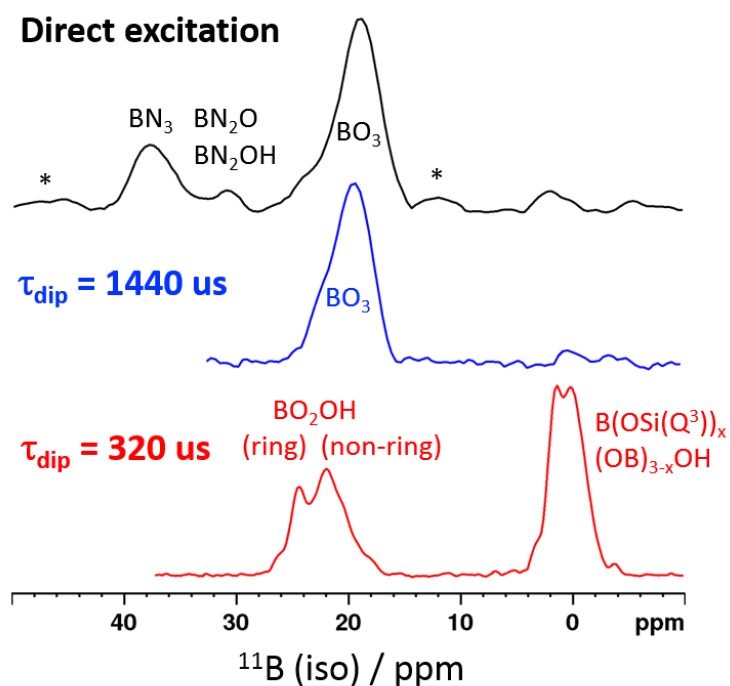


**Figure 69.** Isotropic projection of the 2D  $^{11}\text{B}$  high-resolution MQMAS spectra of DFNS/BN presented in Fig. 68.

## DNP-ENHANCED SOLID-STATE NMR OF QUADRUPOLEAR NUCLEI IN MoO<sub>3</sub>/TiO<sub>2</sub> NANOPARTICLES

MoO<sub>3</sub> supported on TiO<sub>2</sub> are important heterogeneous catalysts used for the selective oxidation of hydrocarbons and alcohols, as well as a precursor of hydrodesulfurization catalysts (HDS).<sup>1-4</sup> The catalytic activity of MoO<sub>3</sub>/TiO<sub>2</sub> is notably related to its Brønsted acidity, resulting from the presence of OH groups on their surface. However, the local environment of these OH groups, and in general, of their surface sites remains elusive.

Recently, Nagashima *et al.*<sup>5</sup> were able to record the <sup>17</sup>O, <sup>47,49</sup>Ti and <sup>95</sup>Mo NMR spectra of the surface of these catalysts, thanks to the nuclear dynamic polarization technique (DNP). These results were obtained by impregnating MoO<sub>3</sub>/TiO<sub>2</sub>(P25) catalysts with solutions of nitroxide biradicals of TEKPol type in 1,1,2,2-tetrachloroethane (TCE). TiO<sub>2</sub>(P25) nanoparticles contain anatase, rutile and amorphous phases. However, NMR and EPR experiments indicated the reduction of the radical, notably TEKPol, to hydroxylamines by reaction with these catalysts (see Fig. 70). Surprisingly, no TEKPol decomposition was observed for TiO<sub>2</sub> (P25/TiO-15) alone or when MoO<sub>3</sub> was supported on SiO<sub>2</sub> or Al<sub>2</sub>O<sub>3</sub> nanoparticles.

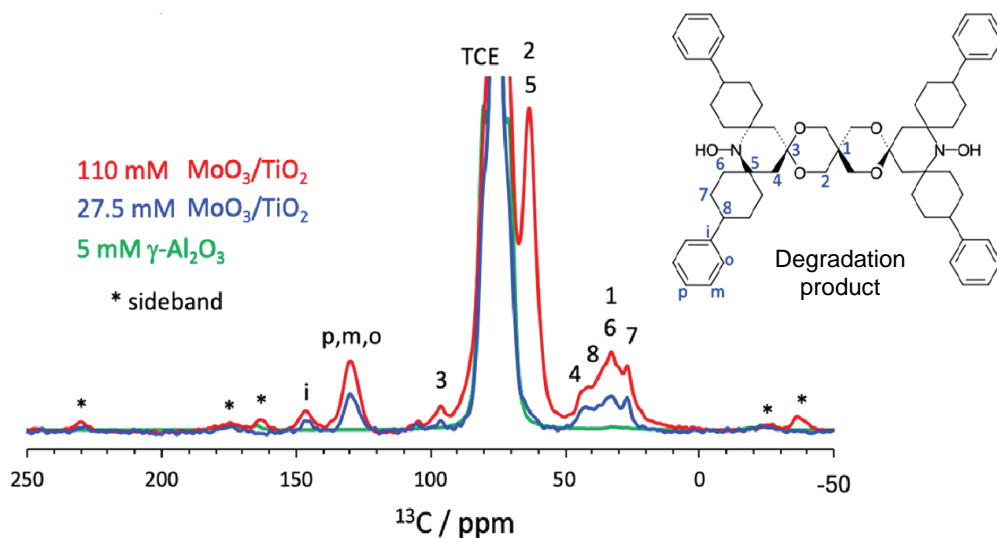


**Figure 70.** DNP-enhanced <sup>1</sup>H→<sup>13</sup>C CPMAS spectra at  $B_0 = 9.4$  T and 105 K with  $\nu_R = 10$  kHz of MoO<sub>3</sub>/TiO<sub>2</sub>(P25) impregnated with TEKPol solution in TCE.<sup>5</sup>

Furthermore, the  $^1\text{H} \rightarrow ^{17}\text{O}$  *D*-RINEPT spectra indicate the presence of both polyoxomolybdate and  $\text{MoO}_3$  nanoparticles, which complicates the analysis of  $^{17}\text{O}$ ,  $^{47,49}\text{Ti}$  and  $^{95}\text{Mo}$  NMR spectra. The DNP-enhanced  $^1\text{H} \rightarrow ^{17}\text{O}$  *D*-RINEPT spectra with short recoupling time allowed the first observation of the Brønsted acid sites of  $\text{MoO}_3/\text{TiO}_2$  corresponding to  $\text{HOMo}_2$  and  $\text{HOMoO}_3$  polyoxomolybdate (see Fig. 71). Nevertheless, the  $\text{MoOTi}$  and  $\text{Mo}_2\text{OTi}$  local environments could not be detected.

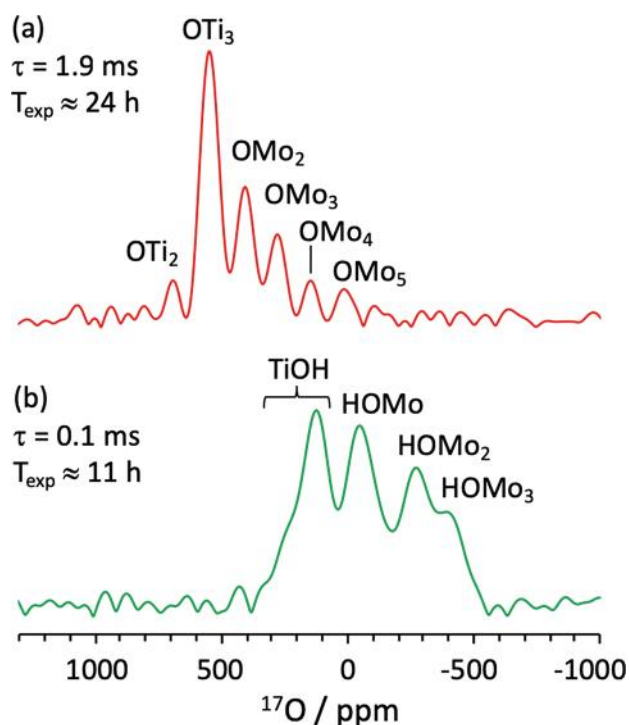


**Figure 71.** DNP-enhanced  $^1\text{H} \rightarrow ^{17}\text{O}$  RINEPT-SR4<sub>1</sub>(tt)-QCPMG spectra of isotopically unmodified  $\text{MoO}_3/\text{TiO}_2$  impregnated with 110 mM TEKPol solution in TCE with  $\tau =$  (a) 1.9 and (b) 0.1 ms at  $B_0 = 9.4$  T and  $\nu_R = 10$  kHz. The spectra are the FT of the sum of QCPMG echoes.<sup>5</sup>

The DNP-enhanced  $^1\text{H} \rightarrow ^{47,49}\text{Ti}$  *D*-RINEPT spectrum indicated that the amorphous phase is located near the surface of the particles (see Fig. 72). Nevertheless, this spectrum lacks resolution since the signals of anatase, rutile and amorphous phases as well as surface sites overlap. Furthermore, the DNP-enhanced  $^1\text{H} \rightarrow ^{95}\text{Mo}$  *D*-RINEPT spectrum shows the presence of tetra- or penta-coordinated Mo sites (not shown). Nevertheless, this spectrum again lacks resolution and the exact coordination number and location of these  $\text{MoO}_4$  or  $\text{MoO}_5$  sites was not determined.



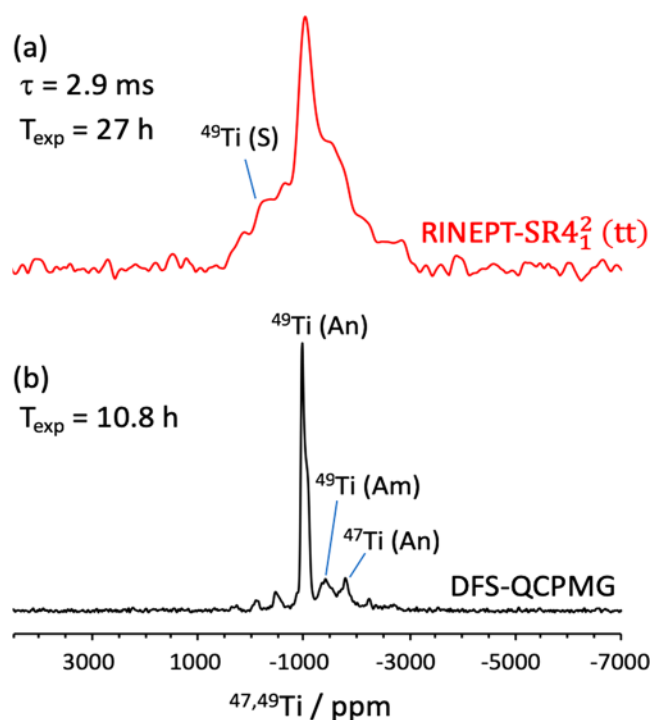


**Figure 72.**  $^{47,49}\text{Ti}$  QCPMG NMR spectra of isotopically unmodified  $\text{MoO}_3/\text{TiO}_2$  impregnated with 110 mM TEKPol solution in TCE at  $B_0 = 9.4$  T with  $\nu_R = 10$  kHz enhanced by (a) indirect DNP using  $^1\text{H} \rightarrow ^{47,49}\text{Ti}$  RINEPT-SR4<sub>1</sub><sup>2</sup>(tt) transfer with  $\tau = 2.9$  ms and (b) DFS scheme. The spectra are the FT of the sum of QCPMG echoes.<sup>5</sup>

In order to improve the characterization of the atomic-level structure of  $\text{MoO}_3/\text{TiO}_2$ , it is necessary to prepare samples with lower number of local environments and to characterize them with other techniques than DNP-NMR, including Raman and X-ray photoelectron spectroscopy. This project aims at answering several questions:

- i) which reaction degrades TEKPol? Are the electrons provided by Mo atoms with oxidation number +V or  $\text{TiO}_2$  phase? Where are located the Mo(V) species;
- ii) can  $\text{MoOTi}$  and  $\text{Mo}_2\text{OTi}$  local environments be detected by DNP-NMR?;
- iii) do the  $\text{MoO}_3/\text{TiO}_2$  contain  $\text{MoO}_4$  or  $\text{MoO}_5$  sites and where are they located?;
- iv) how does the support influence the structure of polyoxomolybdate and the amount of amorphous  $\text{TiO}_2$  phase?

## Synthesis of catalysts

We synthesized MoO<sub>3</sub>/TiO<sub>2</sub> with TiO<sub>2</sub>(rutile) support and various content of MoO<sub>3</sub> (see Table 19). Other MoO<sub>3</sub>/TiO<sub>2</sub> samples with TiO<sub>2</sub> anatase and P25 and various content of MoO<sub>3</sub>, will be synthesized as well. The surface area and porous volume of the TiO<sub>2</sub> supports were determined using N<sub>2</sub> adsorption (see Table 20).

**Table 19.** Synthesized MoO<sub>3</sub>/TiO<sub>2</sub>(rutile) catalysts with various content of MoO<sub>3</sub>.

Samples	MoO <sub>3</sub> / wt%
MoO <sub>3</sub> /TiO <sub>2</sub> (rutile)	2
	5
	7
	10
	20

**Table 20.** Specific area BET and pore volume for the various TiO<sub>2</sub> supports.

Sample	Specific area BET /m <sup>2</sup> .g <sup>-1</sup>	Pore volume in air /cm <sup>3</sup> .g <sup>-1</sup>	Porous volume in water /mL.g <sup>-1</sup>
TiO <sub>2</sub> (rutile)	89.46	0.485	1.00
TiO <sub>2</sub> (P25)	47.05	0.126	0.60
TiO <sub>2</sub> (anatase)	76.13	0.318	0.71

The MoO<sub>3</sub>/TiO<sub>2</sub>(rutile) catalysts (Table 20) were prepared by impregnation of TiO<sub>2</sub>(rutile) with an aqueous solution containing a known quantity of (NH<sub>4</sub>)<sub>6</sub>Mo<sub>7</sub>O<sub>24</sub>·4H<sub>2</sub>O (HMA). The samples were dried at 80°C for 48 h, followed by calcination in air at 450°C for 3 h.

## Raman

Raman spectroscopy allows easily distinguishing the MoO<sub>3</sub> particles and polyoxomolybdates in these materials since they give distinct Raman resonances (see Fig. 73). Polyoxomolybdates are the active phase of the MoO<sub>3</sub>/TiO<sub>2</sub> catalysts and responsible for their catalytic activity. MoO<sub>3</sub>/TiO<sub>2</sub>(rutile) catalysts with various content of MoO<sub>3</sub> were characterized by Raman. As seen in Fig. 74, Raman spectra reveal the presence of polyoxomolybdates for 7 wt% MoO<sub>3</sub>/TiO<sub>2</sub>(rutile) and 10 wt% MoO<sub>3</sub>/TiO<sub>2</sub>(rutile) samples, possibly species of type Mo<sub>7</sub>O<sub>24</sub><sup>6-</sup> and Mo<sub>8</sub>O<sub>26</sub><sup>4-</sup>. For 2

wt% MoO<sub>3</sub>/TiO<sub>2</sub>(rutile) Raman spectrum reveals the presence of MoO<sub>4</sub><sup>2-</sup> (monomer). These results indicate that samples prepared with 7 and 10 wt% MoO<sub>3</sub> content give rise to a higher proportion of dispersed polyoxomolybdates and are suitable for indirect DNP experiments.

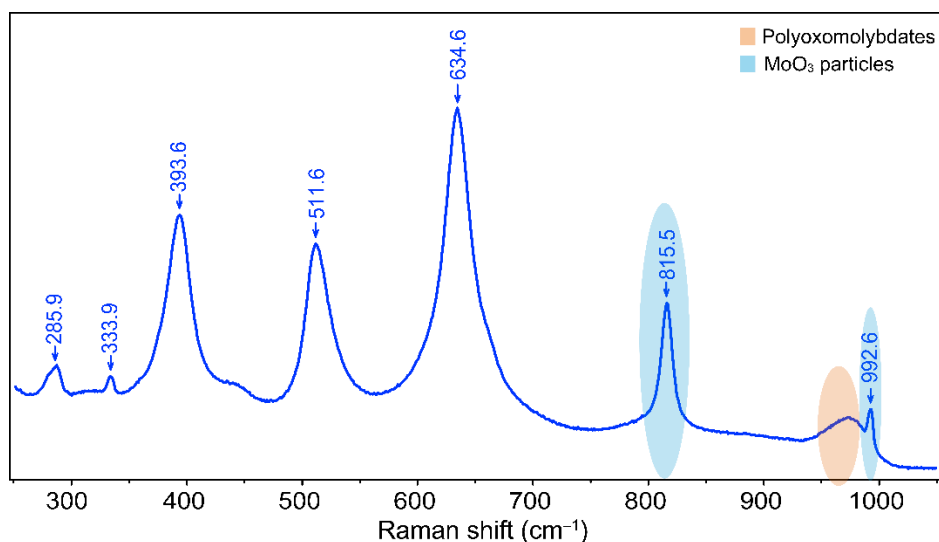


**Figure 73.** Raman spectrum of MoO<sub>3</sub>/TiO<sub>2</sub>(P25). The signals corresponding to the MoO<sub>3</sub> particles are observed at ~815 and 992 cm<sup>-1</sup>, while the signal from the polyoxomolybdates phase appears at ~980 cm<sup>-1</sup>.

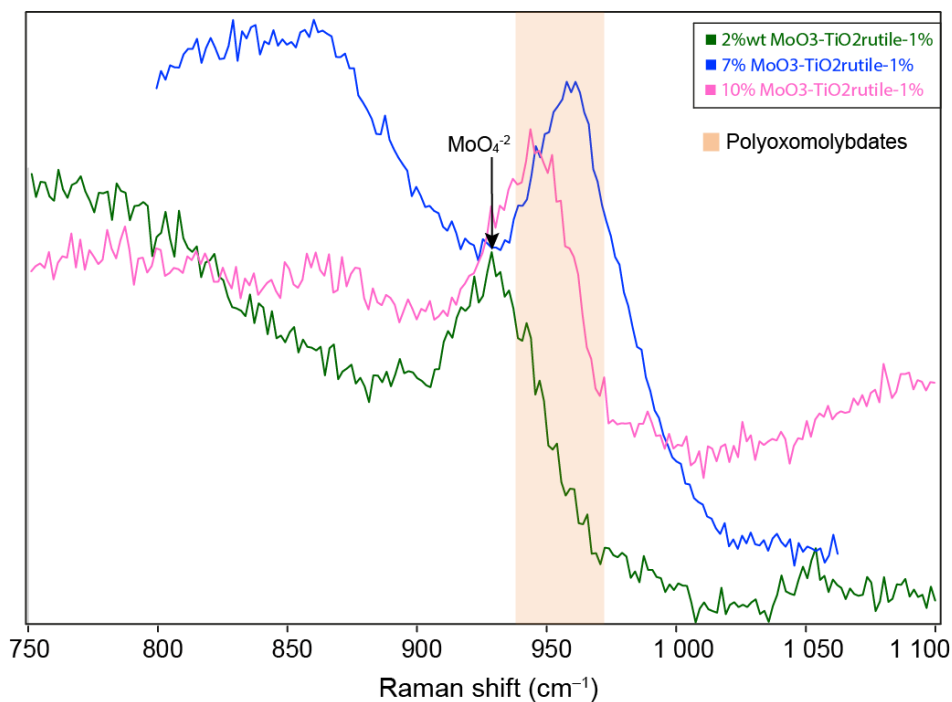


**Figure 74.** Raman spectrum of MoO<sub>3</sub>/TiO<sub>2</sub>(rutile) with 2, 7 and 10 %wt content of MoO<sub>3</sub>.

## XPS

XPS spectra were acquired to detect Mo(V) sites and check if these sites are involved in the degradation of TEKPol. As seen in Fig. 75, XPS spectrum of pristine MoO<sub>3</sub>/TiO<sub>2</sub>(P25) reveals the presence of Mo(V) atoms. The integrated intensity of this site amounts to 5.1% of the total integrated intensity of Mo 3d XPS spectrum.

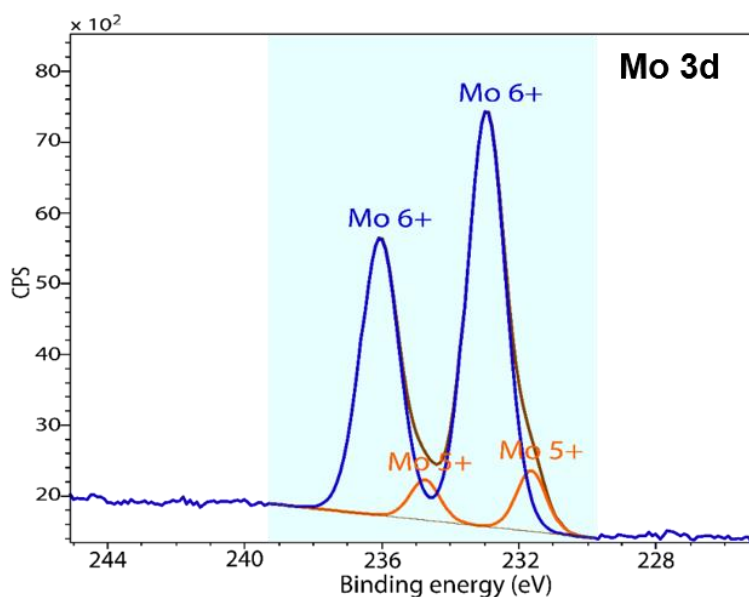


**Figure 75.** Mo 3d XPS spectrum of MoO<sub>3</sub>/TiO<sub>2</sub>(P25) indicating the presence of Mo(V) and Mo(VI) species.

XPS was also used to determine if the proportion of these Mo(V) atoms decreases when these samples are impregnated with a TEKPol solution, which would indicate that Mo(V) atoms reduce TEKPol molecules. Two samples were used for these experiments: 10% wt MoO<sub>3</sub>/TiO<sub>2</sub>(rutile) and 10 wt% MoO<sub>3</sub>/TiO<sub>2</sub>(P25), which were impregnated with 58 mM and 71 mM of TEKPol solution, respectively. The proportion of Mo(V) species detected before and after impregnation is listed in Table 21.

After impregnation, the amount of Mo(V) detected for both MoO<sub>3</sub>/TiO<sub>2</sub> (P25) and MoO<sub>3</sub>/TiO<sub>2</sub> (rutile) are reduced by 2.6 and 1.7%, respectively. This result suggests that TEKPol radical reacts with Mo(V) sites. An open question is whether these Mo(V) sites are only located in MoO<sub>3</sub> particles or also in polyoxomolybdate. No other significant changes for other elements before and after impregnation are observed.

**Table 21.** Proportion of Mo(V) species found in MoO<sub>3</sub>/TiO<sub>2</sub> catalysts before and after impregnation with TEKPol solutions.

Sample	Amount of Mo(V) species before impregnation (%)	Amount of Mo(V) species after impregnation (%)
10 wt% MoO <sub>3</sub> /TiO <sub>2</sub> (rutile)	4.2	2.5
10 wt% MoO <sub>3</sub> /TiO <sub>2</sub> (P25)	5.1	2.5

### DNP at high field

In order to improve the resolution of <sup>17</sup>O NMR spectra of MoO<sub>3</sub>/TiO<sub>2</sub>, we also performed DNP-enhanced NMR experiments on this sample at 18.8 T since high magnetic field reduce the second-order quadrupole broadening. We recorded the <sup>17</sup>O NMR spectrum at 18.8 T of MoO<sub>3</sub>/TiO<sub>2</sub>(P25) impregnated with 110 mM TEKPol solution in TCE using DFS-QCPMG sequence and enhanced by direct DNP (see Fig. 76). This spectrum exhibits signals of OMo<sub>4</sub>, OMo<sub>5</sub> and HOMo sites. Nevertheless, no signal was detected for <sup>1</sup>H→<sup>17</sup>O *D*-RINEPT-CWc-SR4<sub>1</sub><sup>2</sup>(tt) experiment owing to the lower DNP enhancement ( $\epsilon_{\text{on/off}} = 9$ ) and longer build-up time ( $\tau_{\text{RD}} = 2.9$  s) at 18.8 T, instead of  $\epsilon_{\text{on/off}} = 76$  and  $\tau_{\text{RD}} = 1$  s at 9.4 T. We also impregnated MoO<sub>3</sub>/TiO<sub>2</sub>(P25) nanoparticles with solution of AsympolPOK<sup>6</sup> nitroxide biradical in [<sup>2</sup>H<sub>8</sub>]-glycerol/<sup>2</sup>H<sub>2</sub>O/H<sub>2</sub>O mixture with volume fractions 60/30/10 v/v/v. This radical solution leads to slightly higher DNP enhancement of <sup>1</sup>H signal ( $\epsilon_{\text{on/off}} = 11$ ) and shorter build-up times ( $\tau_{\text{RD}} = 1.5$  s) than those measured for TEKPol solution in TCE. Nevertheless, <sup>1</sup>H→<sup>17</sup>O *D*-RINEPT-CWc-SR4<sub>1</sub><sup>2</sup>(tt) spectrum of this sample only exhibits the <sup>17</sup>O signal of water. In the future, we plan to test other radicals, such as HyTEK2<sup>7</sup> in TCE, in order to improve the sensitivity.

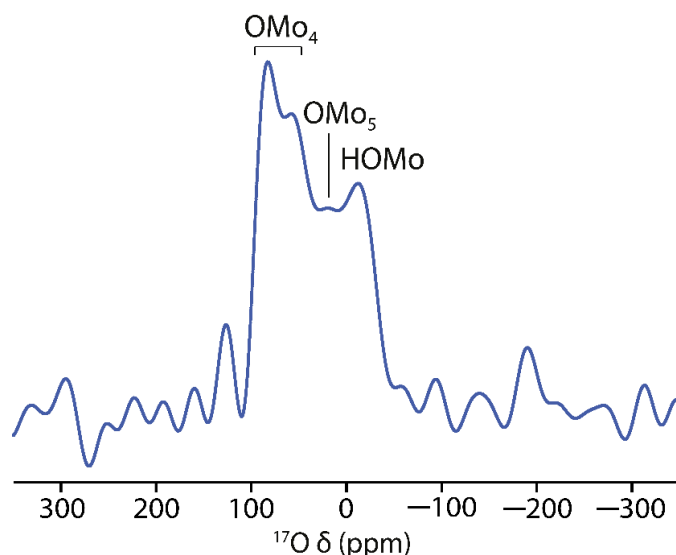


**Figure 76.** DNP-enhanced  $^{17}\text{O}$  DFS-QCPMG NMR spectrum of  $\text{MoO}_3/\text{TiO}_2(\text{P25})$  impregnated with 110 mM TEKPol solution in TCE acquired at  $B_0 = 18.8$  T and  $\nu_R = 10$  kHz.

## References

- (1) Edwards, J. C.; Adams, R. D.; Ellis, P. D. A Molybdenum-95 Solid-State NMR Study of Hydrodesulfurization Catalysts. 1. Formation of Fresh HDS Catalyst Precursors by Adsorption of Polyoxomolybdates onto Gamma-Alumina. *J. Am. Chem. Soc.* **1990**, *112* (23), 8349–8364. <https://doi.org/10.1021/ja00179a020>.
- (2) d’Espinose de Lacaillerie, J.-B.; Gan, Z. MAS NMR Strategies for the Characterization of Supported Molybdenum Catalysts. *Appl. Magn. Reson.* **2007**, *32* (4), 499–511. <https://doi.org/10.1007/s00723-007-0033-0>.
- (3) Liu, K.; Huang, X.; Pidko, E. A.; Hensen, E. J. M.  $\text{MoO}_3$ – $\text{TiO}_2$  Synergy in Oxidative Dehydrogenation of Lactic Acid to Pyruvic Acid. *Green Chem.* **2017**, *19* (13), 3014–3022. <https://doi.org/10.1039/C7GC00807D>.
- (4) Kon, Y.; Fujitani, T.; Nakashima, T.; Murayama, T.; Ueda, W. Versatile Etherification of Alcohols with Allyl Alcohol by a Titanium Oxide-Supported Molybdenum Oxide Catalyst: Gradual Generation from Titanium Oxide and Molybdenum Oxide. *Catal. Sci. Technol.* **2018**, *8* (18), 4618–4625. <https://doi.org/10.1039/C8CY00613J>.
- (5) Nagashima, H.; Trébosc, J.; Kon, Y.; Sato, K.; Lafon, O.; Amoureux, J.-P. Observation of Low- $\gamma$  Quadrupolar Nuclei by Surface-Enhanced NMR Spectroscopy. *J. Am. Chem. Soc.* **2020**, *142* (24), 10659–10672. <https://doi.org/10.1021/jacs.9b13838>.
- (6) Mentink-Vigier, F.; Marin-Montesinos, I.; Jagtap, A. P.; Halbritter, T.; van Tol, J.; Hediger, S.; Lee, D.; Sigurdsson, S. Th.; De Paëpe, G. Computationally Assisted Design of Polarizing Agents for Dynamic Nuclear Polarization Enhanced NMR: The AsymPol Family. *J. Am. Chem. Soc.* **2018**, *140* (35), 11013–11019. <https://doi.org/10.1021/jacs.8b04911>.
- (7) Wissler, D.; Karthikeyan, G.; Lund, A.; Casano, G.; Karoui, H.; Yulikov, M.; Menzildjian, G.; Pinon, A. C.; Porea, A.; Engelke, F.; Chaudhari, S. R.; Kubicki, D.; Rossini, A. J.; Moroz, I. B.; Gajan, D.; Copéret, C.; Jeschke, G.; Lelli, M.; Emsley, L.; Lesage, A.; Ouari, O. BDPA-Nitroxide Biradicals Tailored for Efficient Dynamic Nuclear Polarization Enhanced Solid-State NMR at Magnetic Fields up to 21.1 T. *J. Am. Chem. Soc.* **2018**, *140* (41), 13340–13349. <https://doi.org/10.1021/jacs.8b08081>.

# Curriculum vitae

---

## Jennifer Sarely GÓMEZ BADILLO

Nationality: Colombian · Date of birth: 6 May 1991  
Université de Lille, CNRS UMR 8181, UCCS, 59652 Villeneuve d'Ascq, France  
jennifer.gomezbadillo.etu@univ-lille.fr  
saregomez0506@gmail.com  
linkedin.com/in/jennifer-gomez-badillo

### Education:

2018-2021. **Ph.D. Materials Chemistry**: Development of high-field (DNP)-NMR methods to detect quadrupolar nuclei on surfaces.

2015-2018. **M.Sc. Chemistry**: Study of the effect of the deactivation conditions of fluidized catalytic cracking catalysts by solid state NMR.

2007-2015. **B.Sc. Chemistry**: Synthesis of 8-nitro-2-propyl-1,2,3,4-tetrahydrolepidines by basic hydrolysis and study of their oxidation with sulphur.

### Professional experience:

**2021-2022. Postdoctoral researcher**: Radboud University. Nijmegen, Netherlands.

**2018-2021. Junior researcher**: University of Lille, France. Project funded by the European Soft Matter Infrastructure EUSMI (H2020 INFRAIA 2016-eusmi-h2020.eu).

**2017 (3 months) Research intern**: Interdisciplinary Nanoscience Center - Aarhus University, Denmark. Travel stipend from ECOPETROL (Colombian Petrol Company).

**2016-2017. Young research and innovator**: Industrial University of Santander, Colombia  
Set-up of a national collaboration: 1-year project funded by COLCIENCIAS (Colombian Department of Science, Technology and Innovation)

### Publications:

1) R. Belgamwar, A. G. M. Rankin, A. Maity, A. K. Mishra, J. S. Gómez, J. Trébosc, C. P. Vinod, O. Lafon, V. Polshettiwar. Boron Nitride and Oxide Supported on Dendritic Fibrous Nanosilica for Catalytic Oxidative Dehydrogenation of Propane. *ACS Sustainable Chem. Eng.*, **2020**, 8, 43, 16124–16135. DOI: <https://doi.org/10.1021/acssuschemeng.0c04148>.

2) J.S. Gómez, A. G. M. Rankin, J. Trébosc, F. Pourpoint, Y. Tsutsumi, H. Nagashima, O. Lafon, J.-P. Amoureux. Improved NMR transfer of magnetization from protons to half-integer spin quadrupolar nuclei at moderate and high MAS frequencies. *Magn. Reson.*, **2021**, 2(1), 447-464. DOI: <https://doi.org/10.5194/mr-2-447-2021>.

3) H. Nagashima, J. Trébosc, J. S. Gómez, O. Lafon, J.-P. Amoureux. High-resolution MQMAS spectra of half-integer quadrupolar nuclei observed with DNP. (In preparation).

4) J. S. Gómez, J. Trébosc, N. T. Duong, O. Lafon, J.-P. Amoureux. Comparison of double and single quantum dipolar NMR correlations of quadrupolar nuclei. (In preparation).

### Presentations:

**2021. J. S. Gómez**, A. G. M. Rankin, J. Trébosc, F. Pourpoint, H. Nagashima, O. Lafon, J.-P. Amoureux Comparison of different methods to transfer <sup>1</sup>H magnetization to half-integer quadrupolar nuclei in solid-state NMR. ENC conference 2021 – virtual meeting. Poster.

**2020.** J. S. Gómez, J. Trébosc, F. Pourpoint, H. Nagashima, O. Lafon, J-P. Amoureux. Probing the surface of colloidal particles by transferring magnetization magnetization from protons to half-integer quadrupolar nuclei. EUSMI user meeting 2020 – virtual meeting. Poster.

**2018.** J. C. Poveda, J. S. Gómez, D. Molina, A. Guzmán. Probing the acidity in FCC catalysts by TMP/TPPO and solid-state NMR Small Molecule NMR Conference SMASH - Philadelphia, E.U. Poster.

**2017.** J. S. Gómez, J. C. Poveda, D. Molina, A. Guzmán. Small probe molecules, Trimethylphosphine and  $^{15}\text{N}$ -Acetonitrile, as probes of acidity in FCC catalysts. Small Molecule NMR Conference SMASH - Baveno, Italy. Poster.

**2014.** J. S. Gómez, S. Flórez, J. M. Urbina. One-pot telescoping synthesis of *N*-acetyl-4-methyl-8-nitro-2-propyl-1,2,3,4-tetrahydroquinolines and its hydrolysis product. 31 Latin American Chemistry Congress CLAQ-2014. XXVII Peruvian Congress of Chemistry. Lima, Peru. Poster.



# Appendices

---

## Appendix A

### A.1. SIMPSON input file for $D$ -RINEPT-CWc-SR4<sub>1</sub><sup>2</sup>(tt)

```
spinsys {
  channels 1H 13C
  nuclei 1H 13C 1H 1H 1H
# single pair
  shift 1 0 6000 0 0 30 0
  dipole 1 2 -2575 0 0 0
# 2 1H
  shift 3 0 6000 0 0 30 0
  dipole 3 2 0 0 109 0
  dipole 1 3 -7000 0 109 0
# 3 1H
  shift 4 0 6000 0 0 30 0
  dipole 4 2 0 0 109 120
  dipole 1 4 -7000 0 109 120
  dipole 3 4 -7000 0 90 30
# 4 1H
  shift 5 0 6000 0 0 30 0
  dipole 5 2 0 0 109 240
  dipole 1 5 -7000 0 109 240
  dipole 3 5 -7000 0 90 90
  dipole 4 5 -7000 0 90 330
}

par {
  proton_      frequency 400e6
  spin_rate    12500
  sw           spin_rate/2.0
  np          30
  crystal_file rep66
  gamma_angles 7
  start_operator I1z
  detect_operator I2p
  verbose     1101
  variable HRF 100000
  variable DRF 92000
  variable CRF 100000
  variable RFmax spin_rate*11
  variable offmax 2000000
  variable I    1.0/2.0
}

proc gen_tanhtan_shape {pulse_length steps offmax xi K} {
# generate a tanhtan shape with given :
# pulse_length : length of ulse in us
```

```

# steps : number of steps defining the shape
# offset : maximum frequency offset of tanhtan sweep
# xi : tanhtan xi parameter
# K : tanhtan kappa parameter
set nhalf [expr $steps/2]
set amp_list [list ]
set phase_list [list ]
for {set i 0} {$i < $steps} {incr i} {
  set x [expr 1.0*$i/(1.0*$steps)]
  if {$i < $nhalf} {
    lappend amp_list [expr tanh(2*$xi*$x)]
  } else {
    lappend amp_list [expr tanh(2*$xi*(1-$x))]
  }
  lappend phase_list [expr -360*$offmax*$pulse_length*(1e-6)*log(abs(cos($K*(1-2*$x))))/(2*tan($K)*$K)]
}
set Tinc [expr 1.0*$pulse_length/$steps]
return [list $amp_list $phase_list $Tinc]
}

```

```

proc tanhtan_pulse {shape RF phase} {
# generate simpson pulse following shape argument containing amplitude and phase lists
# shape: as generated by gen_tanhtan_shape procedure
# RF : global maximum RFfield of shape
# phase : global phase of shape
  set amp_list [lindex $shape 0]
  set phase_list [lindex $shape 1]
  set Tinc [lindex $shape 2]
  foreach amp $amp_list phi $phase_list {
    pulse $Tinc [expr $amp*$RF] [expr $phase+$phi] 0 0
  }
}

```

```

proc pulseseq {} {
  global par
  maxdt 6.0

  set H90 [expr 0.25e6/$par(HRF)]
  set H180 [expr 0.50e6/$par(HRF)]
  set C90 [expr 0.25e6/$par(CRF)]
  set C180 [expr 0.50e6/$par(CRF)]
  set Taur [expr 1.0e6/$par(spin_rate)]
  set Td90 [expr 0.5e6/$par(spin_rate)-$H90/2]
  set Td180 [expr 0.5e6/$par(spin_rate)-$H180/2]
  # RN_n^nu parameters
  set N 4.
  set nu 2.
  # set n 1.
  set php [expr 180*$nu/$N]
  set S90 [expr 0.25e6/$par(RFmax)]
  set S180 [expr 0.50e6/$par(RFmax)]

  set n 100

```

```

set Tp [expr 0.25*$Taur]
set Tpd [expr 0.25*$Taur]
# set Q 7.7
set xi 10.0
set K atan(20)
set pi [expr atan(1)*4]

set shape [gen_tanhtan_shape $Tp $n $par(offmax) $xi $K ]

set ph1 0
set ph2 120
set ph3 240

# SR4 using tanhtan inversion
# full block with supercycling
set superCycling {0 180 120 300 240 60}
reset
foreach ph1 $superCycling {
reset
for {set s 0} {$s<$N/2} {incr s} {
    delay [expr $Tpd/2-$Tp/2]
    tanhtan_pulse $shape $par(RFmax) [expr $php+$ph1]
    delay [expr $Tpd/2-$Tp/2]
    delay [expr $Tpd/2-$Tp/2]
    tanhtan_pulse $shape $par(RFmax) [expr -$php+$ph1]
    delay [expr $Tpd/2-$Tp/2]
}
store $ph1
}

reset [expr -$H90]
pulse $H90 $par(HRF) 90 0 0
# pulse $Td90 $par(DRF) 0 0 0
store 19

reset
pulse $Td180 $par(DRF) 0 0 0
pulse $H180 $par(HRF) 0 $par(CRF) 0
pulse $Td180 $par(DRF) 180 0 0
store 20

reset
pulse $Td90 $par(DRF) 0 0 0
pulse $H90 $par(HRF) 0 $par(CRF) 0
pulse $Td90 $par(DRF) 180 0 0
store 21

reset
pulse $Td180 $par(DRF) 0 0 0
pulse $H180 $par(HRF) 0 $par(CRF) 0
pulse $Td180 $par(DRF) 180 0 0
store 22

reset

```

```

# prop [expr (0%[llength $superCycling])*[lindex $superCycling 1]]
  prop [lindex $superCycling 0]
store 10

for {set i 0} {$i < $par(np)} {incr i} {
#reset
reset [expr -$H90]
# pulseid $H90 $par(HRF) 90 0 0
prop 19
prop 10
prop 20
prop 10
prop 21
prop 10
prop 22
prop 10
pulse [expr $Taur/2.0] $par(DRF) 0 0 0
acq

reset
prop 10
# puts [expr ((i+1)%[llength $superCycling])*[lindex $superCycling 1]]
# prop [expr ((i+1)%[llength $superCycling])*[lindex $superCycling 1]]
prop [lindex $superCycling [expr ((i+1)%6)]]
store 10

}
}

proc main {} {
global par

set FileRe [open "$par(name)-Re.res" w]
set FileIm [open "$par(name)-Im.res" w]
set FileAbs [open "$par(name)-Abs.res" w]

set f [fsimpson]
set c 0
for {set i 1} {$i <= $par(np)} {incr i} {
incr c
set Sr [findex $f $c -re]
set Si [findex $f $c -im]
puts $FileRe "[expr 1.0e3*$i/$par(sw)] [expr $Sr]"
puts $FileIm "[expr 1.0e3*$i/$par(sw)] [expr $Si]"
puts $FileAbs "[expr 1.0e3*$i/$par(sw)] [expr sqrt($Sr**2+$Si**2)]"
}
funload $f
close $FileRe
close $FileIm
close $FileAbs
}

```

## A.2. SIMPSON input file for *D-HOMCOR-DQ-SQ-BR2<sub>1</sub><sup>2</sup>*

```
#Homonuclear correlation
#Dipolar recoupling sequences
#Nghia_June2020
#Modified_JGomez_10_Feb_2021
#BR2^1_2
#Autocorrelation peak (delta V_iso=0 kHz) BO3

spinsys {
  channels          11B
  nuclei            11B 11B
  shift             1 1500 0p   0 0 0 0
  shift             2 1500 0p   0 0 0 0
  quadrupole        1 2 2.6e6 0.2 10 20 30
  quadrupole        2 2 2.6e6 0.2 31 42 53
  dipole            1 2 -269    0 0 0
}

par {
  proton_frequency  800e6
  spin_rate         20000
  start_operator    I1z
  detect_operator   0.247*I2c

# the factor of 0.247 is for normalized to single pulse
# you run the file 11B-11B_single-pulse.in
# inverse the value in 11B-11B_single-pulse.fid

  np                51
  sw                spin_rate/4.0
  crystal_file      zcw143
  gamma_angles     15
  method            direct
  verbose           1111
  variable I        1.5
  variable CQ1      2.6e6
  variable CQ2      2.6e6
  variable eta      0.2
  conjugate_fid     false
}

proc pulseseq {} {
  global par
  maxdt 1

  set rf             [expr $par(spin_rate)/(2*$par(I)+1.0)]
  set t180           [expr 1.0e6/$par(spin_rate)]
  set tau            [expr ($t180-31.25)/2.0]

  reset
  pulse $t180 $rf 90
  pulse $t180 $rf 270
  store 10
}
```

```

reset
pulse $t180 $rf 270
pulse $t180 $rf 90
store 11

matrix set 2 coherence {{-1 -1} {+1 +1}}
matrix set 3 coherence {{+1 +1} {-1 -1}}
matrix set 4 coherence {{0 0}}

reset
acq

for {set i 1} {$i < $par(np)} {incr i} {
reset
  prop 10 $i
  prop 11 $i
  filter 2
  delay $tau
  pulse 31.25 8000 0
  filter 3
  delay $tau
  prop 10 $i
  prop 11 $i
  filter 4
  pulse 15.625 8000 90
  acq
}
}

proc main {} {
  global par

  set FileRe [open "$par(name)-Re.res" w]
  set FileIm [open "$par(name)-Im.res" w]
  set FileAbs [open "$par(name)-Abs.res" w]

  set Larmor [resfreq 11B $par(proton_frequency)]
  set QIS1 [expr -
25000*(1+$par(eta)*$par(eta)/3.0)*($par(CQ1)/$Larmor)*($par(CQ1)/$Larmor)*($Larmor/
1.0e6)]
  set QIS2 [expr -
25000*(1+$par(eta)*$par(eta)/3.0)*($par(CQ2)/$Larmor)*($par(CQ2)/$Larmor)*($Larmor/
1.0e6)]

  set f [fsimpson [list [list shift_1_iso [expr ($QIS1+$QIS2)/2-(-3000)]] [list shift_2_iso
[expr ($QIS1+$QIS2)/2-(-3000)]]]]
  set c 0
  for {set i 1} {$i <= $par(np)} {incr i} {
  incr c
  set Sr [findex $f $c -re]
  set Si [findex $f $c -im]
  puts $FileRe "[expr 1.0e3*$i/$par(sw)] [expr $Sr]"
  puts $FileIm "[expr 1.0e3*$i/$par(sw)] [expr $Si]"
}
}

```

```

    puts $FileAbs "[expr 1.0e3*$/par(sw)] [expr sqrt($Sr**2+$Si**2)]"
  }
  funload $f
  close $FileRe
  close $FileIm
  close $FileAbs
}

```

### A.3. SIMPSON input file for $D$ -HOMCOR-SQ-SQ- $(SR_2^1)_4$

```

#Homonuclear correlation
#Dipolar recoupling sequences
#Nghia_June2020
#Modified_JGomez_15_Feb_2021
#SQ-SQ (SR212)4
#Autocorrelation peak (delta V_iso=0 kHz) BO3

spinsys {
  channels          11B
  nuclei            11B 11B
  shift             1 -500 0p    0 0 0 0
  shift             2 -500 0p    0 0 0 0
  quadrupole        1 2 2.6e6     0.2 10 20 30
  quadrupole        2 2 2.6e6     0.2 31 42 53
  dipole            1 2 -269      0 0 0
}

par {
  proton_frequency  800e6
  spin_rate         20000
  start_operator    I1z
  detect_operator   0.247*I2c
  np               151
  sw               spin_rate/4.0
  crystal_file     zcw143
  gamma_angles     15
  method           direct
  verbose          1111
  variable I       1.5
  variable CQ1     2.6e6
  variable CQ2     2.6e6
  variable eta     0.2
  conjugate_fid    false
}

proc pulseseq {} {
  global par
  maxdt 1

  set rf [expr $par(spin_rate)/(2*$par(I)+1.0)]
  set t180 [expr 1.0e6/$par(spin_rate)]
  set t360 [expr $t180*2.0]

  reset [expr 15.625*2]
}

```

```

pulse $t180 $rf 90
pulse $t360 $rf 270
pulse $t180 $rf 90

pulse $t180 $rf 180
pulse $t360 $rf 0
pulse $t180 $rf 180

pulse $t180 $rf 270
pulse $t360 $rf 90
pulse $t180 $rf 270

pulse $t180 $rf 0
pulse $t360 $rf 180
pulse $t180 $rf 0
store 13

matrix set 1 coherence {{-1 0} {+1 0} {0 -1} {0 +1}}

for {set i 0} {$i < $par(np)} {incr i} {
  reset
pulse 15.625 8000 90
  filter 1
  pulse 15.625 8000 270
prop 13 $i
  pulse 15.625 8000 90
  acq
}
}

proc main {} {
  global par

  set FileRe [open "$par(name)-Re.res" w]
  set FileIm [open "$par(name)-Im.res" w]
  set FileAbs [open "$par(name)-Abs.res" w]

  set Larmor [resfreq 11B $par(proton_frequency)]
  set QIS1 [expr -
25000*(1+$par(eta)*$par(eta)/3.0)*($par(CQ1)/$Larmor)*($par(CQ1)/$Larmor)*($Larmor/
1.0e6)]
  set QIS2 [expr -
25000*(1+$par(eta)*$par(eta)/3.0)*($par(CQ2)/$Larmor)*($par(CQ2)/$Larmor)*($Larmor/
1.0e6)]

  set f [fsimpson [list [list shift_1_iso [expr ($QIS1+$QIS2)/2-(-500)]] [list shift_2_iso
[expr ($QIS1+$QIS2)/2-(-500)]]]]
  set c 0
  for {set i 1} {$i <= $par(np)} {incr i} {
    incr c
    set Sr [findex $f $c -re]
    set Si [findex $f $c -im]
    puts $FileRe "[expr 1.0e3*$i/$par(sw)] [expr $Sr]"
    puts $FileIm "[expr 1.0e3*$i/$par(sw)] [expr $Si]"
    puts $FileAbs "[expr 1.0e3*$i/$par(sw)] [expr sqrt($Sr**2+$Si**2)]"
  }
}

```



```

}
funload $f
close $FileRe
close $FileIm
close $FileAbs
}

```

## Appendix B

### B.1. Pulse sequence for *D*-RINEPT using $SR4_1^2(270_090_{180})$ or $R12_3^5(270_090_{180})$ recouplings

```

;INEPT for non-selective polarization transfer
;with decoupling during acquisition
;made of 2 pulses
;different recoupling sequences and composite pulses available
;modified by Julien Trébosc and Jennifer Gómez (2020)
;AVANCE NEO

```

```

;d0 initial t1 evolution time (=0)
;d6 probe dead time (should be D6=DE)
;d7 RF offset delay
;d5 Delay after last recoupling for Tr/2
;d8 Delay after last recoupling for Tr/4
;p11 p1 and p2 power level
;p12 Heteronuclear dipolar decoupling
;p19 Presat pulse
;p2 not used
;p20 Presat pulse
;p21 p3 and p4 power level
;p22 initial spin lock
;p33 CW23 decoupling
;p43 CW45 decoupling
;p44 CW67 decoupling
;p11 dipolar recoupling power (sr4/sfam)
;spnam5 dipolar recoupling shape pulse
;sp5 power for recoupling shape
;p16 : requested recoupling time
;p17 : actual recoupling time
;l11 sr4/sfam repetition
;cnst30: Tanh/tan offset
;cnst31: spinning speed in Hz
;cnst3: Tanh/tan shape pulse step (ns)
;p1 90 degree pulse for X
;p2 180 degree pulse for X
;p3 90 degree pulse for 1H
;p4 180 degree pulse for 1H
;p6 pulse of the recoupling sequence
;p19 presat pulse for 1H
;p20 presat pulse for X
;p22 initial spin lock for Tr/2
;p23 initial spin lock for Tr/4

```

```

;p33 CW45 decoupling for Tr/2
;p34 CW45 decoupling for Tr/4
;p43 CW23 decoupling for Tr/2
;p44 CW67 decoupling for Tr/2
;p45 CW23 decoupling for Tr/4
;p46 CW67 decoupling for Tr/4

;d1 : relaxation delay; 1-5 * T1
;NS: 16 * n, total number of scans: NS * TD0
;DS: 16
;cpd1: decoupling during R3
;cpdprg1: decoupling during R3
;cpd2: decoupling during AQ and t1
;cpdprg2: decoupling during AQ and t1
;cpd3: decoupling during AQ
;cpdprg3: decoupling during AQ

#include <Avance.incl>

; storeVC option to store VClst used when popting MAS
#ifdef storeVC
#define VCstored vclab, 1u \n lo to vclab times c
#else
#define VCstored
#endif

;-))))))
#include "presat.incl"
;-)
#ifndef PRESATf2
#undef PRESAT2
#define PRESAT2(f2)
#endif
;-)
#ifndef PRESATf1
#undef PRESAT1
#define PRESAT1(f1)
#endif
;-((((((
;------ DECOUPLING -----
#include "decouple.incl"

#ifdef decF2
#define decF2off do:f2
#define decF2aqon cpds2:f2
#else
#define decF2aqon
#define decF2off
#endif

define delay RF
define delay dummy

#ifdef _SR4_cp1

```

```

;this is SR4 sequence using composite pulse 270(0)-90(180)
#define phaseRN (360) {{{90 270 270 90}*2}^180}^120^240
"p6=0.25s/cnst31"
"p7=p6*3/4.0" ; p270 deg
"p8=p6/4.0" ; p90 deg
; we have p6 = p7 + p8
;"111=trunc((p16/p6)/4+0.5)" ; +0.5 will round to nearest integer
"p17=2*p6*2*111"
"RF=250e3/p8"
"dummy=RF+p17"
#endif

```

```

#ifdef _R1235_cp1
;this is R12_3^5 sequence using composite pulse 270(0)-90(180)
#define phaseRN (360) 75 255 285 105
"p6=0.25s/cnst31"
"p7=p6*3/4.0" ; p270 deg
"p8=p6/4.0" ; p90 deg
; we have p6 = p7 + p8
;"111=trunc((p16/p6)/4+0.5)" ; +0.5 will round to nearest integer
"p17=2*p6*2*111"
"RF=250e3/p8"
"dummy=RF+p17"
#endif

```

```

;.....
"d24=p3"
"p2=p1*2"
"p4=p3*2"
;"d6=de"
"p22=0.5s/(cnst31)-p3/2.0"
"p23=0.25s/(cnst31)-p3/2.0"
"d5=0.5s/(cnst31)-d6"
"d8=0.25s/(cnst31)-d6"
"p33=0.5s/(cnst31)-p3"
"p34=0.25s/(cnst31)-p3-p4"
"p44=0.5s/(cnst31)-p4/2.0"
"p46=0.25s/(cnst31)-p4/2.0"
"p55=0.5s/(cnst31)-d6"
"p43=0.5s/(cnst31)-p4/2.0-p3"
"p45=0.25s/(cnst31)-p4/2.0"
"d7=0.00000005s"
"plw43=plw33"
"plw44=plw33"

```

```
"in0=inf1"
```

```

define delay showInAsed
"showInAsed=cnst3+dummy"

```

```

1 ze
VCstored
"showInAsed=cnst3+dummy"

```

```
2 30m decF2off
```

```

PRESAT2(f2)
d1 rpp16 rpp17 rpp14 rpp15 ; not necessary to use different phases and reset but...
PRESAT1(f1)
(10u pl21):f2 (10u pl1 ph2):f1
(p3 ph1):f2

```

```

#ifdef _iSL
if "l11 % 2 == 0"
{
(p22 pl22 ph27):f2
}
else
{
(p23 pl22 ph27):f2
}
#endif

```

```
d0
```

```

sr4_1, (p7 pl11 ph16^):f2
(p8 pl11 ph16^):f2
(p7 pl11 ph16^):f2
(p8 pl11 ph16^):f2
lo to sr4_1 times l11

```

```

if "l11 % 2 == 0"
{
(center (p3 pl21 ph18 p43 pl43 ph21 p4 pl21 ph2 p43 pl43 ph22 p3 pl21 ph18):f2 (p2
ph11):f1 )
}
else
{
(center (p45 pl43 ph18 p4 pl21 ph2 p45 pl43 ph18):f2 (p2 ph11):f1 )
}

```

```

sr4_2, (p7 pl11 ph17^):f2
(p8 pl11 ph17^):f2
(p7 pl11 ph17^):f2
(p8 pl11 ph17^):f2
lo to sr4_2 times l11

```

```

if "l11%2 == 0"
{
(center (p3 pl21 ph18 p33 pl33 ph23 p33 pl33 ph24 p3 pl21 ph3):f2 (p1 ph12):f1 )
}
else
{
(center (p4 pl21 ph5 p3 pl21 ph3 p34 pl33 ph21 p34 pl33 ph22 p4 pl21 ph5 p3 pl21 ph3):f2
(p1 ph12):f1 )
}

```

```

sr4_3, (p7 pl11 ph15^):f2
(p8 pl11 ph15^):f2
(p7 pl11 ph15^):f2

```

```

      (p8 pl11 ph15^):f2
    lo to sr4_3 times l11

if "l11%2 == 0"
{
  (center (p44 pl44 ph25 p4 pl21 ph2 p44 pl44 ph26):f2 (p2 ph13):f1 )
}
else
{
  (center (p46 pl44 ph25 p4 pl21 ph2 p46 pl44 ph26):f2 (p2 ph13):f1 )
}

sr4_4, (p7 pl11 ph14^):f2
      (p8 pl11 ph14^):f2
      (p7 pl11 ph14^):f2
      (p8 pl11 ph14^):f2
    lo to sr4_4 times l11

if "l11%2 == 0"
{
  d5 decF2aqon
}
else
{
  d8 decF2aqon
}
go=2 ph31
10u decF2off
30m mc #0 to 2 F1PH(ip1,id0)

HaltAQ, 1m

exit

ph0=0
ph2=0
ph3=0
ph4=0
ph5= (360) 45
ph6=0
ph7=0
ph10=0
ph11={ {0}*2 }^2
ph12={ {0}*4 }^2
ph13={ {0}*8 }^2^1^3
ph18=1
ph21=0
ph22=2
ph23=0
ph24=2
ph25=0
ph26=2
ph27=0 2
ph28=0
ph29=3

```

```

ph16= phaseRN
ph17= phaseRN
ph15= phaseRN
ph14= phaseRN

#ifdef opt1D
ph1=1 3 0 2
ph31=3 1 2 0
#else
ph1=1 3
ph31={{1 3}^0}^2}^0^2^2
#endif
presatPH

```

## B.2. Pulse sequence for *D*-HOMCOR-DQ-SQ using BR<sub>2</sub><sup>2</sup><sub>1</sub> recoupling

;DQ-SQ experiment for quadrupolar nuclei with +2 -> -2 DQ filter

```

;p11: RECOUPLING power
;p11: RECOUPLING pulse (180 pulse)
;p9: 90 pulse
;p19: 90 power
;p10: 180 pulse
;l11: RECOUPLING counter
;d3: z-filter (=100us)
;ZGOPTNS: -D_FAM -D_HS
;p11 not used
;cnst31 spinning speed
;p17 mixing time used
;ns multiple of 64
define delay showInAsed
"showInAsed=1u"
#ifdef _HS
;p2 HS pulse use HS.jt or dfs to generate
;cnst1 DFS start freq in kHz
;cnst2 DFS stop freq in kHz
;cnst3 shape step length in ns

"showInAsed=cnst3+cnst1+cnst2"
#endif

#ifdef _FAM
;p14 FAM power
;p22 FAM pulse
;l17 FAM loop
#endif

#include "presat.incl"
#ifdef PRESAT
#undef PRESAT1
#define PRESAT1(f1)

```

```

#endif

#ifdef decF2
#define decF2OFF do:f2
#define decF2ON cpds2:f2
#else
#define decF2OFF
#define decF2ON
#endif

"p11=1s/cnst31"

"p10=p9*2"

define delay Dmin
define loopcounter lmin
define delay delA
"Dmin=2u+p10+d0"
"lmin=Dmin*cnst31+1"
"delA=(lmin*(1s/cnst31)-2u-p10-d0)/2"

"in0=inf1"
define delay mixtime
"mixtime=111*4s/cnst31"
"p17=mixtime"

; not used if AVIII
;define delay dummy
;"dummy=mixtime"

1 ze ;accumulate into an empty memory
"p17=mixtime"
"showInAseed=1"
2 10m decF2OFF

"Dmin=2u+p10+d0"
"lmin=Dmin*cnst31+1"
"delA=(lmin*(1s/cnst31)-2u-p10-d0)/2"

PRESAT1(f1)

d1 ;recycle delay, decoupler off in go-loop

#ifdef _FAM
;;;;; FAM ;;;;;;;;;;;;;;
1u p14 :f1
55
(p22 ph3) :f1
0.4u
(p22 ph4) :f1
0.4u
lo to 55 times l17
;;;;; FAM -----;
#endif

```

```

#ifdef _HS
(p8:sp8 ph0 ):f1
#endif

20u

10u decF2ON
15
(p11 ph24 pl11):f1
(p11 ph25 pl11):f1
lo to 15 times l11

16
(p11 ph25 pl11):f1
(p11 ph24 pl11):f1
lo to 16 times l11

1u pl9:f1
delA
(p10 ph27):f1
delA
1u pl11:f1

d0
25
(p11 ph21 pl11):f1
(p11 ph22 pl11):f1
lo to 25 times l11

26
(p11 ph22 pl11):f1
(p11 ph21 pl11):f1
lo to 26 times l11

.....
d3
1u pl9:f1
(p9 ph28):f1
.....

go=2 ph31 decF2ON
1m decF2OFF
10m mc #0 to 2 F1PH(calph(ph24,+45) & calph(ph25, +45) & calph(ph27, +45)
,caldel(d0,+in0))
exit

;DQ CT selective pulse cycled on 8 phases mandatory
;ph27= (8) 0 0 0 0 2 2 2 2 4 4 4 4 4 4 6 6 6 6 ; wrong
ph27= (8) {0 0 0 0}^1^2^3^4^5^6^7
ph28={{0}*32}^2
ph9= (8) 2 ;1 1 1 1 2 2 2 2 3 3 3 3
ph24=(8) 0 2 4 6
ph25=(8) 4 6 0 2

```



```

ph21=0
ph22=2
ph31={ {0 2 0 2}^2^0^2^0^2^0^2}^2

```

```

; phases for CT enhancement
ph3=(8) {0}*32 {1}*32 {2}*32 {3}*32 {4}*32 {5}*32 {6}*32 {7}*32
ph4=(8) {4}*32 {5}*32 {6}*32 {7}*32 {0}*32 {1}*32 {2}*32 {3}*32
ph0=0
; set phases for presat : ph19 and ph20
presatPH

```

### B.3. Pulse sequence for *D*-HOMCOR-DQ-SQ using [BR2<sub>1</sub><sup>2</sup>] recoupling

```

;2D DQ excitation sequence br2-(1)-2 with CP and decoupling
;for setup of 1D experiments on labeled alanine
;for yield measurements

```

```

;$COMMENT=DQ excitation sequence mpcpbr212
;$CLASS=Solids
;$DIM=1D
;$TYPE=direct excitation
;$SUBTYPE=homonuclear correlation
;$OWNER=Bruker
;ns : n*64
;#include <trigg.incl>

```

```

#include <Avance.incl>
#ifdef PRESAT
#include "presat.incl"
#endif

```

```

;p12 decoupling power level
;pcpd2 : pulse length in decoupling sequence
;cpdprg2 : cw, tppm, spinal (at p12)

```

```

;;;;;;;;;;;;;qDQSQ-br212 part
;p11: RECOUPLING power
;p11: RECOUPLING pulse (180 pulse)
;p9: 90 pulse
;p10: 180 pulse
;p19: 90 power
;l0: RECOUPLING counter
;d3: z-filter (=100us)
;cnst31 spinning speed
"p11=1s/cnst31"
define delay mixtime
"mixtime=10*4s/cnst31"
define delay Dmin
"Dmin=2u+2*p10+d0"
define loopcounter lmin
"lmin=Dmin*cnst31+1"
define delay delA

```

```
"delA=(lmin*(1s/cnst31)-2u-2*p10-d0)/2"  
:qDQSQ-br212 part
```

```
define delay showInAsed  
"showInAsed=mixtime+delA"
```

```
"in0=inf1"
```

```
1 ze  
2 100m
```

```
"p11=1s/cnst31"  
"mixtime=10*4s/cnst31"  
"Dmin=2u+2*p10+d0"  
"lmin=Dmin*cnst31+1"  
"delA=(lmin*(1s/cnst31)-2u-p10-d0-2*p9)/2"
```

```
#ifdef PRESAT  
PRESAT1(f1)  
#endif
```

```
d1 do:f2
```

```
1u p11:f1 cpds2:f2
```

```
:qDQSQ-br212 part
```

```
(p9 ph4 pl9):f1  
4 (p11 ph23 pl11):f1  
(p11 ph24 pl11):f1  
lo to 4 times l0  
5 (p11 ph24 pl11):f1  
(p11 ph23 pl11):f1  
lo to 5 times l0  
(p9 ph5 pl9):f1
```

```
1u pl9:f1  
delA  
(p10 ph6):f1  
delA  
1u  
d0
```

```
(p9 ph7 pl9):f1  
6 (p11 ph25 pl11):f1  
(p11 ph26 pl11):f1  
lo to 6 times l0  
7 (p11 ph26 pl11):f1  
(p11 ph25 pl11):f1  
lo to 7 times l0  
(p9 ph8 pl9):f1
```

```

0.3u do:f2
d3
1u pl9:f1 cpds2:f2
(p9 ph28):f1
go=2 ph31
1m do:f2
,,,,,,,,,,,,,,,,,,,,,,,,,,,,,,,,,,,,qDQSQ-br212 part

100m mc #0 to 2 F1PH(calph(ph4, +45) & calph(ph23, +45) & calph(ph24,+45) &
calph(ph5, +45) & calph(ph6, +45), caldel(d0,+in0))
exit

;NSmin = 64
;Delta p = +2 or -2 for first [BR2] block
ph4=(8) 2 4 6 0
ph23=(8) 0 2 4 6
ph24=(8) 4 6 0 2
ph5=(8) 6 0 2 4

;Delta p = +2 or -2 for central pi pulse
ph6=(8) {0 0 0 0}^1^2^3^4^5^6^7

ph7=(8) 4
ph25=(8) 2
ph26=(8) 6
ph8=(8) 0

;Delta p = -1 for reading pulse
ph28={{0}*32}^2
ph31={{0 2 0 2}^2^0^2^0^2^0^2}^2
#ifdef PRESAT
presatPH
#endif

```

## Appendix C

### AU program for shearing the DQ-SQ HOMCOR 2D spectra

```

/*****
/*   babaAU.jt                21-10-2005                */
/*****
/*   Short Description :                */
/*   Program for shearing of 2D BABA spectra                */
/*   can be used for apodisation of any 2D spectrum were echo */
/*   occurs along any slope */
/*   Data need to be aquired in                */
/*   States States-TTPI or Echo-Antiecho Mode                */
/*
/*****
/*   Keywords :                */
/*   shear, double quantum, BABA C7 , exchange                */
/*****
/*   Description/Usage :                */
/*   Program is used                */
/*   a) for 2D MQ experiments on                */
/*   including 2DFT and referencing in F1 dimension                */
/*   A F1 frequency shift in ppm is asked for to compensate */
/*   for malchosen o1 setting. This value is stored and                */
/*   suggested for any repeated processing.                */
/*****
/* author : Julien TREBOSC */
/* e-mail julien.trebosc@univ-lille1.fr */
/* program adapted from xfshear 2005 */
/*****
/* trebosc                20051021                created
/* trebosc                20051103                fix bug when TDEFF applied
*/
/*****
/* BUGS :
/*
/*           one must have SI>= TD
*/

#include <math.h>

void calculateShear(char *curdat ,double ratio,   double F1shift, double *ph0, double
*ph1,double *ph2) ;
void doshear(char *,double , double, double ) ;
void newdoshear(char *, double ,double , double ) ;

void apod(char *curdat) ;
void fetchparmod(char *curdat,int *wdw, int *phmod, int *bcmmod, int *ftmod, int *memod) ;
void zeroparmod(char *curdat) ;
void storeparmod(char *curdat,int wdw, int phmod, int bcmmod, int ftmod, int memod) ;
void ft2(char *curdat);
void ift2(char *curdat);
void xfb(char *curdat) ;
```

```

int parmode;
int mq, nspin, wdw2, bcmmod, phmod, stsr2, stsi1, stsi2, fnmode, mc2;
int option1=0, option2=0;

double ratio, final, ph0, ph1, ph2;

float Noise, spin, offset1, offset2, off2, off1, sr2, sr1;

char nucl[80], yes[20],
      pulprog[80], ti[80], ShearOpt[PATH_MAX];

// select current dataset
// =====
GETCURDATA;
(void) strepy (yes,"yes");

// is-it a 2D spectrum and taken in States, States-TPPI or EA?
// =====
FETCHPARS("PPARMOD",&parmode);
if ( parmode != 1 )
  { STOPMSG("Program is only suitable for 2D data!");}
FETCHPAR1S("FnMODE",&fnmode);
if ( fnmode == 0 ) {
  FETCHPAR("MC2",&mc2);
  if ( mc2 != 3 && mc2 != 4 && mc2 != 5 ) STOPMSG("mc2 must be States, States-
TPPI, or Echo-Antiecho!");
}
else if ( fnmode != 4 && fnmode != 5 && fnmode != 6 ) STOPMSG("FnMode must be in
States, States-TPPI, or Echo-Antiecho!");

// if auto selected, don't aks for ABS2 and additional F1 shift
// =====

// automatic baseline correction for MQMAS and STMAS ?
// =====
FETCHPARS("USERP1",yes);
GETSTRING("Apply ABS2 ? : ",yes);

// additional F1 shift ?
// =====
f1=0.;
FETCHPAR1S("NOISF1",&Noise);
FETCHPARS("TI",ti);
if (!strcmp(ti,"shearing done")) f1=Noise;
if (mq != 1) GETFLOAT(" F1 shift in ppm ? : ",f1);

// init some variables
// =====
FETCHPAR("WDW",&wdw2)
STOREPAR("WDW",0)

ratio=2.;
final=1.;

```

```

GETDOUBLE(" Enter initial slope ratio :",ratio);
GETDOUBLE(" Enter final slope ratio :",final);

// ignore all strip parameters
// =====
        FETCHPAR("STSI",&stsi2);
        FETCHPAR1("STSI",&stsi1);
        STOREPAR("STSR",0);
        STOREPAR("STSI",0);
        STOREPAR1("STSR",0);
        STOREPAR1("STSI",0);
        if (stsi2 != 0 || stsi1 != 0) Proc_err(0,"Strip-FT not yet
implemented,\nparameters disabled");

// calculate F2 transform
// =====
SETCURDATA
XPY("apod2D")
XF2
// AUERR=CPR_exec( "xf2 raw",WAIT_TERM);
if ( yes[0]!='y') {ABS2 XHT2}
int PH_mod2;
FETCHPAR("PH_mod",&PH_mod2)
STOREPAR("PH_mod",0)
calculateShear(curdat, ratio, f1, &ph0, &ph1, &ph2);

newdoshear(curdat, ph0, ph1, ph2);
//Apply apodisation
// ift2(curdat);
// apod(curdat);
// ft2(curdat);
// shift time domain back to t=0 with final R ratio
newdoshear(curdat,-ph0,-ph1/ratio*final,0);

// direct shearing
//newdoshear(curdat,/*ph0=*/0,ph1/*ratio*/(ratio-final)*/0);

// store TI to recall shearing and shifting
// =====
STOREPARS("TI","shearing done");
STOREPAR1S("NOISF1",f1);
STOREPARS("USERP1",yes);

// inverse F2 and subsequent F2+F1 transform
// =====
XHT2
ift2(curdat);
xfb(curdat);
STOREPAR("PH_mod",PH_mod2)
VIEWDATA
QUITMSG(" Shearing-FT done!")

//=====
//=====

```

```

//=====
void calculateShear(char *curdat ,double ratio, double F1shift, double *ph0, double
*ph1,double *ph2) {
//=====
//=====
        double sw2,dw2,sfo1 ;
        float swh1;
        int si2,td,n,tdeff;

        FETCHPARS("SW_p",&sw2);
        FETCHPARIS("SWH", &swh1);
        FETCHPARS("SFO1",&sfo1);
        FETCHPARS("SI",&si2);
        FETCHPARS("TDEFF",&tdeff);
        FETCHPARS("TD",&td);
        if (tdeff>0 && tdeff<td) td=tdeff;

// calculate phase for shearing and scaling for MQMAS/STMAS F1
// =====
        *ph0= -M_PI * td / 2 /(double)(si2);
// *ph1= -2.*3.141529*ratio*sw2 / swh1 / (double)(si2);
        *ph1 = -M_PI * ratio * sw2 / swh1 / (double)si2;

// additional F1 shift
// =====
// *ph2= -2.*3.141529*F1shift*sfo1/(double)swh1;
        *ph2= -M_PI * F1shift * sfo1 / swh1;

}

// =====
// =====
// =====
void newdoshear(char *curdat , double ph0,double ph1, double ph2) {
//=====
//=== ph0 shift in t2 ; ph1 shear in F1 ; ph2 shift in F1 ===
// ph0 is a first order phase applied in F2 that will shift echo in time (t2) after IFT
// ph1 is first order phase in t1/f2 (proportional to t1 and f2) to produce shearing
// ph2 is first order phase in t1 only (proportional to t1) to shift resonances in F1
//=====
        char name2rr[PATH_LENGTH],name2ir[PATH_LENGTH];
        int loopcount1, loopcount2, loopcount3, loopcount4;
        int *in2rr,*in2ir;
        int nbytes, sizeofint, nbytesread, xdim2, xdim1 ;

        int si2, si1, tdeff1, infile2rr,infile2ir;
        off_t pos = 0;

/* get required status parameters after F2 transform
===== */
        FETCHPARS("SI",&si2)
        FETCHPARS("XDIM",&xdim2)
        FETCHPARIS("SI",&si1)

```

```

FETCHPAR1S("XDIM",&xdim1)
FETCHPAR1S("TDef",&tdeff1)
// read 2 submatrix rows
nbytes = xdim2 * (2 * (int)sizeof(int));

/* allocate memory for I/O buffer
===== */
in2rr = (int*)malloc(nbytes);
if (in2rr == 0)
    STOPMSG("Not enough memory");

in2ir = (int*)malloc(nbytes);
if (in2ir == 0)
    STOPMSG("Not enough memory");

/* Open source file RR
===== */
sprintf(name2rr,"%s/%s/%d/pdata/%d/2rr",
        disk, name, expno, procno);
infile2rr = open(name2rr, O_RDWR);

if (infile2rr == -1)
{
    /* on Windows GUI may access */
    sleep(1); /* 2rr exclusively */
    infile2rr = open(name2rr, O_RDWR); /* second attempt */
}

if (infile2rr == -1)
{
    Perror(DEF_ERR_OPT, name2rr);
    return -1;
}

/* Open source file IR
===== */
sprintf(name2ir,"%s/%s/%d/pdata/%d/2ir",
        disk, name, expno, procno);
infile2ir = open(name2ir, O_RDWR);

if (infile2ir == -1)
{
    /* on Windows GUI may access */
    sleep(1); /* 2ir exclusively */
    infile2ir = open(name2ir, O_RDWR); /* second attempt */
}

if (infile2ir == -1)
{
    Perror(DEF_ERR_OPT, name2ir);
    return -1;
}

Show_status("shearing calculation");

```



```

/* Read data in submatrix
===== */

/*
file is read in submatrix 2 rows by 2 rows (even and odd)
data are (f2,t1) with t1 in States or States-TPPI
loopcount1 contains the global index of current submatrix in t1
loopcount2 contains the global index of current submatrix in f2 (0 is the spectrum center)
loopcount3 is the t1 index within a submatrix
loopcount4 is the f2 index within a submatrix
this means that global index in the full matrix coordinates is
    loopcount1+loopcount3 for t1 dimension
and loopcount2+loopcount4 for f2
*/

for (loopcount1 = 0; loopcount1 < tdeff1; loopcount1 += xdim1) {
  for (loopcount2 = -si2 / 2; loopcount2 < si2 / 2; loopcount2 += xdim2)
  {
    for (loopcount3 = loopcount1; loopcount3 < loopcount1 + xdim1 &&
        loopcount3 < tdeff1; loopcount3 += 2)
    {

      if ((nbytesread=read(infile2rr,in2rr,nbytes)) != nbytes) /* Read 2 rows ! */
      {
        if (nbytesread < 0)
          Perror(DEF_ERR_OPT, name2rr);
        else
          Proc_err(DEF_ERR_OPT, "%s\nread off file limits", name2rr);

        return -1;
      }
      if ((nbytesread=read(infile2ir,in2ir,nbytes)) != nbytes) /* Read 2 rows ! */
      {
        if (nbytesread < 0)
          Perror(DEF_ERR_OPT, name2ir);
        else
          Proc_err(DEF_ERR_OPT, "%s\nread off file limits", name2ir);

        return -1;
      }

      for (loopcount4 = 0; loopcount4 < xdim2; loopcount4++)
      {
//      evr is real/even (Sx_r) value with coordinates (F2 | t1)=(loopcount2+loopcount4 |
loopcount3 /2)
        double evr = in2rr[loopcount4];
        double odr = in2rr[loopcount4 + xdim2];
        double evi = in2ir[loopcount4];
        double odi = in2ir[loopcount4 + xdim2];
        double ph = (ph1 * (loopcount2 + loopcount4) + ph2) * loopcount3;
        double phc0 =ph0*(loopcount2 + loopcount4);
        double co = cos(ph);
        double si = sin(ph);
        double co0 = cos(phc0);

```

```

    double si0 = sin(phc0);

/* perform shearing transformation
===== */
    double xr= (evr * co + odr * si);
    double yr= (odr * co - evr * si);
    double xi= (evi * co + odi * si);
    double yi= (odi * co - evi * si);

    in2rr[loopcount4]      = (int)(xr);
    in2rr[loopcount4 + xdim2] = (int)(yr);

//    in2rr[loopcount4]      = (int)(xr * co0 - xi * si0);
//    in2rr[loopcount4 + xdim2] = (int)( yr * co0 - yi * si0);
//    in2ir[loopcount4]      = (int)(xr * si0 + xi * co0 );
//    in2ir[loopcount4 + xdim2] = (int)(yr * si0 + yi * co0);
    }

/* Save
===== */
    if (lseek(infile2rr, pos, SEEK_SET) == -1 ||
        write(infile2rr,in2rr,nbytes) < 0)
    {
        Perror(DEF_ERR_OPT, name2rr);
        return -1;
    }
/*
    if (lseek(infile2ir, pos, SEEK_SET) == -1 ||
        write(infile2ir,in2ir,nbytes) < 0)
    {
        Perror(DEF_ERR_OPT, name2ir);
        return -1;
    }
*/
    pos += nbytes;
    }
    if (loopcount1 + xdim1 > tdeff1)
        pos += nbytes * ((loopcount1 + xdim1 - (tdeff1 - 1)) / 2);
    }
}
close(infile2rr);
close(infile2ir);

    }

void fetchparmod(char *curdat,int *wdw, int *phmod, int *bcmmod, int *ftmod, int *memod) {
    FETCHPAR("WDW",wdw);
    FETCHPAR("BC_mod",bcmmod);
    FETCHPAR("PH_mod",phmod);
    FETCHPAR("FT_mod",ftmod);
    FETCHPAR("ME_mod",memod);
}

void zeroparmod(char *curdat) {
    STOREPAR("WDW",0);
}

```

```

STOREPAR("BC_mod",0);
STOREPAR("PH_mod",0);
STOREPAR("FT_mod",0);
STOREPAR("ME_mod",0);
}

void storeparmod(char *curdat,int wdw, int phmod, int bcm, int ftmod, int memod) {
STOREPAR("WDW",wdw);
STOREPAR("BC_mod",bcm);
STOREPAR("PH_mod",phmod);
STOREPAR("FT_mod",ftmod);
STOREPAR("ME_mod",memod);
}

void apod(char *curdat) {
int wdw, phmod, bcm, ftmod, memod;
float lb=-0.;
fetchparmod(curdat, &wdw, &phmod, &bcm, &ftmod, &memod);
zeroparmod(curdat);
STOREPAR("WDW",2);
STOREPAR("GB",0.5);
FETCHPAR("LB",&lb);
if (lb>0.0) {lb=-lb; STOREPAR("LB",lb);}
XTRFP2;
storeparmod(curdat, wdw, phmod, bcm, ftmod, memod);
}

void ft2(char *curdat) {
int wdw, phmod, bcm, ftmod, memod;
fetchparmod(curdat, &wdw, &phmod, &bcm, &ftmod, &memod);
zeroparmod(curdat);
STOREPAR("FT_mod",6);
XTRFP2
storeparmod(curdat, wdw, phmod, bcm, ftmod, memod);
}

void ift2(char *curdat) {
int wdw, phmod, bcm, ftmod, memod;
fetchparmod(curdat, &wdw, &phmod, &bcm, &ftmod, &memod);
zeroparmod(curdat);
STOREPAR("FT_mod",2);
XTRFP2
storeparmod(curdat, wdw, phmod, bcm, ftmod, memod);
}

void xfb(char *curdat) {
int wdw, phmod, bcm, ftmod, memod;
fetchparmod(curdat, &wdw, &phmod, &bcm, &ftmod, &memod);
zeroparmod(curdat);
CPR_exec("xfb nc_proc 0",WAIT_TERM);
storeparmod(curdat, wdw, phmod, bcm, ftmod, memod);
}

```